

## Abstract

# Teleported operations between logical qubits in circuit quantum electrodynamics

Kevin S. Chou

2018

A quantum computer has the potential to efficiently solve problems that are intractable for classical computers. Constructing a large-scale quantum processor, however, is challenging due to errors and noise inherent in real-world quantum systems. One approach to this challenge is to utilize modularity—a pervasive strategy found throughout nature and engineering—to build complex systems robustly. Such an approach manages complexity and uncertainty by assembling small, specialized components into a larger architecture. These considerations motivate the development of a quantum modular architecture, where separate quantum systems are combined via communication channels into a quantum network. In this architecture, an essential tool for universal quantum computation is the teleportation of an entangling quantum gate, a technique originally proposed in 1999 which, until now, has not been realized deterministically. Using the circuit quantum electrodynamics platform, this thesis reports on the experimental demonstration of a teleported controlled-NOT operation made deterministic by utilizing real-time adaptive control. Additionally, we take a crucial step towards implementing robust, error-correctable modules by enacting the gate between logical qubits, encoding quantum information redundantly in the states of superconducting cavities. Such teleported operations have significant implications for fault-tolerant quantum computation, and when realized within a network can have broad applications in quantum communication, metrology, and simulations. Our results illustrate a compelling approach for implementing multi-qubit operations on logical qubits within an error-protected quantum modular architecture.

# Teleported operations between logical qubits in circuit quantum electrodynamics

A Dissertation  
Presented to the Faculty of the Graduate School  
of  
Yale University  
in Candidacy for the Degree of  
Doctor of Philosophy

by  
Kevin S. Chou

Dissertation Director: Robert Schoelkopf

May 2018

Copyright © 2018 by Kevin S. Chou  
All rights reserved.

# Contents

<b>Contents</b>	iii
<b>List of Figures</b>	vi
<b>List of Tables</b>	viii
<b>Acknowledgements</b>	x
<b>1 Introduction</b>	<b>1</b>
1.1 The digital computing revolution . . . . .	1
1.2 Information processing with quantum mechanics . . . . .	2
1.3 Challenges facing quantum computing . . . . .	4
1.4 Overview of thesis . . . . .	6
<b>2 Quantum information concepts</b>	<b>9</b>
2.1 Quantum information in closed systems . . . . .	10
2.1.1 From bit to qubit . . . . .	11
2.1.2 Multiple qubits and qudits . . . . .	13
2.1.3 Unitary operations . . . . .	15
2.1.4 Quantum measurement . . . . .	19
2.2 Quantum information in open systems . . . . .	21
2.2.1 Density operator . . . . .	21
2.2.2 Quantum operations formalism . . . . .	23
2.2.3 Quantum channels on a single qubit . . . . .	25
2.2.4 Extracting information about quantum states . . . . .	27
2.2.5 Types of quantum operations . . . . .	30
2.3 Entanglement . . . . .	31
2.3.1 Bell's Inequality . . . . .	33
2.3.2 Quantum teleportation . . . . .	36
2.4 Assessing quantum states and processes . . . . .	37
2.4.1 Measures of quantum states . . . . .	39
2.4.2 Measures of quantum processes . . . . .	43
2.5 Toward quantum information processing . . . . .	44
2.5.1 DiVincenzo criteria . . . . .	44
2.5.2 Quantum error correction . . . . .	48

2.5.3	Toward fault-tolerant quantum computation	54
<b>3</b>	<b>Superconducting qubits and cQED</b>	<b>56</b>
3.1	Building blocks of quantum circuits	58
3.1.1	Quantum LC oscillator	59
3.1.2	Adding the Josephson junction	63
3.1.3	Quantum circuits with Josephson junctions	64
3.2	Quantum electrodynamics with circuits and cavities	68
3.2.1	Jaynes-Cummings Hamiltonian	69
3.2.2	Quantizing nonlinear quantum circuits	71
3.2.3	Common cQED Hamiltonians	80
3.3	Quantum control	85
3.3.1	Applying a classical drive	85
3.3.2	Off-resonant drives	87
3.3.3	Dispersive qubit measurement	88
3.4	Conclusion	90
<b>4</b>	<b>Experimental hardware</b>	<b>93</b>
4.1	3D cQED device design and implementation	93
4.1.1	3D cavities	94
4.1.2	3D transmon qubits	98
4.1.3	Constructing cQED devices	100
4.1.4	Building modular hardware	107
4.2	Experimental control hardware	108
4.2.1	Device preparation: thermalization and shielding	109
4.2.2	Microwave control lines	110
4.2.3	Experimental control hardware	114
<b>5</b>	<b>Experimental techniques</b>	<b>117</b>
5.1	Basic system tuneup	118
5.1.1	Finding the system modes	118
5.1.2	Tuning up readout	121
5.1.3	Measuring coherences	123
5.2	Transmon and cavity operations	125
5.2.1	Qubit rotations	125
5.2.2	Cavity displacements	127
5.2.3	Complex transmon-cavity operations	128
5.3	System Hamiltonian characterization	131
5.3.1	General methods	133
5.3.2	self-Kerr of transmon and cavity	136
5.3.3	cross-Kerr between qubit and cavity	140
5.3.4	cross-Kerr between two qubits	144
5.3.5	cross-Kerr between two cavities	147
5.4	State preparation	151
5.5	Analysis methods	155

5.5.1	Quantum state tomography . . . . .	155
5.5.2	Quantum process tomography . . . . .	160
5.5.3	Reconstruction techniques . . . . .	161
<b>6</b>	<b>Teleportation of a quantum gate</b>	<b>163</b>
6.1	Modular quantum systems . . . . .	164
6.1.1	The quantum modular architecture . . . . .	165
6.2	Basics of gate teleportation . . . . .	167
6.2.1	Walkthrough of the teleported gate . . . . .	168
6.3	Logical qubits . . . . .	170
6.3.1	Binomial logical encoding . . . . .	171
6.3.2	Fock encoding . . . . .	172
6.4	Physical implementation . . . . .	172
6.4.1	Device implementation . . . . .	172
6.4.2	System characterization . . . . .	174
6.4.3	Assessing independence of the modules . . . . .	177
6.5	Implementation of the teleported CNOT protocol . . . . .	179
6.6	Assembling the teleported gate . . . . .	180
6.6.1	Generating communication qubit Bell pair . . . . .	180
6.6.2	Implementing local operations . . . . .	183
6.6.3	Measurement and feedback . . . . .	190
6.6.4	Analyzing transmon reset . . . . .	191
6.7	Tuning up the teleported CNOT . . . . .	193
6.7.1	Logical vs. Reference phases . . . . .	193
6.7.2	Reference phases due to Bell state generation . . . . .	195
6.7.3	Reference phases due to measurements . . . . .	196
6.7.4	Communication qubit measurement basis . . . . .	198
6.8	Demonstrating the teleported CNOT gate . . . . .	200
6.8.1	Generating the CNOT truth table . . . . .	200
6.8.2	Generating a logical Bell state . . . . .	202
6.8.3	Upper bound to logical Bell state fidelity . . . . .	203
6.8.4	Analyzing the role of feedforward . . . . .	207
6.8.5	Quantum Process tomography . . . . .	208
6.9	Extended Teleported CNOT results . . . . .	209
6.9.1	Teleported CNOT performance . . . . .	209
6.10	Error budget . . . . .	213
6.10.1	Contributions to infidelity . . . . .	217
6.11	Discussion . . . . .	217
<b>7</b>	<b>Conclusions and perspectives</b>	<b>220</b>
7.1	Future work toward the quantum modular architecture . . . . .	221
7.1.1	Remote modules . . . . .	221
7.1.2	Towards error-correctable logical gates . . . . .	223
7.1.3	Building the quantum module . . . . .	224
7.1.4	Connecting the modules . . . . .	226

7.1.5 Tools to applications . . . . .	226
7.2 Closing remarks . . . . .	226
<b>Bibliography</b>	<b>228</b>

# List of Figures

2.1	The Bloch Sphere . . . . .	12
2.2	Rotations about the Bloch Sphere . . . . .	17
2.3	Examples of single-qubit quantum channels . . . . .	28
2.4	Types of quantum channels . . . . .	32
2.5	State teleportation circuit . . . . .	38
3.1	Quantum LC oscillator . . . . .	59
3.2	The Josephson junction and Transmon qubit . . . . .	66
3.3	Jaynes-Cummings energy spectrum . . . . .	72
3.4	Black-box quantization circuits . . . . .	75
3.5	Common cavity-transmon primitives . . . . .	81
3.6	Dispersive cQED measurement . . . . .	92
4.1	Survey of 3D cavity implementations . . . . .	95
4.2	Examples of transmon and 3D cavity integration . . . . .	101
4.3	Experimental wiring diagram . . . . .	113
5.1	Spectroscopy experiments . . . . .	120
5.2	Cavity displacement calibration . . . . .	128
5.3	Characterization experiments for optimal control pulses . . . . .	132
5.4	General techniques for extracting Hamiltonian parameters . . . . .	133
5.5	Cavity frequency and self-Kerr . . . . .	138
5.6	Qubit number-splitting spectroscopy . . . . .	143
5.7	Transmon-cavity Ramsey interferometry . . . . .	145
5.8	Transmon-Transmon cross-Kerr measurement via Ramsey interferometry . . . . .	148
5.9	Cavity-readout cross-Kerr measurement via Stark shifts . . . . .	150
5.10	Feedback cooling sequences . . . . .	154
6.1	Constructing a quantum modular architecture . . . . .	166
6.2	Quantum modules and the teleported CNOT circuit . . . . .	168
6.3	Logical Bloch sphere for the binomial code encoding . . . . .	172
6.4	Overview of teleported gate device . . . . .	175
6.5	Experimental realization of the teleported gate . . . . .	176
6.6	Detailed circuit diagram for the teleported CNOT gate protocol . . . . .	181
6.7	Teleported CNOT gate timing diagram . . . . .	182

6.8	RIP gate tune-up protocol . . . . .	184
6.9	Generation of communication qubit Bell pair . . . . .	185
6.10	Assessing independence of single qubit measurements . . . . .	192
6.11	Communication qubit measurement and reset . . . . .	194
6.12	Measurement reference phase due to Bell state generation . . . . .	197
6.13	Measurement-induced reference phase shift . . . . .	199
6.14	Communication qubit 2 measurement angle . . . . .	201
6.15	Teleported CNOT truth table . . . . .	202
6.16	Quantum correlations of a logical Bell state . . . . .	204
6.17	State reconstruction for the logical Bell state . . . . .	206
6.18	Quantum state tomography of logical Bell state . . . . .	207
6.19	Effect of feedforward operations . . . . .	209
6.20	Quantum process tomography of the teleported CNOT gate . . . . .	210
6.21	Extended Binomial QPT data . . . . .	211
6.22	xtended Fock QPT data . . . . .	212

# List of Tables

6.1	System coherences . . . . .	174
6.2	Measured Hamiltonian parameters . . . . .	178
6.3	Local operation infidelities . . . . .	188
6.4	Experimental process fidelities . . . . .	213
6.5	Error budget, theory . . . . .	217

# Acknowledgements

During my time in graduate school, I have had the great fortune to be surrounded and supported by so many fantastic people. In the lab, I have worked with and learned from some of the smartest and talented researchers that I know; these same colleagues continually amaze me with their patience and generosity. Outside of the lab, I have had the support of a great circle of family and friends, and my experience during graduate school would have been far less without you. All of you have made this journey that much more fulfilling, and for that you have my immense gratitude.

First and foremost, I thank my advisor Rob Schoelkopf for the opportunity to work in your lab for the past six years. His vision and approach to research is continually inspiring and motivating. Rob has the uncanny ability to quickly determine the essence of whatever we were talking about, asking probing questions that will turn out to be important later on. Additionally, he has given me the latitude to determine how to tackle problems myself, allowing me to develop experience in developing and managing complex projects. I have learned not only how to be a better scientist from Rob, but also discovered the importance of communicating it effectively. However, perhaps the most important lesson I have learned from Rob is that a waveguide is, indeed, a high pass-filter.

Michel Devoret has played a crucial role in expanding my understanding of physics and has constantly amazed me with both his breadth and depth of knowledge. His insights and ability to explain complicated topics with clarity is inspirational (and aspirational). Michel is incredibly generous with his time; his patience is inspiring, scheduling meetings that go late into the weekend night to explain physics to a first-year graduate student. I admire Michel's thoroughness and

attention to detail in all sorts of matters, from physics to the particular shade of green for an electron.

I have had the great fortune to collaborate with Liang Jiang for the two main projects in my thesis. He is always eager to listen to my questions and from our discussions is able to propose creative and useful solutions. It is often that I leave Liang's office with renewed optimism and excitement, and working with Liang has been a wonderful and productive experience for me.

I would also like to acknowledge and thank Steve Girvin and Dan Prober for the support over the years. I have always appreciated discussions with Steve, who is somehow able provide such concise insight while juggling so many other responsibilities all at the same time. Dan has an enthusiasm for science that is infectious and inspiring, and he is also an encyclopedia for all things related to superconductivity.

I would be sorely remiss without thanking Luigi Frunzio. He has taught me everything there is to know about device fabrication and keeps all parts of the lab running smoothly. He is in many ways a perpetual machine with his boundless (youthful, even) enthusiasm that permeates throughout the research groups.

I worked closely with Jacob Blumoff for the majority of graduate school, starting from our first year building a wooden "sound insulation" box for a new dilution refrigerator in BCT 412. Since then we have moved on to make superconducting boxes, tackling projects that require building arguably the most complex devices in the lab. Somehow, between the two of us, we were able to make sense of it all. He is persistent in his drive to provide an intuitive understanding for whatever he approaches, and his focus—evidenced by his knack for making to-do lists—continues to inspire me today. Jacob has indubitably made me a better scientist and researcher, and I am glad to be able to call him both a colleague and a friend.

Most recently, I have had the pleasure of working with Chris Wang and Sal Elder. Chris joined Jacob and myself for the later stages of the gate teleportation project. In short time, he successfully navigated this complex project and was able to tackle some of the numerical simulations to benchmark the gate performance. Chris approaches research with a critical eye that will serve him well in graduate school and beyond. Sal, even as a first year graduate student,

has become a productive member of the lab. His insightful questions are matched by his creative solutions, which has led to the successful development of the “boson buffer”. I am confident that the next generation of the lab will be well positioned to accomplish great things.

Much of my success in graduate school was the direct product of working with Matt Reed on the flux-tunable 3D transmon experiment in the first few years of graduate school. Matt was instrumental in training me to be a cQED experimentalist, patiently teaching me—sometimes, more than a few times—how to properly setup an experiment: from the microwave engineering required to wire up a fridge to the many techniques necessary for controlling an experiment. He showed me that it was possible to handle a complex experiment by taking a systematic approach so that even the most confusing issues became tractable. Matt is a talented scientist, both from his experimental prowess, but more importantly, because of his generosity and willingness to offer a helping hand.

I would also like to thank Andrew Houck, James Sturm, and John Bollinger for instilling in me an excitement for research and science during my undergraduate years. The lessons (and sometimes painful mistakes) I learned in these early days have served me well during my graduate school, and I will always remember that the devil is in the details. I would also like to thank John Bollinger for serving as my external reader for this dissertation.

I also would like to acknowledge my Applied Physics and Physics cohort in Becton—Teresa Brecht, Eric Jin, Zlatko Mineev, Anirudh Narla, Jacob Blumoff, and Uri Vool. They were among the first people I met at Yale, and I have been fortunate to remain close friends and colleagues throughout graduate school.

To all the graduate students and postdocs—past and present—that have made working in the 4<sup>th</sup> floor of Becton and at YQI a motivating and fun experience everyday. You all have brought your own perspective and expertise to bear on some challenging problems, and I am constantly amazed at the creativity of your solutions. I am very fortunate to be surrounded by so many motivated and driven individuals who have simultaneously shown me camaraderie and have made working with all of you a truly special experience.

In particular, I would like to thank several people for their technical contributions that enabled

the experimental work described in this dissertation. First, I would like to thank Nissim Ofek, Yehan Liu, Reinier Heeres, and Phil Reinhold for developing the FPGA-based control hardware that has enabled many of our modern experiments. The real-time adaptive control capabilities afforded by this controller enabled the gate teleportation experiment. I would also like to thank the Qulab amplifier team—Michael Hatridge, Katrina Sliwa, Anirudh Narla, and Nick Frattini—both for providing me with an exquisite selection of the finest quantum limited amplifiers of all varieties and for teaching me how to properly calibrate and use these devices. On the hardware side, I would like to acknowledge Matt Reagor and Chris Axline for developing the latest generation of experimental devices that used for the experiments in this dissertation. Matt spearheaded the effort to build increasingly long-lived 3D cavities and to understand how to preserve such performance when integrating 3D transmons. Chris developed the aptly named “co-axline resonators” that have become the standard for readout resonators. Finally, on the equipment side of things, I would like to thank Anirudh Narla and Chris Axline who served as the “fridge masters” and ensured the health and safety of all the dilution refrigerators. I learned a great deal about fridge disaster management from Anirudh and Chris as we addressed emergencies at all hours of the day (and night). Additionally, Anirudh and Chris, along with myself, formed the Applied Plumbing (AP) team in Becton. Thank you both for your assistance (and moral support) in plugging water leaks, power failures, and anything else Becton held in store for us.

Finally, there are many people in the lab I have had the pleasure of working with that I would like to acknowledge: Chris Axline, Luke Burkhart, Yiwon Chu, Nick Frattini, Yvonne Gao, Kurtis Geerlings, Alex Grimm, Reinier Heeres, Eric Holland, Gerhard Kirchmair, Zaki Leghtas, Chan U Lei, Brian Lester, Shantanu Mundadha, Zlatko Minev, Nissim Ofek, Hanhee Paik, Andrei Petrenko, Wolfgang Pfaff, Ioan Pop, Matt Reagor, Philip Reinhold, Serge Rosenblum, Adam Sears, Kyle Serniak, Shyam Shankar, Katrina Sliwa, Luyan Sun, Steven Touzard, Ioannis Tsioutsios, Brian Vlastakis, Uri Vool, Chen Wang, and Evan Zalys-Geller.

I would also like to thank Giselle DeVito, Maria Rao, Terri Evangeliste, Nuch Graves, Florian Carle, Racquel Miller, and Devon Cimini for all the help over the years. Much of my graduate work was possible in large part because of your efforts. I appreciate the warmth you have always

shown me.

To my dancing friends of Yale Swing, Blues, & Fusion, I thank you for providing me with a wonderfully warm and welcoming community—Isabel Bate, Anne Carroll, Ning Dai, Adam Goff, Eric Jin, Nell McGloin-King, Susan Knox, Rasmus Kyng, Laurel McCormack, Emily Pan, Dan Rathbone, Dov Salkoff, Meaghan Sullivan, Renee Wasko, and many more. You have always been able to put a smile on my face even during the most difficult times. Please save a swing-out for me the next time we dance!

I have been very fortunate to meet some fantastic people outside of working in the lab: Michael Chang, Greg Hutchings, Michelle Hutchings, Eric Jin, Thoe Michaelos, Angela Steinauer, Andrew Sinclair, and Julie Sinclair. Our (somewhat) regularly scheduled weekend dinners at “Narli’s Kitchen” will be a gathering that I will cherish for many years to come.

Finally, I would like to thank my family: my parents, Shih-Hung Chou and Chi-Huei Yu, and my brother Alan Chou. Their selfless support and confidence in me have gotten me to where I am today. My gratitude to them cannot be stated enough. I would like to also thank Min-Young Kim, my partner and friend who has made the last few years of graduate school such a wonderful time of my life.

I am indebted to each of you and feel humbled to know so many excellent people whom I can call colleagues and friends. Thank you all!

# 1

## Introduction

### 1.1 The digital computing revolution

The development of digital computing has ushered an era of rapid technological progress that still continues even today [1]. As with many technological advances, the demands of war provided the impetus for the development of modern electronic computation. The second World War saw a need to speed up calculations necessary for the war effort. Initially, trajectory calculations for long-range artillery were performed by an army of “human” computers, using mechanical devices like the Differential Analyzer (a mechanical contraption used to numerically integrate differential equations) to aid in the calculations. However, because each calculation relied on numerous parameters—each new shell required tables for all sorts of environmental factors—compiling firing tables was a tedious and detailed process taking on the order of weeks to months to complete, a rate far too slow to win the war. This set the stage for the development of the *electronic digital* computer, one that used vacuum tubes in place of the ball-and-disk integrator central to mechanical devices, initially proposed by researchers at the Moore School in Philadelphia. One result of this effort was the *Electronic Numerical Integrator and Computer* (ENIAC), though arriving too late to play a large role in winning the war, was an impressive feat of engineering, combining disparate technologies together to produce a machine that could perform calculations close to one hundred times faster than even the most nimble human computer. The ENIAC and later versions found much use toward performing calculations necessary for the hydrogen

bomb. Building upon this early demonstration of electronic computing, John von Neumann led the construction of one of the first general-purpose and universal, or Turing-complete, computers and also codified the architecture upon which all modern computers are based, aptly named the von-Neumann architecture.

Our demands for ever more computational power to solve ever more complicated problems have lead to breathtaking capabilities, from atomic bomb calculations in the 1950s and 1960s to advanced machine learning algorithms today that can best even the greatest human Go player [2]. Despite these advances, there remain problems that are difficult or even impossible to solve even with our most powerful supercomputers. Furthermore, the celebrated “Moore’s Law” scaling of computing power may be leveling off, and recent advances in computing have more to do with advances in power consumption or parallelism rather than clock speed or more transistors. Fortunately, quantum technologies have emerged as a promising candidate to address some of these concerns, and this thesis will focus on one particular aspect of quantum computation. To set the stage for this thesis, we begin by motivating why there is a broad interest in quantum computing, what we mean by quantum information and computing, and finally, how this thesis contributes to the quantum computing field in general.

## 1.2 Information processing with quantum mechanics

Arguably, the field of computation with quantum mechanics began with the insight by Richard Feynman that complex physical systems that are described quantum mechanically may be efficiently simulated with a universal quantum simulator [3]. A few years later, David Deutsch extended the ideas of universal computability via a Turing machine to quantum systems and suggested that universal quantum computers would have computational capabilities beyond that of classical computers [4]. The first proposals for quantum algorithms with practical applications occurred a decade later with two key discoveries illustrating that a quantum computer can solve certain problems more efficiently than any known classical computer. In 1994, Peter Shor proposed a quantum algorithm [5] for integer-factorization based on an efficient implementation

of the quantum Fourier transform that performs exponentially faster than typical classical algorithms. Because factorization is at the heart of almost all RSA-type public-key cryptography strategies, the development of this algorithm has deep implications for secure communication and spurred new interest by information-gathering security agencies around the world. A few years later, Lev Grover [6] developed a general-purpose quantum algorithm that offers a polynomial speedup ( $\mathcal{O}(\sqrt{N})$  vs.  $\mathcal{O}(N)$ ) to the problem of database search, one of the most fundamental computational problems to-date; this algorithm was later proved to be the optimal quantum solution [7, 8]. Among other examples, these two algorithms provided tangible evidence that a quantum computer may have certain benefits over classical computers. However, it is widely believed that a quantum computer will not be able to address the central question in computational complexity whether NP (problems that are verifiable in polynomial time, but may not be solvable in polynomial time) problems may be solved in polynomial time (e.g. does  $P = NP$ ?). It is an open research question to understand the extent of the advantage of quantum devices over classical computers [9, 10], and new insights in the future may allow us to qualify the previous statement. Fortunately, there is a parallel research effort to determine problems of intermediate difficulty that quantum computers may be well suited for; for example, one direction gaining popularity is to apply quantum devices to solve quantum simulation and chemistry problems. Such problems have immediate practical consequences and it is possible that near-term quantum processors will be directed to solve similar problems.

On initial inspection, a quantum computation is structured similarly to classical computation: both require encoding information and manipulating this information to effect a particular outcome that is the answer. For quantum information, this information is now encoded within the states of a quantum system, and we refer to the fundamental unit of quantum information as a quantum bit, or qubit. Quantum systems are represented not as definite states, but simultaneously as a superposition of all possible intermediate states. This property leads to a feature known as quantum parallelism where all possible input state may be operated upon simultaneously. In order for this parallelism to be computationally useful, manipulations of this quantum information during a particular computation should transform the system into the correct answer. This

is accomplished through judiciously designing manipulations to take advantage of interference, where the states that correspond to incorrect answers will destructively interfere and the states that correspond to the correct answer will constructively interfere and have a high probability of being measured. Because these systems obey the rules of quantum mechanics, in order to effect quantum computation, it is necessary to develop a new set of tools to control, manipulate, and extract this information. Ultimately, classical information must be extracted from quantum systems to learn of the outcome of a particular computation; as such, quantum play an important role in quantum information—it is the only way that we, as “classical computers”, can see observe the result of the quantum algorithm.

### 1.3 Challenges facing quantum computing

Despite the thirty years that have spanned since the discovery of the first quantum algorithms, experimental efforts to realize quantum computers are still quite nascent. Chief among the challenges facing quantum computation is the presence of errors that befall any quantum system, which, if left unchecked, will cause a given quantum computation to fail. Thus, one of the first requirements when developing a platform for quantum computation is to sufficiently isolate the quantum system from the surrounding environment. To quantify this, we discuss the coherence of a quantum system, or the length of time that quantum information is accurately stored in the system before the information is lost to the environment. While such isolation improves the robustness of quantum systems, it also reduces controllability as well as the ability of an individual quantum systems to interact with one another. For successful quantum computation, all three are necessary. Additionally, despite consistent improvements in coherences, it is still unclear (and seems highly unlikely) whether these quantum systems can attain the low errors rates similar to classical systems that are required for reliable quantum computation<sup>1</sup>.

This conundrum has a fortunate resolution, that of quantum error correction [11, 12, 13,

---

1. Modern transistors have soft error rates around  $10^{-4}$  errors per billion hours of operation, while the best quantum bits that are used in superconducting qubits have memory error rates of  $\sim 100Hz$ . Soft errors in classical computers are generally caused by high-energy radiation and can induce correlated errors across the chip. Even with these small error rates, most computers do execute classical error correcting codes.

14]. In such a paradigm, instead of encoding information within a single physical qubit where decoherence would completely destroy the quantum information, quantum information is instead encoded across several individual physical qubits in a redundant fashion so that an error on any physical qubit can be detected, and if designed cleverly, also corrected. This collection of physical qubits encoded to allow the detection and correction of errors composes what is called a logical qubit. While the discovery of quantum error correction was a truly remarkable feat, it also introduced additional complexity to any error-corrected quantum computation. Importantly using multiple physical qubits to store a single quantum bit, the base error rate of the logical qubit will first increase and possibly introduce new types of errors. Additionally, manipulations on logical qubits will require a complex series of manipulations on the constituent physical qubits, which can reduce the performance of logical operations necessary for quantum computation. Ultimately, it will be necessary to address other types of errors, including those induced by manipulations—logical operations, measurements, and error correction operations—on quantum information to enable fault-tolerant quantum computation. Designing an appropriate logical qubit, much like designing an appropriate physical qubit, is an omnipresent task in the quantum information community; experiments, like those presented in this thesis will aid in understanding how to design these more complex systems.

Our chosen platform of superconducting qubits and cavities offers an attractive approach to build a quantum computer. Within the circuit quantum electrodynamics paradigm, it is possible to tailor the Hamiltonian with high precision, affording us the capability to work with “designer atoms”. These devices are fairly straightforward to assemble, typically consisting of a lithographically fabricated device on a sapphire or silicon substrate. As we will see, the introduction of high-Q superconducting cavities has opened the door to a new way to use these structures for quantum computation, where the cavities themselves store the quantum information. Finally, control over these superconducting devices can take advantage of the extensive industry of microwave-frequency components and are easily adapted for use in our experiments. Superconducting qubits are rapidly maturing as a quantum technology with individual coherences and performances sufficient to construct increasingly complex devices.

While the two main experimental projects performed in this thesis, of which we will describe one, investigate fairly distinct areas of quantum information processing, there are a few unifying motifs that tie the essence of this thesis together. The work presented here focuses on combining individual quantum systems and technologies that have been demonstrated in isolation to implement new capabilities that are greater than the sum of their parts. As these systems become more complex, it will be ever more important to develop strategies for manipulating them and for understanding how to characterize and benchmark their performance. A critical challenge when scaling up quantum systems in any platform is the simultaneous goal of maintaining coherences and control while mitigating crosstalk and residual interactions. A thorough discussion of the first experiment can be found in the thesis of Jacob Blumoff [15]. Here, instead of repeating such content, here we will instead focus on the lessons learned from constructing and controlling a multi-qubit experiment. The second experiment will be the focus of this thesis, namely the deterministic teleportation of a two-qubit gate between two logical qubits. In this experiment, the two logical qubits are not directly interacting, and we implement a teleported controlled-NOT (CNOT) gate between them. The implementation of a teleported gate is an important ingredient for a modular quantum computation, and its implementation is being actively pursued here in the Yale quantum information group.

## 1.4 Overview of thesis

This thesis reports on the experimental realization of a teleported quantum operation using superconducting qubits.

We start with a broad and short overview of quantum information in [chapter 2](#), introducing several concepts that will be useful throughout this thesis. We describe quantum bits, operations on quantum systems, and measurement. Additionally we describe quantum entanglement, the essential feature of quantum mechanics that we utilize for quantum computation. We then describe methods by which we characterize and assess quantum states and processes. From here we go detail some of the outstanding challenges toward building a quantum computer, for

which we will need quantum error correction to one day realize fault-tolerance in our quantum computation.

**chapter 3** describes our chosen quantum information platform, superconducting qubits and circuit quantum electrodynamics (cQED). We first describe how we can treat electrical circuits quantum mechanically and make the connection that we have the tools necessary to construct such quantum electrical circuits. We introduce the Josephson junction as the critical circuit element with which we construct all of our superconducting qubits. Having described these tools, we introduce circuit quantum electrodynamics as our approach to build our superconducting quantum systems. We describe black-box quantization as a method for extracting the Hamiltonian of an arbitrary nonlinear circuit network. From here, we discuss the dispersive Hamiltonian and go through several common examples to better motivate the more complicated devices used in this thesis. We conclude this chapter by briefly explaining how we achieve quantum control over our superconducting qubits, detailing both how we apply classical drives to manipulate our qubits and how we perform dispersive measurements.

In **chapter 4** we discuss the physical realization of our superconducting qubits with a focus on some guidelines and design considerations for constructing our cQED devices. We focus on the three-dimensional (3D) cQED architecture, describing several designs for 3D cavities and 3D transmons. We describe how these two fundamental building blocks can be combined to give us access to the wonderful physics described in the previous two chapters. Furthermore, we briefly discuss some of the benefits from our 3D approach from a practical perspective. We then turn to describe our control hardware. We first briefly describe how our device preparation and how they are cooled in a dilution refrigerator before turning to the microwave control lines. We emphasize the importance of good microwave hygiene to ensure that noise on our input and output lines are sufficiently suppressed through the combination of filters, attenuators, and directional components. We end this chapter with a brief discussion of how we control and program our experiments.

Having a foundation for designing, constructing, and preparing a cQED device, we turn to describe our experimental techniques in **chapter 5**, with an emphasis for extracting the parameters

of a cQED Hamiltonian. We describe methods for extracting a host of Hamiltonian parameters. We describe several methods and explain the relative trade-offs for various parameter regimes. The organization of this section roughly follows a standard cQED bring-up and can serve as a checklist for a system characterization. As our experimental devices grow in complexity, so do the requirements of careful and thorough characterization. Any experiment begins with state preparation and we describe one method for initializing in the ground state. We close this section by discussing how we characterize quantum states and processes through tomography.

The techniques and methods discussed in the previous chapters enable the experiment described in [chapter 6](#). Here, we detail the implementation of a teleported CNOT gate between two logical qubits. We start by describing the quantum modular architecture, a promising approach for building a quantum computer. We detail the teleported circuit and our implementation of this protocol using superconducting qubits and cavities. We then detail the implementation of each component required for this protocol. We then assemble all of these components to realize the teleported gate, and we present a thorough characterization of the entire gate. We establish that the behavior of the gate closely matches the expectation from device parameters and from the performance of each individual component. The teleported gate is a fundamental building block for the quantum modular architecture and we explore several future directions to improve its performance.

Finally, in [chapter 7](#), we offer perspective of the accomplishments of this thesis and use these to describe some possible next steps for the quantum modular architecture. The result of the teleported CNOT gate provides more confidence that such an architecture can be made a reality. There are, of course, many area that require further investigation and development, such as the integration of quantum error correction and the demonstration of this teleported operation between *remote* modules. While the challenges toward realizing a fully-fledged quantum computer remain numerous and formidable, the rapid progress achieved by superconducting qubits and by quantum information as a whole lend some (cautious) optimism that quantum information processing can and will be a useful technology in the years to come.

# 2

## Quantum information concepts

This initial chapter sets the theoretical groundwork that is fundamental to all quantum information processing. Unifying the various approaches for quantum computation are the requirements of state initialization, quantum operations, and quantum measurements [16, 17]. In [section 2.1](#), we start with a treatment of quantum computations with closed quantum systems, where the dynamics of the system are completely encapsulated by the Hamiltonian. We introduce the representations of quantum states, starting from a single quantum bit of information in [subsection 2.1.1](#) to describing multi-dimensional systems in [subsection 2.1.2](#) where we introduce harmonic oscillators as a particularly useful example. Having established a firm description of the state vector, we proceed to describe quantum operations in [section subsection 2.1.3](#), paying close attention to single-qubit and two-qubit quantum gates in [Equation 2.1.3](#) as well as harmonic oscillator displacements in [Equation 2.1.3](#). In [subsection 2.1.4](#), we describe how to perform measurements to complete our discussion on closed quantum systems.

The second part of this chapter deals with quantum information of open quantum systems, where the system of interest couples to other uncontrolled degrees of freedom. In [subsection 2.2.1](#), we introduce the density operator as the representation of general quantum states, particularly those that have classical uncertainty. We then describe two representations of quantum operations in [subsection 2.2.2](#) and provide several examples of single-qubit quantum channels [subsection 2.2.3](#). With this formalism in hand, we can describe the quantum measurements in a more general context in [section 2.2.4](#).

Quantum entanglement is a critical feature of quantum mechanics used repeatedly throughout this thesis. As a primer, we provide an introduction in section 2.3, focusing on distinguishing quantum and classical correlations and providing a specific example of quantum state teleportation. This example provides a striking example of entanglement and how it enables quantum systems to perform otherwise impossible operations. In addition, this serves as a useful precursor to the demonstration of a teleported gate in chapter 6.

Experimental characterization of quantum states and processes is crucial for assessing the quality of a quantum computation. Such verification and validation requires defining quality measures to describe how well we have done. In section 2.4, we introduce two common measures—fidelity and distance—and describe several ways these can be used as a quantitative metric to compare states and processes.

The remaining section of this chapter provides a broader perspective of quantum computation. In particular, we outline the DiVincenzo criteria in subsection 2.5.1, a canonical set of properties that any practical quantum computer should have. We then detail some of the practical challenges facing the construction of a quantum computer. In particular, quantum error correction is necessary to deal with unavoidable noise and errors in any real-world quantum system. In addition to error correction, a practical quantum computer will need a strategy to perform computation using imperfect components and operations. We end this brief introduction by describing the fundamentals for fault-tolerant quantum computation and the threshold theorem.

## 2.1 Quantum information in closed systems

We first explore the fundamental concepts of quantum computation in the context of closed quantum systems, where the quantum state is isolated from any other system, quantum or classical. This introduction serves to treat several ideas in a simple context to be further developed later in this chapter and throughout this thesis. We begin with a discussion of representations of quantum states, starting from the simplest description—a two-dimensional quantum system—and moving to higher-dimensional multi-qubit and multi-level systems. With these states defined,

we can move to a discussion of how to manipulate these states by applying unitary operations. Finally, we describe the measurement process for extracting information from a quantum state.

### 2.1.1 From bit to qubit

In classical information processing, the fundamental unit is called the bit, a description of a physical system that has two possible states, generically labeled “0” and “1”. A coin that is either heads-up or tails-up can physically represent a bit of information. On the other hand, a quantum bit, or qubit, is superficially similar, but introduces a richer set of possibilities. The qubit state space is spanned by two states, represented as  $|0\rangle$  and  $|1\rangle$ . Crucially, quantum mechanics allows a quantum state to exist as a superposition; that is, a qubit may exist simultaneously in both states. We represent a qubit state via the wavefunction

$$|\psi\rangle = a|0\rangle + b|1\rangle. \quad (2.1)$$

The amplitudes  $a$  and  $b$  are complex numbers subject to the normalization constraint  $|a|^2 + |b|^2 = 1$ . The probability that we find the state in  $|0\rangle$  is  $|a|^2$ , and likewise the probability we find the state in  $|1\rangle$  to be  $|b|^2$ . For this reason, these coefficients are often called probability amplitudes. With the normalization constraint, we can recast the qubit state vector by re-parameterizing the probability amplitudes and instead write

$$\begin{aligned} |\psi\rangle &= \cos\left(\frac{\theta}{2}\right)e^{i\phi_0}|0\rangle + \sin\left(\frac{\theta}{2}\right)e^{i\phi_1}|1\rangle \\ &\rightarrow \cos\left(\frac{\theta}{2}\right)|0\rangle + \sin\left(\frac{\theta}{2}\right)e^{i\phi}|1\rangle, \end{aligned} \quad (2.2)$$

where  $\theta$  and  $\phi = \phi_1 - \phi_0$  represent the longitudinal and azimuthal angle of the state vector, respectively. In the second line, we factor out an unnecessary global phase. Equation 2.2 leads to a useful geometrical representation called the “Bloch sphere.” The quantum state  $|\psi\rangle$  can be described as a vector on the surface of a unit sphere. The angle  $\theta$  indicates the projection onto the z-axis and the angle  $\phi$  indicates the angle about the z-axis.

Quantum states are specified according to some Hamiltonian; for example, the simplest

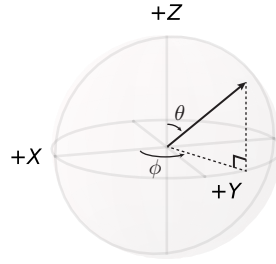


Figure 2.1 | **The Bloch Sphere.** A pure quantum state can be represented as a vector on a unit sphere, parameterized by a polar ( $\theta$ ) and azimuthal ( $\phi$ ) angle.

Hamiltonian that defines a qubit can be written as

$$\mathcal{H}_{\text{qubit}} = \frac{\hbar\omega}{2}\sigma_z \quad (2.3)$$

where  $\sigma_z$  is one of the *Pauli operators*

$$\hat{\sigma}_x \equiv \begin{pmatrix} 0 & 1 \\ 1 & 0 \end{pmatrix} \rightarrow \hat{X} \quad \hat{\sigma}_y \equiv \begin{pmatrix} 0 & -i \\ i & 0 \end{pmatrix} \rightarrow \hat{Y} \quad \hat{\sigma}_z \equiv \begin{pmatrix} 1 & 0 \\ 0 & -1 \end{pmatrix} \rightarrow \hat{Z}. \quad (2.4)$$

The basis states  $|0\rangle$  and  $|1\rangle$  are eigenstates of  $Z$  with energies  $\pm\hbar\omega/2$ , respectively. As a result, we will sometimes refer to the basis states as  $|\pm Z\rangle$  to emphasize they are the  $\pm 1$  eigenstates of  $\sigma_z$ . Similarly, we can write down the eigenstates for the other Pauli operators:

$$\begin{aligned} |\pm X\rangle &= \frac{1}{\sqrt{2}} (|0\rangle \pm |1\rangle) \\ |\pm Y\rangle &= \frac{1}{\sqrt{2}} (|0\rangle \pm i|1\rangle) \\ | +Z\rangle &= |0\rangle; | -Z\rangle = |1\rangle \end{aligned} \quad (2.5)$$

These states have a useful Bloch sphere representation: the eigenstates for each of the Pauli matrices represent the poles along the respective axes (e.g.  $\sigma_x \rightarrow x$ ) in the Bloch sphere representation.

**Distinguishing a qubit from a bit** How is a quantum bit distinct from a probabilistic classical bit, like a weighted coin? After all, the fact that there is a relative phase between  $|0\rangle$  and  $|1\rangle$  is not important when we consider the probability of finding the qubit in  $|0\rangle$  or  $|1\rangle$ . Let's consider an example where this relative phase is crucial. The answer lies in that a quantum bit has a multitude of representations, while a classical bit only has one [18].

The representation of the quantum state in the  $\{|0\rangle, |1\rangle\}$  basis described above is known as the “computational basis.” We may choose to represent the state in a different basis. Consider the state  $|\psi\rangle = |0\rangle$ . We can describe the state in the  $X$  basis described in Equation 2.5 as  $|\psi\rangle = (|+X\rangle + |-X\rangle)/\sqrt{2}$ . What is the probability that the state is in  $|0\rangle$ ? Classically, we are either in  $|+X\rangle$  or  $|-X\rangle$  with probability  $1/2$ . In either case, we will be in  $|0\rangle$  half of the time. Therefore, the total probability that we get  $|0\rangle$  is  $1/2$ . But, obviously the correct answer is that we will find  $|0\rangle$  with unit probability. The addition of probability amplitudes leads to interference effects that may add constructively or destructively in ways that we will not observe classically. In section 2.2 we will formalize when there is classical uncertainty in quantum states.

### 2.1.2 Multiple qubits and qudits

We can, of course, put multiple qubits together to produce a multi-partite quantum state. To achieve this, we use a mathematical tool called the tensor product to specify a new Hilbert space that spans the combined system. For a two-qubit system, the basis now consists of four states:  $\{|0\rangle_1 \otimes |0\rangle_2, |0\rangle_1 \otimes |1\rangle_2, |1\rangle_1 \otimes |0\rangle_2, |1\rangle_1 \otimes |1\rangle_2\}$ , which we will typically shorten to  $|i\rangle_1 \otimes |j\rangle_2 \rightarrow |ij\rangle$ . We describe this state with four complex amplitudes:  $|\psi\rangle = a|00\rangle + b|01\rangle + c|10\rangle + d|11\rangle$  with the normalization constraint  $|a|^2 + |b|^2 + |c|^2 + |d|^2 = 1$ . With three qubits, we have eight complex amplitudes. With  $N$  qubits, we will have to specify probability amplitudes for  $2^N$  basis states<sup>1</sup>. This exponential growth in complexity affords us many of the interesting opportunities for quantum information processing, as we will see over the course of this thesis.

We can also have quantum states that encode information in more than just two levels.

1. The normalization constraint and the insignificance of a global phase removes two parameters, leaving a total of  $2^{N+1} - 2$  real numbers to specify an  $N$ -qubit state

These states are called *qudits* and span  $d$  levels:  $\{|0\rangle, |1\rangle, \dots, |d\rangle\}$ . The multi-level structure of qudits implies that multiple quantum bits of information can be stored by these systems. For example, a  $d = 4$  qudit encodes two bits of quantum information and has the same size Hilbert space as a two-qubit system—both are described with four complex numbers. The distinction, then, is that the latter is composed of two single-qubit subsystems while the former is a single quantum entity.

### Harmonic oscillator

The quantum harmonic oscillator is characterized by an infinite-level (or dimensional) Hilbert space where the energy difference between consecutive levels is equal. A harmonic oscillator is characterized by the following Hamiltonian

$$\mathcal{H} = \hbar\omega \left( \hat{a}^\dagger \hat{a} + \frac{1}{2} \right), \quad (2.6)$$

where  $\hat{a}$  is the annihilation operator and  $\hbar\omega$  is the characteristic energy (or frequency) difference. The eigenstates of the harmonic oscillator are given as Fock states,  $|n\rangle$ , each with fixed photon number  $n$ . Here we include the zero-point energy term so that the ground state  $|0\rangle$  has a non-zero energy of  $\hbar\omega/2$ ; for most future calculations we will drop this term. Typically, we are interested in energy differences, and a static offset in the Hamiltonian does not influence the dynamics. A harmonic oscillator quantum state can be expressed in the Fock basis,

$$|\psi\rangle = \sum_{n=0}^{\infty} c_n |n\rangle, \quad (2.7)$$

with probability amplitudes  $\{c_n\}$ .

In addition to Fock states, we often use coherent states [19, 20]. These states are characterized not by a distinct photon number, but rather by an average position  $\langle x \rangle$  and momentum  $\langle p \rangle$  that minimizes the Heisenberg uncertainty relation between these conjugate variables. Just as an oscillating pendulum has a well defined amplitude and phase, a coherent state can also be described by a complex amplitude  $\alpha = |\alpha|e^{i\phi}$ . Importantly, this state  $|\alpha\rangle$  is an eigenstate of the

annihilation operator  $\hat{a}|\alpha\rangle = \alpha|\alpha\rangle$ , a key relation that is the basis for quantum error correction with harmonic oscillators [21]. In the Fock basis, a coherent state is described as

$$|\alpha\rangle = e^{-|\alpha|^2/2} \sum_{n=0}^{\infty} \frac{\alpha^n}{\sqrt{n!}} |n\rangle, \quad (2.8)$$

with probability amplitudes  $c_n$  following a Poisson distribution. Note that while the coherent state has a well-specified amplitude and phase (up to the limits imposed by the Heisenberg uncertainty principle), the photon number is not well-defined; in contrast, for a Fock state, the photon number is well-specified, but no well-defined phase.

What may be taught in an introductory quantum mechanics class is that a harmonic oscillator is a terrible quantum system to use to encode quantum information: if all energy levels are equally spaced, how does one isolate two to specify a qubit? We will see over the course of this thesis how we actually can utilize a harmonic oscillator for quantum information processing.

### 2.1.3 Unitary operations

Now that we can represent the state of a quantum system, in order to effect a computation, we need an additional ingredient: the ability to effect changes to the system. In quantum mechanics, the equation of motion for a quantum state is governed by the Schrodinger equation,

$$i\hbar \frac{d|\psi\rangle}{dt} = \mathcal{H}(t)|\psi\rangle. \quad (2.9)$$

For a time-independent Hamiltonian  $\mathcal{H}(t) \rightarrow \mathcal{H}$ , the evolution of the quantum state is given simply by  $|\psi(t)\rangle = U(t)|\psi(t=0)\rangle$  where  $U(t) = \exp(-i\mathcal{H}t/\hbar)$ . If the initial state is an eigenstate with eigenenergy  $E_i$  of the Hamiltonian  $\mathcal{H}$ , then the evolution merely applies a phase to the state,  $|\psi(t)\rangle = e^{-iE_it/\hbar}|\psi(t=0)\rangle$ . A general state (with non-definite energy) can be decomposed as a superposition of eigenstates  $\{|\psi_i\rangle\}$  each with eigenenergy  $\{E_i\}$ :  $|\psi\rangle = \sum_i c_i |\psi_i\rangle$ , with quantum amplitudes  $c_i$ . The evolution under a static Hamiltonian will take this state to  $|\psi(t)\rangle = \sum_i c_i e^{-i\omega_i t} |\psi_i\rangle$ , where each term rotates at a frequency  $\omega_i = E_i/\hbar$ . More generally, evolution under a time-dependent Hamiltonian will cause transitions between eigenstates, which

we use to our advantage when performing a quantum computation.

### Gates on qubits

A common set of unitary operations on qubits is generated by the set of Pauli matrices (Equation 2.4). These are often called rotation operators, as they induce a rotation around a particular axis of the Bloch sphere (Figure 2.2). They are given as

$$\begin{aligned}\hat{R}_x(\theta) &\equiv \hat{X}_\theta = e^{-i\theta\sigma_x/2} = \begin{pmatrix} \cos \frac{\theta}{2} & -i \sin \frac{\theta}{2} \\ -i \sin \frac{\theta}{2} & \cos \frac{\theta}{2} \end{pmatrix} \\ \hat{R}_y(\theta) &\equiv \hat{Y}_\theta = e^{-i\theta\sigma_y/2} = \begin{pmatrix} \cos \frac{\theta}{2} & -\sin \frac{\theta}{2} \\ \sin \frac{\theta}{2} & \cos \frac{\theta}{2} \end{pmatrix} \\ \hat{R}_z(\theta) &\equiv \hat{Z}_\theta = e^{-i\theta\sigma_z/2} = \begin{pmatrix} e^{-i\theta/2} & 0 \\ 0 & -e^{-i\theta/2} \end{pmatrix}.\end{aligned}\tag{2.10}$$

These can be combined to define a generalized rotation operator around any axis  $\hat{n} = (n_x, n_y, n_z)$ :

$$\hat{R}_{\hat{n}}(\theta) \equiv e^{-i\theta\hat{n}/2} = \cos\left(\frac{\theta}{2}\right) \mathbb{1} - i \sin\left(\frac{\theta}{2}\right) (n_x\hat{\sigma}_x + n_y\hat{\sigma}_y + n_z\hat{\sigma}_z).\tag{2.11}$$

For example, a  $\pi$ -pulse around the y-axis is given as  $\hat{Y}_\pi = i\hat{\sigma}_y$  and a  $\pi/2$ -pulse around the x-axis is given as  $\hat{X}_{\pi/2} = (\mathbb{1} - i\hat{\sigma}_x)/\sqrt{2}$ . In many of our experiments, we use a finite set of rotations with angles  $\theta = \pm\pi/2, \pm\pi$ , often called  $\pi/2$ - and  $\pi$ -pulses. This allow access to all six of the cardinal points of the Bloch sphere, are preferred by experimentalists, and are members of the Clifford group<sup>2</sup>. Another useful single-qubit gate is the Hadamard gate ( $\hat{H}$ -gate), which is a

2. From [22], the Clifford group is defined as a subgroup of unitary operations on  $N$  qubits,  $U(2^N)$ , generated by the composition of three types of gates applied to any combination of qubits:  $H$ -gates,  $S$ -gates, and CNOT gates. The  $S$ -gate, or phase-shift gate, is defined as  $S = \begin{pmatrix} 1 & 0 \\ 0 & i \end{pmatrix}$ .

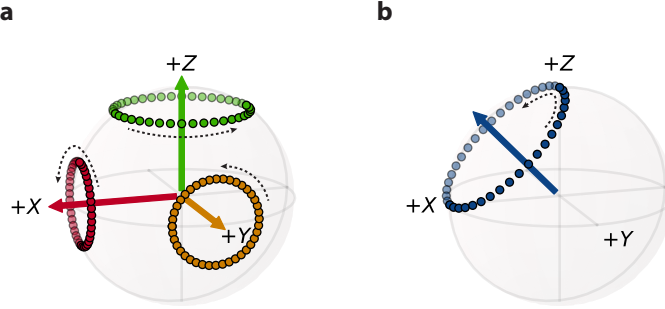


Figure 2.2 | **Rotations about the Bloch Sphere.** **a** The three Pauli operations,  $\sigma_x$ ,  $\sigma_y$ , and  $\sigma_z$ , generate rotations about the respective axes in the Bloch sphere representation. For each, we represent the effect of each rotation  $R_i(\theta)$  at differing angles  $\theta$ . **b** We apply the Hadamard rotation,  $R_H(\theta) = \exp(i\theta\hat{H}/2)$  for varying  $\theta$ . The Hadamard operator generates effects a rotation about the  $(\hat{X} + \hat{Z})/2$  axis.

rotation of  $\theta = \pi$  around the  $\hat{n} = (\hat{X} + \hat{Z})/\sqrt{2}$  axis, is given as

$$\hat{H} = \frac{1}{2} \begin{pmatrix} 1 & 1 \\ 1 & -1 \end{pmatrix} \quad (2.12)$$

and can be generated up to a global phase factor using three gates:  $\hat{H} = \hat{X}_{\pi/2}\hat{Z}_{\pi/2}\hat{X}_{\pi/2}$ . Alternatively, the Hadamard gate can be constructed from two rotations,  $\hat{X}_{\pi}\hat{Y}_{\pi/2}$ . The Hadamard gate is useful for construction quantum circuits because it performs a basis transformation from  $\hat{Z}$  to  $\hat{X}$ ; that is, the Hadamard gate takes  $|0\rangle \rightarrow |+X\rangle$  and  $|1\rangle \rightarrow |-X\rangle$ . It is also important to note that the Hadamard is distinct from a  $\pi/2$ -pulse: two applications of the Hadamard gate effects an identity operation  $\hat{H}\hat{H} = \mathbb{1}$ , while such is not true for two applications of a  $\pi/2$ -pulse (which would of course effect a  $\pi$ -pulse).

Manipulations on multiple qubits admit a much richer set of unitary operations. In addition to simple products of single qubit gates, there are two-qubit gates that operate distinctly within a two-qubit Hilbert space and cannot be separated. Controlled operations are one common family of two-qubit gates. Similar to conditional gates in classical boolean logic, these operations enact an operation on a target qubit conditioned on the state of a control qubit. In contrast to classical

logical gates, controlled quantum gates operate on the superposition states and are the basis for generating entanglement between qubits, which we will describe in more detail in [section 2.3](#). These controlled operations, when combined with single-qubit gates (for example, the  $H$ -gate and a non-Clifford operation such as the  $T$ -gate, a  $\pi/4$ -rotation about the  $Z$ -axis<sup>3</sup>), form a set of controls necessary for universal quantum computation [[16](#), [22](#)].

The controlled-NOT (CNOT) and controlled-PHASE (CPHASE) gates are perhaps the two most common two-qubit gates found in quantum algorithms. Both gates take a two qubit state as an input and return a two qubit state as an output. The two gates are described by the following unitaries

$$\hat{U}_{CNOT} = \begin{pmatrix} 1 & 0 & 0 & 0 \\ 0 & 1 & 0 & 0 \\ 0 & 0 & 0 & 1 \\ 0 & 0 & 1 & 0 \end{pmatrix} \quad \hat{U}_{PHASE} = \begin{pmatrix} 1 & 0 & 0 & 0 \\ 0 & 1 & 0 & 0 \\ 0 & 0 & 1 & 0 \\ 0 & 0 & 0 & -1 \end{pmatrix} \quad (2.13)$$

The CNOT operation performs a NOT operation (e.g.  $X$ -gate) on the target qubit if the first is in the excited state:  $\hat{U}_{CNOT} = |0\rangle\langle 0| \otimes \mathbb{1} + |1\rangle\langle 1| \otimes \hat{X}$ . The CNOT gate is most similar to a classical XOR operation in which one input bit is copied as an output: both have the same truth table when acting on the set of product states. Of course, quantum gates can operate upon quantum superpositions, so the truth table plays a only small part of the characterization of a two-qubit gate. For example, if we act the CNOT gate on a superposition state  $(|00\rangle + |10\rangle)/\sqrt{2}$ , the resulting state is the entangled state  $(|00\rangle + |11\rangle)/\sqrt{2}$ , which cannot be described by a product of single qubit states. We will revisit this crucial property of quantum states in [section 2.3](#).

While the CNOT gate is preferred by when describing algorithms, the CPHASE gate is another useful two-qubit gate that generally reflects the physical interaction between two qubits. The two-qubit Hamiltonian

$$\mathcal{H} = \frac{\hbar g}{2} \sigma_z^{(1)} \otimes \sigma_z^{(2)} \quad (2.14)$$

---

3. The  $T$ -gate also has the misleading name, the  $\pi/8$ -gate. This is because the unitary can be factored as  $T = \begin{pmatrix} 1 & 0 \\ 0 & e^{i\pi/4} \end{pmatrix} = e^{i\pi/8} \begin{pmatrix} e^{-i\pi/8} & 0 \\ 0 & e^{i\pi/8} \end{pmatrix} \rightarrow e^{i\hat{\sigma}_z \pi/8}$

naturally generates a CPHASE operation. As we will see in the next chapter, the dispersive interaction that is fundamental to cQED systems generates a CPHASE-like interaction between two quantum modes. Functionally, the CPHASE gate applies a  $\pi$ -phase shift on  $|11\rangle$  relative to the other three product states. The CNOT and CPHASE operations are related and can be transformed into one another by single-qubit rotations. Specifically sandwiching the CPHASE operation between two Hadamard gates on the target qubit results in a CNOT gate. Universal quantum computation requires one nontrivial (e.g. entangling) two-qubit operation, which can be satisfied by either a CNOT or CPHASE gate.

### Operations on harmonic oscillators

An important unitary operation on harmonic oscillators is called the displacement operator,  $\hat{D}(\alpha)$ , given as

$$\hat{D}(\alpha) = e^{\alpha\hat{a}^\dagger - \alpha^*\hat{a}}. \quad (2.15)$$

For example, a coherent state is generated from a displacement of the vacuum state:  $\hat{D}(\alpha)|0\rangle \rightarrow |\alpha\rangle$ , and in general  $\hat{D}(\alpha)|\beta\rangle \rightarrow |\alpha + \beta\rangle$ . The displacement operator is very natural to produce in practice, requiring only a classically oscillating field that implements the Hamiltonian term  $\mathcal{H}_d = \epsilon\hat{a}^\dagger + \epsilon^*\hat{a}$ . When applied for some time  $t$ , this displacement Hamiltonian generates the coherent state with  $\alpha = i\epsilon t$ . In order for the harmonic oscillator to be useful for quantum information, however, we will require an additional (nonlinear) control that enables more complex control over the harmonic oscillator Hilbert space. Control and manipulation of harmonic oscillators will be discussed in subsequent chapters of this thesis.

#### 2.1.4 Quantum measurement

So far, we have a concept of quantum states and manipulations upon them. We are, however, missing one piece before we can discuss computations with quantum systems. Measurement is this final piece. In contrast with the classical experimentalist, the quantum experimentalist will have restrictions on what information can be simultaneously accessed. The wavefunction

description of a quantum state, described by a set of complex amplitudes  $c_n$ , is a purely theoretical construction: we do not directly measure these amplitudes. Quantum measurements are fundamentally different from the unitary evolution described in the previous section.

A quantum measurement is described by a set of measurement operations  $\{M_m\}$ , each of which reports a different measurement outcome. Given a state  $|\psi\rangle$ , the probability of measuring outcome  $m$  is given by  $\pi_m = \langle\psi|M_m^\dagger M_m|\psi\rangle$ . The set of measurement operators satisfies the completeness relation  $\sum_m M_m^\dagger M_m = I$ , which essentially states that we will get an outcome when we perform the measurement; the probabilities sum to 1. The resulting state after the measurement of outcome  $m$  is  $|\psi\rangle_{\text{out}} = M_m |\psi\rangle / \sqrt{\pi_m}$ . Unlike classical measurements, where we simply use measurements or observations to reveal some property of an object, quantum measurements can irreversibly modify the state.

Consider a special case of measurement operators, the projection operator:  $P_m = M_m^\dagger M_m = M_m$ , from which we can define an observable as  $O = \sum_m m P_m$ . For a single qubit, one such set of projection operators is the pair of operators,  $P_0 = |0\rangle\langle 0|$  and  $P_1 = |1\rangle\langle 1|$ . If we apply this projective measurement to the state  $|\psi\rangle = a|0\rangle + b|1\rangle$  and obtain a measurement outcome  $m = 0$  (with probability  $\pi_0 = \langle\psi|P_0|\psi\rangle = |a|^2$ ), then the resulting state of that measurement has been collapsed or projected to  $|0\rangle$ . If we apply the  $P_0$  again, we actually will report the same outcome with probability 1. This property of a measurement is called quantum non-demolition (QND), where repeated measurements will give the same result<sup>4</sup>. While the initial superposition of  $|\psi\rangle$  is destroyed as a consequence of the measurement, the state is not demolished<sup>5</sup> [24].

Experimentally, we are often interested in extracting the probability  $\pi_m$  of measuring outcome  $m$ . Because a single measurement of a quantum state reports one of the eigenvalues of the measurement, e.g. 0 or 1, to extract this probability we repeat this measurement many times to build statistics on the distribution of outcomes. This is often called taking an “ensemble average”

4. For measurements with multiple eigenstates for a particular measurement outcome, the story can be more complicated. Some have introduced the concept of a degeneracy-preserving QND measurement for such systems with multi-dimensional subspaces [23].

5. An example of a measurement that demolishes the state is  $\{|0\rangle\langle 0|, |0\rangle\langle 1|\}$ , one where the measurement always leaves the state in  $|0\rangle$

as we prepare the initial quantum state  $|\psi\rangle$  many times and perform the measurement.

## 2.2 Quantum information in open systems

While our previous description of quantum states and manipulations on these systems is instructive, real-world quantum systems are not closed systems. Rather, the quantum systems we aim to control can (and generally do) couple to other, potentially unknown, degrees of freedom. This situation introduces classical uncertainty to our description of quantum states, requiring a new representation, the density operator. After defining the density operator, we extend our discussion of unitary operations and measurements for a more general discussion of quantum channels, or different actions that we can execute on quantum states.

### 2.2.1 Density operator

This new perspective requires a representation of a quantum state that can distill the relevant information about these extra degrees of freedom onto the subsystem of interest. This new construction is called the density operator, and is expressed in terms of an orthogonal basis  $|\psi_n\rangle$ ,

$$\rho = \sum_n p_n |\psi_n\rangle \langle \psi_n|. \quad (2.16)$$

The coefficients  $p_n$  represent the probability that the state  $\rho$  is in basis state  $|\psi_n\rangle$ , and therefore must sum to unity:  $\sum_n p_n = 1$ .

There are several important properties of the density operator. First, as a consequence of the probability interpretation of the coefficients,  $\text{Tr}(\rho) = 1$ . Second,  $\rho$  is a positive operator, meaning that its eigenvalues are all nonnegative. Formally, this means that  $\langle \phi | \rho | \phi \rangle \geq 0$  for any  $|\phi\rangle$ . And finally, the density operator is Hermitian,  $\rho = \rho^\dagger$ . Taken together, these properties imply that the eigenvalues are real, non-negative and collectively sum to 1.

If we only have one element in this summation, i.e.  $\rho = |\psi\rangle \langle \psi|$ , then the state is pure and describe all states discussed in the previous section. If there is more than one element in the summation, then the state is mixed. A mixed state is classical mixture of several pure states and

represents our classical uncertainty about which pure state the system is in. This interpretation of a density operator can also be seen by considering the expectation value for an observable  $A$ ,

$$\langle A \rangle = \text{Tr}(A\rho) = \sum_n p_n \langle \psi_n | A | \psi_n \rangle. \quad (2.17)$$

The expectation value is the sum of expectation values of pure states  $|\psi_n\rangle$ , weighted by the probabilities  $p_n$ . We can define a quantity called *state purity* as  $\text{Tr}(\rho^2)$ . For a pure state,  $\text{Tr}(\rho^2) = 1$ , while for a mixed state  $\text{Tr}(\rho^2) < 1$ .

We can apply the density operator representation to be more precise when distinguishing a probabilistic classical bit from a qubit. The density operator representation for a pure state  $|\psi\rangle = a|0\rangle + b|1\rangle$  is

$$\rho = |\psi\rangle\langle\psi| = |a|^2 |0\rangle\langle 0| + ab^* |0\rangle\langle 1| + a^*b |1\rangle\langle 0| + |b|^2 |1\rangle\langle 1| = \begin{pmatrix} |a|^2 & ab^* \\ a^*b & |b|^2 \end{pmatrix} \quad (2.18)$$

The density operator representation for a probabilistic classical bit can be represented as a mixed state:

$$\rho_{\text{cl}} = |a|^2 |0\rangle\langle 0| + |b|^2 |1\rangle\langle 1| = \begin{pmatrix} |a|^2 & 0 \\ 0 & |b|^2 \end{pmatrix}. \quad (2.19)$$

These two density operators are clearly different. The presence of the off-diagonal elements in the pure state density operator are indicative of coherences between the two basis states  $|0\rangle$  and  $|1\rangle$ , while there are no such coherence terms for a probabilistic classical bit.

For a qubit, the density matrix can be described compactly in terms of the Pauli operators,

$$\rho = \frac{1}{2} (I + \lambda_x \hat{\sigma}_x + \lambda_y \hat{\sigma}_y + \lambda_z \hat{\sigma}_z), \quad (2.20)$$

From here we can describe the qubit state using a vector of real numbers,  $\vec{p} = (\lambda_x, \lambda_y, \lambda_z)$ , each corresponding to the expectation value of the respective Pauli operators. These three numbers correspond to a vector contained in the Bloch sphere; each coordinate corresponds to

the projection onto the three axes. The set of three Pauli matrices, along with the identity, form a complete basis that can be used to describe any single-qubit state, and will be used throughout this thesis.

### 2.2.2 Quantum operations formalism

We seek a more general description of dynamics of quantum systems. Unitary evolution generated by a Hamiltonian is but one type of dynamical evolution that can take place for quantum systems. In general, quantum operations can be split into two general categories: quantum channels and quantum measurements, essentially grouping together different classes of actions that can be taken on quantum states. We seek a description of the map  $\mathcal{E}$ , which takes an input density operator  $\rho_{\text{in}}$  to a corresponding output  $\rho_{\text{out}}$ .

$$\rho_{\text{in}} \rightarrow \mathcal{E}(\rho_{\text{in}}) = \rho_{\text{out}} \quad (2.21)$$

This channel  $\mathcal{E}$  is also known as a *superoperator*, with the superlative added because it is an operator that maps operators to new operators rather than state vectors to state vectors. It is also a *completely positive, trace preserving* (CPTP) map. These superoperators have the following properties:

1. Linearity:  $\mathcal{E}(a\rho_1 + b\rho_2) = a\mathcal{E}(\rho_1) + b\mathcal{E}(\rho_2)$
2. Preserves Hermeticity:  $\mathcal{E}(\rho) = \mathcal{E}(\rho)^\dagger$  if  $\rho = \rho^\dagger$
3. Completely positive: Positivity implies that  $\mathcal{E}(\rho) \equiv \langle \psi | \mathcal{E}(\rho) | \psi \rangle \geq 0 \forall |\psi\rangle$ . Complete positivity states that the process (acting in Hilbert space  $A$ ) remains positive even when combined with an auxillary dimension (in Hilbert space  $B$ ):  $\langle \psi | (\mathcal{E}_A \otimes \mathbb{I}_B) (\rho_{AB}) | \psi \rangle \geq 0 \forall |\psi\rangle_{AB}$ .
4. Trace preserving:  $\text{Tr}(\mathcal{E}(\rho)) = \text{Tr}(\rho)$ .

In the next two sections, we present two equivalent perspectives for understanding the behavior of quantum channels [16]. The first is more intuitive, while the second describes a formalism

that is useful for performing calculations.

**System + Environment representation** In the first representation, the quantum system (“the system”) is coupled to additional degrees of freedom (“the environment”). Together the system and environment form a closed quantum system. Starting with an initially unentangled bipartite system  $\rho_{\text{sys}} \otimes \sigma_{\text{env}}$ , we allow the system to interact with the environment according to a global unitary  $U_{\text{SE}}$  which produces joint system+environment state. As observers, we only have access to the system degrees of freedom, so we are forced to trace out the environment and consider the density operator for the system only. The action of this quantum operation can be written as

$$\mathcal{E}(\rho) = \text{Tr}_{\text{env}} \left[ U_{\text{SE}} (\rho_{\text{sys}} \otimes \sigma_{\text{env}}) U_{\text{SE}}^\dagger \right]. \quad (2.22)$$

**Operator-sum representation** Carrying around a unitary that describes the dynamics of both the system and environment will be quite cumbersome (and often times extremely difficult). Furthermore, we are only interested in the dynamics of the quantum system of interest. The operator-sum representation neatly reduces the dynamics to that which acts on only the system, leading to the following description

$$\mathcal{E}(\rho) = \sum_n K_n \rho K_n^\dagger. \quad (2.23)$$

Here,  $\{K_n\}$  are called Kraus operators and satisfy the completeness relation:  $\sum_n K_n^\dagger K_n = I$ . For unitary dynamics, the superoperator has only a single Kraus operator,  $K_0 = U$ , and is represented by  $\mathcal{E}(\rho) = U\rho U^\dagger$ . The set of Kraus operators  $K_n$  is not a unique representation of the quantum channel. We can apply a unitary basis change for these operators to generate a new, perfectly valid set of Kraus operators that describe the same quantum operation.

This representation also allows simple composition (or concatenation) of several quantum channels. For example, say that we want to apply  $\mathcal{E}_1$  to  $\rho$  and then  $\mathcal{E}_2$  to the resulting state. If  $\mathcal{E}_1$  is described by the set of  $k$  Kraus operators  $\{K_m\}$  while  $\mathcal{E}_2$  is described by the set of  $l$  Kraus

operators  $\{L_n\}$ , then

$$\mathcal{E}_2 \circ \mathcal{E}_1(\rho) = \sum_{m,n} L_n K_m \rho K_m^\dagger L_n^\dagger. \quad (2.24)$$

We see that the composed operation  $\mathcal{E}_2 \circ \mathcal{E}_1$  can be represented by a set  $k \times l$  operator elements, given by  $\{L_n K_m\}$ .

### 2.2.3 Quantum channels on a single qubit

Here we describe some common examples of quantum channels acting on a single qubit: the amplitude damping channel, the dephasing channel, and the depolarizing channel .

**Amplitude damping channel** The amplitude damping channel describes the situation when a qubit may spontaneously emit a photon into the environment, relaxing from the excited state to the ground state. The Kraus representation is given by two operators:

$$K_0 = |0\rangle\langle 0| + \sqrt{1-p}|1\rangle\langle 1| \quad K_1 = \sqrt{p}|0\rangle\langle 1|. \quad (2.25)$$

We can associate  $K_1$  with the case when the qubit has jumped from  $|1\rangle$  to  $|0\rangle$ , and  $K_0$  with the evolution of the state when no jump has occurred. The peculiar form of  $K_0$  also accounts for the possibility that the qubit is actually in  $|0\rangle$ , in which case there is no possibility for the qubit to jump. That is, the quantum state undergoes an evolution even when “no jump” occurs. The time dependence for the amplitude damping channel can be calculated in a similar fashion as above and leads to the evolution

$$\rho_{\text{out}}(t) = \begin{pmatrix} \rho_{00} + (1 - e^{-\Gamma_a t})\rho_{11} & e^{-\Gamma_a t/2}\rho_{01} \\ e^{-\Gamma_a t/2}\rho_{10} & e^{-\Gamma_a t}\rho_{11} \end{pmatrix}. \quad (2.26)$$

The  $|1\rangle\langle 1|$  state decays with rate  $\Gamma$ , while the off diagonal elements decay at rate  $\Gamma_a/2$ . In this case the characteristic time  $T_1 = \Gamma_a^{-1}$  represents the rate at which the qubit decays from  $|1\rangle$  to  $|0\rangle$ . We also note that the off-diagonal components decay with a decay constant that is  $2T_1$ .

**Dephasing channel** The dephasing channel has the following Kraus representation:

$$K_0 = \sqrt{1-p}I \quad K_1 = \sqrt{p}|0\rangle\langle 0| \quad K_2 = \sqrt{p}|1\rangle\langle 1|. \quad (2.27)$$

Applying the dephasing channel effects the transformation

$$\rho_{\text{in}} = \begin{pmatrix} \rho_{00} & \rho_{01} \\ \rho_{10} & \rho_{11} \end{pmatrix} \rightarrow \rho_{\text{in}} = \begin{pmatrix} \rho_{00} & (1-p)\rho_{01} \\ (1-p)\rho_{10} & \rho_{11} \end{pmatrix}. \quad (2.28)$$

We see that the off-diagonal components are damped under the action of this channel. The environment probabilistically projects the qubit into either the ground (i.e.  $K_1$  is applied) or excited state (i.e.  $K_2$  is applied), thus erasing the phase information between the two basis states.

We can also describe the dephasing channel under continuous application. Let  $\Gamma_d$  be the dephasing rate such that  $p = \Gamma_d \Delta t$ . We apply this channel  $N$  times in succession to evolve the system for a time  $t = N\Delta t$  during a small time  $\Delta t$ . In the limit as  $\Delta t \rightarrow 0$  (while preserving  $t$ ),  $p \ll 1$  and so the off diagonal elements will evolve  $(1-p)^N = (1 - \Gamma_d t/N)^N \rightarrow e^{-\Gamma_d t}$ . Thus the density operator has a time evolution under the dephasing channel

$$\rho_{\text{out}}(t) = \begin{pmatrix} \rho_{00} & e^{-\Gamma_d t} \rho_{01} \\ e^{-\Gamma_d t} \rho_{10} & \rho_{11} \end{pmatrix} \quad (2.29)$$

The dephasing rate  $\Gamma$  is often quoted in literature as the pure dephasing time  $T_\phi = \Gamma_d^{-1}$ .

**Depolarizing channel** The depolarizing channel has the following description: with probability  $p$ , the channel will do nothing to the qubit ( $|\psi\rangle \rightarrow \hat{I}|\psi\rangle$ ). Each with probability  $p/3$ , the qubit will undergo one of three types of errors: a bit flip ( $|\psi\rangle \rightarrow \hat{\sigma}_x|\psi\rangle$ ), phase flip ( $|\psi\rangle \rightarrow \hat{\sigma}_z|\psi\rangle$ ), or both ( $|\psi\rangle \rightarrow \hat{\sigma}_y|\psi\rangle$ ). This leads to the following Kraus representation:

$$K_0 = \sqrt{1-p}I \quad K_1 = \sqrt{\frac{p}{3}}\sigma_x \quad K_2 = \sqrt{\frac{p}{3}}\sigma_y \quad K_3 = \sqrt{\frac{p}{3}}\sigma_z. \quad (2.30)$$

This channel brings an initial state  $\rho_{\text{in}}$  to the output state  $\rho_{\text{out}} = (1 - \frac{4}{3}p)\rho_{\text{in}} + \frac{4}{3}pI$ . This channel is quite destructive to the initial state: with probability  $p$  the channel scrambles the input and spits out a completely random state. For a simple single qubit channel like the depolarizing channel, it is fairly straightforward to write out a system-environment unitary which generates the correct dynamics. Since we have four elements in the operator-sum representation, it will be necessary to encode the environment into at least a four-dimensional Hilbert space. This particular unitary has a peculiar shape as it maps a state in the system Hilbert space (2-dimensional) to a state in the system+environment Hilbert space ( $2 \times 4$ -dimensional). The action of this unitary on an input state  $|\psi\rangle$  is

$$U_{\text{depolarizing}} : |\psi\rangle \rightarrow \sqrt{1-p}|\psi\rangle \otimes |0\rangle_E + \sqrt{\frac{p}{3}}\sigma_x|\psi\rangle \otimes |1\rangle_E \\ + \sqrt{\frac{p}{3}}\sigma_y|\psi\rangle \otimes |2\rangle_E + \sqrt{\frac{p}{3}}\sigma_z|\psi\rangle \otimes |3\rangle_E \quad (2.31)$$

The environment records which outcome actually happened, although to the experimenter this information is inaccessible.

The three channels discussed in this section are but a small subset of possible quantum channels that we may encounter for physical quantum systems. A geometric picture of each of these channels in the Bloch sphere representation is shown in [Figure 2.3](#). These channels are used quite frequently both because they are easy to model and also because they are related to physical phenomena—dephasing and energy relaxation. In general, however, the challenge will be to determine the correct model to accurately predict behavior of these open quantum systems.

#### 2.2.4 Extracting information about quantum states

Here we extend our introduction to measurements of quantum systems that we began in [Section 2.1.4](#). The formalism for describing quantum channels discussed in the previous section can be used for a more general treatment of quantum measurement. In such a picture, the environment serves as a probe system that serves as an intermediary between the quantum system and the

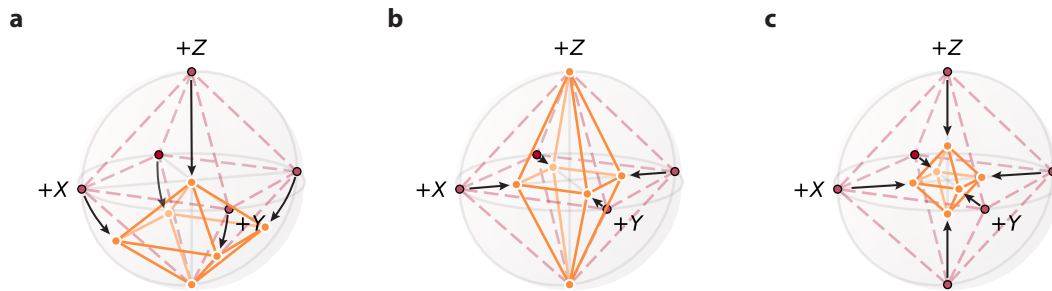


Figure 2.3 | **Examples of single-qubit quantum channels.** We represent the effect of several single-qubit quantum channels by mapping its effect on the six cardinal states on the Bloch sphere. For each channel, the red dots and dashed lines indicate an ideal pure state (or,  $p = 0$ ). We draw the effect of each channel as an octahedron displayed with orange dots and solid lines. **a** The amplitude damping channel shrinks the octahedron toward the ground state, here the south pole. **b** The dephasing channel causes the loss of phase information and is characterized by the Bloch sphere contracting about the equator toward the Z axis. **c** The depolarizing channel effects an isotropic contraction of the Bloch sphere toward the center, which represents a completely mixed state.

classical world. We will use the story of the Stern-Gerlach experiment as an introduction to this description. The discussion of quantum measurement requires treatment of two important concepts. The first is the detector, which is used when we only consider the classical measurement outcome. The mathematical construction that we use to describe detectors is the positive operator valued measure. The second is to consider the entire measurement process, where we also consider the effect of back-action of the measurement itself on the quantum system.

### Von Neumann quantum measurement

In the von Neumann model for quantum measurement, the measurement of an observable is accomplished by a two step process [25, 26]. For this model, we have a quantum system  $S$  and a probe system  $P$  that are initially separable, and we want to measure an observable  $\hat{O}$ . In the first step of the measurement process, the quantum state is allowed to interact with a probe system according an interaction Hamiltonian that couples the two systems. This interaction entangles the probe state with the quantum state. Second, the probe state is measured with a classical meter; the result of the measurement informs the experimenter of the outcome on the original

quantum system. The Stern-Gerlach experiment [27, 28] is a canonical example of this model of measurement. In this experiment, Stern and Gerlach sent a beam of silver atoms through an inhomogeneous magnetic field that induced a spin-dependent force on the atom, thus coupling the atomic spin (system) to the position of the atom (probe). This force caused the atoms to be deflected up or down depending on the orientation of the atomic spin angular momentum; the position and spin degrees of freedom are entangled. The measurement apparatus in their experiment was a silver screen that would record the final position of the atom. From measuring the final position of the atom, we can infer the spin projection of the atom. As we will see in chapter 3, the projective dispersive measurement that are central to cavity and circuit QED experiments are another example a von Neumann quantum measurement.

### Positive operator valued measure

We can extend the discussion of measurements in subsection 2.1.4 with the most general form of quantum measurements, the positive operator-valued measure (POVM). A POVM is specified by a set of operators  $\{E_n\}$ , which are related to the measurement operators in subsection 2.1.4 by  $E_n = M_n^\dagger M_n$ . The probability of measuring outcome  $n$  when applying the generalized measurement on a state  $\rho$  is given by  $\pi_n = \text{Tr}(E_n \rho)$ , and the elements of the POVM satisfy the completeness relation,  $\sum_n E_n = I$ . What makes this formalism a generalized measurement is that we have not specified any particular relationship between the POVM elements: the final states after the measurement need not be orthogonal. The operators satisfy several properties. First, they are Hermitian,  $E_n = E_n^\dagger$ ; they are positive,  $E_n \geq 0$ ; and finally, the set of  $E_n$  are complete,  $\sum_n E_n = I$ . Note that we have not specified the relationship *between* POVM elements: that is because in this generalized theory of measurements, these operators need not be orthogonal.

### Measurement operator

What is the connection to an actual measurement operator—that operator that also specifies the action on the quantum state? First, let's describe what we mean by a measurement operator.

Let  $M_m$  represent the measurement operator for outcome  $m$ . The probability,  $\pi_m$  of outcome  $m$  when applying  $M_m$  to a state  $\rho$  is given by

$$\pi_m = \text{Tr} \left( M_m^\dagger M_m \rho \right). \quad (2.32)$$

The outcome of this measurement leaves the state in

$$\rho_m = \frac{M_m \rho M_m^\dagger}{\pi_m}. \quad (2.33)$$

Thus, these  $M_m$  operators not only specify the measurement outcome distribution, but also describe the result of the measurement on the density operator, which we call *back-action*. Contrast this behavior to the POVM, which specifies the probability distribution of possible outcomes, but does not specify what happens to the state after the measurement. Indeed, the measurement operators and POVM elements are generally related by a unitary evolution and can be decomposed as

$$M_n = U_n \sqrt{E_n}, \quad (2.34)$$

such that  $M_n^\dagger M_n = E_n$ . This is an important distinction. The POVM specifies the measurement outcome up to an unspecified unitary rotation. As a final note, if the measurement outcomes  $m$  are discarded, then the measurement process will transform the state to  $\rho \rightarrow \sum_m M_m \rho M_m^\dagger$ , a process that is identical to our description of a quantum channel. Thus, it is often the case that we interpret a quantum channel as an unread measurement process.

### 2.2.5 Types of quantum operations

We have detailed several transformations that a quantum state can undergo. To conclude this section, we will provide a neat formalism from [17] that unifies different types of quantum operations. Here, each operation takes as an input a quantum state,  $\rho_{\text{in}}$ , then acts on the state according to the state and outputs a new density operator  $\rho_{\text{out}}$ . The output state can encode a quantum state, a classical state, or even a state that combines both. We detail three common

types of quantum operations, which are illustrated in [Figure 2.4](#).

**Quantum evolution channel, [Figure 2.4a](#)** This type of channel takes an input quantum state and outputs a transformed quantum state and is the type of quantum channel discussed in [subsection 2.2.2](#). Such a channel describes both unitary operations ( $\mathcal{E}(\rho) = U\rho U^\dagger$ ) and general quantum evolutions described by the Kraus formalism.

**Quantum-to-classical channel, [Figure 2.4b](#)** This type of channel, also called a measurement (or detector) channel, transforms the input quantum state into a classical output with dimension  $C$ , which is described a diagonal density operator:  $\rho_{\text{out}} = \sum_m p_m |m\rangle\langle m|_C$ . The set  $\{p_m = \text{Tr}(E_m\rho)\}$  represents the probability distribution of possible outcomes. Measurement channels are useful constructions to describe POVM-type measurements, where we do not consider the resulting quantum state of a measurement.

**Quantum instrument channel, [Figure 2.4c](#)** The final type of quantum channel is the combination of the two previous examples. The output of a quantum instrument channel includes both a quantum and classical component:  $\rho_{\text{out}} = \sum_m \mathcal{E}_m(\rho)_Q \otimes |m\rangle\langle m|_C$ . This hybrid quantum channel is a useful tool to model measurement processes, where we include backaction on the input quantum state.

## 2.3 Entanglement

One of the most surprising and important findings of quantum theory is the entanglement of quantum states. This key feature of quantum mechanics is at the heart of quantum information processing. Consider the following state:  $|\Phi^+\rangle = \frac{1}{\sqrt{2}}(|00\rangle + |11\rangle)$ . If we measure the first qubit in the  $\{|0\rangle, |1\rangle\}$  basis, we will measure either outcome with equal probability. We will find the same distribution if we individually measure the second qubit. However, if we find that qubit to be in  $|0\rangle$ , then the state of the second qubit is immediately determined to also be  $|0\rangle$ . We have the same situation when we measure  $|1\rangle$ . Though the measurement result of the first qubit

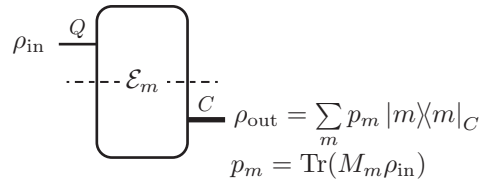
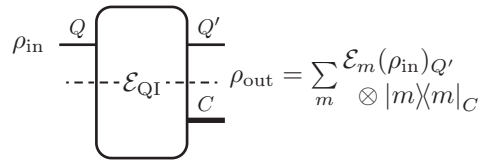
**a** Quantum-quantum channel**b** Measurement channel**c** Quantum instrument channel

Figure 2.4 | **Types of quantum channels.** **a** A quantum-quantum channel describes the quantum evolution of a given input state. The output of such a channel is another quantum state. **b** A quantum-classical, or measurement, channel transforms an input quantum state into a classical outcome distribution. **c** A quantum instrument channel combines a quantum output with a classical degree of freedom. Such a channel can be used to describe measurements as a quantum operation.

is random, as soon as we know what it is, we know the state of the second qubit. Clearly the states of the two qubits are correlated. As we have discussed previously, a quantum state has a multitude of representations. We can represent  $|\Phi^+\rangle$  in the  $|\pm X\rangle = |\pm\rangle = (|0\rangle + |1\rangle)/\sqrt{2}$  basis:  $|\Phi^+\rangle = (|++\rangle + |--\rangle)/\sqrt{2}$ . If we now measure in the  $|\pm\rangle$  basis, we again find that the two qubits are correlated. This feature of quantum entanglement distinguishes quantum correlations from more straightforward classical correlations.

Formally, for two qubits in a composite system  $A+B$ , we can write any pure state in Schmidt form [16]:

$$|\psi\rangle = \sum_n c_n |\phi_n\rangle_A |\mu_n\rangle_B \quad (2.35)$$

If there is only one term, then it is a *separable* and thus unentangled state:  $|\psi\rangle_{AB} = |\phi\rangle_A |\mu\rangle_B$ . The minimum number of terms in the Schmidt decomposition is called the *Schmidt number*; if the Schmidt number is greater than one, the state is entangled. A second way to quantify the entanglement in a given state is to consider the purity of individual subsystems. The idea is that if the two systems are entangled, then a description that involves only a single system cannot fully describe the state and will be mixed:  $\text{Tr}_B(\rho_A^2) = \text{Tr}_A(\rho_B^2) < 1$ , where  $\rho_A = \text{Tr}_B(\rho_{AB})$  and  $\rho_B = \text{Tr}_A(\rho_{AB})$ . For the state  $|\Phi^+\rangle$ , the state is completely mixed if we trace out either subsystem:  $\rho_A = (|0\rangle\langle 0| + |1\rangle\langle 1|) / 2$  and thus  $\text{Tr}_A(\rho_A^2) = 0.5 < 1$ . From this we can say that the information about the entangled state is stored nonlocally between the two qubits, hidden in such a way such that we cannot access the information from measurements on only one qubit.

In the next two sections, we will use the examples of Bell's inequality and quantum state teleportation to explore the uniqueness of quantum entanglement.

### 2.3.1 Bell's Inequality

The early development of quantum theory induced some consternation among leading physicists at the time. Among these, Einstein, Podolsky, and Rosen were the chief skeptics, detailing their view that quantum mechanics is an incomplete description of reality in the famous "EPR paper" [29]. They posited that a complete physical theory would be able to describe all "elements of reality," that there are certain immutable properties associated with an object that would not be in any way disturbed by observation. Quantum systems do not obey this property; the measurement outcomes inherently depend on how and in what order they are measured. Therefore, EPR believed that the description of quantum mechanics must be an incomplete physical theory because it neglected certain elements of reality in its construction. The inclusion of certain "hidden variables" in the theory would allow us to treat physical properties as inherent to the state and remove any uncertainty in the description of its physical reality. Furthermore, Einstein was disturbed by the philosophical implications of quantum entanglement, that two entangled particles, no matter how far separated they might be, could somehow influence each other without any apparent (classical) interaction. According to Einstein, this "spooky action at

a distance” implied some nonlocal behavior of quantum theory that violated relativity, in which states that information cannot travel faster than the speed of light. Nowadays, we do believe that quantum theory is indeed “nonlocal” based on the results of a number of experiments [30, 31, 32], but Einstein was absolutely correct that information cannot be transferred instantaneously—the communication of the measurement result sets the speed limit here.

John S. Bell proposed a test [33] to settle the controversy whether quantum mechanics could be explained through local hidden-variable theories. Bell proposed a series of experiments upon an entangled state, comparing results predicted by local theories versus those predicted by quantum mechanics. From this, he developed the celebrated Bell’s inequalities, which set a limit to what could be observed according to a local theory; a violation of this inequality would indicate that quantum mechanics is indeed a nonlocal theory. One of the most popular versions of this test is the Clauser-Horne-Shimony-Holt (CHSH) inequality [34].

Consider the following gedankenexperiment involving Alice, Bob, and Charlie. Charlie prepares a two-particle state, and gives one particle to Alice and the other to Bob. Alice and Bob are far apart and cannot communicate with each other. Alice and Bob each have at their disposal a pair of different measurement apparatuses. Alice may use  $M_Q$  or  $M_R$  to measure property Q or R, respectively, of her particle. Likewise, Bob may use  $M_S$  or  $M_T$  to measure property S or T, respectively, of his particle. Let’s assume that the measurements can take one of two values:  $\pm 1$ . Assume also that the measurements do not influence each other. They each can pick a random measurement to perform on their particle and perform them simultaneously. They each report both the measurement type and the result of their measurement to Charlie who will compile both in a particular way.

Consider the following quantity:

$$QS + RS + RT - QT \tag{2.36}$$

From direct substitution, we can see that the value of this quantity will be  $\pm 2$  for any of the four measurement outcome combinations. Now, consider the same experiment when there is

some statistical uncertainty to the measurement value that Alice and Bob may measure. If the experiment is repeated many times with Charlie preparing the same initial state, we may obtain an average value for each of the products. For example, to obtain the expectation value  $\langle QS \rangle$ , Charlie will compile all of the runs where Alice used  $M_Q$  and Bob used  $M_S$ . Charlie will multiply the two values reported by Alice and Bob to produce one realization of the product  $QS$ , and subsequently take an average over all realizations of the product. We will find that the average value for this quantity is bounded,

$$\mathcal{B}_{EPR} = \langle QS \rangle + \langle RS \rangle + \langle RT \rangle - \langle QT \rangle \leq 2 \quad (2.37)$$

This equation is one of *Bell's inequalities*, specifically the *CHSH inequality*.

Now consider a quantum mechanical version of this experiment. Charlie prepares the the initial state  $(|01\rangle - |10\rangle)/\sqrt{2}$ . Alice and Bob use the following set of measurement observables

$$Q = Z_a \quad R = X_a \quad S = \frac{-Z_b - X_b}{\sqrt{2}} \quad T = \frac{-X_b - Z_b}{\sqrt{2}}, \quad (2.38)$$

where the subscript associates the measurement to the appropriate party. Now what happens when we apply these and calculate the Bell inequality? We will find the following expectation values:  $\langle QS \rangle = 1/\sqrt{2}$ ,  $\langle RS \rangle = 1/\sqrt{2}$ ,  $\langle RT \rangle = 1/\sqrt{2}$ , and  $\langle QT \rangle = -1/\sqrt{2}$ . Combining these into the Bell test, we find a very surprising result:

$$\mathcal{B}_{QM} = \langle QS \rangle + \langle RS \rangle + \langle RT \rangle - \langle QT \rangle = 2\sqrt{2} \quad (2.39)$$

Let's reiterate: we just found that  $\mathcal{B}_{QM} = 2\sqrt{2}$ , a value greater than the bound of  $\mathcal{B}_{EPR} \leq 2$  we determined in Equation 2.37! How can this be? It appears that some of the assumptions that were made to develop the Bell inequality are erroneous. The first assumption is that the physical properties have definite values that are intrinsic to the state. The second is that the measurement that Alice performs does not influence the result of the measurement that Bob performs and vice versa. At least one of these two assumptions, individually called *realism* and

*locality*, is incorrect.

Since the first tests of Bell's inequality [30, 31, 32], there have been increasingly sophisticated Bell tests to rule out experimental “loopholes.” By and large, we do believe that quantum mechanics is not explained by “local realism”, and these tests add increasingly positive evidence to that conclusion. As such, in this thesis, we are more interested in two broad questions: (1) how do we generate and quantify entanglement and (2) how do we use entanglement for quantum information processing? As we will see, entanglement is a crucial resource for quantum computation, and we use the particularly illustrative example of quantum state teleportation to demonstrate how entanglement can be used for quantum information processing. This example also serves as a preview of the experiment described in [chapter 6](#).

### 2.3.2 Quantum teleportation

One dramatic example of the utility of entanglement for quantum information processing is quantum state teleportation [35]. In this protocol, shown in [Figure 2.5](#), an unknown quantum state can be sent from one party to another without the use of a direct quantum channel or any direct coupling. Instead, the two parties initially share a maximally entangled state and use local operations and classical communication (LOCC). To illustrate this protocol, Alice wishes to send an unknown quantum state  $|\psi_1\rangle = \alpha|0\rangle + \beta|1\rangle$  (qubit 1) to Bob who may be physically distant from Alice. Alice and Bob initially share a maximally entangled state (qubits 2 and 3, respectively), for example, the Bell state  $|\Phi_{23}^+\rangle = (|0_20_3\rangle + |1_21_3\rangle)/\sqrt{2}$ . The joint state can be written as the following

$$|\psi_1\rangle |\Psi_{23}^-\rangle = \frac{1}{\sqrt{2}} (\alpha|0\rangle + \beta|1\rangle) (|0_20_3\rangle + |1_21_3\rangle) \quad (2.40)$$

$$= \frac{1}{2} \left[ \begin{array}{l} |\Phi_{12}^+\rangle (\alpha|0_3\rangle - \beta|1_3\rangle) + |\Phi_{12}^-\rangle (\alpha|0_3\rangle - \beta|1_3\rangle) \\ + |\Psi_{12}^+\rangle (\alpha|1_3\rangle + \beta|0_3\rangle) + |\Psi_{12}^-\rangle (\alpha|1_3\rangle - \beta|0_3\rangle) \end{array} \right], \quad (2.41)$$

where the four Bell states are defined as  $|\Psi^\pm\rangle = (|01\rangle \pm |10\rangle)/\sqrt{2}$  and  $|\Phi^\pm\rangle = (|00\rangle \pm |11\rangle)/\sqrt{2}$ .

Then, Alice performs a Bell state measurement (e.g. a measurement that distinguishes among

the four Bell pairs) on qubits 1 and 2. This measurement projects Bob's qubit (qubit 3) into the original state  $|\psi_1\rangle$  up to single qubit operations, conditioned on the measurement outcome. To recover the original state, Alice sends the result of her measurements to Bob through classical channels, and based on those results, Bob performs appropriate single-qubit operations.

Teleportation of quantum states, initially discovered in 1993 by Bennett, et al., has deep implications in quantum information with applications ranging from communication and cryptography via quantum repeaters [36], to the development of distributed quantum networks [37]. The first experimental demonstration of state teleportation was accomplished using photons in Bouwmeester, et al. [38] using a probabilistic scheme that did not apply the conditional operations and thus succeeded 1/4 of the time. Later demonstrations in a variety of platforms and implementations, showed deterministic state teleportation [39, 40] as well as teleportation over very long distances [41, 42]. [43] provides a good review of quantum teleportation as well as challenges facing different platforms.

What is remarkable in this protocol is that no quantum channel (e.g. operation) is ever performed between Alice's qubits or Bob's qubits. Instead the quantum state teleportation protocol requires entangled pair, a Bell state measurement, and classical communication to transmit an unknown state from Alice's qubit to Bob's qubit. Indeed, the idea of using "entanglement as a resource" is a very powerful concept in quantum information (and this thesis) [44]. Without entanglement, such remote quantum information transfer would not be possible [43]. These same concepts will play a critical role in [chapter 6](#), when we describe the experimental teleportation of a two-qubit operation.

## 2.4 Assessing quantum states and processes

By knowing a quantum state via its density operator or a process via its superoperator, we have complete information about the respective state or process. If we know these representations of states and processes, then we can answer any question we might have about them. Additionally—and most importantly—we can also use these representations to predict the behavior within a

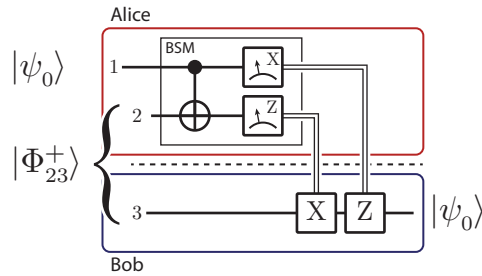


Figure 2.5 | **State teleportation circuit.** Circuit describing the state teleportation protocol. Alice initially owns a quantum state,  $|\psi\rangle$ , that she wishes to send to Bob. The protocol starts with a shared entangled pair between Alice and Bob,  $|\Psi^+\rangle$ . Then, Alice performs a Bell state measurement on her two qubits; here, we illustrate one realization of such a measurement. We label the outcomes as:  $\{|\Phi^+\rangle \rightarrow 00, |\Phi^-\rangle \rightarrow 01, |\Psi^+\rangle \rightarrow 10, |\Psi^-\rangle \rightarrow 11\}_{12}$ . Two classical bits are extracted from the measurement, and they are sent to Bob over classical channels. Based on these two bits, Bob performs conditional operations on his qubit:  $\{00 : \hat{I}, 01 : \hat{Z}, 10 : \hat{X}, 11 : \hat{X}\hat{Z}\}$ .

larger algorithm. As experimentalists, we obsess over methods to accurately and efficiently reconstruct the states and processes that we create in the lab. Often, however, it is useful to provide a more direct description of the quantum object, distilling the complex representation down to one or a few key parameters that are physically motivated. For example, we may be interested in quantifying the amount of entanglement in a given quantum state. Another figure of merit is a measure of how similar two states or processes are to each other, one that we often call *fidelity*. It is by no means a straightforward or unique process to construct these measures, and often times, the interpretation of the parameter is not exactly clear. In addition, a single measure can never hope to provide as much information about the state as the full description; it is unlikely that we will discover a “gold standard” quantum measure. Instead, perhaps a suite of these measures is necessary to provide sufficient characterization. Nevertheless, it is critical that we continue to develop these tools in order to characterize, validate, compare, and benchmark our experimental efforts.

### 2.4.1 Measures of quantum states

We provide a few common methods to characterize a quantum state. We can split these figures of merit into two categories: absolute and relative. *Absolute measures* are properties that can be extracted from the description of the quantum state itself. *Relative measures* are useful when we want to compare two quantum states, where one is typically an ideal or target state.

#### Absolute measures

Perhaps the most fundamental absolute measure is the *purity* of a quantum state. Purity is a measure that describes to what degree the quantum state is a pure quantum state as opposed to a incoherent mixture of pure states. Any density operator,  $\rho$ , can be decomposed into its eigenvalues and eigenvectors:  $\rho = \sum_n p_n |\psi_n\rangle\langle\psi_n|$  with  $\sum_n p_n = 1$ . The purity  $\mathcal{P}(\rho)$  is given as

$$\mathcal{P}(\rho) = \text{Tr}(\rho^2) = \sum_n p_n^2. \quad (2.42)$$

For a state  $\rho$  in a  $d$ -dimensional Hilbert space, the purity is bounded by  $\mathcal{P}(\rho) \in [\frac{1}{d}, 1]$ . If the state is pure, then there is only a single eigenvalue ( $p_0 = 1$ ) and therefore we have unit purity. On the other hand, the lower-bound for purity is found if the state is completely mixed,  $\rho_{\text{mixed}} = \frac{1}{d}\mathbb{1}_d$ .

A second measure takes inspiration from classical thermodynamics. The classical entropy is defined as  $\mathcal{S}_{\text{cl}} \propto \sum_n p_n \ln(p_n)$ , where  $p_n$  is the probability of finding the the system in state  $n$ . We can define a quantum version called the *von Neumann entropy*, given as

$$\mathcal{S}_{\text{q}} = -\text{Tr}(\rho \ln(\rho)) = -\sum_n p_n \ln p_n, \quad (2.43)$$

where we decompose the state  $\rho$  into eigenvalues and vectors in the second equality as before. For a pure state we have  $\mathcal{S}_{\text{q}}(|\psi\rangle\langle\psi|) = 0$ , while for a completely mixed state, the von Neumann entropy is maximal,  $\mathcal{S}_{\text{q}}(\rho_{\text{mixed}}) = \ln d$ .

Since entanglement is such an important aspect of quantum mechanics there are numerous entanglement measures. In the previous section, we defined an entangled state as one that

cannot be expressed as a simple tensor product of pure states or a sum over tensor products for mixed states. Accordingly, common strategies to develop entanglement measures focus on extracting the separability of the quantum state. We will focus our attention on a few measures using a two-qubit state to serve as a model quantum system. Multi-partite entanglement admits a very rich set of possibilities, but is much more difficult to characterize. Consider a bipartite quantum state composed of two qubits  $A$  and  $B$  in a pure state  $\psi_{AB}$ . We define an *entropy of entanglement*,  $E_e$ , as the von Neumann entropy of one subsystem after performing a partial trace over the other:

$$E_e(\psi_{AB}) = \mathcal{S}_q(\rho_A) = \mathcal{S}_q(\rho_B), \quad (2.44)$$

with  $\rho_A = \text{Tr}_B(|\psi_{AB}\rangle\langle\psi_{AB}|)$  and vice versa for  $\rho_B$ . If a state can be represented as a product of pure states, such as  $|\psi\rangle_{AB} = |\phi_A\rangle|\phi_B\rangle$ , then after the partial trace we find a pure state  $\rho_A = |\phi_A\rangle\langle\phi_A|$  and therefore,  $E_e(|\psi\rangle_{AB}) = 0$ . This state is not entangled. If instead we consider a maximally entangled state, such as  $|\psi_{AB}\rangle = (|00\rangle + |11\rangle)/\sqrt{2}$ , then the entropy of entanglement is maximized  $E_e(|\psi_{AB}\rangle) = 1$ . The entropy of entanglement can be interpreted as the number of qubits that need to be exchanged in order to share the state  $|\psi\rangle_{AB}$  [45].

If the state  $\rho_{AB}$  is mixed, then we define the *entanglement of formation* [45],  $E_f$ , as the minimization of  $E_e$  over all possible decompositions of  $\rho_{AB} = \sum_n p_n |\psi_n\rangle\langle\psi_n|_{AB}$ :

$$E_f = \min \sum_n p_n E_e(\psi_{AB}). \quad (2.45)$$

This minimization can be tricky to perform, but fortunately there is a direct method to calculate the formation of entanglement by calculating the *concurrence* [45]. The calculation first requires the computing the “spin-flipped state”

$$\tilde{\rho} = (\sigma_y \otimes \sigma_y) \rho^* (\sigma_y \otimes \sigma_y). \quad (2.46)$$

Then we calculate the concurrence matrix  $R = \sqrt{\sqrt{\rho}\tilde{\rho}\sqrt{\rho}}$  and extract the eigenvalues of  $R$  in

decreasing order  $\{\lambda_i\}$ . The concurrence is then given as

$$C(\rho) = \max\{0, \lambda_1 - \lambda_2 - \lambda_3, -\lambda_4\} \quad (2.47)$$

For a separable state,  $C(\rho) = 0$ , while for a non-separable state, the concurrence is positive, making this a useful measure for quantifying the entanglement of a state. We should also note that this measure is invariant to the basis of  $\rho$ .

### Relative measures

While the previous section described measures that can be extracted from knowledge of a particular quantum state, we often find it necessary to compare one state with another, perhaps ideal, quantum state. In this section we will cover two common *relative measures* [17, 46, 47].

*Trace distance* (or trace norm) is a measure that quantifies the distinguishability between two quantum states:

$$\mathcal{D}(\rho, \sigma) \equiv \frac{1}{2} \|\rho - \sigma\|_{tr}, \quad (2.48)$$

where  $\|X\|_{tr} = \text{Tr}(\sqrt{X^\dagger X})$  and is equal the sum of its singular values. A convenient way to calculate the trace distance is to compute sum of the absolute values of the eigenvalues:  $\|X\|_{tr} = \sum_n |\lambda_i|$ . This measure has a nice physical interpretation [47]: the probability of distinguishing the two quantum states  $\rho$  and  $\sigma$  using the optimal measurement strategy is given by  $(1 + \mathcal{D}(\rho, \sigma)) / 2$ . The trace distance has an additional property that it is a genuine *metric* on quantum states with values from 0 when  $\rho = \sigma$  to 1 when the states have the maximal distance.

The trace distance has several key properties that are worth enumerating that make it a reasonable measure between quantum states:

1. Normalization:  $0 \leq \mathcal{D}(\rho, \phi) \leq 1$
2. Definitivity:  $\mathcal{D}(\rho, \rho) = 0$ .
3. Symmetry:  $\mathcal{D}(\rho, \phi) = \mathcal{D}(\phi, \rho)$
4. Triangle inequality:  $\mathcal{M}(\rho, \phi) \leq \mathcal{M}(\rho, \sigma) + \mathcal{M}(\sigma, \phi)$

5. Contractivity:  $\mathcal{D}(\mathcal{E}(\rho_1), \mathcal{E}(\rho_2)) \leq \mathcal{D}(\rho_1, \rho_2)$  for any quantum operation,  $\mathcal{E}$ .

6. Double convexity:  $\mathcal{D}(\sum_n p_n \rho_n, \sum_n p_n \phi_n) \leq \sum_n p_n \mathcal{D}(\rho_n, \phi_n)$

Properties 1-4 are requirements for a genuine metric. The property of contractivity that states that a quantum operation applied to two states  $\rho$  and  $\phi$  can only decrease the trace distance—one cannot better distinguish them by applying an operation to both states [47]. The property of double convexity also has a nice physical interpretation: the distance between two mixed states can be no larger than the weighted average of the trace distance between each basis state [47]. These two properties, in addition to the ones listed above, make trace distance a useful measure for theoretical calculations, and is often the choice for accuracy threshold calculations [47, 48].

The *fidelity* between a trial state  $|\psi\rangle$  and a ideal state  $|\phi\rangle$  is defined as the probability that the trial state is the ideal state. When the fidelity is unit, then the two states are identical; when the two states are orthogonal, then the fidelity is zero. For two pure states  $|\psi\rangle$  and  $|\phi\rangle$ , the fidelity is given as  $\mathcal{F}(|\psi\rangle, |\phi\rangle) = |\langle\psi|\phi\rangle|^2$ . This has the interpretation that follows from Born's rule: "what is the probability that  $|\psi\rangle$  has been prepared as  $|\phi\rangle$ ?" <sup>6</sup> If the trial state is a mixed state  $\rho$ , we can generalize the fidelity function to

$$\mathcal{F}(\rho, \psi) = \langle\psi|\rho|\psi\rangle = \text{Tr}(\rho|\psi\rangle\langle\psi|). \quad (2.49)$$

If both trial and ideal state are mixed states, then we use the *Uhlmann fidelity* [46, 49]

$$\mathcal{F}(\rho, \sigma) = \text{Tr} \left( \sqrt{\sqrt{\sigma}\rho\sqrt{\sigma}} \right)^2. \quad (2.50)$$

This new definition is needed in order to maintain the definitivity property for fidelity: if  $\sigma = \rho$ , then  $\mathcal{F}(\rho, \sigma) = \text{Tr}(\rho^2) \leq 1$ . In addition, fidelity has the property of monotonicity, defined as  $\mathcal{F}(\mathcal{E}(\rho_1), \mathcal{E}(\rho_2)) \geq \mathcal{F}(\rho_1, \rho_2)$  for any quantum operation,  $\mathcal{E}$ . This basically states that a quantum

---

6. An alternate definition of fidelity is one that reports the "overlap" between the two states,  $\langle\psi|\phi\rangle$ , or the square-root of the fidelity. The physical interpretation of this quantity is less clear, but has the benefit of reporting larger numbers. In this thesis, we use the probability definition, and in general, one should check which definition of fidelity is used.

operation cannot decrease the fidelity between two states and is the analog of concavity for trace distance. This definition of fidelity will be used throughout this thesis, and is often the quantity that is quoted in experimental work.

Trace distance and fidelity are related by the following inequality:

$$1 - \sqrt{\mathcal{F}(\rho, \sigma)} \leq \mathcal{D}(\rho, \sigma) \leq \sqrt{1 - \mathcal{F}(\rho, \sigma)}. \quad (2.51)$$

If the two states are pure, then the right-hand side becomes an equality. While trace distance is a metric, fidelity is not as it is maximized (instead of minimized) when  $\mathcal{F} = 1$ . There are several fidelity-related measures that are genuine metrics, such as the Bures metric, which is a simple transformation on the Uhlmann fidelity, and the angle metric, the later is related to a new measure developed in [50].

### 2.4.2 Measures of quantum processes

Just as we compare quantum states to each other, it is often necessary to compare quantum processes with each other. Indeed, it is certainly common to perform operations on quantum states, it is only natural to ask how close (or similar) the implemented operation is to the target operation. Despite the additional complexity when working with superoperators (versus operators), identifying quality measures on quantum process is actually quite similar to those for quantum states. This is due to a correspondence between quantum channels and states, often formalized as Choi-Jamiołkowski isomorphism [26, 47, 51, 52]. Consider a quantum process that acts on a system  $S$ ,  $\mathcal{E} : \rho \rightarrow \mathcal{E}(\rho)$ . We introduce an auxiliary system  $A$  with the same dimension as  $S$ . From here we can construct a maximally entangled state in the combined  $S + A$  space:  $|\tilde{\Phi}\rangle_{SA} = \sum_{n=0}^d |n\rangle_S \otimes |n\rangle_A$ . If  $\mathcal{E}$  is completely positive, then the process  $(\mathcal{E} \otimes \mathbb{1})$  maps  $|\tilde{\Phi}\rangle\langle\tilde{\Phi}|$  to a density operator on the combined space:

$$(\mathcal{E} \otimes \mathbb{1}) \left( |\tilde{\Phi}\rangle\langle\tilde{\Phi}| \right) = \sum_a |\tilde{\Psi}_a\rangle\langle\tilde{\Psi}_a| = \rho_{\mathcal{E}}, \quad (2.52)$$

up to normalization factors that are absorbed into the states. The resulting density operator  $\rho_{\mathcal{E}}$  is equivalent to a superoperator called the *Jamiołkowski matrix*. This result is incredibly powerful: we can use many of the same techniques for developing quality measures for quantum processes. Based on this insight, there are several distance-and fidelity-based measures that can be developed for quantum processes. A more detailed comparison of these process measures is out of scope of this work; here, we note a useful resource [47] that provides a pedagogical survey of three ways to extract figures of merit for a quantum process: (1) based on the process matrix; (2) based on average-case behavior; (3) and based on worst-case behavior. This reference was used extensively in work related to this thesis [50].

## 2.5 Toward quantum information processing

We conclude this chapter with a brief overview of the challenges and requirements for implementing a quantum computer. We will keep the discussion general, starting from the DiVincenzo criteria as a canonical list of requirements for a physical implementation of a quantum computer. Next, we will briefly comment on one of the greatest challenges toward realizing a practical quantum processor: the need for quantum error correction (QEC). The implementation of QEC necessitates the development of logically-encoded quantum information and introduces additional complexity to manipulating quantum information. In particular, we discuss in what way a future quantum computer should be resilient to errors when performing manipulations on logical qubits, an property called *fault-tolerance*.

### 2.5.1 DiVincenzo criteria

Any physical implementation of a quantum computer will have to fulfill a set of properties for it to be useful for performing quantum information processing. David DiVincenzo, in 2000 [53], enumerated the most famous list of requirements that has become the standard set of criteria that any quantum processing device must satisfy.

**“A scalable physical system with well characterized qubits.”** Any attempt to construct a quantum computer inevitably will face the question: “how do we define our physical qubit?”. There is a myriad of possibilities, of which superconducting qubits and cavities will be the focus of this thesis. These qubits should demonstrate the properties of quantum two-level systems as discussed throughout this chapter; if the physical realization has more than two levels, then the design of the system must ensure that higher states have a negligible probability of being occupied. Any implementation for a quantum computer will be composed of many qubits, each coupled to one another in a particular manner. For the implementation to be scalable, the quantum computer architect must have a sustainable method to assemble this collection of qubits to be useful for quantum computation while avoiding any undesired side effects that may arise from increased complexity. Finally, it will be necessary to define the parameters of the complete physical system, from defining the qubit energy levels to the couplings to other degrees of freedom. A thorough characterization of a quantum device including higher order effects will be crucial to accurate and precise control of the quantum computer.

**“The ability to initialize the state of the qubits to a simple fiducial state, such as  $|000\dots\rangle$ .”**

This requirement arises from a simple consideration: a (quantum) computation ought to start with an initially *known* state. It becomes quite reasonable to wish to initialize the qubits into the ground state, the state with lowest entropy. When we discuss state initialization, it will often specifically be preparation of the ground state. Perhaps a more stringent requirement is the ability to *quickly* and *repeatedly* prepare a register of qubits into this low-entropy state, a requirement that will arise for quantum error correction. Thus an additional requirement will be a “continuous supply” of qubits initialized to the ground state throughout the computation. DiVincenzo discussed two main approaches for realizing state initialization: either through thermalization to the ground state or by measurement and feedback. The main consideration in any approach will be the timescale in which the state can reliably prepared. Some approaches, such as passive thermalization (e.g. via a cold bath), will occur on the same timescale as certain decoherence events in the system. This long timescale renders such an approach untenable for

quantum error correction. A potentially faster approach is through measurement and feedback. While a seemingly daunting technical challenge, this approach is already becoming quite commonplace in many implementations of quantum computation, including the approach taken at Yale.

**“Long relevant decoherence times, much longer than the gate operation time”** Decoherence is the bane of any quantum system, causing the loss of information stored in a quantum system over time. Indeed, decreasing the decoherence rate in our qubits is a major, continuing area of research and informs many considerations in the physical implementation of a qubit. A related issue is the rate at which operations can be performed on the qubit. Of course, we would like to perform many operations on our qubits within a decoherence time. But this also seems impossible: as we scale up the quantum system, we also scale up the number of decoherence channels, thus implying that there are very strict requirements on the decoherence within our system. Luckily, quantum error correction comes to the rescue. The idea is that despite having imperfect qubits, we can redundantly encode a collection of qubits to provide some resilience to errors. There are many realizations of this idea, but all of them inevitably place a “threshold” on the natural error rate of operations.

**“A “universal” set of quantum gates”** In a gate-based approach to quantum computing, a quantum algorithm can be thought of as a sequence of unitary operations acting upon a register of qubits. This in turn can be described as a sequence of different Hamiltonians  $\hat{H}_i$  that generate each unitary operation  $\hat{U}_i = \exp(i\hat{H}_i t_i/\hbar)$ . To run an algorithm, we would apply  $\hat{H}_1$  for a period of time to generate  $\hat{U}_1$ , turn it off, turn on  $\hat{H}_2$  for some time to generate  $\hat{U}_2$ , and so on. Building a large library of arbitrary Hamiltonians can be a daunting, and at times impossible, task. It is often prudent to reduce the number of necessary operations into a minimal instruction set such that any desired computation may be constructed as a finite sequence of operations within this set. In digital computing, any desired logical function (AND, OR, etc.) may be expressed in terms of NAND logic gates. In quantum computing, one such minimal instruction set consists of single qubit Hadamard gates, single qubit “ $\pi/8$ ” gates (which are single qubit Z rotations

by the angle  $\pi/4$ ), and CNOT gates. This instruction set turns out to be “universal,” and one can build a quantum computing processing using only those three unitary operations if desired. An important finding by Solovay and Kitaev proved that universality was actually possible; they showed that any desired unitary can be efficiently approximated using this universal set to high precision by classical means [54]. The price paid for a minimal instruction set is a potentially large overhead in the number of gates when constructing a desired unitary. This translates into a longer effective gate time, which leads to increased decoherence effects. Clearly, there are some important design choices that must be made when developing the universal gate set, and it may not be necessary to stick with the absolute minimal set.

**”A qubit-specific measurement capability”** We will be required to retrieve information from the quantum computer at the end of the computation, indicating that some sort of measurement apparatus will be necessary. It will also likely be necessary to extract intermediate information over the course of a computation (e.g. for quantum error correction). If possible, the measurements should be accurate and quantum non-demolition (meaning that the measurement leaves the quantum state in the eigenstate of the measurement outcome), though there are methods for modifying the computation to account for lower measurement efficiencies. We can broadly categorize these “qubit-specific” measurements into two categories: individual qubit measurement and measurement of a property of many qubits. For the former, the qubit will be projected into, say, the  $Z$ -basis, and all coherences will be lost. For applications such as quantum error correction, we may not wish to completely project a register of qubits into a distinct state; rather, we may want to measure a joint property, like the parity of a register of qubits.

**Additional desiderata** These five requirements compactly summarize what is necessary for quantum computation. For other quantum information processing tasks, such as quantum communication, there are two additional abilities that would be advantageous. Quantum communication often involves moving quantum information from one physical location to another. Thus, the two additional items are the ability to convert *stationary* qubits to *flying* qubits (and vice versa) and the ability to transmit these flying qubits from one location to another. Flying qubits

are often of a very different flavor than those discussed so far, thus motivating their new moniker.

These additional requirements have also found a direct application in quantum computation. There have been recent proposals for implementations of quantum processors that utilize these flying modes to enable on-demand nonlocal gates between qubits that may not otherwise have a direct interaction [44, 55]. These nonlocal gates are the subject of experimental work to be discussed in [chapter 6](#).

### 2.5.2 Quantum error correction

Noise is ubiquitous in all information processing systems, classical and quantum alike, and threatens the reliability of a given computation. One strategy to mitigate such errors induced by noise is to reduce its magnitude to an acceptably small level. Another strategy is to develop techniques that protect against such errors: to perform error-correction. Both strategies are actively pursued in quantum information science.

Where and how does noise arise in quantum systems? This chapter has given a theoretical prescription of how to control and measure properties of quantum states. However, this ability is not unique to the experimenter. Though quantum systems continue to be designed to avoid interaction with a malicious environment, there will be inevitable noise that will decohere the quantum system and erase information about the computation. This persistent decoherence will spell doom to any quantum computer without amazingly low loss channels. Fortunately, the development of quantum error correction (QEC) allows a theoretical resolution to the fragility of quantum states. The fundamental concept for error-correction in general is to redundantly encode information so that it is not completely destroyed if a particular error occurs. An additional complexity for quantum systems is that errors may occur in a continuous fashion. QEC protocols typically use measurements to force the system to choose whether the error has occurred or not. Once we remove the ambiguity, then we have a hope of performing a correction when an error has been detected.

**Correcting classical errors** As a primer to error correction, we will go through the example of a simple majority-vote classical error-correction code. Consider a single bit of information that is sent through a lossy channel. This channel has the property that the input bit will be flipped with probability  $p$  (and probability  $1 - p$  that the bit will pass through the channel unharmed). This channel describes a binary symmetric channel, where the processes taking  $0 \rightarrow 1$  and  $1 \rightarrow 0$  have the same probabilities. Obviously, if Alice uses this channel to send Bob a bit of information, then Bob will receive a wrong bit with probability  $p$ . A simple strategy to improve (that is, decrease) this error probability is to redundantly encode the information in multiple bits. For example, a three-bit repetition code will have the following encoding:  $0 \rightarrow 000$  and  $1 \rightarrow 111$ . When we send each of the three bits through our error-prone channel, each bit will still be subject to individual errors. However, when Bob receives the three bits, he may use a majority-vote approach to detect and correct errors from the channel. The probabilities of zero, one, two, and three errors are:  $(1-p)^3$ ,  $3p(1-p)^2$ ,  $3p^2(1-p)$ , and  $p^3$ , respectively. Bob can decode correctly if there are either 0 or 1 errors and will decode incorrectly if there are 2 or 3 errors. Thus, the new error probability is  $3p^2(1-p) + p^3 = 3p^2 - 2p^3$ . With this simple repetition code to redundantly encode a bit of classical information, the error probability has been improved to  $\mathcal{O}(p^2)$ .

### Challenges for quantum error correction

The majority-voting example serves to illustrate several important concepts for any error-correction strategy. First, an error-correction scheme is only useful if the initial error rate is below a sufficient threshold. For the above example, we see an improvement when using majority voting when  $p < 1/2$ . This is due to an inevitable overhead (e.g. using three bits instead of one) in the base error rate when redundantly encoding information. Additionally, the error-corrected bit can still suffer from errors that cannot be corrected (e.g. if two errors occur), and depending on the situation, it may be important to correct these second-order errors. Finally, it should be noted that the new error probability is not zero; rather, with this error-correction protocol, we can push the error probability from  $\mathcal{O}(p)$  to  $\mathcal{O}(p^2)$ . If this new error rate is not sufficient, then one may require a different code that is sensitive to even more errors (for example, using majority

voting on five bits of information will push the error rate from  $\mathcal{O}(p)$  to  $\mathcal{O}(p^3)$ ). In addition to these generic properties of error-correction strategies, there are three additional challenges that distinguish quantum from classical error-correction protocols.

1. **No-cloning theorem.** Unfortunately, in quantum mechanics it is impossible to clone quantum states to make several copies. Indeed, as a consequence, the simple repetition code described above will not work for quantum states. The no-cloning theorem can be shown quite simply. Suppose we have two qubits,  $A$  and  $B$ , and a theoretical quantum cloning device. The action of this device would be to implement a unitary  $U_{cl}$  on the input states  $U_{cl} |\psi\rangle_A \otimes |n\rangle_B = |\psi\rangle_A \otimes |\psi\rangle_B$ , where the initial state of  $B$  is an arbitrary, but known, state  $|n\rangle_B$ . For an initial superposition state  $|\psi\rangle_A = \alpha |0\rangle_A + \beta |1\rangle_A$  we would expect to find:  $U_{cl} |\psi\rangle_A \otimes |n\rangle_B = (\alpha |0\rangle_A + \beta |1\rangle_A) \otimes (\alpha |0\rangle_B + \beta |1\rangle_B)$ . However, because of the linearity of quantum mechanics, we should also be able to achieve the same output if we apply the unitary to the individual superposition components:  $U_{cl} (|\psi\rangle_A \otimes |n\rangle_B) = \alpha U_{cl} |0\rangle_A |n\rangle_B + \beta U_{cl} |1\rangle_A |n\rangle_B = \alpha |0\rangle_A |0\rangle_B + \beta |1\rangle_A |1\rangle_B$ . These two results contradict each other, so our initial assumption that a unitary can clone quantum states is false.
2. **Continuous errors and noise.** In our classical example, a lossy channel, though probabilistic, results in only two possible outcomes for the classical bit: it is either 0 or 1. This discrete set of outcomes is essential for determining whether an error occurred or not. As we have seen in the previous sections, a qubit is specified by two continuous values. The general impact of quantum noise or control errors will be to adjust these values in some unspecified way, say shifting the Bloch vector by an angle  $\epsilon$ . In some sense, we could say that a qubit can suffer from a continuum of errors—in two dimensions! How can we correct an error on a qubit when it is continuous? Can we do this efficiently, or will there be an explosion in the resources required to track all of these errors?
3. **Measurement.** In any model of computation, we learn information about our state by measurement. In the classical example, Bob measures each of his three bits to determine how many have flipped. However, we have learned that the backaction of projective

quantum measurements can modify the quantum state. This raises some serious questions about a quantum approach to error correction: how do we learn about the errors that may corrupt our quantum state without learning what the quantum state is, or even worse, altering it? How do we perform a measurement that tells us not what the quantum state is, but rather, whether an error has occurred or not?

Due to these concerns, for some time before the seminal work of Peter Shor [11], it was feared that any computation advantages of quantum computing may never be realized due to the presence of noise. Shor presented the first QEC protocol, using nine qubits to encode a single error-correctable quantum bit of information. This protocol could protect against any single bit or phase flip error on the nine qubits. Instead of working through the nine-qubit code, we will briefly describe the main principles of a general quantum error correction strategy. We will specify these principles further by describing a powerful tool for constructing QEC protocols, the *stabilizer formalism*.

### Correcting quantum errors

A QEC protocol, like its classical counterpart, is specified by a set of error-protected codewords, a set of errors that can be corrected, and a set of measurements to check if an error has occurred. These codewords specify the *logical qubit*, which we define as an encoded quantum bit of information to be used for an error-correction protocol. Logical qubits are generally composed of several *physical qubits* and exploit redundancy by moving to a larger dimensional system. The structure of the encoding defines two special subspaces within the full Hilbert space of the logical encoding. The first is the codespace, which represents the subspace in which the logical qubit is defined; the second is the errorspace, a subspace (or subspaces) into which the logical qubit state is transformed when an error occurs. Importantly, the codespace and errorspace should be orthogonal subspaces to allow the QEC protocol to be able to distinguish when the logical qubit has suffered an error. Finally, when an error does occur, it is important that the state in the errorspace retains the original quantum superposition, as any distortion will result in loss of information and a failure of the QEC protocol.

We can construct a quantum version of the repetition code. We protect a single qubit  $|\psi\rangle = \alpha|0\rangle + \beta|1\rangle$  by encoding it into a register of three qubits, where the codewords are defined as  $|0\rangle \rightarrow |0_L\rangle \equiv |000\rangle$  and  $|1\rangle \rightarrow |1_L\rangle \equiv |111\rangle$ . An arbitrary logical qubit state can be written as

$$|\psi\rangle = \alpha|0\rangle + \beta|1\rangle \rightarrow |\psi_L\rangle = \alpha|000\rangle + \beta|111\rangle. \quad (2.53)$$

Crucially, this new entangled state is not the initial state copied three times; rather, we have performed a particular encoding so that the information about the original state contained in the coefficients  $\alpha$  and  $\beta$  is now distributed among three qubits. We get around the no-cloning theorem by utilizing entanglement to generate our encoded quantum bit of information.

Let's consider a single  $X$  bit-flip error on any of the three physical qubits, which induces the following transformations:

$$\begin{aligned} |\psi_L\rangle = \alpha|000\rangle + \beta|111\rangle &\xrightarrow{XII} |\psi_E\rangle = \alpha|100\rangle + \beta|011\rangle \\ |\psi_L\rangle = \alpha|000\rangle + \beta|111\rangle &\xrightarrow{IXI} |\psi_E\rangle = \alpha|010\rangle + \beta|101\rangle \\ |\psi_L\rangle = \alpha|000\rangle + \beta|111\rangle &\xrightarrow{IIX} |\psi_E\rangle = \alpha|001\rangle + \beta|110\rangle \end{aligned} \quad (2.54)$$

For this particular encoding and particular error type, we see that the quantum amplitudes are not distorted when we suffer an error. We also see that each errorspace is orthogonal to the codespace. If we measure the state with a particular set of operators,  $S_1 = ZZI$  and  $S_2 = IZZ$ , then we can identify whether bit flip has occurred. The logical qubit without any errors returns the measurement pattern  $S_1, S_2 = +1, +1$ . If we find the measurement pattern  $S_1, S_2 = -1, +1$ , then we have suffered an error on the first qubit, which flips the measurement result of  $S_1$ . The pattern  $S_1, S_2 = -1, -1$  indicates a bit-flip on qubit 2, and  $S_1, S_2 = +1, -1$  indicates a bit-flip error on qubit 3. Importantly, the pair of measurements does not tell us anything about the the superposition; rather, it uniquely informs us which codespace or errorspace the logical qubit is in (assuming that at most only one error occurred). Once we have this information we can correct the error either by performing a  $X$  gate on the qubit that has flipped, or by keeping a (classical) record that this error has happened and updating the rest of the computation accordingly.

Errors in real quantum systems occur continuously, and we will see now that this additional complexity can be handled by a QEC protocol. We can use this code to protect against the bit-flip channel, which is the quantum analog of a lossy classical channel, described by the following evolution on single physical qubit:  $\rho \rightarrow (1 - p)\rho + p\hat{X}\rho\hat{X}$ . The input state is flipped with probability  $p$  and let through unchanged with probability  $1 - p$ . This interpretation makes it clear how the QEC protocol handles continuous and partial errors. The act of measurement projects the logical qubit into a definite state, digitizing the evolution so that either an error has not occurred or an error has occurred.

Whether a particular protocol is an effective QEC protocol can be formalized using the *quantum error correcting criteria*. Say we have a set of errors,  $\{E_i\}$  describing a error process  $\mathcal{E}$ , that we would like to correct, and we design a QEC protocol for a logical qubit with codewords  $\{|\phi_n\rangle\}$ . The goal for an error correcting protocol is to determine an appropriate code for which we can design a recovery operation  $\mathcal{R}$  such that  $(\mathcal{R} \circ \mathcal{E})(\rho) \propto \rho$  for states  $\rho$  that are spanned by the code. It can be shown [56] that a necessary and sufficient condition to construct recovery operations to correct the error-prone state is given by

$$\langle \phi_n | E_k^\dagger E_l | \phi_m \rangle = C_{kl} \delta_{mn}, \quad (2.55)$$

where  $C_{kl}$  is a Hermitian matrix. This simple form of the quantum error-correction conditions compactly describes the constraints for a “good” protocol. The first requirement is that the error subspaces should remain orthogonal so the QEC protocol can reliably distinguish among the different types of errors. This is satisfied for  $n \neq m$ , the criteria enforce orthogonality between two error states  $E_l |\phi_m\rangle$  and  $E_k |\phi_n\rangle$ . The second requirement is that the error subspaces should be related to the original subspace; an error should not distort a superposition of codewords. When  $n = m$ ,  $\langle \phi_m | E_k^\dagger E_l | \phi_m \rangle = C_{kl}$  independent of  $m$ . It is important that information about a particular state does not leak out when a particular error subspace is identified.

One useful tool for developing QEC protocols is the stabilizer formalism developed by Daniel Gottesman [14]. In this formalism we specify a set of stabilizers  $\{S_i\}$  that all commute with

one another and have a  $+1$  eigenvalue for each codeword  $|\phi_n\rangle$ :  $S_i |\phi_n\rangle = +|\phi_n\rangle$ . The stabilizers are also designed to either commute or anti-commute with each error  $\{E_n\}$ . If an error  $E_n$  has occurred and this particular error anticommutes with  $S_i$ , then the error state is the  $-1$  eigenvalue of the stabilizer operator:  $S_i (E_n |\phi_n\rangle) = -(E_n |\phi_n\rangle)$ . If we perform measurements of all stabilizers, the outcome of these measurements provide a signature indicating what, if any, error occurred. For the repetition code described previously, the stabilizer group is  $\{ZZI, IZZ\}$  which stabilizes the codewords  $\{|000\rangle, |111\rangle$  against the errors  $\{XII, IXI, IIX\}$ . Using this formalism, five physical qubits is the smallest logical qubit needed to correct for arbitrary single bit- and phase-flip errors [12]. For this five-qubit code, the stabilizers require a curious joint measurement of four of the five qubits (e.g.  $XZZXI$ ). Implementing these complex measurement operators is the subject of work performed as a part of this thesis [50].

### 2.5.3 Toward fault-tolerant quantum computation

Thus far, our discussion of quantum error mitigation revolved around correcting errors without admitting any faults due to the correction procedure itself. Effecting a meaningful quantum computation will require manipulations on quantum information beyond just quantum error correction. These manipulations will likely be executed upon logical qubits and rely on components that are themselves lossy. If the errors induced during an operation are error-correctable, then the operation is said to be *fault-tolerant* [57, 58, 59]. However, if the errors induced by the operation are not correctable by QEC, then these errors may propagate and cause the entire computation to fail. More formally, an error during a fault-tolerant operation will result in at most one error for each logical qubit that is used for the operation. This error can then be detected by the subsequent round of error-correction. We must consider fault-tolerance of all aspects of a quantum computation, from the state preparation, to gates, measurements, and even the QEC protocol itself. Achieving fault-tolerance in quantum operations is a major milestone for quantum information processing.

Typical QEC protocols bring the error probability from  $p$  to  $cp^2$ , where  $c$  represents the

overhead of using a QEC code<sup>7</sup>. What if the new error rate is still too high for a computation? After all, the new error probability is still finite and non-zero. Remarkably, there is a prescription to further improve (e.g. decrease) the error rate. The strategy is to concatenate fault-tolerant QEC codes. In such a scheme, the logical qubits defining a first-level encoding act as physical qubits for a second-level encoding. This second-level encoding will enable correction of higher-order errors uncorrectable in the first encoding. If the base error rate is low enough, then the concatenated code will result in an overall reduced error rate at the expense of a larger quantum computer and a more complex circuit. Below some threshold error rate  $p_{\text{thresh}}$ , it is possible to use concatenation to achieve arbitrarily low logical error rates with a modest (polylogarithmic) overhead in the system size (e.g. the number of physical qubits and gates). This statement is often called the *threshold theorem* [57]. Although the first estimated thresholds required gate errors below  $10^{-6}$ , more modern topological codes, such as the surface code, have less daunting thresholds, up to 1% [60, 61]. Current state-of-the-art error rates are at or below this threshold in several different platforms, including superconducting qubits [62, 63] and trapped ions [64]. Due to current technical challenges for building large-scale quantum systems, in practice, we may want to operate far below the threshold to reduce the overhead in number of qubits.

---

7. Higher order QEC protocols certainly exist. For example, an  $n^{\text{th}}$  order QEC code can take the error probability from  $p$  to  $dp^n$ , where  $d$  is the overhead.

# 3

## Superconducting qubits and cQED

In the previous chapter, we generically described the requirements and properties of quantum computation without focusing on any physical implementation for building a quantum computer. Such a choice is critical for determining the actual manifestation of the quantum gates and measurements as well as the method by which qubits will be coupled together into a useful processor. The DiVincenzo criteria described in [subsection 2.5.1](#) serve as a useful starting point, providing a minimal set of requirements for defining a physical qubit. Implementing any useful physical qubit faces competing requirements: it is necessary to decouple the qubit sufficiently from the environment to extend coherence times, while maintaining sufficient coupling for control and measurement of the qubits. Each physical implementation will have its own set of strengths and challenges, and it will be essential to leverage the advantages of a given platform to address the shortcomings. There are a myriad of different approaches, with each platform encoding information in one of several quantum degrees of freedom: nuclear spins, electron spins, hyperfine atomic levels, photons, or charge, phase, or flux in superconducting circuits. Physical realizations of these quantum systems include nuclear spin systems [65], trapped ions and neutral atoms [66, 67, 68, 69, 70, 71, 72, 73], linear optics [74, 75], solid state quantum dots [76, 77, 78, 79, 80, 81], solid state defects [81, 82, 83, 84, 85], and superconducting qubits [86]. Each comes with its own set of advantages and challenges to achieve sufficient coherence, to enable quantum control and measurement, and to couple multiple qubits together in a scalable fashion. In some sense, experimental quantum information processing is at the stage of development where we are trying

---

to perfect the quantum analog of the semiconductor transistor.

Nuclear magnetic resonance (NMR) emerged as one of the first systems that could be manipulated quantum mechanically and demonstrated several seminal experiments including one of the first experimental realizations of a quantum algorithm [87], quantum error correction [88], and quantum state teleportation [89]. Because these experiments are performed using carefully engineered molecules, one significant challenge for NMR systems is its ability to scale to larger systems. Another pioneering quantum technology is that of trapped ions, which are still among the most mature and promising platforms to date, owing to their excellent coherence properties and high gate fidelities [64, 69, 73, 90]. Though scalability has been a question for trapped ion systems (a question common to all platforms), there are several approaches [91, 92] currently under investigation to address this outstanding question. Solid state approaches to quantum information have seen dramatic development in recent years. Electronic spin based systems aim to leverage proven fabrication technologies from the silicon integrated circuit industry to address the issue of scaling quantum systems [77]. Other approaches, like defect-based color centers, use a combination of optical and electronic control to interface remote systems into a quantum network [85, 93, 94, 95].

In this thesis we present experiments using superconducting qubits. These are quantum machines built from assembling quantum electrical circuits out of superconducting wire and circuit elements. The flavor of superconducting qubits used in this thesis follows from the combination of quantum electrical circuits and quantum electrodynamics, leading to development of circuit quantum electrodynamics [96, 97, 98, 99]. Superconducting qubit systems are perhaps distinctive among the previously described implementations as they offer highly tunable quantum characteristics by simply modifying macroscopic parameters.

In this chapter, we describe the physics of quantum computation with superconducting qubits with the circuit quantum electrodynamics (cQED) platform. In [section 3.1](#), we start by describing the formalism for treating simple electrical circuits as quantum mechanical systems. Such circuit quantization is necessary to understand how macroscopic parameters such as capacitance and inductance can give rise to quantum mechanical behavior [100, 101]. We then introduce the

Josephson junction in [subsection 3.1.2](#) as the essential circuit element distinctive to superconducting circuits. The nonlinearity added by the Josephson junction affords the crucial quantum mechanical properties that make these superconducting circuits useful for quantum information processing. With this theoretical basis, we describe how these nonlinear quantum circuits can be constructed to describe physical qubits. In particular, by focusing on coupling transmon qubits to linear harmonic oscillators, we enter the regime of cQED. After a brief historical overview of the Jaynes-Cummings Hamiltonian in [subsection 3.2.1](#), we describe a general technique called Black-box quantization in [subsection 3.2.2](#) for extracting the physical Hamiltonian for a given nonlinear electrical circuits. In [subsection 3.2.3](#), we then detail several useful transmon-cavity primitives and detail important Hamiltonian parameters that will be useful in succeeded chapters. In [section 3.3](#), we formalize our understanding of manipulation and measurement of cQED systems using time-dependent drives.

## 3.1 Building blocks of quantum circuits

Circuit quantum electrodynamics relies on constructing electrical circuits in a way that collective phenomena such as current or voltage can be treated quantum mechanically. Such circuits utilize many of the common classical circuit elements we know from electrical engineering—inductors, capacitors, and resistors<sup>1</sup>. This quantization of an electrical circuit distills the dynamics of these macroscopic circuits into few collective degrees of freedom that behave quantum mechanically. These “mesoscopic” systems occupy some intermediate space between the classical world and the quantum realm of single atoms and electrons.

Our chosen physical implementation of these quantum circuits utilizes circuit elements made from superconductors, which when cooled below their critical temperature, for our circuits  $T_c \sim 1\text{K}$ , are ideally lossless. One additional circuit element distinctive to superconducting circuits is the Josephson tunnel junction [[103](#), [104](#)], which currently the only known nondissipa-

---

1. In most cases, we consider only inductors and capacitors for two reasons: first, resistors typically cause unwanted dissipation, and we work hard to reduce these effects in our experimental implementations; second, it is possible to model resistors through a combination of lossless elements via the Caldeira-Leggett model of dissipative systems [[102](#)].

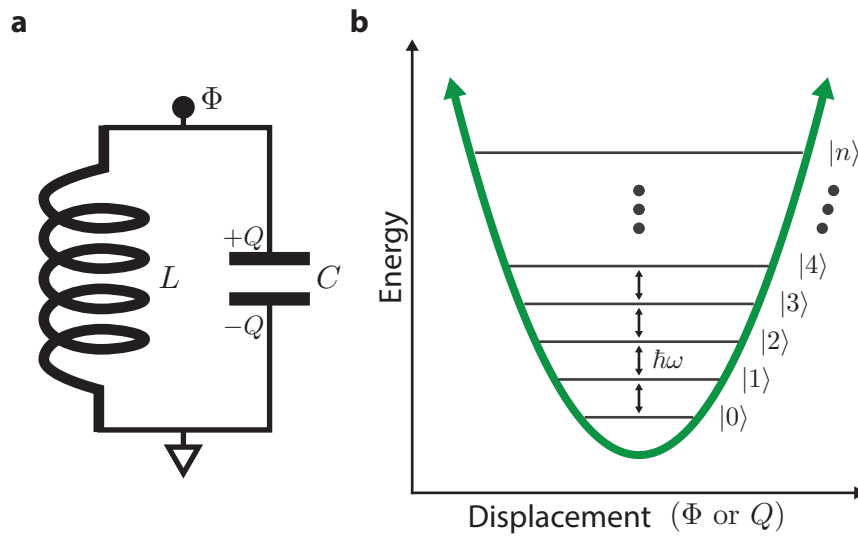


Figure 3.1 | **Quantum LC oscillator.** **a**, The LC circuit consists of an inductance  $L$  and capacitance  $C$  and can be characterized in terms of a node flux  $\Phi$  and charge  $Q$ . Node flux and charge are conjugate variables, akin to position and momentum of a classical pendulum. **b**, Upon quantization of the LC oscillator, promoting  $\Phi$  and  $Q$  to quantum mechanical operators, the quadratic potential gives rise to energy levels that are all even spaced, by  $\hbar\omega$ .

tive, nonlinear circuit element. This nonlinearity is necessary to develop and observe quantum mechanical effects that are central for quantum information processing. In this section we explore the basic building blocks for the quantization of quantum electrical circuits.

### 3.1.1 Quantum LC oscillator

Our discussion of electrical circuits begins, unsurprisingly, at one of the most simplest examples, the quantum parallel LC oscillator. Developing a formalism to understand the dynamics of such a circuit allows us to describe its behavior in the quantum regime as well as construct more complex circuits to evaluate its quantum properties. A comprehensive discussion of quantum electrical circuits can be found in several resources, notably [101, 105, 106].

The parallel combination of an LC circuit, the electromagnetic analog of a mass and spring, can be analyzed by considering current  $I$  through the inductor (with inductance  $L$ ) and the charge  $Q$  accumulated on the capacitor (with capacitance  $C$ ) as its two (conjugate) degrees of freedom, shown in Figure 3.1. We will choose to use the node flux  $\Phi$  to represent the coordinate-like

degree of freedom for the LC oscillator. The node flux as is defined to be

$$\Phi(t) = \int_{-\infty}^t V(\tau) d\tau. \quad (3.1)$$

or equivalently  $V(t) = \dot{\Phi}$ . The kinetic energy in this representation is stored by the charge on the capacitor

$$T = \frac{Q^2}{2C} = \frac{1}{2} C \dot{\Phi}^2. \quad (3.2)$$

To write down the potential energy, we also have the relation that  $V = L\dot{I} = \dot{\Phi}$ , which says that  $\Phi$  is equivalent to the magnetic flux winding through the inductor. The potential energy stored in the inductor is

$$U = \frac{1}{2} LI^2 = \frac{\Phi^2}{2L} \quad (3.3)$$

The Lagrangian can be written as

$$\mathcal{L} = \frac{Q^2}{2C} - \frac{LI^2}{2} = \frac{C\dot{\Phi}^2}{2} - \frac{\Phi^2}{2L} \quad (3.4)$$

And variable conjugate to the node flux is the charge

$$Q = \frac{\partial \mathcal{L}}{\partial \dot{\Phi}} = C\dot{\Phi} \quad (3.5)$$

The Hamiltonian can be written as

$$\mathcal{H} = Q\dot{\Phi} - \mathcal{L} = \frac{Q^2}{2C} + \frac{\Phi^2}{2L} \quad (3.6)$$

The equation of motion for the two conjugate variables  $\phi$  and  $Q$  follow from Hamilton's equations of motion

$$\begin{aligned} \dot{\Phi} &= +\frac{\partial \mathcal{H}}{\partial Q} = +\frac{Q}{C} \\ \dot{Q} &= -\frac{\partial \mathcal{H}}{\partial \Phi} = -\frac{\Phi}{L} \end{aligned} \quad (3.7)$$

We can move to a quantum mechanical description of the harmonic oscillator by promoting

the variables to operators (e.g.  $Q \rightarrow \hat{Q}$ ). The commutation relation between the two conjugate operators,  $\hat{\Phi}$  and  $\hat{Q}$ .

$$[\hat{\Phi}, \hat{Q}] = +i\hbar \quad (3.8)$$

We can write the Hamiltonian using the lowering and raising operators

$$\begin{aligned} \hat{\Phi} &= \Phi_{ZPF} (\hat{a}^\dagger + \hat{a}) \\ \hat{Q} &= -iQ_{ZPF} (\hat{a}^\dagger - \hat{a}) \end{aligned} \quad (3.9)$$

where  $Q_{ZPF} = \sqrt{\hbar/2Z}$ ,  $\Phi_{ZPF} = \sqrt{\hbar Z/2}$ , and the characteristic impedance  $Z = \sqrt{L/C}$ . These operators obey the commutation relation

$$[\hat{a}, \hat{a}^\dagger] = 1. \quad (3.10)$$

The quantum LC circuit Hamiltonian is therefore equivalent to the quantum harmonic oscillator,

$$\hat{\mathcal{H}} = \hbar\omega \left( \hat{a}^\dagger \hat{a} + \frac{1}{2} \right). \quad (3.11)$$

The energy eigenstates of the harmonic oscillator are called Fock states, and each Fock state  $|n\rangle$  has energy  $E_n = \hbar\omega (n + \frac{1}{2})$ . The raising and lowering operators increase or decrease the excitation number by one:  $\hat{a}^\dagger |n\rangle = \sqrt{n+1} |n+1\rangle$  and  $\hat{a} |n\rangle = \sqrt{n} |n-1\rangle$ . Notice that the ground state energy is nonzero,  $E_0 = \hbar\omega/2$  owing to the inherent zero-point fluctuations of the vacuum state. For many calculations, we offset the Hamiltonian to define the zero energy as the energy of the ground state. We can also define ground-state zero-point fluctuations (ZPF) in the charge and flux as

$$\begin{aligned} \langle 0 | \hat{Q}^2 | 0 \rangle &= Q_{ZPF}^2 \\ \langle 0 | \hat{\Phi}^2 | 0 \rangle &= \Phi_{ZPF}^2 \end{aligned} \quad (3.12)$$

One truly remarkable aspect of this analysis is that the essential quantum mechanical properties of the harmonic oscillator, including the resonance frequency  $\omega$  and zero-point energy  $E_0$ , are governed by the inductance  $L$  and capacitance  $C$ . These macroscopic parameters can be

freely engineered, indicating that we have exquisite control over the properties of these quantum harmonic oscillators. Furthermore, we have developed experimental techniques that allow us to observe and manipulate the quantum mechanical properties of these oscillators. Before discussing another essential circuit element for building quantum electrical circuits, we will briefly detail the common argument why it is difficult to use a harmonic oscillator as a quantum bit of information.

### Addressing the harmonic oscillator

One challenge in using harmonic oscillators for quantum information processing lies in the experimenter's ability to exercise sufficient quantum control over its state evolution. A simple model to manipulate the state of a harmonic oscillator is to hook it up in parallel with an ideal current source<sup>2</sup> [107]. Given the classical bias current  $I_b(t)$ , the driven Hamiltonian is given as

$$\mathcal{H} = \frac{\hat{Q}^2}{2C} + \frac{\hat{\Phi}^2}{2L} - I_b(t)\hat{\Phi} \quad (3.13)$$

the current acts as a force that couples to the  $\hat{\Phi}$  coordinate. Written using the raising and lowering operators,

$$\mathcal{H} = \hbar\omega\hat{a}^\dagger\hat{a} + \hbar\epsilon(t)\left(\hat{a}^\dagger + \hat{a}\right), \quad (3.14)$$

where  $\epsilon(t) \propto I_b(t)$ . This classical drive generates the displacement operator, written using  $\hat{a}$  and  $\hat{a}^\dagger$  as

$$D(\alpha) = e^{\alpha\hat{a}^\dagger - \alpha^*\hat{a}} \quad (3.15)$$

In the excitation basis, this drive will take the vacuum state to a coherent state with amplitude  $\alpha$ :  $D(\alpha)|0\rangle = |\alpha\rangle$ . Recall from [subsection 2.1.2](#) that such a coherent state is described by a superposition of Fock states:  $|\alpha\rangle = \sum_n c_n |n\rangle$ . If we initialize our harmonic oscillator in  $|0\rangle$  (for example, by cooling to the ground state), then the displacement operator gives us access to coherent states,  $|\alpha\rangle$ . Such a system is limiting in two ways: first, defining an appropriate qubit

---

2. An ideal current source has infinite impedance and will not affect the properties of the oscillator. In contrast, an ideal voltage source will have zero impedance and at zero bias will short out the resonance of the oscillator. If we had considered a series LC oscillator, then we would model the drive as a voltage source.

using continuous variables is challenging; second, linear displacements will not give us sufficient control over our oscillator. Indeed naively, one might choose to encode a quantum bit in the lowest two Fock state  $|0\rangle$  and  $|1\rangle$ ; our simple classical control gives us no way to manipulate this subspace individually. This limitation can be also be understood by noting that the energy levels of the harmonic oscillator are all equally spaced in energy by  $\hbar\omega$ ; a drive that can induce a transition from  $|0\rangle$  to  $|1\rangle$  will also be able to induce a transition from  $|n\rangle$  to  $|n+1\rangle$ . To enable more exquisite control over the harmonic oscillator we will need an additional nonlinear control.

### 3.1.2 Adding the Josephson junction

Accessing more interesting dynamics of our quantum electrical circuits requires an additional circuit element that is not standard in the electrical engineer's toolbox: the Josephson tunnel junction (JJ) [103, 104]. The tunnel junction can be constructed using several methods including as a thin region of insulator or normal metal sandwiched by two superconducting islands. In our experiments, we construct JJs in this fashion and create a stack of superconductor, insulator, and superconductor. In such a system, Cooper pairs can coherently tunnel through the junction, setting up a nontrivial current through the JJ element. As we will see, the JJ can be thought of as an nonlinear inductor whose inductance depends on the phase difference across the junction. We refer the interested reader to numerous texts that provide a comprehensive derivation of the results described in this section [106, 108, 109].

The JJ is governed by two relations, dubbed the Josephson equations [103, 104, 108, 109]:

$$\begin{aligned} I(\varphi) &= I_c \sin \varphi \\ \frac{\partial \varphi}{\partial t} &= \frac{2e}{\hbar} V = \frac{V}{\phi_0}, \end{aligned} \tag{3.16}$$

where  $\phi_0 \equiv \Phi_0/2\pi = \hbar/2e$  is the reduced magnetic flux quantum. For the first equation:  $I(\varphi)$  is the current flowing through the junction;  $I_c$  is critical current and is the maximum possible supercurrent that the JJ can coherently support; and  $\varphi$  is the phase difference between the two superconducting wave functions on either side of the junction. For the second:  $e$  is the electron

charge; and  $V$  is an applied potential difference across the junction.

We first describe how the Josephson junction behaves like a nonlinear inductor by developing the relationship between voltage and phase,  $L \equiv V/\dot{I}$ . We take the time derivative of the first Josephson equation and combine the result with the second

$$\frac{\partial I(\varphi)}{\partial t} = I_c \cos \varphi \times \frac{\partial \varphi}{\partial t} = \frac{I_c \cos \varphi}{\phi_0} \times V. \quad (3.17)$$

Then we can define the Josephson inductance as

$$L_J = \frac{\phi_0}{I_c \cos \varphi}, \quad (3.18)$$

which shows that the inductance is dependent on the  $\varphi$  across the junction. We typically report the maximum  $L_J$ , with  $\varphi = 0$ . In practice, we can make Josephson junctions with  $L_J \approx 1\text{--}15$  nH with standard lithography techniques [110, 111].

Next, we can write down the Hamiltonian for a bare Josephson junction [100]. We parameterize it in terms of  $E_J \equiv \phi_0 I_c$ , the Josephson energy, which describes the energy cost to tunnel an electron across the Josephson junction.

$$\mathcal{H}_{JJ} = -E_J \cos(\varphi) - 2eV\hat{n} \quad (3.19)$$

where  $\hat{n} = i\frac{\partial}{\partial \varphi}$ , which is the number operator, representing the number of Cooper pairs that have tunneled across the junction. The addition of the Josephson junction to our library of circuit elements is the key ingredient that allows us to realize a veritable zoo of nonlinear quantum circuits, of which we focus on only one exceedingly simple variety.

### 3.1.3 Quantum circuits with Josephson junctions

One primary attraction for studying Josephson junction quantum devices is the incredible flexibility and controllability in constructing these circuits. The properties that govern its quantum dynamics are macroscopic parameters—like capacitance and linear and Josephson inductance—all

of which can be robustly and reliably tuned to precise design specifications. In the field of superconducting qubits and cQED, these circuits play the role of “artificial atoms”, emulating their natural counterpart in terms of energy level structure while allowing us to custom design the properties of the atoms.

There are three main types of superconducting qubits that utilize a single Josephson junction as the nonlinear element, each relying on a different physical macroscopic degree of freedom as the parameter that enables quantum control over the qubit [112]: the phase qubit [112, 113, 114], the flux qubit [115, 116, 117], and the charge qubit [118, 119]. Two of the popular designs extensively studied at Yale are the transmon qubit, where a small junction is shunted by a large capacitance [120], and the fluxonium qubit, where a small junction is shunted by a large linear inductance [121]. Both circuit topologies aim to suppress one dominant noise mechanism, offset charge noise. In this thesis, the transmon qubit will serve as the workhorse for the quantum information experiments we will describe in the following chapters. The fundamental physics that describe the transmon qubit have been exhaustively address in numerous texts [120, 122]; here we will mention the primary reasons why the transmon qubit has become such a popular choice for experiments with superconducting qubits.

The transmon qubit consists of two superconducting electrodes (or islands) that are connected by a Josephson junction. The Hamiltonian for such a circuit, called the Cooper pair box (CPB), is given as

$$\mathcal{H}_{\text{CPB}} = 4E_C(\hat{n} - n_g)^2 - E_J \cos \varphi \quad (3.20)$$

where the charging energy,  $E_C \equiv e^2/(2C_\Sigma)$ , represents the energy of a single electron stored on the capacitance <sup>3</sup> and the Josephson energy written in terms of the Josephson inductance is  $E_J \equiv 2\pi\phi_0^2/L_J$ . The gate or offset charge,  $n_g \equiv -C_g V/2e$  is a continuous (classical) variable that can be used to modify the Hamiltonian (with the application of a voltage bias, for example). The CPB operated in a regime where  $E_J \ll E_C$ , where the quantum information is stored in number of Cooper pairs that has tunneled across the junction. However,  $n_g$  can also fluctuate

---

3. Since electrons tunnel in pairs across a Josephson junction, the total energy is four times the energy of a single electron.

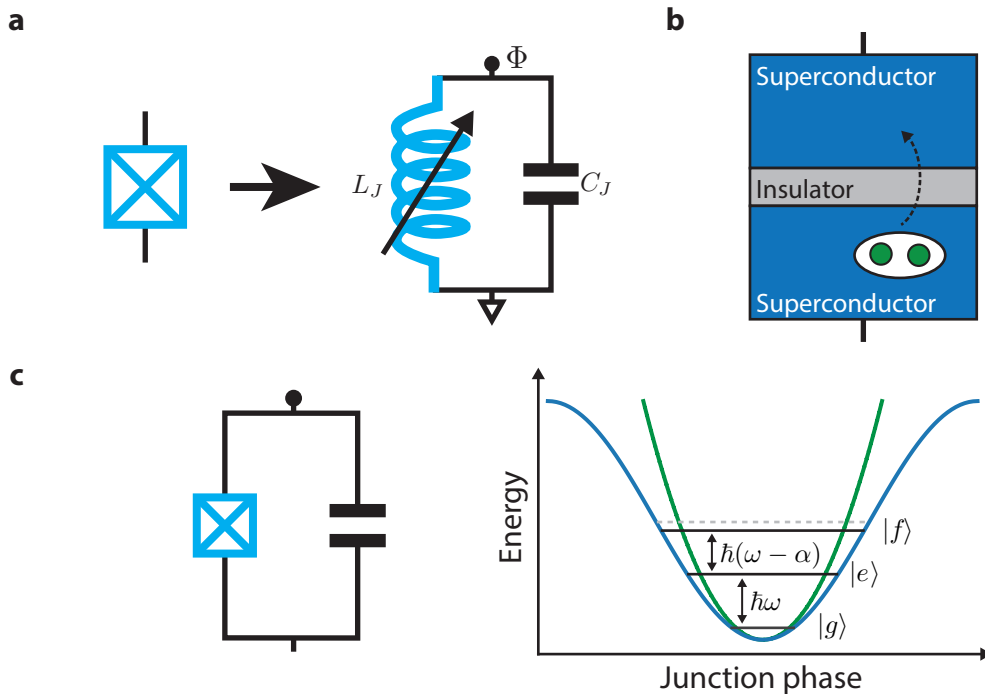


Figure 3.2 | **The Josephson junction and transmon qubit.** **a**, The circuit representation of a Josephson junction is square with an X drawn inside. The decomposition of the Josephson junction can be represented as a nonlinear Josephson inductance  $L_J$  in parallel with a Josephson capacitance  $C_J$ . **b**, While there are many physical implementations for such a nonlinear circuit element, here we construct our Josephson junctions from a three layer stack consisting of a superconductor, a thin layer of insulator, and superconductor that only allows Cooper pairs to tunnel between the superconductor terminals. The superconductor is Aluminum, and the insulator is a thin layer Aluminum oxide. **c**, A transmon consists of a Josephson junction in parallel with a large shunt capacitance. This shunt capacitance serves to dramatically reduce the transmon susceptibility to charge noise. The energy spectrum of a transmon qubit is no longer a simple quadratic potential; the presence of the nonlinear junction replaces the quadratic potential with a cosine-shaped potential. For small excursions of the junction phase, we can consider the transmon as a slightly anharmonic oscillator. The transition frequency between the ground and first-excited level is  $\omega$  and the anharmonicity is  $\alpha$ . For transmon qubits, the anharmonicity is around 5% of the transition frequency, sufficient in most cases to approximate the transmon as a simple two-level system. However, the presence of higher-levels (such as the  $|f\rangle$ ) can modify the quality of control of the two-level subspace. Additionally, certain experiments can also utilize higher-level excitations to store and process quantum information.

randomly, which results in uncertainty in the exact energy level spacing, ultimately placing a limit on the coherence on early charge qubits.

By moving to a regime where  $E_J/E_C \gg 1$  we can address this issue of “charge dispersion”, resulting in the development of the transmon qubit [120]. There are two main effects when increasing  $E_J/E_C$ . First, increasing this critical parameter exponentially reduces the dependence of the energy level on the  $n_g$ . The important result is that the energy levels—and thus qubit frequency—are far less sensitive to random fluctuations of the gate charge, dramatically improving the coherence of transmon qubits. Second, this suppression of charge dispersion comes at a cost of linearizing the transmon qubit spectrum. At very large  $E_J/E_C$ , the circuit Hamiltonian will reflect that of a harmonic oscillator, and it will be no longer possible to address individual energy levels. Fortunately, the decrease in the *anharmonicity*—the energy difference between the lowest energy level splitting and the next splitting—occurs only polynomially with this critical parameter; therefore, it is possible to maintain sufficient nonlinearity while sufficiently suppressing charge dispersion so it is no longer the dominant decoherence mechanism.

When operating in the transmon regime, the large  $E_J/E_C$  limits the phase to small excursions about  $\varphi = 0$ . We can then expand around this small parameter to explicitly treat the transmon as an anharmonic oscillator

$$\mathcal{H}_{\text{transmon}} = \underbrace{4E_C \hat{n}^2 - \frac{E_J}{2} \varphi^2}_{\text{linear terms}} + E_J \underbrace{\left( -\frac{\varphi^4}{4!} - \frac{\varphi^6}{6!} \right)}_{\text{nonlinear terms}}. \quad (3.21)$$

This Hamiltonian can be recast in second quantization using 3.9. After making these substitutions, we expand the cosine to fourth order in  $\varphi$  and apply the rotating wave approximation (which removes fast-oscillating terms that do not conserve energy, like  $\hat{a}\hat{a}$ ) to find the transmon Hamiltonian

$$\mathcal{H}_{\text{transmon}} = \hbar\omega \hat{a}^\dagger \hat{a} - \frac{\hbar\alpha}{2} \hat{a}^\dagger \hat{a}^\dagger \hat{a} \hat{a}, \quad (3.22)$$

where the (linear) frequency of the transmon is given as  $\omega = (\sqrt{8E_J E_C} - E_C)/\hbar$  and the anharmonicity  $\alpha = E_C/\hbar$ . The anharmonicity is defined as  $\alpha = \omega_{ef} - \omega_{ge}$ , or the frequency difference between successive transitions on the transmon spectrum. As we will describe in more detail in chapter 4, our transmons are typically designed to have frequencies  $\omega/2\pi \approx$

4–10 GHz and anharmonicities of  $\alpha/2\pi \approx 100–300$  MHz. This  $\sim 5\%$  anharmonicity is sufficient to define the lowest two levels as a qubit.

## 3.2 Quantum electrodynamics with circuits and cavities

To access the quantized levels of any quantum system, it is necessary to decouple it from its external environment. The first experimental examples of individual quantum systems achieving this level of quantum control are trapped ions [66, 123]. Individual charged particles are confined in an ultra-high vacuum trap through the combination of lasers and EM fields, cooled the ion electronic ground state and coupled to only mechanical motion governed by the shape of the confining potential. Cavity quantum electrodynamics (CQED, with a capital “C”) is the second prototypical experimental implementation achieving quantum control over individual quantum systems [20]. In such experiments, the interaction between light and matter is explored through coupling neutral (Rydberg) atoms with a high quality superconducting cavity, either in the optical or microwave frequency domain [71, 80]. As a testament to the remarkable achievements in both of these fields, David Wineland and Serge Haroche were awarded the Nobel Prize in 2012 for their work demonstrating “ground-breaking experimental methods that enable measuring and manipulation of individual quantum systems” [72, 80]. Circuit-QED takes inspiration from Cavity-QED and explores the physics of coupling our superconducting artificial atoms made with Josephson junction(s) to microwave superconducting resonators.

Perhaps the original result that has enabled these remarkable achievements is a short note by Edward Purcell in 1946 [124]. Purcell realized that the atom’s rate of spontaneous emission can be modified—either enhanced or suppressed—by placing the atom within a cavity, a resonant EM circuit with well defined modes. This insight was based on a Fermi’s Golden Rule argument: the rate of spontaneous emission is related to the environmental density of states that the atom will see at its resonance frequency. In the original work, the goal was to increase the rate of spontaneous emission for spins in an NMR experiment. By tuning a resonant electrical circuit into resonance with the spin, Purcell correctly proposed that the rate of spontaneous emission

would dramatically increase compared to the free space case by concentrating the mode density at the resonance frequency of the spin. It was a few decades later that Kleppner, et al. [20, 125] detailed how the the “Purcell effect” could be used to suppress the rate of spontaneous emission, which, for the purposes of quantum information processing, is this regime we want to achieve in our cQED systems.

### 3.2.1 Jaynes-Cummings Hamiltonian

Historically, the interaction between an atom (real or artificial) and photons confined in a harmonic oscillator—or more generically, a spin-1/2 particle coupled to a spring—is well-described by the Jaynes-Cummings Hamiltonian [126]. In such a system, the atomic dipole couples to the electric field of the oscillator, leading to the

$$\begin{aligned}\mathcal{H}_{JC}/\hbar &= \omega_a \hat{a}^\dagger \hat{a} + \frac{\omega_q}{2} \hat{\sigma}_z + g (\hat{a}^\dagger + \hat{a}) (\hat{\sigma}_+ + \hat{\sigma}_-) \\ \mathcal{H}_{JC}/\hbar &\approx \omega_a \hat{a}^\dagger \hat{a} + \frac{\omega_q}{2} \hat{\sigma}_z + g (\hat{a} \hat{\sigma}_+ + \hat{a} \hat{\sigma}_-)\end{aligned}\tag{3.23}$$

where  $\hat{a}$  is the annihilation operator for the resonator mode;  $\hat{\sigma}_z$  is the Pauli-Z operator for the spin mode;  $\omega_a$  and  $\omega_q$  are the resonance frequencies for the resonator and spin, respectively; and  $g$  is the coupling strength between the resonator and spin. In the second line we took what is called the *rotating-wave approximation*, removing fast-oscillating terms that do not conserve energy (e.g.  $\hat{a}^\dagger \hat{\sigma}_+$  which adds both a resonator excitation and an spin excitation). This approximation is valid in the regime where the atom-resonator coupling strength is much smaller than the resonance frequencies  $g \ll \omega_a, \omega_q$ .

In the case when the spin and resonator are completely decoupled,  $g = 0$ , then the eigenstates of the system are product states of the spin and resonator photon number:  $|g/e, n\rangle$ . For non-zero coupling, we will find that the eigenstates of this coupled systems are no longer purely spin or purely resonator—the new eigenstates of the system have “mixed” spin-photon character, resulting

in the “dressed states”,

$$\begin{aligned} |+, n\rangle &= \cos \frac{\theta}{2} |e, n\rangle + \sin \frac{\theta}{2} |g, n+1\rangle \\ |-, n\rangle &= \sin \frac{\theta}{2} |e, n\rangle - \cos \frac{\theta}{2} |g, n+1\rangle \end{aligned} \quad (3.24)$$

with the “mixing angle”  $\theta = 2 \arctan(\Omega_n/\Delta)$ , “n-photon Rabi frequency” [20]  $\Omega_n = 2g\sqrt{n+1}$ , and the spin-resonator detuning,  $\Delta = |\omega_a - \omega_q|$ . This pair of states forms a manifold where the total number of excitations is conserved and form what is called the Jaynes-Cummings ladder [99]. The eigenfrequencies for this coupled system are

$$w_n^\pm = \omega_a n \pm \frac{1}{2} \sqrt{\Delta^2 + \Omega_n^2} \quad (3.25)$$

In the resonant case  $\Delta = 0$ , we enter what is called the “vacuum-Rabi” regime, where the eigenstates from Equation 3.24 are equally weighted superpositions of  $|e, n\rangle$  and  $|g, n+1\rangle$ . In “strong coupling regime” where the dissipation rate of both the spin and oscillator is smaller than  $g$ , then if the system is prepared in either product state one will observe oscillations between the two product states. The observation of vacuum-Rabi oscillations in CQED [127, 128] and in cQED [96] was an important demonstration indicating that these quantum systems can be designed with interaction strengths far greater than dissipation rates.

It is typical nowadays to operate in the regime of large detuning  $\Delta \gg g$ , in what is called the “dispersive regime” where no actual excitation (energy) is exchanged between spin and resonator. In this regime, we see that the eigenstates are only slightly dressed as a result of the interaction Hamiltonian. As such we can use perturbation theory to arrive at the dispersive Jaynes-Cummings Hamiltonian. Expanding Equation 3.23 in powers of  $(g/\Delta)$  and taking the RWA, we arrive at the Hamiltonian,

$$\mathcal{H}_{\text{disp}}/\hbar = \left( \omega_a - \frac{g^2}{\Delta} \hat{\sigma}_z \right) \hat{a}^\dagger \hat{a} + \frac{\omega_q}{2} \hat{\sigma}_z \quad (3.26)$$

$$= \omega_a \hat{a}^\dagger \hat{a} + \left( \frac{\omega_q}{2} - \frac{g^2}{\Delta} \hat{a}^\dagger \hat{a} \right) \hat{\sigma}_z \quad (3.27)$$

We typically parameterize the interaction strength  $\chi = g^2/\Delta$ . The first line highlights that the

interaction causes a qubit-state dependent frequency shift. It is this energy shift of the resonator that is typically used for qubit state measurement. Equivalently, the second line stresses the effect of the interaction on the qubit frequency, which experiences a Stark shift of  $n\chi$  for  $n$  photons in the resonator. This Stark shift will turn out to be an incredibly powerful tool that enables complex qubit-cavity manipulations. Typically in our experiments we will work in the “strong dispersive limit” where the dispersive interaction strength  $\chi$  dominates over any dissipation term in the system. In this regime, we can isolate and manipulate these state-dependent transitions many times before quantum information is lost to dissipation. In [Figure 3.3](#), we show the energy level diagram and spectrum for a coupled qubit-cavity Jaynes-Cumming system.

This simple-looking Hamiltonian has enabled a perhaps surprisingly rich collection of quantum information experiments in cQED. However, as our level of control becomes more demanding and our experimental devices more complicated, we will need a more detailed translation of our quantum circuits into a Hamiltonian. There are a few issues with the standard Jaynes-Cumming approach. First, the Josephson circuits are described by a cosine Hamiltonian ([Equation 3.19](#)) and have more levels than the simple two-level spin that is described by the Jaynes-Cummings Hamiltonian. Additionally, the cosine term leads to an interaction Hamiltonian that is more complex than the simple dipole coupling between spin and resonator. Second, our implementations of resonators are in reality multi-mode resonant structures; even though these modes can be far detuned from the frequencies of interest, they can dramatically influence the behavior of our qubits. Finally, the size-scale and frequency range of our devices requires that we treat them as distributed elements, increasing the number of circuit elements required for an accurate model. A more general treatment is required for turning a given physical implementation into a Hamiltonian.

### 3.2.2 Quantizing nonlinear quantum circuits

If we have a given circuit model, then there are straightforward techniques to quantize it and determine the Hamiltonian [[101](#), [129](#)]. Furthermore, it is also possible to include the effect of dissipation by decomposing resistors according to the Caldeira-Leggett model [[102](#), [130](#)].

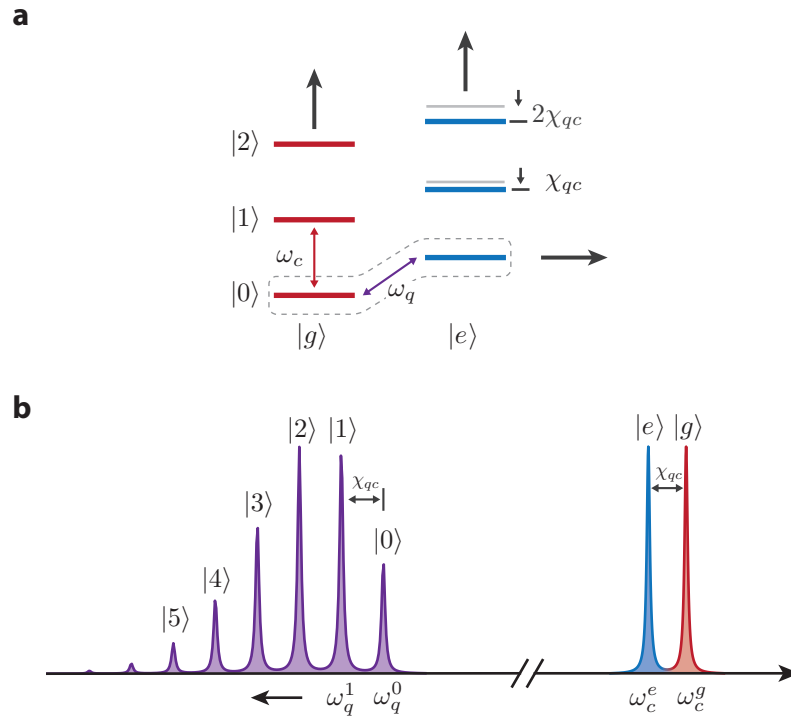


Figure 3.3 | **Jaynes-Cummings energy spectrum.** **a** We depict the energy levels for a coupled qubit-cavity system that follows from the Jaynes-Cummings model. The vertical axis shows the cavity Fock states ( $|n\rangle$ ) and the horizontal axis shows the qubit states ( $\{|g\rangle, |e\rangle\}$ ). The frequency of the cavity transition when the qubit is in  $|g\rangle$  is  $\omega_c$ , and the frequency of the qubit transition when there are zero photons in the cavity is  $\omega_q$ . According to the Jaynes-Cummings interaction, the transition frequencies of one mode shifts linearly, by  $-\chi_{qc}$ , depending on the number of excitations in the other mode. **b** We illustrate the frequency spectrum of the coupled qubit-cavity system. On the left, we illustrate the qubit transition spectrum when there are photons in the cavity. The transition frequency (that is, the energy difference between  $|e\rangle$  and  $|g\rangle$ ) of the qubit shifts by  $-\chi_{qc}$  for each photon in the cavity. The spectrum shown here, simulates the spectrum when the cavity is populated with a coherent state, which results in Poisson-weighted photon number populations. On the right, we show the cavity spectrum when the qubit is in either  $|g\rangle$  or  $|e\rangle$ . Similar to the qubit spectrum, the cavity transition frequency is shifted by  $-\chi_{qc}$  when the qubit is in  $|e\rangle$ .

However, the challenge is that its not always clear how to decompose a complex electromagnetic structure into inductors, capacitors, and resistors. The story becomes even more complex when we add Josephson junctions into the mix. Fortunately, there are several approaches to model such systems [131, 132] using what is called *black-box quantization* (BBQ). The key insight is that any general circuit network can be re-synthesized in a well-described circuit with an equivalent

impedance function,  $Z(\omega)$ , that unambiguously exposes the normal modes of the circuit. Such a decomposition makes it straightforward to quantize linear circuit networks while also accounting for classical coupling between different modes in a black box. For systems with only weak anharmonicity, like transmon qubits, the effect of the Josephson junction nonlinearity can be then added perturbatively. The two main circuit decompositions discussed in the literature are the Foster-equivalent [133] and Brune-equivalent [134] circuits. When designing experimental devices, we have typically utilized the Foster approach based on the work of [131]. Indeed, for our highly coherent transmons and cavities, we have found remarkably good agreement between our model and experiment. The Brune-equivalent circuit is especially useful when considering lossy circuit networks, improving upon some shortcomings of the “lossy Foster” approach. More recently, an approach based on energy participation ratios between the modes of a given circuit is yet another promising approach for quantizing an arbitrary circuit network (Mineev 2018, in prep).

### Black-box quantization

In the following, we summarize the main results of the black-box quantization theory [131]. We start with an arbitrary circuit network composed of purely-reactive elements: inductors, capacitors, and Josephson junctions. We will first consider a system with a single junction. We split the Josephson junction into two parallel circuit components: first, a linear component, characterized by the Josephson inductance  $L_J$  and capacitance  $C_J$ ; second, and nonlinear component, where we take all higher orders of the Josephson potential. We call this strictly nonlinear component, the “spider element”. According to BBQ, we first begin our analysis by computing the normal modes of the *linear* circuit. We assign a port across the spider element and extract the impedance of the linear part of the black-box circuit (including the linear component of the Josephson junction, but excluding the nonlinear part). According to Foster’s reactance theorem [133], any passive network (one without any current or voltage sources) the impedance of any

given network can be compactly described as

$$Z(\omega) = \sum_m \left( j\omega C_m + \frac{1}{j\omega L_m} + \frac{1}{R_m} \right)^{-1} \quad (3.28)$$

$$\rightarrow \sum_m \frac{j\omega/C_m}{\omega_m^2 - \omega^2} \quad (3.29)$$

where  $M$  is the number of modes and  $j = -\sqrt{-1}$ . When the dissipation is small,  $R_m \gg Z_m = \sqrt{L_m/C_m}$ , the resonance frequencies are defined as  $\omega_m = 1/\sqrt{L_m C_m}$  corresponding to a pole (e.g.  $Z(\omega_m) \rightarrow \infty$ ) in the impedance function. Equivalently, when considering a circuit network with a single port we can extract the zeros of the admittance function,  $Y(\omega_m) = Z(\omega_m)^{-1} = 0$ . When performing BBQ, it is also important to calculate the derivative of the admittance at each resonance frequency:  $Y'(\omega_m) = j2C_m$ .

Given the impedance or admittance function of a given network, we can quantize the electrical circuit. The Foster equivalent circuit neatly casts the circuit as a series of independent LC oscillators, which we quantized back in [subsection 3.1.1](#). In terms of the normal coordinates  $\hat{\Phi}_m$  and  $\hat{Q}_m$  for each individual LC circuit, the Hamiltonian can be written as

$$\mathcal{H}_{\text{lin}} = \sum_m \left( \frac{\hat{Q}_m^2}{2C_m} + \frac{\hat{\Phi}_m^2}{2L_m} \right) = \sum_m \hbar\omega_m \hat{a}_m^\dagger \hat{a}_m \quad (3.30)$$

with

$$\hat{\Phi}_m = \Phi_m^{(ZPF)} (\hat{a}_m^\dagger + \hat{a}_m) \quad \hat{Q}_m = -\frac{j\hbar}{2\Phi_m^{(ZPF)}} (\hat{a}_m^\dagger - \hat{a}_m) \quad (3.31)$$

$$\Phi_m^{(ZPF)} = \sqrt{\frac{\hbar}{\omega_m \text{Im}Y'(\omega_m)}}. \quad (3.32)$$

Now that we can produce the linear spectrum of a given black-box circuit, we can now append the nonlinearity provided by the Josephson junction. First, consider a single junction attached to a linear circuit for which we have determined the linear modes. The junction adds a potential to the Hamiltonian

$$\mathcal{H}_{JJ} = -E_J \cos(\hat{\varphi}) \quad (3.33)$$

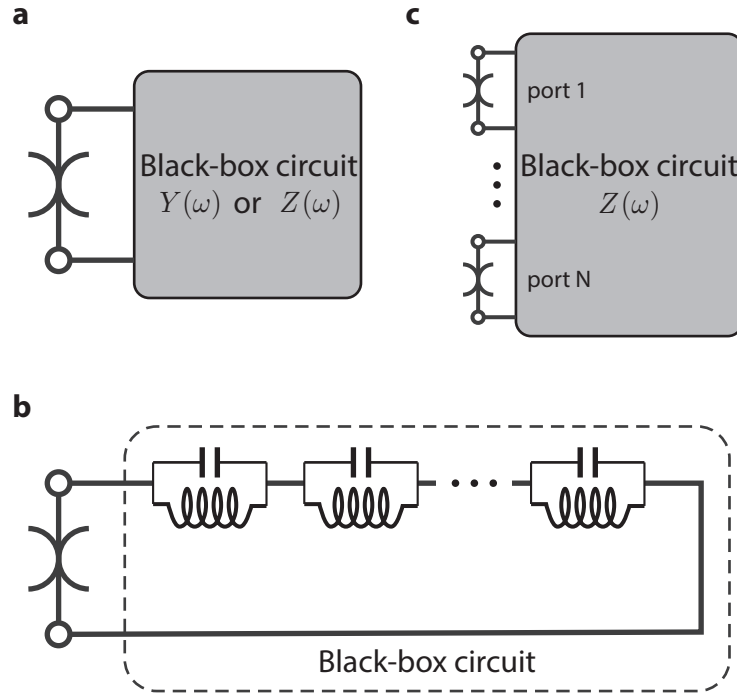


Figure 3.4 | **Black-box quantization circuits.** **a**, In the Black-box formalism, a Josephson junction connected to a generic linear circuit can be recast so that the nonlinear component of the Josephson junction, represented by a “spider” element, is connected a completely linear impedance environment that consists of the linear component of the junction as well as the rest of the linear circuit. When we perform black box quantization, we first solve the linear circuit to extract the normal modes of the system before adding the effect of the nonlinear component. **b**, Any lossless linear circuit can be decomposed according to Foster’s theorem, expressed as a series combination of parallel LC circuits. Each individual LC circuit represents one normal mode of the system, and by extracting the slope of  $Y(\omega)$  at its resonance frequency, we can determine the effective zero-point fluctuations (or voltage) that each linear mode drives across the junction. **c**, Schematically the generalization of one-port black box quantization to  $N$ -ports merely adds additional ports for additional Josephson junctions. Here, the quantization requires extracting the full  $N \times N$  impedance matrix,  $Z(\omega)$ . Note that each junction will observe a different impedance looking into the black-box.

From the second Josephson relation [Equation 3.16](#), we can relate the phase difference across the junction to the total node flux. We will also use Kirchoff's voltage law the node flux across the junction spider element should equal the sum of the (complex) fluxes across each linear mode up to an arbitrary reference phase that we will set to zero.

$$\hat{\varphi} = \sum_{m=1}^M \hat{\Phi}_m \longrightarrow \hat{\varphi} = \sum_m \Phi_m^{(ZPF)} (\hat{a}_m^\dagger + \hat{a}_m) \quad (3.34)$$

Then we can write the argument for the Josephson junction potential in terms of each of the individual mode fluxes, leading to the black-box Hamiltonian

$$\mathcal{H}_{\text{BBQ}} = \mathcal{H}_{\text{lin.}} - \mathcal{H}_{\text{nl}} \quad (3.35)$$

$$\mathcal{H}_{\text{lin}} = \sum_m \hbar \omega_m \hat{a}_m^\dagger \hat{a}_m \quad (3.36)$$

$$\mathcal{H}_{\text{nl}} = E_J \left[ \cos(\hat{\varphi}) - \left( 1 - \frac{1}{2} \hat{\varphi}^2 \right) \right] = E_J \left[ \frac{\hat{\varphi}^4}{4!} - \frac{\hat{\varphi}^6}{6!} + \mathcal{O}(\hat{\varphi}^8) \right] \quad (3.37)$$

where the last two terms in the  $E_J$  term correspond to the linear part of the Hamiltonian that we have already included with the first part of the Hamiltonian.

We note a few important conclusions from this analysis. The effect of adding the cosine Josephson junction potential first is to induce some anharmonicity in the otherwise harmonic potential, shifting higher energy levels down in frequency. Second, any effect from charge dispersion as discussed in [subsection 3.1.3](#) is neglected in this analysis; it will be necessary to separately verify that this ignoring the effect of offset-charges is valid. These are valid assumptions to make for the case of transmons coupled to linear oscillators.

### Multiple junctions

The single-junction BBQ process can be generalized for multiple junctions. Similar to the single-junction analysis, we hook up each junction to a black-box circuit. Each junction represents a port, and we now consider a multi-port circuit with  $p$  junctions/ports. For such a network, we can generate an impedance matrix  $\mathbf{Z}(\omega)$ , a complex-valued, frequency-dependent matrix that

relates the current  $\vec{I}$  and voltage  $\vec{V}$  at each port.

$$Z_{ij}(\omega) = \left. \frac{V_i(\omega)}{I_j(\omega)} \right|_{I_k=0, k \neq j} \quad (3.38)$$

Note that the self-admittances that are important for single-port BBQ are calculated slightly differently for the multi-port case:  $Y_p = Z_{pp}^{-1}$ . These quantities are no longer simply the inverse of the impedance matrix. As such, if we choose to stick with the impedance matrix, the resonances are found by the poles of  $Z$  in the lossless case. The procedure for multi-junction BBQ is detailed in the original paper [131] as well as Jacob Blumoff's thesis [15]; so here, we will provide a summary.

For multi-port BBQ, we want to determine the node flux  $\varphi_p$  for each port  $p$ . Even though the eigenfrequencies of the black-box is the same (independent) of the choice of port, the impedances (or eigenmodes) that are seen from each port can differ dramatically. We first select a port to serve as a reference; the choice is not important. We will label this port  $r$ . From this reference port and knowing the frequency-dependent impedance matrix  $Z(\omega)$ , we can determine the flux across any other port  $p \neq r$ . These calculated by first noting that the ratio of voltages is equivalent to the ratio of trans-impedance and self-impedance,  $V_p/V_r = Z_{pr}/Z_{rr}$ . Then, the node fluxes are defined as the derivative of the voltages,  $j\omega\phi_p(\omega) = V_p$ , we can determine the relative node flux for port  $p$  as

$$\varphi_p(\omega) = \frac{Z_{pr}}{Z_{rr}} \varphi_r(\omega) \quad (3.39)$$

Then, the total flux across port  $p$ ,

$$\hat{\varphi}_p^{(r)} = \sum_m \frac{Z_{pr}(\omega_m)}{Z_{rr}(\omega_m)} \Phi_{rm}^{(ZPF)} \left( \hat{a}_m^\dagger + \hat{a}_m \right) \quad \Phi_{rm}^{(ZPF)} = \sqrt{\frac{\hbar}{\omega_m \text{Im} Y_r'(\omega_m)}} \quad (3.40)$$

Thus in order to calculate the port flux, we need the mode frequencies  $\omega_m$ , the slope of the admittance function  $\text{Im} Y_r'$  at each resonance frequency. In addition, we require the first column  $Z_{pr}$  of the impedance function at each mode frequency.

While it is fine in principle to calculate the  $\hat{\varphi}_p^{(r)}$  using this reference-port approach, it is not

what we typically do in practice. It can be challenging to determine the node fluxes  $Z_{pr}$  for  $p \neq r$ . For example, if the junctions associated with port  $p$  and  $r$  are very weakly coupled, then it will be numerically difficult to accurately extract the impedance matrix. Instead, it turns out that we can directly calculate each node flux setting the reference port as the desired port,  $r = p$ .

In this case, the situation looks similar to that of single-port BBQ, where the node flux variable is given as  $\hat{\varphi}_p = \sum_m f_{pr}(\omega_m) \Phi_{pm}^{(ZPF)} (\hat{a}_m^\dagger + \hat{a}_m)$ . Here, to calculate  $\Phi_{pm}^{(ZPF)}$ , we need to only consider the diagonal components of  $Z(\omega)$  to calculate  $Y'_k$  at each of mode frequencies. Additionally, there is a slight modification we have to make using this multi-port approach. We have to correctly choose the “sign” of the zero-point flux relative to a global reference port  $r$ , mathematically given by  $f_{pr}(\omega_m) = \text{sgn} [Z_{pr}(\omega_m)]$ . Basically, we need to establish a global phase convention dictating whether an excitation in mode  $m$  leads to a voltage that is in phase or out of phase on port  $p$  that is consistent across all ports/junctions in the network. We typically set the standard so that all phases are positive for junction  $p = 1$ , and we take the signs for each other junction from the first column of  $Z(\omega)$ . See [15], Figure 3.7 for a particularly useful illustration of this phase convention.

With the junction phases in hand, we can calculate the entire multi-junction Hamiltonian. As before, the Hamiltonian includes the linear component  $\mathcal{H}_{lin}$ ; now, we include a cosine contribution for each for each junction in the circuit. For a circuit with  $m$  normal modes and  $p$  junctions

$$\mathcal{H} = \mathcal{H}_{lin} - \sum_p \mathcal{H}_{p, nl} \quad (3.41)$$

$$\mathcal{H}_{p, nl} = E_{J,p} \left[ \cos(\hat{\varphi}_p) + \frac{1}{2} \hat{\varphi}_p^2 \right] \quad (3.42)$$

As in the single-junction case, we ignore charge dispersion in this analysis and make an assumption that we are working in the low excitation regime where the argument in each cosine term is much smaller than  $\pi$ . According to [131], mathematically we require

$$\frac{\pi}{\Phi_0} \sqrt{\langle (\hat{\varphi})^2 \rangle_{\{n_p\}}} \ll \pi \rightarrow \sum_p \left( \frac{\Phi_p^{(ZPF)}}{\Phi_0} \right)^2 (2n_p + 1) \ll 1 \quad (3.43)$$

where  $n_p = \langle \hat{a}_p^\dagger \hat{a}_p \rangle$ , which is the photon occupation number of the  $p$ -th mode.

### Lossy quantum circuits

So far, we have focused on extracting the quantum dynamics of these cQED systems. A full treatment will require analyzing inevitable energy dissipation associated with any physical implementation. Indeed, as our demands for quantum systems increase, so does our need to accurately model and predict these losses; otherwise, any attempt to construct a large-scale quantum computer will likely fail. These losses can be broadly classified in two categories, one that is intentionally introduced into the quantum system for the purpose of manipulating and measuring the quantum system. The second type of loss is unexpected, corresponding to nonidealities in the physical implementation of the system and can be related to imperfections in materials or in packaging. A discussion of the latter requires focusing on the physical implementation, and will be treated in some more detail in the following chapter.

When we attach input and output ports to our device for control and measurement, we couple each mode to the outside environment. This has two related, but separate, effects: First, this coupling to a continuum can directly limit the lifetime of a particular mode (e.g. an over-coupled resonator); Second, the lifetime of a mode may be limited (or enhanced) through spontaneous emission through its coupling to a separate lossy mode, a phenomenon known as the Purcell effect [124]. Indeed, when we label a mode “Purcell-limited”, this indicates that the lifetime of an excitation in this mode is limited by this rate of spontaneous emission. This is an important quantity to calculate as we ideally want to be operating in a regime far from the Purcell limit to faithfully preserve quantum information within our transmons and memory cavities.

Previous work [135] in understanding this effect has led to two important considerations. First, our resonators support multiple modes and in some cases it is necessary to consider the combined effect in what is now called the “multi-mode” Purcell effect. Second, the location of loss sources can have a significant impact on the Purcell limit. The work in [135] is a particularly illustrative example. In this experiment, two transmons were placed at the opposite ends of a  $\lambda/2$  transmission line resonator. The resonator was asymmetrically coupled to the outside world

with a strongly coupled output port and a weakly coupled input port. Naïvely one might expect that the transmon physically closer to the strongly coupled port would have a lower Purcell limit and exhibit a lower lifetime; however the opposite situation was experimentally observed. Indeed, a circuit model where the resonator is modeled as an LCR resonator fails to predict this behavior. Instead to accurately model the transmon lifetimes, it was necessary to include the full model of the transmission line resonator, transmons, and input-output ports. From this experiment, it is clear that one should consider the actual complex impedance environment of the coupled system.

Currently, our approach to estimate Purcell limits for our experiments rely on the use of 3D electromagnetic simulation tools. This approach can accurately handle the complex renormalization of the (now lossy) modes, provided that we correctly identify the dominant loss mechanisms of a particular implementation. There have been several approaches to treat the effect of loss from a circuit quantization approach [130, 132, 136]; determining an accurate underlying circuit model of a complex impedance matrix is in general a challenging task.

### 3.2.3 Common cQED Hamiltonians

In this section, we will explore some common transmon-cavity systems that will be important in this thesis. Illustrated in [Figure 3.5](#), these serve as useful primitives from which we will build more complex coupled systems.

#### Transmon coupled to cavity

Consider a transmon coupled to a cavity, the simplest Hamiltonian that has been widely used in cQED experiments. here we label the transmon mode  $\hat{q}$  and the cavity mode  $\hat{c}$ . The black-box Hamiltonian is given as

$$\begin{aligned} \mathcal{H}_{1T,1C}/\hbar &= \sum_{m=q,c} \omega_m \hat{m}^\dagger \hat{m} - \mathcal{H}_n \\ \hat{\varphi} &= \Phi_q (\hat{q}^\dagger + \hat{q}) + \Phi_c (\hat{c}^\dagger + \hat{c}), \end{aligned} \tag{3.44}$$

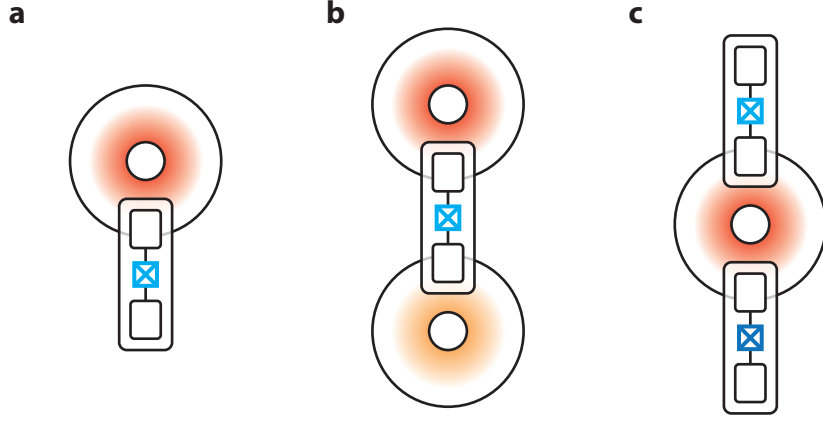


**Figure 3.5 | Common cavity-transmon primitives.** We depict several standard 3D cavity-transmon subsystems common in many modern experiments. For illustrative purposes, we depict the cavities using a cartoon of the now popular coaxial  $\lambda/4$  3D cavities, to be discussed in further detail in the next chapter. The transmon qubit is depicted as a Josephson junction that is attached to two superconducting pads that serve as an antenna to couple to the field of the cavity mode. In **a**, we show the simplest system, a cavity coupled to a single transmon. In **b**, a transmon qubit is coupled to two cavity modes. We typically see this device architecture used in two situations: first, one cavity may be used as a quantum memory and one as a readout for the transmon qubit; second, the two cavities are both quantum memories and the transmon qubit serves as an element to couple the two cavity modes. In **c**, we can couple multiple transmons to a single cavity mode. The cavity mode can be used to mediate interactions between the two (or more) transmon qubits via the dispersive interaction.

where  $\mathcal{H}_{nl}$  is defined in [Equation 3.37](#). It is first useful to expand the cosine to fourth order in  $\varphi$ . Taking the rotating wave approximation to  $\varphi^4$ , we arrive at the dispersive Hamiltonian,

$$\mathcal{H}_{1T,1C}/\hbar = \omega_q \hat{q}^\dagger \hat{q} + \omega_c \hat{c}^\dagger \hat{c} - \frac{K_q}{2} \hat{q}^\dagger \hat{q}^\dagger \hat{q} \hat{q} - \frac{K_c}{2} \hat{c}^\dagger \hat{c}^\dagger \hat{c} \hat{c} - \chi_{qc} \hat{q}^\dagger \hat{q} \hat{c}^\dagger \hat{c}. \quad (3.45)$$

$\left. \begin{array}{l} -\frac{K_q}{2} \hat{q}^\dagger \hat{q}^\dagger \hat{q} \hat{q} - \frac{K_c}{2} \hat{c}^\dagger \hat{c}^\dagger \hat{c} \hat{c} \\ -\chi_{qc} \hat{q}^\dagger \hat{q} \hat{c}^\dagger \hat{c} \end{array} \right\} \mathcal{H}_{1T,1C}^{(4)}$

The first line specifies frequencies of the transmon and cavity, the second line specifies the anharmonicity, or “self-Kerr” of each mode, and the third line describes the dispersive coupling, or “cross-Kerr”, between the transmon and cavity. In the literature we will often see the self-Kerr of the transmon labeled as anharmonicity,  $\alpha_q$ . We can relate each Hamiltonian term to the

underlying circuit parameters,

$$K_m = \frac{E_J}{2} |\Phi_m|^4 \quad (3.46)$$

$$\chi_{qc} = E_J |\Phi_q|^2 |\Phi_c|^2 \quad (3.47)$$

From here, we can see that  $\chi_{qc}$  can be written in terms of the self-Kerrs:  $\chi_{qc} = \sqrt{2K_q K_c}$ .

In some cases it is necessary to consider higher-order terms of the dispersive Hamiltonian. In particular, one important sixth-order term is the the nonlinearity of  $\chi$ , which can take two forms

$$\mathcal{H}_{1T,1C}^{(6)} = \frac{\chi_{qqc}}{2} \hat{q}^\dagger \hat{q}^\dagger \hat{q} \hat{q} \hat{c}^\dagger \hat{c} + \frac{\chi_{qcc}}{2} \hat{q}^\dagger \hat{q} \hat{c}^\dagger \hat{c}^\dagger \hat{c} \hat{c} \quad (3.48)$$

The first term  $\chi_{qqc}$  is the nonlinearity of the dispersive shift as we add excitations to the qubit mode, and the second term  $\chi_{qcc}$  is the nonlinearity of the dispersive shift as we add excitations to the cavity mode. As we generally operate the transmon in the lowest two energy levels, we only consider the second term for experiments in this thesis. This term is more commonly called  $\chi'_{qc}$ , and we will follow this convention for the remainder of this thesis. The effect of  $\chi'_{qc}$  can be clearly write the transmon-cavity coupling term to sixth order as  $(\chi_{qc} + \chi'_{qc} \hat{c}^\dagger \hat{c}) \hat{q}^\dagger \hat{q} \hat{c}^\dagger \hat{c}$ . In this form, the effective dispersive shift is a linear function of the number of photons in the cavity.

We use a additive approach to build these Hamiltonians, where we normal order each term and construct the Hamiltonian with successively higher number of raising and lower operators pairs, e.g. we prefer a term like  $\hat{c}^\dagger \hat{c}^\dagger \hat{c} \hat{c}$  as opposed to  $(\hat{c}^\dagger \hat{c})^2$ . In this way, higher order terms will not modify the lower-order Hamiltonian terms, e.g. normal ordering  $(\hat{c}^\dagger \hat{c})^2$  will add a  $\hat{c}^\dagger \hat{c}$  term. Additionally, the dispersive Hamiltonian is written such that it only contains diagonal terms in the static case, where we have transitions that are directly extracted from experiment. This convention also explains why certain terms have a prefactor, e.g. 1/2 for the self-Kerr terms. We define the anharmonicity as  $K = \omega_{12} - \omega_{01}$ ; and in our convention, the relevant Hamiltonian term  $-\frac{K}{2} \hat{c}^\dagger \hat{c}^\dagger \hat{c} \hat{c}$  shifts the energy of the  $|2\rangle$  level down by  $K$ .

### Transmon coupled to two cavity

For many of our experiments, we couple a single transmon qubit to two cavity modes. There are two separate scenarios when this subsystem is used: first, one cavity serves as a memory mode while the other serves as a readout mode to measure the transmon; second, both cavities serve as memories and the transmon is used to mediate interactions between the two. Whatever the purpose, the underlying Hamiltonian has the same structure. Using our one-transmon, one-cavity Hamiltonian as a primitive, we can write the combined Hamiltonian and highlight the relevant new terms in such a system. We write down the fourth order terms using  $\hat{q}$ ,  $\hat{c}_1$ , and  $\hat{c}_2$  to represent the transmon, cavity 1, and cavity 2:

$$\mathcal{H}_{1T,2C}^{(4)}/\hbar = \mathcal{H}_{1T,1C}^{(4)}(\hat{q}, \hat{c}_1) + \mathcal{H}_{1T,1C}^{(4)}(\hat{q}, \hat{c}_2) + \chi_{c1c2} \hat{c}_1^\dagger \hat{c}_1 \hat{c}_2^\dagger \hat{c}_2 \quad (3.49)$$

The final term,  $\chi_{c1c2}$ , is the cross-Kerr between the two cavities,

$$\chi_{c1c2} = E_J |\Phi_{c1}|^2 |\Phi_{c2}|^2. \quad (3.50)$$

From this expression, we can write the cross-Kerr in terms of other Hamiltonian parameters,  $\chi_{c1c2} = \chi_{qc1} \chi_{qc2} / (2K_q)$ . In the case where one cavity mode serves as a readout of the transmon,  $\chi_{c1c2}$  is a undesirable term as it causes the readout mode to be dependent on the number of photons in the memory cavity mode. In other cases, this coupling can enable useful operations between the two cavities. In recent years, this term has enabled faithful conversion of the cavity mode to the readout mode, either for rapid reset of the cavity mode or for transmission of the cavity mode into a propogating mode for remote state transfer [137, 138]. In other cases, this term can enable operations between two cavity modes.

### Two transmons coupled to a cavity

One final primitive system is the case when two transmons are coupled to a single cavity. The presence of two junctions that may couple with one another introduces additional complexity,

but the broad Hamiltonian terms are no different than in the previous examples. Critical in such a system is the coupling between the two transmon qubits. Physically, this interaction consists of two contributions: first, a direct dipole coupling arising from overlaps in the electric field from each transmon mode; second, a cavity-mediated coupling from virtual interaction with the common cavity mode. The cavity-mediated contribution can be determined via perturbation theory in the large detuning, weak interaction limit (carefully treated in [139] among other sources<sup>4</sup>).

From the expansion of the multi-junction Hamiltonian Equation 3.41 we can determine the value of this coupling

$$\mathcal{H}_{2J,1C}^{(4)}/\hbar = -E_{J1} \cos(\hat{\varphi}_{J1}) - E_{J2} \cos(\hat{\varphi}_{J2}) \quad (3.51)$$

$$\varphi_{Ji} = \tilde{\Phi}_{J1}^{(i)} \hat{q}_1^\dagger + \tilde{\Phi}_{J2}^{(i)} \hat{q}_2^\dagger + \tilde{\Phi}_c^{(i)} \hat{c}^\dagger + \text{h.c.}, \quad (3.52)$$

What is important to note here that we should treat the contributions from *both* junctions, noting that we may have dramatically different magnitudes for each  $\tilde{\Phi}_{Jm}^{(i)}$  term. Expanding this term to fourth order and taking the rotating-wave approximation, we find terms that are proportional to  $\hat{q}_1^\dagger \hat{q}_1 \hat{q}_2^\dagger \hat{q}_2$ . We define the coefficient to this term,  $\zeta_{12}$ , as the dispersive interaction between the two transmon qubit modes, and has the form

$$\zeta_{12} \approx E_{J1} |\Phi_{J1}^{(1)}|^2 |\Phi_{J2}^{(1)}|^2 + E_{J2} |\Phi_{J1}^{(2)}|^2 |\Phi_{J2}^{(2)}|^2 \quad (3.53)$$

From this term, we see that there are contributions to this coupling term from each junction, making it generally a trickier term to estimate. However if the two junctions are identical and each contribute constructively to  $\zeta_{12}$ , then we can treat this coupling term approximately like a “cross-Kerr” between the two transmon qubits. In this case, we can estimate this coupling in terms of the single junction interaction terms:  $\zeta_{12} \approx \chi_1 \chi_2 / (2K_c)$ .

---

4. The magnitude of the virtual interaction is given as  $\zeta_{12,med.} \propto \chi_1 \chi_2 \left( \frac{1}{\Delta_1} + \frac{1}{\Delta_2} \right)$

### 3.3 Quantum control

Performing quantum computation will also require means to perform quantum operations and measurements on these quantum systems. The customary method to do this is to couple our transmons and cavities to input and output ports, performing manipulations by applying classical control tones on the input ports and recording the field that leaks into the output ports. In this final section, we first discuss how we apply classical tones to our cQED system to effect quantum control over our transmons and cavities. Second, we also describe how we extract information from our quantum system, namely through dispersive measurement of the transmon via a readout cavity.

#### 3.3.1 Applying a classical drive

In this section, we will provide an overview of how we apply a drive to our quantum system, based on an input-output approach. Specifically we consider cavity connected to a port through which energy can be delivered to the cavity and lost by the cavity. Many details of this analysis can be found in other pedagogical references, including [106, 140]. These treatments model a transmission line that couples to a cavity mode as a continuum of bath modes that weakly couple to the cavity mode. Taken together, these bath modes form the input and output modes for the quantum system. For a drive, we consider the input mode as a displaced harmonic oscillator that can exchange excitations with the cavity mode. The equation of motion for a single cavity ( $\hat{a}$ ) coupled to a single input mode  $\hat{b}_{in}$  is given as

$$\begin{aligned}\dot{\hat{a}} &= \frac{i}{\hbar} [\mathcal{H}_{sys}, \hat{a}] - \frac{\kappa}{2} \hat{a} - \sqrt{\kappa} \hat{b}_{in}(t) \\ \dot{\hat{a}} &= -i \left( \omega_c + \frac{\kappa}{2} \right) \hat{a} - \sqrt{\kappa} \hat{b}_{in}(t)\end{aligned}\tag{3.54}$$

In the second line we took the specific case where the cavity mode is a linear oscillator, described by  $\mathcal{H}_{sys}/\hbar = \omega_c \hat{a}^\dagger \hat{a}$ . Following [106, 140], we consider the incoming field,  $\hat{b}_{in}$ , as a classical field based on the average value of the incoming field with  $\bar{b}_{in} \rightarrow \epsilon_{in}$ , where  $\epsilon_{in}$  is a parameter that

describes the strength of the drive. We can write the drive Hamiltonian as

$$\mathcal{H}_D = \epsilon_{in}(t)\hat{a}^\dagger + \epsilon_{in}^*(t)\hat{a} \quad (3.55)$$

Generally, we choose to drive our system with a control tone with slowly-varying<sup>5</sup> envelope centered at a frequency  $\omega_d$ . In this case we can write the drive amplitude as  $\epsilon_{in}(t) = \epsilon_0(t)e^{-i\omega_d t}$ . When only considering a drive on a harmonic oscillator, this drive Hamiltonian generates the displacement operator, [Equation 3.15](#).

We can use this formalism to describe the effect of a drive on the transmon. For this discussion, we consider a drive that displaces the cavity mode only. We start by writing down the combined driven cosine Hamiltonian using [Equation 3.44](#) and [Equation 3.55](#). We will also move into the rotating frame to remove the frequency terms

$$\mathcal{H} = -E_J \cos\left(\Phi_q\left(\hat{q}^\dagger + \hat{q}\right) + \Phi_c\left(\hat{c}^\dagger + \hat{c}\right)\right) + \epsilon_0(t)e^{-i\Delta t}\hat{c}^\dagger + \epsilon_0^*(t)e^{i\Delta t}\hat{c}, \quad (3.56)$$

with  $\Delta = \omega_d - \omega_c$ . To see how the transmon drive arises, we can move to a displaced frame where we effectively define new raising and lowering operators that separate out the classical displacement amplitude from the quantum operator:  $\hat{c} \rightarrow \hat{c}_{\text{new}} + \xi$ . One can think of  $\xi$  as a classical value (e.g. a number) that represents the amplitude of the displacement on the cavity. From the Langevin equations of motion, at steady state, this average displacement is given as  $\xi = \sqrt{\kappa}\epsilon_0/(\kappa/2 - i\Delta)$ .

After performing this displacement transformation (see [\[137, 140\]](#)), we arrive at the driven, dispersive Hamiltonian

$$\mathcal{H} = -E_J \cos\left[\Phi_q\left(\hat{q}^\dagger + \hat{q}\right) + \Phi_c\left(\hat{c}^\dagger + \hat{c} + \xi e^{i\Delta t} + \xi^* e^{-i\Delta t}\right)\right]. \quad (3.57)$$

This Hamiltonian is similar to the undriven case and contains all of the same self-Kerr and cross-Kerr terms discussed previously. Additionally, we can extract the following displacement-like

---

5. The pulse envelope is slowly varying relative to the frequency.

terms

$$\mathcal{H}_{D,c} = \left( \xi e^{i\Delta t} \hat{c}^\dagger + \xi^* e^{-i\Delta t} \hat{c} \right) \quad \mathcal{H}_{D,q} = \left( \xi e^{i\Delta t} \hat{q}^\dagger + \xi^* e^{-i\Delta t} \hat{q} \right) \quad (3.58)$$

corresponding to a drive on the cavity mode and on the transmon mode, respectively. Because we have control over  $\xi$  and  $\Delta$ , we can perform operations on either the cavity and transmon mode.

In the case of the transmon, the presence of the anharmonicity  $\alpha_q$  causes the higher transition levels to become detuned from the drive. Then, the dynamics are limited to the  $\{|g\rangle, |e\rangle\}$  of the transmon, thus defining our control over our two level system. Applying a drive to the qubit will then induce Rabi oscillations between the two basis states. By tuning the amplitude and phase of this drive, we can perform arbitrary rotations about the Bloch sphere of transmon effective two-level system. In general, this two-level approximation of the transmon is sufficient to extract the relevant physics, but in some cases—particularly when using short, high-bandwidth pulses to perform rotations—the higher levels of the transmon can influence the dynamics of the lowest two levels [141].

### 3.3.2 Off-resonant drives

Resonant interactions are but a limited subset of processes that can be enabled by a classical drive. For example, applying a detuned drive can induce AC Stark shifts that modify the (drive) frequency of our modes. For example, if we consider applying a detuned drive on the cavity, we can find terms in the expansion of the cosine from [Equation 3.57](#)

$$\mathcal{H}_{ss}/\hbar \approx \Delta_c(\xi) \hat{c}^\dagger \hat{c} + \Delta_q(\xi) \hat{q}^\dagger \hat{q}, \quad (3.59)$$

$$\Delta_c(\xi) = K_c |\xi|^2 \quad \Delta_q(\xi) = \chi_{qc} |\xi|^2, \quad (3.60)$$

the magnitude of the frequency shift is set by the amplitude of the drive,  $|\xi|^2 \propto (\Delta^2 + \kappa^2/4)^{-1}$ .

We will mention only in passing that applying these off-resonant pumps can enable certain multi-photon processes that are normally far detuned. In such situations, we treat the Josephson

junction circuit as a mode mixing element. For example, if we apply two tones separated by  $\Delta$ , then we will enable a mode conversion (or “beam splitter”) Hamiltonian,  $\mathcal{H} \propto g (\hat{q}^\dagger \hat{c} + \hat{q} \hat{c}^\dagger)$ , transferring an excitation of the transmon into the cavity and vice versa. The strength of this interaction can be adjusted by modifying the amplitude of each drive as well as the global detuning of the two drives from the quantum modes:  $g \propto \chi_{qc} \xi_1 \xi_2$ . Alternatively, we can enable a “two-mode squeezing” Hamiltonian,  $\mathcal{H}_{squeeze} \propto g (\hat{q}^\dagger \hat{c}^\dagger + \hat{q} \hat{c})$ , if we apply a drive at the sum of the two modes. We have used the former interaction to reset our system, rapidly transferring energy from one mode (transmon or high-Q cavity) to a low-Q readout resonator [138, 142]. More recently, this interaction has been used to implement interactions between cavity states for multi-cavity operations [143].

### 3.3.3 Dispersive qubit measurement

In addition to absorbing an excitation from the incoming drive field, the cavity can also emit into a propagating mode of the transmission line,  $\hat{b}_{out}$ . For a one port cavity, the outgoing field consists of a contribution from the reflected incoming field and the emitted field from the cavity:

$$\hat{b}_{out}(t) = \hat{b}_{in}(t) + \sqrt{\kappa} \hat{a}(t) \quad (3.61)$$

In many of our experiments, we choose instead to drive the cavity through a weakly coupled port and extract the cavity field through a strongly coupled port, where  $\kappa_{in} \ll \kappa_{out}$ . In this case, we only need to consider the outgoing field from the cavity, and as such:  $\hat{b}_{out}(t) = \sqrt{\kappa} \hat{a}(t)$ .

Through the dispersive interaction between a transmon and cavity, the outgoing field can be used to infer the state of the transmon qubit. The main insight for what is called “dispersive measurements” is that the cavity frequency is shifted by  $\chi$  depending on the state of the transmon. The Hamiltonian describing this is

$$\mathcal{H} = \left( \omega_c - \chi \hat{q}^\dagger \hat{q} \right) \hat{c}^\dagger \hat{c} + \mathcal{H}_D \quad (3.62)$$

In the absence of energy relaxation of the transmon qubit, we can simplify the problem and

consider the Hamiltonian of the cavity degree of freedom only. There are two different responses dependent on the state of the transmon (here we consider the transmon being in either  $|g\rangle$  or  $|e\rangle$ , but the analysis is very similar if we choose to climb the transmon excitation ladder and go to higher level states). Following Equation 3.54, the cavity response when a classical drive is applied is given as

$$\begin{aligned}\dot{\alpha}_g &= -\left(i\omega_c + \frac{\kappa}{2}\right)\alpha_g - \sqrt{\kappa}\xi \\ \dot{\alpha}_e &= -\left(i(\omega_c - \chi) + \frac{\kappa}{2}\right)\alpha_e - \sqrt{\kappa}\xi\end{aligned}\tag{3.63}$$

where  $\alpha_{g,e}$  represents the amplitude of the cavity coherent state. Using the language introduced in Chapter 1, the cavity state becomes a “pointer variable” to the state of the transmon and is entangled with the transmon. In the case where the cavity decay is dominated by energy leakage through the input-output port (e.g.  $\kappa$  dominates over other forms of dissipation in the system), the outgoing field is related to the field inside of the cavity according to Equation 3.61. This outgoing field is then typically amplified and digitized, resulting in a measurement trajectory that we analyze to determine the state of the transmon.

Performing accurate quantum computation requires high fidelity, quantum non-demolition measurements to faithfully extract classical information from our quantum systems. What makes this problem challenging is that our transmon qubits do suffer from energy relaxation during the measurement process <sup>6</sup>. Other than improvements to our transmon lifetimes, there have been several advances in the field that have allowed measurement fidelities in this thesis to exceed 99%. On the hardware side, the development of low noise, nearly quantum-limited amplification [144] (here, we use Josephson Parametric Converters [145]) that acts as a pre-amplifier to the small output field emitted from the cavity. The choice of system parameters can also influence measurement fidelity, in particular the ratio  $\chi/\kappa$  is key parameter to consider when optimizing measurement. This ratio can be understood as how efficiently information about the transmon state is first transferred to intra-cavity photons (via  $\chi$ ) and then to propagating output photons (via  $\kappa$ ). In addition, the shape, frequency, and power of the measurement drive are also

6. It has been also observed that the presence of the measurement drive can enhance the relaxation rate of the transmon, a behavior called “ $T_1$  vs.  $\bar{n}$ ”. Its origins are under current theoretical and experimental investigation.

critical parameters when tuning up transmon readout, which have been extensively discussed in the literature [144] and in various theses [146]. Finally, the digitized measurement trajectories result in a vector of numbers corresponding to the continuous-time nature of our measurement. Our classical processing performs quantum state estimation and assigns “g” or “e” to a given measurement trajectory. This is accomplished through integrating the measurement trajectory according to some filter function that maximizes the signal to noise ratio for each individual record. Typically the filter is simply the vector difference between the “g” and “e” trajectories:  $\beta(t) = |\alpha_e(t) - \alpha_g(t)|$ , though there exist optimal nonlinear filters that take into consideration  $T_1$  of the transmon qubit.

## 3.4 Conclusion

In this chapter we presented the foundations for quantum information processing using superconducting qubits, providing a physical link to the concepts discussed in [chapter 2](#). We started from a discussion of how to think about electrical circuits from a quantum mechanical perspective and added the Josephson junction as the crucial nonlinear circuit element for our cQED experiments. The transmon qubit is the fundamental nonlinear circuit element that is used in this thesis, and we described this particular quantum circuit as a weakly anharmonic oscillator with sufficient nonlinearity to isolate the lowest energy levels to build a basic qubit. We described a general black-box prescription for quantizing weakly non-linear quantum circuits. This process is critical to convert a physical implementation into a well-understood and controllable Hamiltonian. It may be possible in the future to reverse the process: from a target Hamiltonian, construct a physical device that can be easily and accurately constructed. By coupling transmon qubits to linear harmonic oscillators, we enter the realm of circuit QED. Historically, these oscillators are used to protect transmon qubits from the Purcell effect and to measure the state of the transmon qubit. Recent advances that have led to long-lived 3D cavities have shown that harmonic oscillators themselves can be harnessed to perform quantum information processing. This concept is fundamental to the approach taken at Yale. Finally, we discussed how as experimentalists we

may manipulate and measure these delicate quantum systems using simple classical drives.

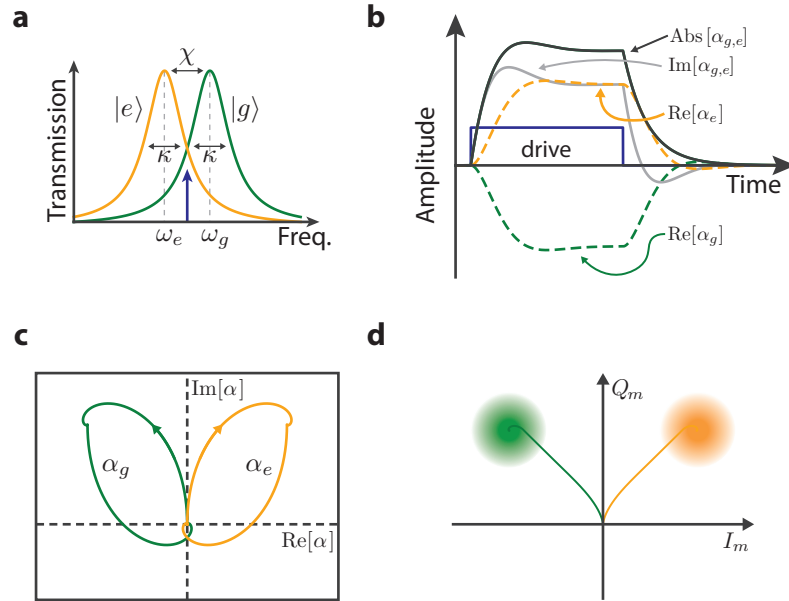


Figure 3.6 | **Dispersive cQED measurement.** **a**, The frequency response of a resonator dispersively coupled to a qubit. The resonance frequency of the resonator is strongly qubit-state dependent, shifting by  $\chi$  when the qubit is in the excited state. Ideally, the linewidth of the cavity is dominated by the coupling to an output port that is connected to the measurement chain. As an example, the dispersive shift  $\chi$  is equal to the linewidth of the cavity mode,  $\kappa = \chi$ , a regime typically used to help optimize measurement fidelity. In other cases, it may be advantageous to operate in other regimes, such as when  $\chi > \kappa$ , where the qubit-state dependent resonances are separated by many linewidths. To effect a qubit measurement, a microwave pulse is applied to the cavity at a frequency near the cavity resonance. As an example (denoted with the blue arrow), we can apply a drive pulse at a frequency halfway between the two cavity resonances. **b**, The cavity response to a simple “square” drive envelope applied at a symmetric detuning to the qubit-state dependent cavity frequencies. The cavity initially rings up to a steady state population until the drive shuts off and the remaining population in the cavity leaks out of the cavity at a rate  $\kappa$ . Here, due to the symmetric drive detuning, information about the qubit state is encoded in the phase of the cavity response, illustrated in the real-component of the cavity response. **c**, The cavity response plotted in IQ-space, illustrating the complex trajectory phase-space response for each qubit state. In this case, the cavity responses only differ by a phase. **d**, When the signal from **b** is integrated, the two cavity responses separate over time with a corresponding increase in signal-to-noise, with the characteristic gaussian noise depicted with the blur in the final histograms.

# 4

## Experimental hardware

With a theoretical basis for quantum information processing and cQED, in this chapter, we turn our attention to the physical realization of our cQED experiments. The experiments described in this thesis represents the culmination of several distinct advances in the field of cQED.

### 4.1 3D cQED device design and implementation

The experimental hardware in this thesis and common for many cQED experiments are transmon qubits and superconducting microwave cavities. While there have been a handful of devices developed toward this thesis, we will focus on the device used for the teleported gate experiment, described in [chapter 6](#). This particular device is the culmination of several important advances in hardware design and serves as an example of the complex designs that are possible with the 3D cQED architecture. To motivate the design process for the experimental hardware used for the teleported gate, we will separately describe some of the various implementations of transmons and cavities, offering some general principles that should be considered when constructing new experimental hardware. When necessary, we will introduce hardware designs from other projects performed for this thesis.

The design process of any experiment begins with a target system Hamiltonian for our system of transmon qubits and cavities. For many of our experiments, this system Hamiltonian is specified by several simple parameters: mode frequencies ( $\omega$ ), mode anharmonicities ( $K$ ), and dispersive couplings between transmons and cavities ( $\chi$ ). Due to the nature of the cosine

Josephson junction potential, however, there also exist higher-order coupling terms that should be accounted for during the design of the experiment, including self-Kerr of cavity modes and other inter-mode couplings. In some cases, these unwanted terms can be eliminated through careful device design (such as taking advantage of geometrical properties to eliminate transmon-transmon coupling [147, 148]). When it is not possible to eliminate such nonideal terms, it is crucial to understand how to suppress them to a tolerable degree and to understand their influence on the experiment at hand. Developing a realistic estimate of a particular physical implementation is at the heart of the black-box quantization procedure [subsection 3.2.2](#) described in the previous chapter and in several other resources [15, 131]. With this technique we are able to predict the Hamiltonian parameters of a given physical implementation with great accuracy; for example, we can predict mode frequencies with accuracy better than 1% and inter-mode couplings  $< 10\%$ , limited by the precision of device assembly. In the following we will describe the typical implementation for our transmon qubits and microwave cavities used as a part of this thesis. Along the way, we will provide considerations and parameters that are important in the device design process.

### 4.1.1 3D cavities

We physically define quantum harmonic oscillators as particular EM modes of a microwave resonator or cavity. Our microwave cavities are typically constructed as enclosed superconducting structures<sup>1</sup> that host an series of standing modes with frequencies and field shapes set by geometry. Our cavities serve one of two functions in our experiments, acting either as quantum memories or as readout resonators for measuring the state of a coupled transmon qubit. The physical implementation of microwave harmonic oscillators for cQED experiments has gone through a significant evolution, see [Figure 4.1](#) for a survey of common 3D cavity implementations.

Early designs of these oscillators were realized as  $\lambda/2$  co-planar waveguide transmission-line resonators and lead to many of the seminal results toward the strong dispersive regime of cQED

---

1. We sometimes construct cavities out of copper, typically when it is necessary to thread magnetic fields into the cavity. For example, in some early 3D cQED experiments we used copper rectangular cavities to be able to vary the frequency of a frequency-tunable transmon.

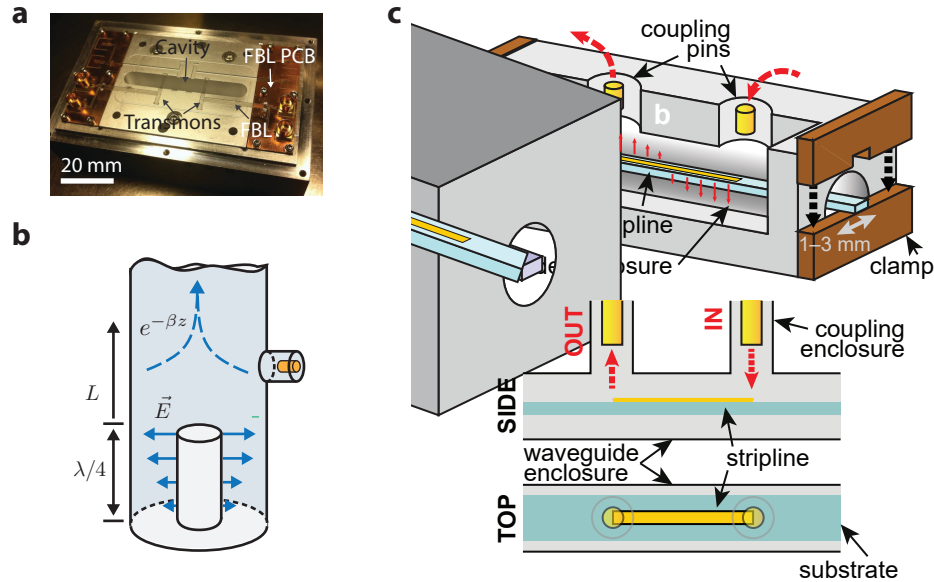


**Figure 4.1 | Survey of 3D cavity implementations.** **a**, A typical rectangular 3D cavity, used for early experiments exploring flux-tunable 3D transmon qubits in this thesis. Here, one-half of the cavity is depicted; the other half is a similarly designed component. The trenches that intersect the cavity are used to install sapphire chips on which transmon qubits are defined. The trenches that are perpendicular to the qubit trenches are for flux bias lines (FBL). The printed circuit board (PCB) on the ends of the device provide a DC interface for the FBLs. **b**, The current variety of high-Q 3D cavity that is used for the experiments in this thesis. This design is called a coaxial  $\lambda/4$  3D cavity. This design is realized as a machined implementation of a coaxial transmission line where one end of the center conductor is short-circuited to the outer conductor and open-circuited at the other end. These boundary conditions along with the length of the center conductor define the frequency of the resonator. This design is also notable as the spatial extent of the mode can be separated from a potentially lossy seam. The mode energy is exponentially attenuated through a natural waveguide with a cutoff frequency that is above the frequency of the cavity. Reprinted from [149], with the permission of American Physical Society. **c**, The coax-line architecture is characterized by: a patterned sapphire chip (blue) housed within a tubular enclosure. The chip is clamped at one or both ends (here, on both ends, in brown). The microwave resonator is defined by a patterned section of superconductor on the sapphire chip that acts as the center conductor of a coaxial  $\lambda/2$  transmission line resonator, and the electric field is represented with the small red arrows. We use standard input and output ports to perform experiments on the device. Reprinted from [150], with the permission of AIP Publishing.

where we design our experiments nowadays [96, 97, 151, 152, 153]. In recent years, the research effort at Yale has focused on cQED using a 3D cavity architecture. The shift from 2D to 3D has resulted in dramatic improvements in transmon coherences, with the original experiment [154] demonstrating over an order of magnitude improvement in qubit lifetimes over typical coherences found in planar devices at that time. Though more mature fabrication technologies have allowed impressive increases in planar transmon qubit lifetimes, as of this writing, 3D transmon qubit designs are still dominant in both record and average coherences times. There are several reasons why a 3D architecture has resulted in improved qubit coherences [154], which we will briefly mention here. First, the 3D cavities that house the transmon qubits have a much larger mode volume (roughly  $10^5$  larger) and have a lower sensitivity to surface dielectric and conductor losses that are believed to limit planar device coherences [155, 156]. Second, a 3D architecture presents a much more well-controlled microwave environment for the transmon qubit with fewer non-ideal “box modes” and other packaging imperfections that are typically associated with planar implementations. Importantly, these benefits do not come at the cost of reduced controllability of the transmon qubit as it is routine nowadays to reach the strong coupling between the transmon and its associated cavity mode(s). Further advances in the design of microwave cavities have opened the door to new possibilities for 3D cavities to serve as carriers of quantum information, which we will also explore further in this section. For these reasons, we will argue that the 3D architecture, therefore, is a powerful platform to build highly coherent quantum machines.

There are three common cavity geometries that can be found in the lab today: the rectangular 3D cavity, the co-axial  $\lambda/4$  3D cavity, and the quasi-planar  $\lambda/2$  stripline resonator.

**Rectangular 3D cavities.** The rectangular cavity was the first implementation of 3D resonators applied to cQED experiments. The modes and frequencies are set by the cavity dimensions, with each mode indexed by the three axis of the cavity. We typically use the  $TE_{101}$  mode to serve as the cavity in these designs. Rectangular cavities are physically realized by machining out a trench that represents half of the cavity on two separate blocks of superconductor. The two halves are then closed to form the cavity. Using the rectangular 3D cavity has enabled a host of early cQED

experiments that collectively demonstrate the high level of control and coherence achievable in the 3D cQED architecture [21, 157, 158, 159].

It was found that the lifetime of this particular cavity implementation limited in large part by the seam that is formed by the two halves of the cavity [149, 155, 160]. The impact of the seam on cavity loss is exacerbated when also considering realistic imperfections such as machine tolerance and the presence of a sapphire chip for transmon qubit integration [155]. Rectangular cavities have been measured with internal quality factors ( $Q$ ) greater than 50 million (equivalent to single-photon lifetimes of around 1 ms) [161]. When integrating transmons—which introduces sapphire chips into the cavity—we typically achieve  $Q \sim 5$  million, or a single-photon lifetime around the 100  $\mu$ s regime.

**Co-axial  $\lambda/4$  3D cavity.** To address these shortcomings, a new type of cavity was developed [149] that has led to record cavity lifetimes in a package that also incorporates transmon qubits. This modern variety of high- $Q$  cavity is a machined-out block of aluminum to form a 3D  $\lambda/4$  section co-axial transmission line. The mode is formed via a short-circuit boundary condition on one end and an open-circuit boundary condition on the other. The mode fundamental mode is determined by the length of this center pin,  $f_0 = c/(4\lambda)$ . Critical in this design is that the position of the seam (which is necessary for the practical reason that the cavity is physically machined and requires an external entry point) can be separated arbitrarily far from the location of the cavity mode used for quantum experiments. This is easily achieved as open-circuit end of the transmission line transitions into a section of circular waveguide. This waveguide is designed to have a cutoff frequency that is much higher than the frequency of the fundamental cavity mode, which causes the cavity field profile to exponentially decay into the waveguide section. This cavity design allows confinement of the fundamental mode energy density away from the potentially lossy seam at the far end of the circular waveguide. Cavities of these types can reliably achieve  $Q$ 's approaching 50 million, or a single-photon lifetime in the ms regime. We will provide additional manufacturing details of this cavity design in our description of our teleported gate device.

**Co-axial  $\lambda/2$  transmission line resonator.** The final type of cavity is a  $\lambda/2$  stripline resonator, or coax-line resonator [150]. This device realizes a quasi-planar architecture in an exceedingly simple manner: the center-pin of the transmission line resonator is formed patterning the  $\lambda/2$  stripline onto a sapphire substrate. The substrate is enclosed in a seamless superconducting enclosure, typically a narrow circular waveguide that acts as a ground plane. The chip is mechanically held in place by clamping on one or both ends of the sapphire chip. To first order, the frequency of the resonator is primarily defined by the length of the resonator, but can be influenced by details in the chip placement within the 3D enclosure. These devices have been shown to have among the highest internal quality factor ( $Q_i \sim 5 \times 10^6$ ) for planar microwave circuit elements. Because of their ease of fabrication and lithographic precision, these planar resonators often serve as readout resonators for transmon qubits. It may also be possible to utilize these planar circuits for more complex signal routing within a 3D cQED architecture.

#### 4.1.2 3D transmon qubits

As we described in [subsection 3.1.3](#), transmon qubits consist of a Josephson junction shunted by a large capacitor. The implementation of a transmon qubit is also quite simple: it is a Josephson junction that is connected to two superconducting electrodes. These electrodes serve as antennas that are used to couple the transmon to neighboring cavity modes. In the 3D cQED architecture, the transmon qubits are lithographically fabricated on a sapphire chip, typically mm in scale. In most experiments, one transmon qubit is printed on a given chip (though there is nothing preventing fabricating multiple transmon qubits on a single chip).

**Transmon design considerations.** Transmon qubit design requires consideration of frequencies ( $\omega$ ), anharmonicities ( $\alpha$ ), and coupling strengths  $\chi$  to other cavity and transmons. While fine-tuning these parameters for a design typically requires a full EM simulation and black-box quantization; here we give some general guidelines for adjusting these parameters during the design process.

We can modify two physical parameters of the transmon qubit: the Josephson inductance,

$L_J$  and the geometry of the antenna pads. The former modifies  $E_J$  and the latter modifies  $E_C$ . The resonance frequency between the lowest two energy levels is given as  $\omega_{ge} \approx \sqrt{8E_J E_C}/\hbar \sim 1/\sqrt{L_J C_\Sigma}$  and the anharmonicity of the transmon qubit is set by the charging energy  $\alpha \approx E_C/\hbar \propto 1/C_\Sigma$  [120].

In addition, one should verify that the chosen parameters (frequency and anharmonicity) place the transmon well within the charge-insensitive regime, typically where  $E_J/E_C \gtrsim 50$ . In the high  $E_J/E_C$  regime, the transmon becomes exponentially insensitive to charge fluctuations on either side of the Josephson junction. This is the primary feature of the transmon. As an example, for a 5 GHz qubit, decreasing the qubit anharmonicity (equivalently  $E_C$ ) from 400 MHz to 200 MHz will increase the charge dispersion limit on  $T_\phi$  by almost  $10^5$ . When using some approximations following a  $1/f$  noise model for charge dispersion [120], for a 5 GHz transmon with  $E_J/E_C \approx 50$ , we estimate a  $T_\phi \sim 40$  ms, far above the typical  $T_1 \approx 100$   $\mu$ s. Therefore, with some care we can design transmon qubits that eliminate charge noise as a relevant noise mechanism.

Moving deeper into the charge noise insensitive regime, however, comes at a cost of decreased transmon anharmonicity. Fortunately, the charge noise sensitivity decreases exponentially as the anharmonicity decreases polynomially, so we can find regimes that balance these two competing considerations. The practical concern for decreased anharmonicity is that we will be required to use longer, more frequency selective transmon pulses to faithfully address only the desired qubit transition. In other words, the two-level approximation becomes less valid as the transmon becomes more harmonic (and less charge-sensitive). We choose relative anharmonicities around 5% of the frequency—around 100 – 300 MHz—which is sufficient to perform fast ( $\sim 10$  ns) manipulations on the transmon qubit <sup>2</sup>.

2. Our qubit operations are typically shaped with a Gaussian envelope, parameterized by the time-domain pulse width  $\sigma_t$ . In frequency space, the bandwidth of the pulse is given by  $\sigma_f = 1/(2\pi\sigma_t)$ . Therefore, we see that as the pulse duration becomes shorter, then the frequency bandwidth increases. When this frequency bandwidth becomes an appreciable fraction of the anharmonicity, the two-level approximation is no longer valid as the pulse can directly drive the  $|e\rangle \leftrightarrow |f\rangle$  transition, causing leakage out of the  $|g\rangle \leftrightarrow |e\rangle$  manifold. In addition to these state leakage errors, the presence of higher excited levels of the transmon can also induce phase errors within the  $\{|g\rangle, |e\rangle\}$  subspace. Fortunately, we can mitigate such errors using more complex pulse shaping techniques, such as Derivative Removal by Adiabatic Gate, or DRAG [141].

**Physical Implementation** Designing a transmon with a particular frequency and anharmonicity (or a particular  $E_J$  and  $E_C$ ) relies on modifying either the Josephson junction or the geometry of the antenna pads. We typically modify the  $L_J$  by changing the area of the junction<sup>3</sup>, with achievable  $L_J = 1\text{--}10$  nH. Designing the physical geometry of the antenna pads is a dramatically under-constrained problem, and there are a number of possible geometries that result in the same Hamiltonian parameters. Not all designs are created equal, however, as certain geometries can increase or suppress the sensitivity to other loss mechanisms such as surface dielectric loss, conductor loss (induced by quasiparticles), and bulk dielectric loss, with a detailed study described in [156]. Though still an outstanding area of research, it is believed that our transmon qubits are limited by a combination of these loss mechanisms with some evidence that surface dielectric loss is dominant in our 3D devices [156]. There are some general guidelines that can be followed that has resulted in some of the best 3D transmon qubit coherence times to date ( $T_1, T_2 > 100 \mu\text{s}$ ). We use well-separated, large-area capacitors to limit the impact of surface dielectric loss. A typical device may have antenna pads with length dimensions on the order of  $100 \mu\text{m}$  and separation between the two superconducting antenna of around  $200 \mu\text{m}$ . At this separation we seem to balance the loss associated with closely space antenna pads with loss associated with having long leads from the antenna pad to the junction [156]. In general, achieving typical performance ( $T_1, T_2 > 50 \mu\text{s}$ ) for 3D transmons has become quite commonplace, enabling the development of more complex devices and experiments.

### 4.1.3 Constructing cQED devices

Designing the geometry of the transmon qubit often occurs in concert with the design of its embedded electromagnetic environment: the cavity mode(s) that couples to the transmon qubit and to input/output coupling ports. Here, we will describe the general designs we use for coupling cavities and transmon qubits.

---

3. The Josephson inductance is also a function of the critical current  $I_c$ . Varying this parameter physically amounts to varying the thickness of the insulating barrier, which changes the Cooper pair tunneling probability. In most transmon qubit fabrication, this thickness is fixed and we modify the area of the junction to tune  $L_J$ .

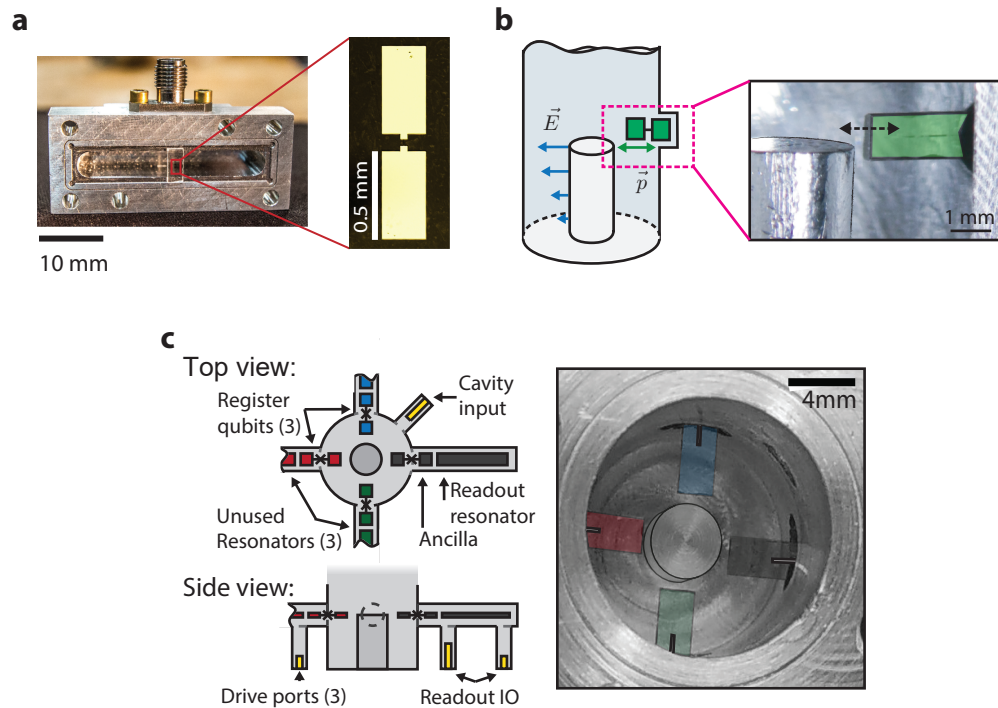


Figure 4.2 | **Examples of transmon and 3D cavity integration.** **a**, Typical design for a 3D transmon coupled to a rectangular cavity. In this photograph, we show one half of the rectangular cavity; on the right is a zoom-in of the 3D transmon, which is realized as Josephson junction connected to two large antenna pads. Reprinted from [162] by permission from Springer Nature. **b**, Schematic of a coaxial  $\lambda/4$  3D cavity with the transmon qubit integrated, shown in green. **c**, Device used in [50] that incorporates the current state-of-the-art device structures. This device consists of a coaxial  $\lambda/4$  3D cavity coupled four 3D transmons. The transmon qubits also couple to individual  $\lambda/2$  quasi-planar resonators, one of which is used as a readout resonator.

### Integrating transmons and cavities

Integrating a transmon qubit with a cavity relies on aligning the electric dipole of the transmon mode with the electric field of the cavity mode [154], see Figure 4.2 for several examples. This coupling can be thought of as a capacitance between the two; diagonalizing such a system results in mode hybridization  $\propto (g/\Delta)^2$ : the new “transmon mode” inherits some component of the original cavity mode and the new “cavity mode” has a component of the original transmon mode. This coupling also gives rise to the critical nonlinear coupling parameter that is central to all of our cQED experiments: the dispersive interaction,  $\chi$ . Engineering a particular interaction strength between a transmon and a cavity is dependent on two physical mechanisms: the size of the linear coupling  $g$  and the detuning  $\Delta$ , and we can approximate  $\chi \approx g^2/\Delta$ .

We can modify the size of the linear coupling by either changing the geometry of the transmon antenna pads or by altering the relative position of the transmon and cavity. For example, increasing the length of the antenna pads increases the transmon dipole moment and will increase the linear coupling between the transmon and cavity. Alternatively, it is also fairly common to physically adjust the position of the transmon qubit relative to the cavity. This can be accomplished either by shifting the transmon qubit further in or out of the cavity mode or by varying the location of the transmon in relation to the electric field profile of the cavity mode. For example, for the fundamental mode of a  $\lambda/2$  resonator, the electric field is maximized on the ends and minimized in the middle of the resonator; as the transmon location is shifted from the end of the resonator to the center, holding all else constant, the coupling strength will decrease proportionally to the size of the electric field.

Transmon qubit designs can be roughly split into two categories based on how they couple to a cavity mode. In the first, the transmon qubit is completely embedded in the cavity mode such that the cavity itself forms the mechanical packaging that houses the transmon in addition to a filter to protect the transmon from spontaneous emission. This variety of transmon qubit along with rectangular cavities formed the initial platform for the 3D cQED architectures, resulting in the early record in transmon qubit coherence times [154, 163]. One significant limitation this

embedded platform is that the transmon qubit is not able to easily couple to other physical cavity modes (other than the higher-order modes of the original cavity). This has motivated alternative transmon designs that are partially-embedded to allow for the transmon to couple to distinct cavity modes. The original designs, dubbed the “vertical transmon”, coupled a transmon qubit to two rectangular cavities [157, 158, 159]. Similar designs have been developed for the more modern  $\lambda/4$  co-axial cavities and quasi-planar  $\lambda/2$  stripline resonators. In the device used for the teleported gate experiment, we utilize a design from [164] to realize a transmon qubit that couples individually to three cavities: two 3D cavities and one stripline resonator.

### Input and output ports

So far, our discussion has focused on guidelines for translating a set of Hamiltonian parameters into a physical device. Actually controlling and measuring these devices in any real experiment requires the capability to exercise external control on the device. In order to achieve this, we add input and output ports to send to and extract signals from the system, respectively. These ports are physically realized as a coaxial coupler with a pin that capacitively couples a particular mode (or modes) of the system to a  $50\ \Omega$  transmission line. The addition of these I/O ports introduces one of the fundamental trade-offs in quantum information processing: while we want our quantum systems to be well isolated from the outside world to preserve its quantum information, we must connect the system to the outside world in order to control and measure it. By introducing a way to control the quantum system we also allow the quantum system to interact with the outside world. If this interaction is too strong, then the quantum system will suffer from unwanted losses; if this interaction is too weak, then we will have trouble manipulating the quantum system. Specifically the losses that we may consider include energy relaxation either due to being overcoupled to the port or due to the Purcell effect and decoherence induced by noise that enters the system through the port (in particular photon shot noise dephasing [165]). These losses must be balanced with our requirements for fast and efficient manipulation and measurement of the system.

This balance motivates several considerations for achieving external control. These include

the number and location of the ports and the magnitude of the coupling of each port to the individual modes of the system. For our devices we design each transmon and high-Q cavity to have individual input ports; readout resonators often share an input port with its coupled transmon qubit. We quantify the strength of coupling to the external environment via its coupling-Q or external Q, defined as  $Q_c = \omega/\kappa_c$ . These input ports are generally designed to be undercoupled so they do not limit the lifetime of our qubits and cavities. For input ports to a transmon, we target  $Q_{c,in} > 10^6$  and for high-Q cavities  $Q_{c,in} > 10^7$ . In some cases, however, it may be advantageous to over-couple to a particular mode to increase the maximum drive strength to that mode. In the teleported gate experiment, one particular mode (the bus) was intentionally overcoupled to implement faster operations.

While input ports are generally undercoupled, output ports are intentionally overcoupled to a readout resonator to efficiently extract energy from that resonator to the output port. For experiments that incorporate a parametric amplifier, we typically choose  $Q_{c,out} \sim 1000$ , which sets the resonator  $\kappa/2\pi \sim 1-5$  MHz so that  $\kappa \approx \chi$ . In this regime, we match the rate of mapping information of the state of the transmon onto a readout photon ( $\chi$ ) with the rate at which a readout photon is emitted into the the output port for detection ( $\kappa$ ) [144, 146]. Such a balance maximizes the information content per emitted photon.

An additional design choice in positioning I/O ports is to determine the relative addressability of a port to each quantum mode. There are two primary concerns related to this choice. First, as a port introduces a new loss channel, its effect on other modes should be quantified<sup>4</sup>. Our current approach for quantifying this indirect coupling loss is to determine a coupling-Q ratio. For example, when computing the Purcell effect for a transmon qubit coupled to a low-Q readout resonator, we can report the ratio  $Q_{\text{transmon}}/Q_{\text{readout}}$  as a useful figure of merit. For this transmon-readout resonator scenario, we typically find coupling-Q ratios on the order of

4. The indirect loss has been observed in some surprising situations. For the device used in [50], there is a central high-Q cavity to which we individually couple four 3D transmons. Each transmon is further coupled to an individual  $\lambda/4$  co-axial quasi-planar resonator. One of these resonators is used as a readout resonator and is strongly coupled to an output port, with  $Q_c \sim 10^3$ . It was found in this device that the readout resonator actually Purcell-limited all three other “blind” resonators (which were observed to have  $Q_c \sim 10^5$ ) despite being separated by two transmon modes and a cavity mode. From simulations we determined that the small detunings between the resonators ( $\Delta \sim 100$  MHz) contributed to the low “blind” resonator Q.

$10^3$ ; when using a Purcell filter [150], we have found coupling-Q ratios on the order of  $10^4$ . Second, we can look at this same situation from the opposite perspective. If a particular port is intended to couple to mode  $a$ , then any residual coupling to a different mode  $b$  results in unwanted classical control crosstalk, which can be a significant concern for large, complex devices. Fortunately, keeping this unwanted crosstalk to a minimum is fairly straightforward due to the coupler mode confinement in our 3D architectures. For example, in [166] we characterized the measurement crosstalk, which we define to be the ratio of the measurement contrast of measuring a qubit through its directly coupled readout resonator/port to that of measuring the qubit through a notionally decoupled readout resonator/port. In that experiment we bounded the measurement crosstalk to be less than  $10^{-4}$ . We can quantify other forms of crosstalk in our devices. For example, in [50] we performed simultaneous randomized benchmarking [167] to quantify direct classical crosstalk in the drives and quantum crosstalk due to residual direct coupling between two transmons.

### Residual population and dephasing

So far we have discussed the choice of coupling strength in the context of energy relaxation. It is also important to consider how the choice of our external coupling can have other physical consequences, specifically residual population that leads to qubit dephasing [168, 169]. The same mechanism that enables quantum control over our system also can allow noise to populate certain modes. Here we focus on the effect of any residual photon population in our cavity modes that potentially arises from additional noise from the external ports. If not properly thermalized and filtered, these ports can induce an elevated thermal population that can dephase our qubits [169]. To explore this additional loss mechanism, we need to explore two related questions. First, how does noise couple into our quantum system through input and output ports? Second, given a residual population in our cavities, how does this result in qubit dephasing?

First, we want to see how signals can be coupled into our system. Consider a cavity with internal loss  $\kappa_{int}$  and a single port with coupling strength  $\kappa_c$  (so that  $\kappa_{tot} = \kappa_{int} + \kappa_c$ ). Using the same formalism in subsection 3.3.3, we can also relate the steady state average photon number

in the cavity  $\bar{n}_{cav}$  to an incident power  $P_{in}$

$$\bar{n}_{cav} = \frac{4\kappa_c P_{in}}{\kappa_{tot}^2 \hbar\omega_c} \quad (4.1)$$

We can define an effective number of incident photons  $\bar{n}_{in}$  over a cavity linewidth by noting that the input power  $P_{in} = \hbar\omega_c \bar{n}_{in} \kappa_{tot}$ .

$$\bar{n}_{cav} = \frac{4\kappa_c}{\kappa_{tot}} \bar{n}_{in} \quad (4.2)$$

From this result we can consider a few regimes. First, if our cavity is undercoupled such that  $\kappa_{tot} \approx \kappa_{int} > \kappa_c$ , then  $\bar{n}_{cav} = \frac{4\kappa_c}{\kappa_{int}} \bar{n}_{in}$ . The number of photons in the cavity is suppressed by the ratio of the coupling rate to the internal loss rate,  $\frac{\kappa_c}{\kappa_{tot}}$ . In this regime, we can think of the coupler as a final (reflective) attenuator before a signal reaches the cavity. On the other hand, when we have an overcoupled cavity  $\kappa_{tot} \approx \kappa_c > \kappa_{int}$ , then we see that  $\bar{n}_{cav} \sim \bar{n}_{in}$ . From this result, we see that an overcoupled cavity thermalizes to its strongly coupled port. This suggests that to achieve a low  $\bar{n}_{cav}$ , then it is crucial to minimize the incident noise power  $P_{in}$ .

The mechanism for describing qubit dephasing due to a population of photons in a coupled mode is well described by the theory of measurement induced dephasing [146, 168]. We can understand how a residual photon population can affect the coherence of a qubit by considering the following situation [169]. A fluctuating population of photons in a cavity induces a random frequency shift on the qubit state to the dispersive interaction as photons jump in and out of the cavity. This frequency shift manifests as a random phase shift of the transmon state thus resulting in decoherence. Equivalently, we can consider this situation from the perspective of a cavity photon: a photon that transits the cavity will perform a complete, unintended measurement of the transmon qubit; this measurement causes mixing of the state of the transmon. We can quantify the effect of a residual thermal photon population  $\bar{n}$  on the dephasing rate  $\gamma_\phi$  of a

transmon following an analysis performed in Ref. [163]<sup>5</sup>

$$\Gamma_\phi = \frac{\kappa_{\text{tot}}}{2} \text{Re} \left[ \sqrt{\left(1 + i \frac{\chi}{\kappa_{\text{tot}}}\right)^2 + i \left(\frac{4\chi n_{\text{th}}^{\text{eff}}}{\kappa_{\text{tot}}}\right)} - 1 \right] \quad (4.3)$$

where  $\kappa_{\text{tot}}$  is the total photon loss rate of the cavity (for the purposes of qubit dephasing, it does not matter how the photon is lost),  $\chi$  is the (full) dispersive shift, and  $n_{\text{th}}^{\text{eff}}$  is the effective number of thermal photons in the cavity.

In the regime where  $\chi > \kappa$ , then we can approximate the dephasing rate  $\Gamma_\phi \approx \bar{n}\kappa$ . We are in this regime for our high-Q cavities. For our longest-lived cavities, with  $T_{\text{cav}} = 1/\kappa \approx 1$  ms, and with typical residual cavity populations of  $\bar{n} < 0.01$ , the measurement induced dephasing bound is roughly  $T_\phi = 1/\Gamma_\phi > 1$  ms. Therefore we can conclude that our high-Q cavities contribute very little to measurement induced dephasing. Next, we consider the dephasing limit for low-Q, readout resonators, where typically  $\kappa \approx \chi$ . In this regime, the dephasing rate scales as  $\Gamma_\phi \approx \bar{n}\chi^2/\kappa$ . This approximation is derived from Ref. [168] where the cavity is coherently driven (as it would be for a dispersive measurement). Given typical parameters,  $\chi/2\pi \approx \kappa/2\pi = 1$  MHz, for a  $\bar{n} = 0.01$ , then we expect a limit to our transmon coherence to be  $T_\phi = 16$   $\mu$ s. This rough calculation illustrates that the photon number population of our readout resonators can play a significant role in the limiting the coherence of our transmon qubits. Further investigations are still required to fully explore the limitations to transmon coherence.

#### 4.1.4 Building modular hardware

We have seen that our devices typically consist of two distinct types of components. First, we have a 3D enclosure, typically machined out of high purity Aluminum, that defines high-Q cavities and also provides housing for our transmon qubits and input-output couplers. Second, we have sapphire chips on which we fabricate our transmon qubits and any quasi-planar resonators. We have designed our system such that each sapphire chip can be modified without affecting other

5. From Ref. [168], the dephasing rate of a transmon subject to a coherent drive populating the cavity with  $\bar{n}$  photons is given by  $\Gamma_\phi = \frac{\bar{n}\kappa\chi^2}{\kappa^2 + \chi^2}$ .

chips in the package. This architecture allows us to carefully optimize individual components of our experiment without affecting other aspects of the device. It is, in fact, common in our experiments to swap out transmon qubits as a normal exercise in experimental optimization; because we can fabricate these transmon qubit chips quite readily, this becomes a powerful tool in the early stages of a new experiment. The ability to build our devices in a LEGO-like fashion is a key principle of our approach and the 3D architecture naturally lends itself to a modular design architecture.

This flexibility will likely become increasingly important as devices become increasingly complex and demanding. Our design architecture allows us to optimize individual device parameters while preserving other components of the experiment. This independent optimization is especially useful for prototyping during the development phase of a particular experiment. Therefore, by pursuing a modular design we can carefully assess the critical parameters for a given architecture *before* devoting additional resources for integrating them together. A modular approach also lends itself to the systematic construction of large-scale devices. Consider a complex devices with  $N$  components, each of which has an average failure rate  $\epsilon$ . If we use a modular approach, then the probability to construct a device where all  $N$  components are functional is  $\sim N(1 - \epsilon)$ . On the other hand, if we use an integrated approach, for a fully functional device, all  $N$  components must simultaneously function; the probability of this simultaneous success is  $\sim (1 - \epsilon)^N$ . This exponential can become quite daunting as  $N$  increases. Eventually, for the purposes of scaling, we will have to look toward integrating modular subsystems together. Our approach for integrating our 3D cQED devices is called the multilayer microwave integrated quantum circuit (MMIQC) architecture [160, 170], which retains many of the advantages of the 3D cQED platform while providing a path to building large quantum devices.

## 4.2 Experimental control hardware

In this section, we detail some of the hardware components necessary to perform quantum information experiments on a chosen cQED device. Some of the techniques used in this thesis

are modified (if at all) from standard techniques described in detail in other sources, such as [99, 139, 151, 155]. As such, we will focus on describing the novel features of our control setup and briefly describe some additional modifications that may be necessary for future cQED experiments. Using the teleported gate experiments as a template, we will describe both the cryogenic and room-temperature hardware used to control and measure our devices as well as the controller that is used to program and design experiments.

### 4.2.1 Device preparation: thermalization and shielding

We operate our experiments at the base stage of a dilution refrigerator with a base temperature of 10 – 20 mK. This low temperature is critical for two reasons. First, to ensure that the superconductors that form our quantum circuits are cooled below the superconducting transition temperature ( $T_c = 1$  K for aluminum); and second, that thermal fluctuations are suppressed so that our quantum systems can (notionally) be cooled to the ground state (for a  $\omega/2\pi = 5$  GHz qubit mode, we require cooling our devices below  $\hbar\omega/k_B < 200$  mK).

Thermalization of our experimental device to the base stage of the dilution refrigerator, therefore, is crucial to our experimental efforts. Our superconducting devices are anchored to the dilution refrigerator via brackets constructed from Oxygen-Free High Conductivity copper, chosen for its high conductivity at cryogenic temperatures.

Our devices are also sensitive to stray magnetic fields and electromagnetic radiation. We employ several techniques to shield our devices from external magnetic fields as it has been observed that magnetic fields can impact device properties and performance [171]. We house our devices inside of a Ammuneal 4K magnetic shield, which is a high permeability material at cryogenic temperatures. Inside of this shield we have eliminated as many magnetic components as possible, replacing couplers, screws, co-axial cables with non-magnetic versions.

We typically consider two ranges of electromagnetic radiation when considering its detrimental effect on our devices. First, radiation around the same microwave frequencies as our devices can lead to residual population and dephasing. On the other hand, high-frequency (infrared) radiation can break Cooper pairs, generating quasiparticles in our superconducting circuits that increase the

rate of energy relaxation [171]. If designed appropriately, our package designs provide a natural first level protection against stray photons<sup>6</sup>. We seal any joint in our devices with indium wire to provide a more light-tight enclosure. In our experiments we also include an infrared absorbing material made from Stycast 2850 and Carbon Black coated on a thermalized copper sheet to absorb any remaining stray radiation.

### 4.2.2 Microwave control lines

#### Input control lines

Next, to perform our experiments it is imperative to design input lines properly to ensure that signals can be delivered and extracted from the experimental device cleanly and efficiently, without introducing additional noise or spurious tones. The challenge is accomplishing this task over a large temperature differential: our input signals begin at 300 K and travel down several temperature stages of the dilution refrigerator through coaxial cables to our experiment at 20 mK. We first describe the wiring for our input lines that carry microwave signals to our experimental system.

Perhaps the most significant concern is ensuring that our device is sufficiently protected from thermal noise generated from higher temperature stages. As is standard nowadays, we accomplish this by using wideband microwave attenuators that thermalize the signal at various stages of the dilution refrigerator. This filtering must be done while ensuring that we can achieve sufficiently fast manipulation of our system. We can quantify the noise seen at the plane of the experimental device by estimating the thermal photon number,  $n_{th}$ . We consider each attenuator as a black-body source that both attenuates the incoming signal by a factor  $A$  and adding to the output thermal noise corresponding to its physical temperature. The thermal noise for a black-body at frequency  $\omega$  and temperature  $T$  is given by

$$n(T) = \frac{1}{\exp(\hbar\omega/k_B T) - 1} \quad (4.4)$$

---

6. Of course, the converse is also true and in some device designs we do observe abnormally high qubit and cavity population and reduced coherence as a result of improper shielding from electromagnetic radiation

. The resulting noise given an input thermal photon number  $n_{in}$

$$n_{out}(T) = An_{in} + n(T) \quad (4.5)$$

A standard set of input lines (to drive a qubit, cavity, or readout resonator), typically has the following set of attenuators: (1) 20 dB at 4 K stage; (2) roughly 10 dB from coaxial cable losses from 4 K to 20 mK<sup>7</sup>; and (3) between 20-50 dB at 20 mK. In some more recent input line configurations, an additional 10 dB attenuator is added to the 1 K stage of the fridge (in our experiments, this additional attenuator is not used).

If we consider 300 K noise at  $\omega/2\pi = 5$  GHz (for an input thermal photon number  $n_{th}(300 \text{ K}) = 1250$ ), then at the base stage of the fridge we expect  $n_{th}(20 \text{ mK}) = 6 \times 10^{-3}$ . While this estimate serves as a good starting point, it also neglects many important details of an actual experiment where we should include any added noise associated with the generation of our pulses, additional noise from amplification, and wiring losses from coaxial cables and other components that route the signal into the dilution refrigerator. The level of required filtering at the base stage depends on the function of input line. For instance, the input line to a transmon and readout resonator is usually connected to a weakly coupled input port (where  $Q_{c,in} \gg Q_{tot}$ ); in this situation, the input port acts provides an additional attenuation factor  $Q_{c,in}/Q_{tot}$  and we may choose to trade-off physical attenuation for  $Q_{c,in}$ . We use 30 dB attenuation for this type of input line. On the other hand, input lines connected to the strongly coupled port (e.g. if we measure in reflection or for the JPC diagnostic line), we may require additional physical attenuation; typically 50 dB is used for these input lines. In practice, we try to design our input lines so that the thermal photon population is kept below  $10^{-3}$  to limit the potential for measurement induced dephasing.

To further clean up the spectrum of our input lines we also include a number of filters. As our experimental devices operate in the 4-10 GHz range, we include reflective low-pass filters (K&L Microwave 6L250) to remove any high-frequency microwaves that may excite higher-order modes of our system. Additionally, we use absorptive, infrared Eccosorb® filters to reduce high-

<sup>7</sup>. To simplify our estimates of thermal noise, we make an assumption that all of the cable loss is thermalized at 1 K instead of distributing it across the temperature gradient.

frequency radiation and noise on each control microwave input line.

### Output control lines

Output signals emitted from the device back to room temperature contain precious information about our qubits. These signals are typically very fragile, making it crucial to minimize the loss throughout the output chain. It is also important to limit the noise that will propagate from higher temperature stages to the device. To address this, we cannot use attenuators, and instead use directional components such as circulators and isolators. These components provide a low-insertion loss path for signals from the sample to travel to room temperature while absorbing thermal noise traveling in the opposite direction. Additionally, we use low-loss superconducting coaxial cables to carry the signal from the base stage of the fridge to the 4 K stage of the fridge.

Here we describe a typical example of an output line. Quantum limited parametric amplifiers have become a mainstay in our measurement apparatuses. These are used as ultra-low noise pre-amplifiers that immediately follow (apart from microwave cables and two circulators) from the output port of the experiment and before the isolators and superconducting coaxial cables. Signals emitted from a readout resonator will travel through a pair of cryogenic circulators in its way to a Josephson Parametric Converter (JPC) [145, 146? ]. These circulators ensure to ensure one-way signal propagation from the device to the JPC and from the JPC to the output line. The signal is amplified by the JPC (with gain  $G = 20$  dB), travels through one of the cryogenic circulators, and a set of low pass and infrared filters. Then, the signal passes through a pair of wideband cryogenic isolators (Quinstar CWJ1019-K414) that attenuate the unwanted signal from higher temperature stages by around 36 dB in total. The signal then travels from 20 mK to 4 K via superconducting coaxial cables before being amplified by a high electron mobility transistor (HEMT) amplifier (from either Caltech or Low Noise Factory). After this, the signal travels to room temperature to be further amplified and processed. In [Figure 4.3](#) we provide an example wiring diagram for the teleported gate experiment that includes these components.

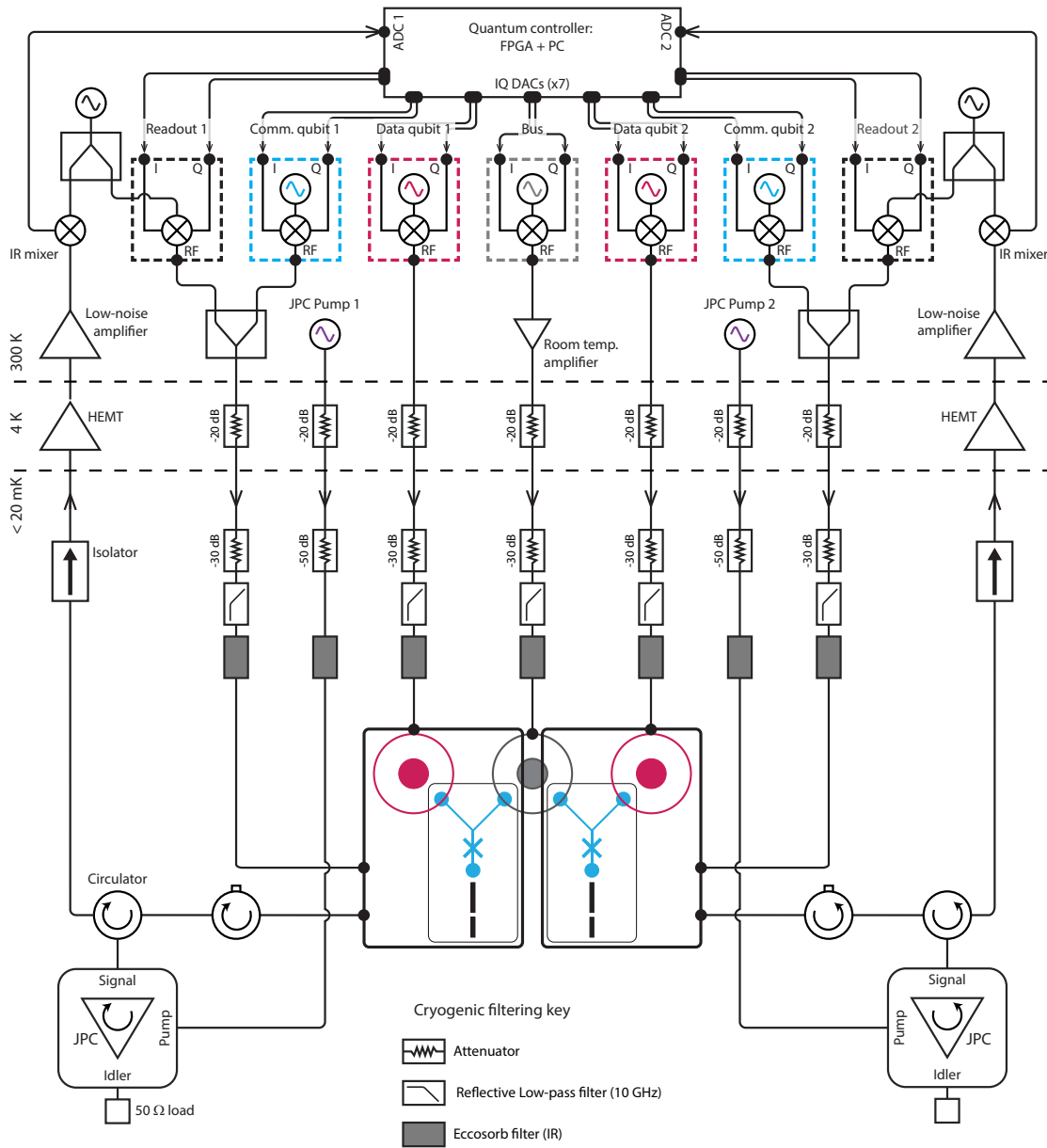


Figure 4.3 | Experimental wiring diagram. Caption next page.

Figure 4.3 | **Experimental wiring diagram.** Input control signals are generated at room temperature using standard cQED microwave techniques and are attenuated and filtered in the refrigerator before reaching the device. At room temperature, each signal is generated using a combination of an RF-microwave generator (data and communication qubits: *Vaunix LabBrick LMS-103-13*, readout resonators and bus: *Agilent/Keysight N5183A* and *E8275D*) and IQ mixer setup (*Marki Microwave IQ-0307LXP*). The bus drive line also includes an amplifier (*MiniCircuits ZVA-183-S+*) and fast microwave switch (*Hittite HMC-C019*) at room temperature. A custom quantum control computer (*Innovative Integration VPXI-ePC with four X6-1000M boards*) calculates and generates IF signals in real-time. Output signals emanate from the strongly coupled port of a readout resonator and travel through two circulators (*Quinstar*), are amplified by a Josephson parametric converter (JPC) that is continuously pumped by microwave generator (*Agilent/Keysight N5183A*). These signals then travel through superconducting transmission lines to an additional cryogenic (*Low Noise Factory LNF-LNC4\_8C*) and room-temperature amplifiers (*Miteq AFS3-00101200-35-ULN*) before being mixed down (*Marki Microwave IR-4509*) to be demodulated and analyzed by the control computer.

### 4.2.3 Experimental control hardware

#### Controlling the experiment

Any cQED quantum information experiment is performed by emitting a series of input pulses that manipulate the quantum system and digitizing a series of output signals from the quantum system to extract information about the quantum system. In this thesis, we have used two different control systems to perform our experiments. Initial experiments for this thesis were performed with separate arbitrary waveform generators (AWG) using the Tektronix AWG 5014C and digitizer/demodulator using the AlazarTech ATS9780. More recent experiments in the lab, including the teleported gate experiment, use a more sophisticated FPGA-based controller hardware consisting of several Innovative Integration X6-1000M installed in a VPXI-ePC chassis. The FPGA-based controller [21, 172, 173] combines the independent functionality of the AWG and the digitizer into a single piece of hardware and provides a framework for communication between these two components. Using this new controller, it was also possible to implement a critical functionality necessary for the teleported gate experiment: real-time, adaptive control of the quantum system.

The result is an all-in-one quantum control architecture that combines three requirements

necessary for performing quantum experiments into one control system: generate and output pulses to manipulate the quantum system, sample input signals for quantum measurements, and perform classical computation based on these input signals to determine the next output. Fulfilling these three requirements opens the door to experiments that incorporate closed-loop control for feedback as well as open-loop control for feedforward.

### Generating control pulses

All modes in the system are controlled at room temperature using microwave-frequency pulses generated through single-sideband modulation (SSB) of an IQ mixer [99]. For each input, a dedicated microwave generator serves as a local oscillator (LO) that up-converts shaped intermediate-frequency (IF) control pulses generated by our quantum controller [subsection 4.2.3](#). Common RF generators that serve as local oscillators are: Vaunix LabBricks (LMS-103 or LMS-802) or an Agilent/Keysight RF generator (N5183A MXG or E8257D PSG). We rely on Marki Microwave double-balanced IQ mixers (models IQ-0307 and IQ-0618 are commonly used).

Because these IQ mixers are so central to the quality of our experiments, it is important to understand the physical characteristics of these components. First, these device have small nonidealities that result in unwanted frequency and phase components. It is commonplace to perform a tuneup procedure (implemented programmatically) to eliminate LO and opposite sideband (OSB) leakage. We add attenuation to the IF inputs to increase the voltage resolution of the IF pairs that improves our ability to tune away offsets for the mixer. When using the FPGA as a controller we use around 6 dB of attenuation, while for the Tektronix AWG 5014C we use between 10 and 20 dB depending on the output voltage setting. Additionally when using an FPGA the output IF signals are not filtered and we can easily resolve the finite DAC steps on an oscilloscope. We remove any high-frequency components by adding a 270 MHz (Mini-circuits BLP-300+). Additionally, the IQ mixers have a input (IF) +1 dB compression point of around 4 or 6 dBm after which the mixer behavior become nonlinear. We generally want to stay far from this nonlinear regime to avoid higher-order effects of the mixer. As a rule of thumb, IF input voltages should be kept less than 0.5 V<sub>pp</sub> (by at least a factor of two). The attenuators described

previously also increase the range of the IF DAC where the mixer is operated is in linear regime.

Now we consider the tone emitted from the IQ mixer. Before entering the dilution refrigerator, this signal passes through a 10 or 12 GHz low-pass filter (K&L Microwave 6L250) to remove any high-frequency harmonics from the mixer (we sometimes see a component at twice the frequency of the local oscillator). Bandpass filters can also be used if additional filtering is required. If additional power is needed, we add in a microwave amplifier (MiniCircuits ZVA-183-S+) followed by a fast microwave switch (Analog/Hittite HMC-C019 or a home-built version). The added noise by the combination of the amplifier and the IQ signals (which has been seen to have a noise temperature  $T_N > 300$  K) can result in reduced qubit coherence and increased qubit temperature. The switch is used to limit the duration that the device is susceptible to this noise to only when a pulse is required. While this has been sufficient to perform many experiments so far, it may be necessary to address for future experiments either by addressing the noisy amplification problem or by increasing the output power of the IQ mixer.

# 5

## Experimental techniques

Accurate and thorough characterization and tuneup of our cQED systems is a fundamental step necessary before performing any quantum information experiment. Such characterization dictates whether the experimental device is within the specifications of the experimental goal. In this chapter we describe some essential techniques required to bring up any cQED experiment. The goal for this chapter is to provide a fairly comprehensive guide for system characterization and tuneup for any experimental cQED system, combining them into a single location. Since many of these techniques have been described in other literature, we focus on a functional description of each techniques, and provide sources for additional details when necessary.

We begin with a description of a basic system tuneup, which begins with finding the frequencies of all modes of the system, tuning up readout, and measuring coherences. The bulk of this chapter is contained in the next section where we describe measurement techniques for characterizing the system Hamiltonian. When appropriate we provide multiple protocols for extracting each parameter, offering general guidelines for cases to prefer one technique over another. Next, we describe our framework for tuning up transmon and cavity operations and detail a powerful technique for developing complex cavity (and transmon) operations using optimal control theory. We finish this chapter by describing our process for implementing high-fidelity ground state preparation.

This chapter sets the stage for any subsequent experiment.

## 5.1 Basic system tuneup

### 5.1.1 Finding the system modes

Any experiment must begin by determining the frequency of each mode. We perform two types of spectroscopy experiments to determine the location of each mode, distinguished by the number of microwave generators needed to effect the measurement.

#### Single-tone spectroscopy

The simplest version, a “single-tone” spectroscopy experiment, is typically used to determine the frequency of readout resonator modes. In such an experiment we sweep the frequency of a probe microwave tone around the frequency where we might expect to find the resonator and record the outgoing field. Measuring a large signal indicates that we have found the resonance frequency of the mode. Often times the characteristic of the resonance is dependent on the pulse power and duration, and it is necessary to iterate the experiment at lower pulse amplitudes to determine the resonance at few- or single-photon drive powers.

#### Two-tone spectroscopy

Determining the frequency of transmon qubits requires an indirect “two-tone” spectroscopy experiment to determine the spectrum of the transmon. We sweep the frequency of a probe tone around the region where we expect to find the transmon and monitor the frequency of a coupled readout resonator through another static microwave tone (i.e. we perform a readout of the transmon state). When initializing a new experiment, it is customary to perform this experiment using a transmon probe tone using a long,  $\tau > T_2$ , weak pulse to saturate the transmon two level system.

#### Cavity spectroscopy

The frequency of cavity modes that do not have a direct output port (which is the situation for quantum memory cavities) can be accomplished through yet another indirect measurement, this

time using the transmon qubit as the probe. Assuming the system is in the strong dispersive regime, then it is possible to drive photon-number selective rotations,  $\hat{Y}_\theta^n$  on the transmon qubit. We apply a spectroscopy tone in the region where we expect the cavity resonance. If the tone is near the cavity resonance frequency, then we will populate the cavity with photons, otherwise, the cavity is left in the vacuum state. The cavity photon number occupation will affect the transmon frequency via the dispersive interaction. We apply a number-selective transmon rotation on the  $n = 0$  peak (an  $\hat{Y}_\pi^0$  rotation) to correlate the state of the transmon qubit with the state of the cavity. When we apply the spectroscopy tone at the cavity resonance, then we can observe a change the transmon state.

### Cascaded indirect characterization

It is advantageous to limit the number of output ports in our experiments, both to simplify the hardware necessary for individual readouts and to mitigate unwanted loss channels associated with adding more output ports. Of course, the trade-off is the additional challenge in reliability controlling and measuring these “hidden” modes.

As a distinct example, in [50], we were required to utilize a “cascaded” measurement approach to characterize a register of transmon qubits that did not have direct readout resonators. In this experiment, the register of transmons and an ancillary transmon qubit were individually coupled to a common storage cavity. The ancilla qubit was independently coupled to a readout resonator and provided the only means to measure the state of the system. Measurements on the register transmon was accomplished in the following steps: first, the state of the register was mapped onto the storage cavity via a qubit-state dependent displacement on the cavity; second, the state of the cavity (now entangled with the state of the register qubit) was mapped onto the ancilla transmon via a photon-number selective rotation; finally, measurement of the ancilla transmon provides an measurement of the state of the register qubit.

This method is a useful approach for characterizing modes that are otherwise unreachable by conventional means and can be extended to other characterization experiments.

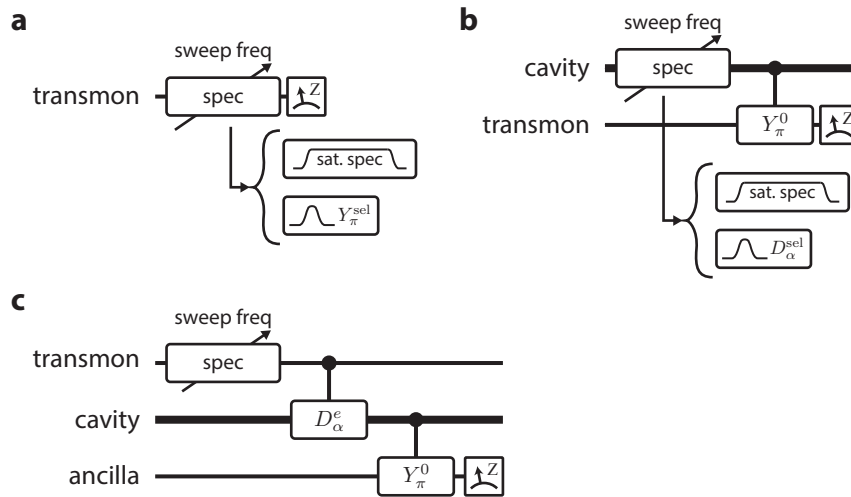


Figure 5.1 | **Spectroscopy experiments.** **a**, Transmon spectroscopy consists of a spectroscopy pulse followed by a measurement of the transmon qubit. The spectroscopy pulse can either be a long, weak saturation tone, where  $\tau > T_2$ , or a selective  $\pi$ -pulse. **b**, Cavity spectroscopy consists of a spectroscopy pulse on the cavity mode followed by a measurement of the photon number population of the cavity state using the transmon. We apply a photon-number selective  $\pi$ -pulse on the transmon (typically  $n = 0$ ) and measure probability the transmon is excited. The cavity spectroscopy pulse can either be a saturation tone or a selective displacement. **c**, For spectroscopy of a transmon that does not directly couple to a readout mode, we can use an indirect approach. After the spectroscopy pulse, we perform a series of selective operations that first, conditionally maps the state of the transmon onto a cavity mode using a selective cavity displacement  $D_{\alpha}^e$ ; and second, conditionally maps the state of the cavity (and therefore the transmon) onto an ancilla qubit using a photon number selective  $\pi$ -pulse on the transmon,  $Y_{\pi}^0$ . A version of this experiment was using in [50].

### 5.1.2 Tuning up readout

Typically after determining the frequency of the readout resonator (using a Vector Network Analyzer), we begin the process of tuning up our readout. In our experiments we tune up strong, projective measurements and will focus on this particular regime of measurement strength. Here we take an operational perspective to this question, describing some of the more practical steps that are necessary to optimize the measurement of transmon and leaving the theoretical details for other references, such as [144, 146, 174]. The process of tuning up readout requires some bootstrapping to optimize: readout of the transmon requires rotations to manipulate the state of the transmon; on the other hand, in order to calibrate these gates (and perform spectroscopy), we require readout that is sensitive to the state of the transmon.

For a generic cQED system, there are a number of parameters to consider when determining the readout protocol. We can split the readout protocol into two parts: first, the readout resonator is used to interrogate the state of the transmon; the second, the signal emitted from the readout resonator is digitized, integrated to extract a measurement result. The first considers the design of the measurement pulse. One will have to choose a particular pulse shape, duration, frequency, and amplitude. The selection of these parameters will depend on several physical parameters of the system, including the transmon lifetime  $T_1$  and dispersive coupling  $\chi$  to the readout as well as the readout  $\kappa$ . We typically choose to set our readout  $\kappa \sim \chi$  to separate the pointer states most efficiently. In this regime, we find the optimal readout frequency is set to halfway between the  $\omega_{ro}^g$  and  $\omega_{ro}^e$  frequencies. In other cases, it can be advantageous to use a  $\kappa < \chi$ , which means that the readout resonator spectrum results in well-separated qubit-state dependent resonances,  $\omega_{ro}^g$  and  $\omega_{ro}^e$ . In such a situation, instead of measuring at a symmetric detuning from both frequencies, it is better to use a measurement pulse with a frequency that is near-resonant to one of the two frequencies. The optimal measurement frequency can directly be calculated from a model that includes  $\chi$  and  $\kappa$ . We typically use either a constant amplitude pulse for measurement or one with smoothed edges to reduce transients. Choosing the pulse length and amplitude requires a balance between separation of the resonator pointer states and

the  $T_1$  of the transmon qubit (and other modes in the system). As discussed in detail in [? ], the finite  $T_1$  results in readout distributions that will be non-Gaussian when preparing computational states  $|g\rangle$  or  $|e\rangle$ , with the “tails” of the distribution proportional to the probability that we observe a  $T_1$  event during the measurement. To address this, it may be possible to compensate by using a higher amplitude for the measurement pulse, but there are experimental limitations to the drive strengths used in practice. First, increased drive amplitude will cause higher-order nonlinear effects, like resonator self-Kerr, to become more relevant. Second, quantum-limited amplifiers that are used to enable single-shot measurement have a finite dynamic range after which there are diminishing returns (and perhaps nonideal amplifier behavior) to increasing the drive strength. Finally, we have observed a shortening of the transmon lifetime as a function of readout photons, a phenomenon that has been called “ $T_1$  vs.  $\bar{n}$ ”.

The second step determines how the readout signal is processed. As the information content for the measurement trajectory is not uniform, we typically apply a digital readout matched filter (or envelope) to appropriately weight the measured signal. Equivalently, this filter accounts for a time-varying SNR of the measurement response. For example, at the beginning of the measurement, the cavity pointer state are not yet well separated and we should weight these points less than the period when the cavity has rung up. We experimentally extract this filter function, and in our regime of  $T_1 > 1/\kappa$ , it is close to the optimal linear filter [175? ]. The filter also has the property that it will project (or rotate) the measurement histograms in such a way that maximizes the information content along a particular axis, which will be useful when selecting a threshold. Next, to effect a single-shot readout, the measurement result should be compared to a threshold to assign whether we measured the transmon to be in the ground or excited state (and higher transmon levels if desired).

In our experiment we perform the following steps to tune up readout, assuming that we have already calibrated qubit  $\pi$ -pulses. For a given measurement pulse we perform the following process to extract the fidelity of the measurement. First, we extract the “pure” measurement trajectories by performing two separate experiments, either preparing the qubit in  $|g\rangle$  or  $|e\rangle$ . Though we will focus on these two levels, this process can be generalized for measurement tuneup to include

higher levels of the transmon (e.g.  $|f\rangle$ ). From these two trajectories, we generate a linear filter by taking the difference between these two trajectories:  $k(t) = |\alpha_e(t) - \alpha_g(t)|$ . This filter will be applied by the digitizer to each measurement trajectory, resulting in the measurement signal  $s$  for a given trajectory  $\psi_\tau$

$$s = \sum_{\tau=0}^{T_m} k[\tau]\psi[\tau] \quad (5.1)$$

In the last step, we determine a threshold from the two weighted histograms that maximizes the assignment fidelity [50], here defined as

$$F_{\text{assign}} = 1 - \frac{1}{2} [P(\text{"g"}| |e\rangle) - P(\text{"e"}| |g\rangle)] \quad (5.2)$$

The conditional probabilities should be read as: the probability of measuring “g” (“e”) when we prepare  $|e\rangle$  ( $|g\rangle$ ). Pictorially, they correspond to the “tails” of the measurement distribution on the wrong side of the threshold. The assignment fidelity is the probability that a given measurement will return the correct answer. For example, consider a completely random measurement where the “g” and “e” distribution are exactly the same. In this case  $F_{\text{assign}} = 0.5$  indicated that a given measurement will return the “correct” answer half of the time. Of course, being a random measurement, there is no useful information that can be extracted using this measurement. As another example, consider the case where we have perfect distinguishability of the probability distributions, but the assignment of “g” and “e” are completely flipped, such that  $P(\text{"g"}| |e\rangle) = P(\text{"e"}| |g\rangle) = 1$ . In this case we always assign the wrong state and as such  $F_{\text{assign}} = 0$ . There are some alternate definitions of the assignment fidelity (sometimes using other names), typically differing in whether the factor of 1/2 is used (e.g. see [146, 174]).

### 5.1.3 Measuring coherences

The quality of any quantum information experiment relies on sufficient coherence. As such it is customary to measure these properties early in the characterization of the device to determine whether it will be a viable candidate for the experiment at hand. We apply a suite of coherence measurements  $T_1$ ,  $T_2^R$ , and  $T_2^E$  to determine the properties of our transmons and cavities. When

performed on a transmon qubit, these experiments are fairly standard [99]. We often modify the basic  $T_2^R$  and  $T_2^E$  experiment. In such an experiment, a static detuning between the drive pulse frequency and the qubit frequency induces a precession in the evolution of the qubit state, where  $(|g\rangle + |e\rangle)/\sqrt{2} \rightarrow (|g\rangle + e^{i\phi}|e\rangle)/\sqrt{2}$ . The phase  $\phi = \delta\omega t$ . For small detunings, this precession can be difficult to distinguish from decoherence. Normally, to deal with this complication, one would apply a global detuning to the  $\pi/2$ -pulses, so that the qubit state performs several full oscillations over the decay time. However, depending on the magnitude of the detuning, this can affect the overall quality of the pulse rotations. Instead, by applying a delay-dependent digital, or “virtual”, phase to the final  $\pi/2$ -pulse to simulate the effect of a detuning. The effect is to induce an oscillation in the measured signal which aids in extracting the real detuning.

Coherence measurements for cavities has become an increasingly important step toward characterizing our cQED systems. The basic premise for a cavity  $T_1$  experiment is the same as for a qubit: generate a non-equilibrium state and measure the rate at which the system returns to thermal equilibrium. The multi-level structure of the cavity gives us several options to perform such an experiment. First, generating the cavity Fock state  $|1\rangle$  will allow us to treat the cavity as an effective two-level system, and we measure a simple exponential decay as the state returns to  $|0\rangle$ . As we will discuss in [subsection 5.2.3](#), generating such non-classical states is possible by using joint transmon-cavity control. An alternative method—and the experiment used more frequently in experiments performed for this thesis—to measure the cavity lifetime is to measure the decay of a coherent state  $|\alpha\rangle$ . Given a model for cavity decay based on single photon loss (i.e. the stochastic application of  $\hat{a}$ ) with rate  $\kappa$ , then the average photon number in a cavity will decay as  $\bar{n}(t) = |\alpha|^2 e^{-\kappa t}$ . In these  $T_1$  experiments we measure the population of the  $n = 0$  peak to infer the state of the cavity. Given the Poisson-distribution of a coherent state, the probability of measuring 0 photons in the cavity for a given average photon population of  $\bar{n}$  is given as  $P_0 = e^{-\bar{n}}$ . Therefore, the probability of measuring zero-photons in the cavity as function of time is the exponential of an exponential,  $P_0 = \exp[-|\alpha|^2 e^{-\kappa t}]$ . Similar functions can be generated to measure the decay of higher photon numbers.

Similar to the first cavity  $T_1$  experiment, we can modify the standard  $T_2$  experiment for

a qubit to be used for a cavity mode by using the cavity's  $\{|0\rangle, |1\rangle\}$  subspace to represent an effective qubit. Using techniques discussed in [subsection 5.2.3](#), we can perform unitary operations on the cavity within this subspace; in particular, we can implement cavity  $\pi/2$ - and  $\pi$ -pulses that are necessary for Ramsey and Echo experiments. The detection used for this experiment requires inferring the  $n = 0$  photon number population of the cavity through the use of selective  $\pi$ -pulse on the transmon qubit. It is also possible to extract the  $T_2$  of a cavity by measuring the rate that a coherent state decoheres [176]. A coherent state should maintain a constant phase relation between Fock states; the effect of decoherence will be to damp out this phase relation as the state approaches a completely mixed state. In practice, however, the presence of cavity self-Kerr can make extracting the pure dephasing of a coherent state difficult. The self-Kerr is not relevant to the dynamics when using only the  $\{|0\rangle, |1\rangle\}$  subspace, and is one motivation for preferring the Ramsey-style measurement.

## 5.2 Transmon and cavity operations

### 5.2.1 Qubit rotations

Having determined the frequency of the transmon qubit, we can proceed to implement universal control over the transmon Bloch sphere defined by the  $|g\rangle \leftrightarrow |e\rangle$  subspace. The basic experiment used to calibrate rotations about the Bloch sphere is to perform a Rabi experiment. Typically, we initialize the qubit in the ground state and subsequently apply a Gaussian shaped pulse resonant on the transmon frequency. By varying either the pulse amplitude (for a “power-Rabi” experiment) or pulse duration (for a “time-Rabi” experiment), we drive rotations about the Bloch sphere. We extract two specific amplitudes corresponding to the set of parameters required to perform a  $\pi$  and  $\pi/2$  rotation about the Bloch sphere.

To achieve high fidelity qubit operations, it is not sufficient to rely on just a Rabi experiment. In practice we supplement the transmon tuneup with several other experiments to fine-tune our qubit operations. One such experiment that further calibrates the pulse amplitude is called an “amplitude train”. We perform a series of  $N$   $\pi$ - or  $\pi/2$ -pulses while varying the global amplitude

of these pulses. The result of such an experiment serves to amplify the rotation error  $\delta$  of an individual experiment by performing multiple pulses so that the total observed rotation error is  $N\delta$ . We typically perform this experiment using  $N$  up to 40 pulses (though this is not a physical limitation of any part of the system). It is imperative that qubit rotations are applied on resonance with the frequency of the transmon. A detuning  $\Delta$  between the drive and the resonance frequency will result in so-called “off-resonant” Rabi oscillations. There are two main effects in the detuned regime. First, the Rabi frequency is modified from  $\Omega \rightarrow \sqrt{\Delta^2 + \Omega^2}$ , and we will select an incorrect amplitude to use for our qubit rotations. Second, a detuning modifies the axis of rotation in the Bloch sphere representation. The main consequence is that the rotation will no longer allow full oscillations between  $|g\rangle$  and  $|e\rangle$ , which will of course, adversely impact the fidelity of our qubit operations. To address this complication, we also perform Ramsey experiments to extract the frequency of the qubit mode.

In our experiments, when we couple a transmon and a cavity, we generally calibrate two pulse variants: an “unselective” version and a “selective” version. We use unselective rotations to perform operations on the transmon independent of the cavity state, and selective pulses to effect conditional operations between the transmon and the cavity. The dispersive interaction strength  $\chi$  sets the relevant timescale for these conditional operations. The “selectivity” of the pulse is dictated by the frequency bandwidth of the pulse; since we typically use gaussian shaped envelopes ( $\epsilon(t) \sim \exp(-t^2/(2\sigma_t^2))$ ), the relevant parameter is  $\sigma_t$ . For these gaussian shaped envelopes, the frequency bandwidth (in real frequency units) is  $\sigma_f = 1/(2\pi\sigma_t)$ . To be selective, the pulse bandwidth should be much smaller than the size of the dispersive interaction  $\sigma_f \ll \chi$ . Here, we define selective as the probability to drive the  $|g \leftrightarrow e, n \pm 1\rangle$  transition if we apply a pulse on the  $|g \leftrightarrow e, n\rangle$  transition. As a rule of thumb, a 99% selective pulse requires a  $\sigma_t > 3/\chi$ . For example, if we have a  $\chi/2\pi = 1$  MHz, then a  $\sigma_t > 500$  ns will suffice for 99% selectivity.

When we perform unselective pulses, we face two competing challenges. The point of an unselective pulse to implement a transmon operation independent of cavity state, which introduces frequency dispersion in the transmon frequency. To first order, this can be accomplished by using a short, wide bandwidth qubit pulse. In our experiment, we use  $\sigma_t = 6$  ns gaussian

pulses, which have a bandwidth of around 26 MHz. For a  $\chi/2\pi \sim 1$  MHz this pulse is sufficiently unselective for low photon numbers ( $\bar{n} < 5$ ). If the photon number distribution is known, then the pulse fidelity can be slightly improved by detuning the pulse to overlap with the average photon number,  $\Delta = \bar{n}\chi$ . While the pulse unselectivity improves with a shorter pulse, the bandwidth of the pulse can become an appreciable fraction of the anharmonicity. In such an extreme, the qubit rotation can result in leakage into the  $|f\rangle$  level. The presence of higher levels of the transmon can also induce phase-type errors in qubit operations. In order to achieve high fidelities for our unselective operations, we employ DRAG [141] to eliminate (to first order) leakage and phase errors due to higher levels of the transmon. The DRAG correction adds a scaled derivative waveform to the out-of-phase component of the pulse, and we calibrate the amplitude of this derivative component relative to the in-phase pulse. Our implementation and tuneup of DRAG follows from the routine described in [99], Section 5.2.3.

Our current recipe for pulse tuneups requires several rounds (typically two rounds) of amplitude (via Rabi and amplitude train) calibrations, frequency tuning, and DRAG corrections. We employ multiple rounds as a bootstrap procedure to ensure that each parameter is simultaneously optimized at the end of the tuneup procedure. We verify our tuneup using one of two experiments, either ALLXY [99] or randomized benchmarking [177, 178]. We generally use the former because it provides visual feedback on the quality of our transmon operations and can use the results to identify distinct gate errors, including pulse amplitude errors, phase errors, detunings, and corrections due to higher transmon levels sufficiently calibrated. Randomized benchmarking provides a measure of the average gate fidelity (assuming a Markovian noise model) [179, 180, 181], and related work has shown that this technique can be used as a metrology tool to determine certain gate errors [182, 183, 184, 185].

### 5.2.2 Cavity displacements

Cavity displacements are calibrated through an experiment that sweeps the amplitude of a short pulse on the cavity. In our experiments we either use a square pulse that is 10 ns in length or a gaussian pulse with a  $\sigma_t = 6$  ns. Immediately after the displacement, we probe the photon

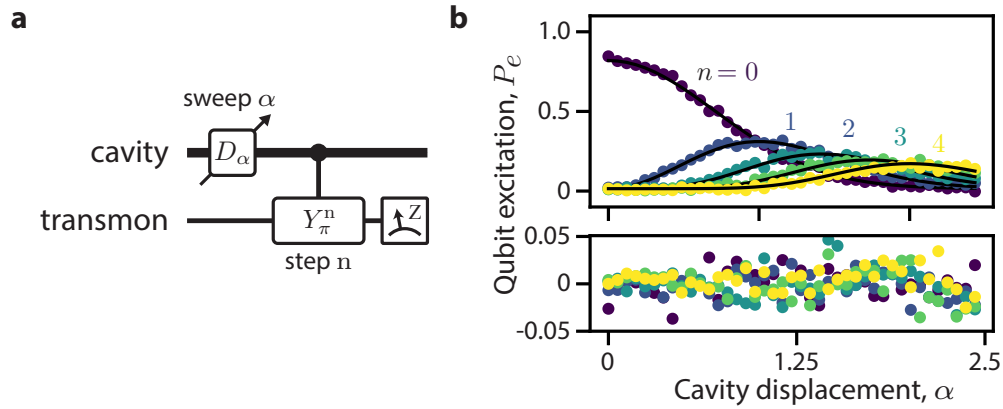


Figure 5.2 | **Cavity displacement calibration.** **a**, Pulse sequence for calibrating cavity displacement amplitude. After a displacement of amplitude  $\alpha$  we perform a photon-number selective  $\pi$ -pulse on the transmon to measure the photon number distribution of the cavity state. **b**, We perform this calibration experiment while sweeping  $\alpha$  for several  $n$ . Each trace can be fit to a Poisson distribution for a given  $n$ . We perform a global fit to extract the relative amplitude for a cavity displacement.

number population in the cavity. Starting from the vacuum state  $|0\rangle$  a displacement generates a coherent state  $|\alpha\rangle$  in the cavity. This state is characterized by photon number population that is Poisson distributed, with a occupation probability distribution given as  $p_n(\alpha) = e^{-|\alpha|^2/2} \frac{|\alpha|^{2n}}{n!}$ . We can measure the photon number population by applying photon-number selective qubit  $\pi$ -pulses conditioned on individual photon number peaks. Often it is sufficient for a quick calibration to use only the  $n = 0$  peak; for a more fine-tuned calibration we can perform an experiment that measures several photon number peaks and perform a global fit.

### 5.2.3 Complex transmon-cavity operations

Our shift to using cavities to store and process quantum information has increased the requirements for quantum control over the state of the oscillator. Our simple control of cavity displacements provide only limited control over the cavity Hilbert space, allowing only access to the space of coherent states when starting from the vacuum state. Enabling more complex control over the cavity the use of an ancillary transmon qubit that is dispersively coupled to the cavity. Previous work has shown that the dispersive coupling between the a qubit and cavity can be utilized to generate arbitrary states in the cavity [186] and even implement universal control over

the cavity [187]. Both of these approaches describe a constructive approach alternating cavity displacements and qubit rotations to implement the target operation. While these techniques have been used to generate high-fidelity operations in the lab [176], here we will briefly describe an alternative technique using optimal control theory to generate transmon-cavity operations.

### Implementation by optimal control

We utilize a numerical technique described in detail in Ref. [185] to design universal operations between the two qubits in each module. In particular, we use the Gradient Ascent Pulse Engineering (GRAPE) algorithm [188] to find a set of time-dependent pulses that implements a particular unitary operation or set of quantum state transfers. Our goal is to use GRAPE to find an operation that acts on a subspace of the complete Hilbert space. We supply the algorithm with a set of  $K$  initial and target states  $\{|\psi_k^{init}\rangle \rightarrow |\phi_k^{target}\rangle\}$  for a given drift Hamiltonian  $H_0$  and set of  $M$  control Hamiltonians  $\{H_m\}$ . The GRAPE algorithm determines a set of  $M$  pulses  $\{\epsilon_m(t)\}$  with length  $T$  to define an operation which maximizes the fidelity over the set of state transfers:

$$F_{OC} = \frac{1}{K^2} \left| \sum_k^K \langle \phi_k^{target} | \hat{U}_{OC} \psi_k^{init} \rangle \right|^2, \quad (5.3)$$

where the calculated operation,  $\hat{U}_{OC}$ , for a given set of control pulses is

$$\hat{U}_{OC}(\{\epsilon_m\}) = \int_0^T \exp \left[ -i(H_0 + \sum_m^M \epsilon_m(t')H_m)/\hbar \right] dt'. \quad (5.4)$$

In our experiments, we implement optimal control pulses by specifying complex-valued driving terms on the cavity and transmon qubits:  $\epsilon_c(t)\hat{c}^\dagger + \epsilon_c^*(t)\hat{c}$  and  $\epsilon_q(t)\hat{q}^\dagger + \epsilon_q^*(t)\hat{q} \approx \epsilon_q(t)(|g\rangle\langle e| + |e\rangle\langle g|)$ , where we have taken a two-level approximation for the transmon qubit. In our numerical optimization we discretize the pulses in 2 ns time steps, taking  $\epsilon_m(t) \rightarrow \epsilon_m(t_i)$ . In order to accurately reflect the dynamics of these complex pulses, it is important to use many levels of the cavity mode; we generate all pulses using a Hilbert space of 23 levels for the cavity and 2 levels for the transmon.

Practically, there are physical limitations to the pulses set by the control hardware; to take

these effects into consideration we include three constraints to the optimization routine. First, we apply an amplitude penalty to ensure that the pulse drive amplitude never exceeds a threshold value. Second, we apply a derivative penalty that gives preference to smooth pulses and lower bandwidth pulses. Finally, we include a final constraint to ensure that the pulse starts and ends with a near-zero amplitude to eliminate the possibility of sharp transients generated by pulse edges.

### Calibration of optimal control pulses

Successful implementation of these optimal control pulses in experiment relies on two broad requirements: first, an accurate knowledge of the drift Hamiltonian,  $H_0$ ; and second, a careful characterization of the experiment control lines. Here, we focus on the second requirement and detail our tune-up protocol for these optimal control pulses. We calibrate five parameters for each module's optimal control pulses: drive amplitudes for the cavity and transmon drives, linear frequency-dependent amplitude dispersion for both drives, and a relative timing between the two drives. The method used here closely matches the approach in Ref. [185]; we perform randomized benchmarking (RB) to extract a metric related to average gate fidelity to optimize over the set of five parameters. We have found most success optimizing optimal control pulses by bootstrapping over single parameter optimization experiments, though we have experimented with some multi-parameter optimizations. Having performed calibrations we proceed to extract experimental optimal control pulse gate fidelities. We utilize interleaved randomized benchmarking (iRB) and quantum process tomography (QPT) to establish the performance of our operations (Figure 5.3). In general, our experimental results are consistent with the simulated fidelities and demonstrate that this technique is a powerful tool to implement complex operations on a logical qubit encoded in the levels of a cavity.

### Limitations to optimal control

As such, a careful analysis of the specific types of errors that may occur during the local operations is important. Our simulations indicate that a large fraction of the errors result in codespace

leakage (e.g. the final state is no longer in the logical subspace of the data qubit with the communication qubit in the ground state,  $(\alpha |0_L\rangle_c + \beta |1_L\rangle_c) |g\rangle_q$ ). The optimal control operation takes the joint state through a complex trajectory in its Hilbert space; an error will induce a new trajectory that will affect the final state, likely resulting in population outside of the logical subspace [185]. From typical simulations we roughly quantify that  $\sim 95\%$  of the total infidelity is due to this leakage; the fidelity of the operation within the codespace is  $>99\%$ . Though the root cause of this error may be due to a combination of factors (here the performance is limited by transmon coherence), the result can be characterized by this single error syndrome. Therefore, an outstanding question to further improve the performance of these optimal control operations will be whether leakage detection circuits can be designed to efficiently herald when these errors occur.

### 5.3 System Hamiltonian characterization

Any cQED experiment will require a careful determination of the system Hamiltonian. In this section, we describe experimental methods to extract two dominant families of Hamiltonian parameters described in [subsection 3.2.3](#): self-Kerr of a single-mode and cross-Kerr between two-modes. The self-Kerr of a mode  $\hat{a}$  gives rise to the Hamiltonian term:

$$\mathcal{H}_K = \frac{K}{2} \hat{a}^\dagger \hat{a}^\dagger \hat{a} \hat{a} \quad (5.5)$$

The cross-Kerr between modes  $\hat{a}$  and  $\hat{b}$  leads to the interaction Hamiltonian, to fourth-order:

$$\mathcal{H}_{ab}^{(4)} = \chi_{ab} \hat{a}^\dagger \hat{a} \hat{b}^\dagger \hat{b} \quad (5.6)$$

Additionally, it can be important to include higher-order terms related to the dispersive interaction. Two sixth-order terms are given as

$$\mathcal{H}_{ab}^{(6)} = \frac{\chi_{abb}}{2} \hat{a}^\dagger \hat{a} \hat{b}^\dagger \hat{b}^\dagger \hat{b} \hat{b} + \frac{\chi_{aab}}{2} \hat{a}^\dagger \hat{a}^\dagger \hat{a} \hat{b}^\dagger \hat{b} \quad (5.7)$$

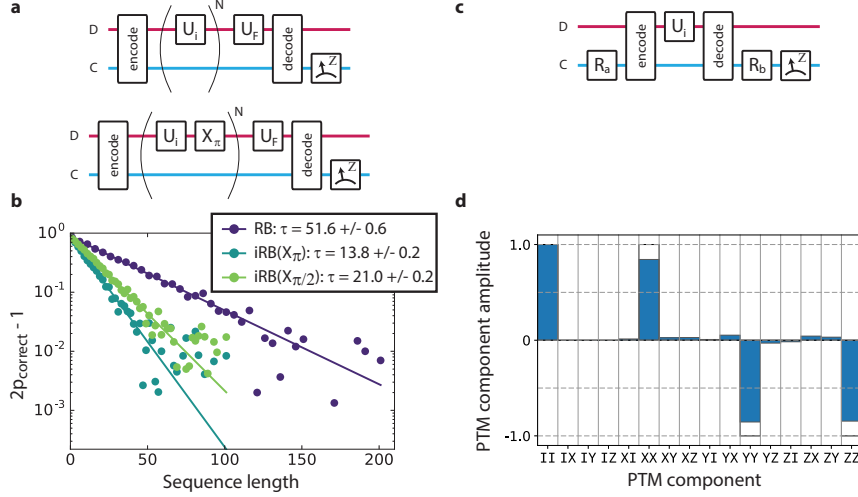


**Figure 5.3 | Characterization experiments for optimal control pulses.** **a** Pulse sequences for randomized benchmarking (RB, top) and iterative randomized benchmarking (iRB, bottom). For RB, a sequence of  $N$  operations ( $\hat{U}_i$ ) are randomly applied to the qubit state and a final correction unitary ( $\hat{U}_F$ ) ideally inverts the effect of the composite sequence. Measurement of the resulting state is then compared to the expected state to establish the error per operation. Here, to utilize RB for characterization of logical operations, the standard RB protocol is modified with an encode pulse before and a decode pulse after the RB sequence. For iRB, to characterize a particular operation (here,  $U_X$ ), this operation is interleaved among the random operations. A comparison with the standard RB sequence allows extraction of the single operation fidelity. In our implementation of RB, a new random sequence is generated for every experimental realization (or shot) and for each length  $N$ ,  $\hat{U}_F$  is chosen to ideally flip the state to both  $|0\rangle_L$  and  $|1\rangle_L$ . **b** Typical results for RB and iRB experiments. We plot data (dots) for a scaled probability of measuring the correct result as a function of the number of random pulses,  $N$ , in the RB sequence. These data are fit to the following model:  $p_{\text{correct}} = 0.5 + Ae^{-\tau/N}$ . From this fit, we estimate an error per gate to be:  $r = (1 - e^{-1/\tau(RB)})/2$ . From these fits, we extract an average gate error for an operation,  $U$ :  $r(U) = (1 - e^{-1/\tau(U)} - 1/\tau RB)/2$ . For the data shown, we extract  $r(X_\pi) = 2.5(2)\%$  and  $r(X_{\pi/2}) = 1.2(1)\%$ . These experimental gate errors are consistent with numerically simulated results that include the finite coherence time of the transmon qubit ( $T_2 \approx 15 \mu\text{s}$ ). **c** Characterization of optimal control operation  $U_i$  using process tomography. To characterize this logical operation we perform communication qubit QPT for the operation  $\hat{U}_{\text{encode}}\hat{U}_i\hat{U}_{\text{encode}}$ . For communication qubit QPT, we perform a set of transmon rotations before ( $\hat{R}_a$ ) and after ( $\hat{R}_b$ ) the operation under test. **d** Typical results for QPT experiments, here an  $X_\pi$  logical gate. We present the results in the Pauli transfer representation, with each bar  $AB$  (with  $A, B \in \{\hat{I}, \hat{X}, \hat{Y}, \hat{Z}\}$ ) representing each element in the Pauli transfer matrix (PTM). The experimentally reconstructed process is shown in blue; the ideal process is shown in hollow, black outlined bars.

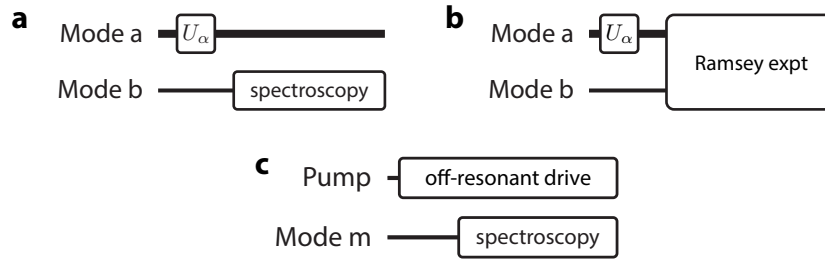


Figure 5.4 | **General techniques for extracting Hamiltonian parameters.** Here we sketch the three types of experiments that can be used to determine Hamiltonian parameters. In **a**, we modify a standard spectroscopy experiment on mode  $b$  to determine the cross-Kerr by including an initial operation (a rotation or displacement) on mode  $a$ . In **b**, we use a Ramsey-style experiment to extract the frequency of mode  $b$  as a function of the state of mode  $a$ . In **c**, an off-resonant pump induces Stark shifts on all mode  $m$ ; by calibrating the drive strength or by comparing the magnitude of the Stark shifts we can extract individual Hamiltonian parameters.

Both of these terms modify the fourth-order dispersive shift  $\chi_{ab}$ , adding a contribution depends nonlinearly with the number of photons in either mode. The effect of these sixth-order terms is to add a photon-number dependence to the magnitude of the dispersive shift. When including these sixth-order corrections, adding another photon to the  $\hat{a}$  mode from  $|n, m\rangle$  to  $|n + 1, m\rangle$  will induce a dispersive shift of  $\chi_{ab}(n) = \chi_{ab} + n\chi_{aab}$  (which normally would be  $\chi_{ab}$  and independent of the number of photons in mode  $\hat{a}$ ). Likewise, if we add another photon to mode  $\hat{b}$ , moving from  $|n, m\rangle$  to  $|n, m + 1\rangle$ , we will observe an energy shift of  $\chi_{ab}(n_b) = \chi_{ab} + m\chi_{abb}$ .

### 5.3.1 General methods

We will describe measurement techniques to extract several important Hamiltonian parameters in the next few sections. Here, we will briefly summarize the general strategies that we have developed for characterizing the Hamiltonian, leaving specific details to be discussed in the subsequent sections. Generally speaking, these parameters can be determined either through spectroscopic techniques or through time-domain measurements. More recently, techniques that rely on Stark shifts induced by off-resonant pumps have become yet another method for system characterization. In this section, we will survey some of these techniques used to characterize the system Hamiltonian of any generic cQED experiment.

### Method 1: Frequency-domain spectroscopy

The most direct approach for extracting relevant Hamiltonian parameters is to directly measure through spectroscopy. To see how this works, consider the following interaction Hamiltonian in the lab frame

$$\mathcal{H}_{ab} = \omega_a \hat{a}^\dagger \hat{a} + \omega_b \hat{b}^\dagger \hat{b} + \chi_{ab} \hat{a}^\dagger \hat{a} \hat{b}^\dagger \hat{b} \quad (5.8a)$$

$$= \left( \omega_a + \chi_{ab} \hat{b}^\dagger \hat{b} \right) \hat{a}^\dagger \hat{a} + \omega_b \hat{b}^\dagger \hat{b} \quad (5.8b)$$

$$= \omega_a \hat{a}^\dagger \hat{a} + \left( \omega_b + \chi_{ab} \hat{a}^\dagger \hat{a} \right) \hat{b}^\dagger \hat{b} \quad (5.8c)$$

In [Equation 5.8b](#) and [Equation 5.8c](#), we have grouped the interaction term with individual frequency terms to highlight that the frequency of mode  $\hat{a}$  ( $\hat{b}$ ) depends on the number of photons in mode  $\hat{b}$  ( $\hat{a}$ ), respectively. Therefore, the standard way this experiment is performed by first exciting one mode with some population and performing spectroscopy on the other mode to measure its photon-dependent frequency spectrum. This type of experiment is often called “number-splitting” [[151](#), [168](#)], calling out the fact that the spectrum is split based on the photon-number distribution of another mode.

### Method 2: Time-domain interferometry

While spectroscopy offers a frequency-domain approach to extract Hamiltonian terms, we can also move to an equivalent time-domain approach that can in some cases offer a simpler experiment for measuring Hamiltonian parameters. The key insight for this type of experiment is to note that the evolution of fourth-order Hamiltonian terms<sup>1</sup> is periodic, and we will observe “revivals” in the initial state at distinct times. For example, consider a general two-body interaction Hamiltonian  $\mathcal{H}_{ab}^{(4)} = \chi_{ab} \hat{a}^\dagger \hat{a} \hat{b}^\dagger \hat{b}$ . The evolution under this interaction Hamiltonian is described by the process

$$|\psi(t=0)\rangle = \sum_{m,n} c_{m,n} |m, n\rangle \rightarrow |\psi(t)\rangle = \sum_{m,n} c_{m,n} e^{i(m+n)\chi_{ab}t} |m, n\rangle \quad (5.9)$$

---

1. Certain sixth-order interactions will violate this working principle and we discuss this in a subsequent sections

If  $|\psi\rangle$  is a separable, superposition state at  $t = 0$ , the dispersive interaction will cause the two modes to become entangled as each Fock state component will gain phase a rate dependent on its photon number. However, at certain times  $\chi_{ab}t_{rev} = 0 \text{ mod } (2\pi)$ , we observe that all of the phases will re-align. At these distinct times, we see that the quantum state returns to the initial state at  $t = 0$ :  $|\psi(t = t_{rev})\rangle = |\psi(t = 0)\rangle$ . Our experiments are designed to extract the frequency of these revival times to determine  $\chi_{ab}$ .

### Method 3: Measurements of pump-induced Stark-shifts

The final method to extract dispersive Hamiltonian terms is to utilize off-resonant drives, or “pumps”, to induce Stark shifts on the spectrum of each mode. Recall from [subsection 3.3.1](#) that applying a detuned drive on mode  $m$  with amplitude  $\xi_m$  will induce a Stark shift on mode  $n$  [[138?](#) ]:

$$\Delta_n = -\chi_{mn}|\xi_m|^2 \quad (5.10)$$

The magnitude of each Stark shift is dependent on a particular Hamiltonian term and the strength of the drive. By calibrating the drive strength we can extract various Hamiltonian terms. Alternatively, because the application of a single pump  $\xi_m$  induces Stark shifts on all coupled modes, we can determine the relative stark shift between mode  $n$  and mode  $p$ :

$$\frac{\Delta_n}{\Delta_p} = \frac{\chi_{mn}}{\chi_{mp}} \quad (5.11)$$

Here we see that the dependence on the exact pump strength can be removed at the cost of knowledge of  $\chi_{mp}$ , which can be extracted by one of the other previously described methods. With this knowledge we can thus extract  $\chi_{mn}$ .

The challenge for this method is ensuring that the pump tone drives only a single mode  $m$ ; the dynamics become more challenging if this assumption is not met. Additionally, if the interaction under study is small, then it may be required to use large pump powers to measure an appreciable Stark shift. In the regime of large pump powers, the simple Stark shift model can break down, and we have observed unexpected transitions come into effect. The limits of mode

pumping is currently under active research.

### 5.3.2 self-Kerr of transmon and cavity

The fourth-order nonlinearity of a given mode  $\hat{a}$  follows from a simple Kerr-Hamiltonian,

$$\mathcal{H}_K = -\frac{K}{2}\hat{a}^\dagger\hat{a}^\dagger\hat{a}\hat{a} \quad (5.12)$$

We measure the self-Kerr of both transmon and cavity modes. Because the transmon anharmonicity is appreciably larger than the linewidth of the resonance ( $K_q \sim 100 - 300$  MHz), we can extract this term through simple spectroscopic means. On the other hand, the self-Kerr of a cavity (especially one that serves as a quantum memory) is generally engineered to be as small as possible, often times  $K_c \sim 1$  kHz, making it more difficult to extract through spectroscopic means. To address this, we will describe a time domain method that takes advantage of bosonic enhancement of the self-Kerr effect.

#### Measuring transmon anharmonicity through pulsed spectroscopy

The anharmonicity of a transmon qubit is most directly found through a spectroscopy experiment. For example, we can directly measure the frequency of the  $|e\rangle \leftrightarrow |f\rangle$  transition by initializing the transmon in the  $|e\rangle$  state via a  $\pi$  pulse and then sweeping the frequency of a second spectroscopy tone to determine the resonance frequency,  $\omega_{ef}$ , typically found 200 MHz below the  $\omega_{ge}$  resonance frequency. The transmon anharmonicity is then given simply as  $\alpha = \omega_{ge} - \omega_{ef}$ . We can also use a simpler pulse sequence that utilizes slightly more complex cQED physics to extract the anharmonicity. Selection rules of the transmon Hamiltonian prevent direct excitation from  $|g\rangle \leftrightarrow |f\rangle$  using a single photon. However, if we apply a strong spectroscopy tone halfway between the  $\omega_{ge}$  and  $\omega_{ef}$ , then we can utilize a two-photon virtual process to effect coherent operations in the  $|g\rangle \leftrightarrow |f\rangle$  manifold. For the purposes of determining the anharmonicity, it is customary to increase the drive amplitude until we observe a second peak arise at  $(\omega_{ge} + \omega_{ef})/2$ . Note that the detuning of this second peak to the fundamental frequency is

actually half of the total anharmonicity.

### Measuring cavity self-Kerr through rotating frame experiment

While a cavity self-Kerr can be directly found through a spectroscopy experiment, we generally rely on a time-domain approach that determines both the cavity resonance frequency as well as the self-Kerr. One can think of this approach as the continuous variable version of a qubit Ramsey experiment, where we use cavity displacements instead of  $\pi/2$ -pulses. An example of this experiment is shown in [Figure 5.5](#). In this experiment we first displace the cavity to some state  $|\alpha\rangle$ . We allow the state to evolve for some time  $t$  according to the detuned Kerr Hamiltonian, modified from [Equation 5.13](#) to include a static detuning  $\Delta$  (the transmon is in  $|g\rangle$  and does not contribute to the cavity dynamics),

$$\mathcal{H}_{\Delta,K} = \Delta \hat{a}^\dagger \hat{a} + \mathcal{H}_K \quad (5.13)$$

The unitary evolution under Kerr, to first order, where  $|\alpha|^2 K t \ll \pi$ , induces a photon-number dependent rotation of the cavity state. After this evolution, the initial state  $|\alpha\rangle$  will evolve to a new state  $|\alpha e^{i\phi_K}\rangle$ , where  $\phi_K(t) = (\Delta + |\alpha|^2 \frac{K}{2}) t$ .

The rest of this experiment serves to measure the phase  $\phi_K(t)$  of the cavity state. Currently we do not have a method for directly measuring the cavity phase. Instead, we will encode the information of the cavity phase into the cavity photon-number. This is the purpose of the second displacement of amplitude  $\tilde{\alpha}$ . One way to extract this phase is to perform a set of displacements  $\tilde{\alpha} = -\alpha e^{i\phi}$ . When  $\phi = \phi_K(t)$ , then the final state will be the vacuum state. Measuring the photon population, typically through a photon-number selective  $\pi$ -pulse on the  $n = 0$  peak, will allow us to extract the phase of the cavity state. In practice we typically perform this experiment while sweeping  $t$ , and we use a second displacement amplitude angle that rotates at some defined frequency  $\omega$ :  $\tilde{\alpha} = -\alpha e^{i\omega t}$ . This frequency is equivalent to the digital detuning that is used in qubit Ramsey experiments.

The probability that the cavity in the vacuum state at the end of the experiment is calculated

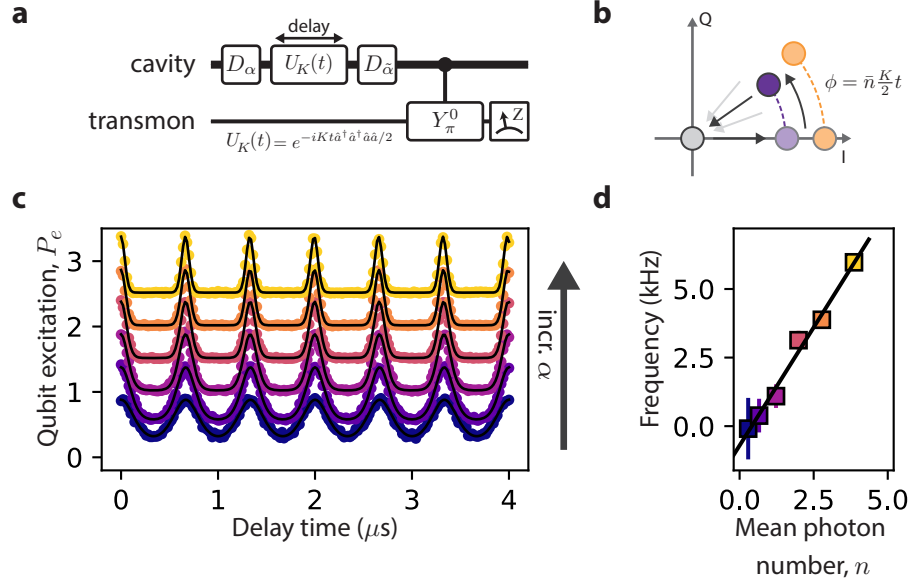


**Figure 5.5 | Cavity frequency and self-Kerr.** In this experiment, we describe the measurement of the cavity frequency and cavity self-Kerr by extracting frequency of cavity state revivals. This experiment is in many ways similar to a continuous-variable Ramsey experiment. **a**, The pulse sequence describing the measurement of the frequency detuning  $\Delta$  of a cavity mode and the self-Kerr  $K$  of the cavity. In **b**, illustrates cavity state evolution in IQ-space. The experiment begins with a displacement of the cavity state to some state  $|\alpha\rangle$ . A subsequent delay  $t$  will bring the state to  $|\alpha e^{-i\phi_K}\rangle$ , where  $\phi_K(t) = (\Delta + |\alpha|^2 \frac{K}{2}) t$ . The next displacement  $\tilde{\alpha} = -\alpha e^{i\omega t}$ , attempts to displace the cavity state to the vacuum. This will occur at discrete revival times, from which we can calculate  $\Delta$  and  $K$ . We then perform a  $n = 0$  number-selective  $\pi$ -pulse on the transmon and measure the transmon state. Because  $\Delta$  and  $K$  can be small compared to the lifetime of the cavity mode, we typically apply a digital frequency detuning  $\omega$  to induce faster revival times to aid in the fit. This experiment is also performed for several initial displacements  $\alpha$  to separate the  $\Delta$  from  $K$ . **c**, We perform this experiment for several displacements, from  $\alpha = 0.5$  (bottom) to  $\alpha = 2$  (top). Each trace shows characteristic revival times where the transmon excitation probability peaks. The black line is a fit for each experiment according to [Equation 5.14](#), where we set  $\omega/2\pi = 1.5$  MHz. We extract the frequency of revivals. **d**, From the fit, we plot the revival frequency as a function of the mean photon population in the cavity. We perform a linear fit, where the y-intercept corresponds to the detuning  $\Delta/2\pi = -0.7 \pm 0.3$  kHz and the slope corresponds to  $K/2\pi = 3.4 \pm 0.2$  kHz. Note that the calculated slope is half of the cavity self-Kerr in our definition,  $m = K/2$ .

from the overlap:

$$\begin{aligned} P_0 &= |\langle 0|D_{\tilde{\alpha}}U_K D_{\alpha}|0\rangle|^2 = \left| \langle -\tilde{\alpha} | \alpha e^{i\phi} \rangle \right|^2 = e^{-|\alpha e^{i\omega t} - \alpha e^{i\phi}|^2} \\ &= e^{-2|\alpha|^2 [1 - \cos((\omega + \Delta + |\alpha|^2 \frac{K}{2})t)]} \end{aligned} \quad (5.14)$$

The evolution is clearly periodic, with revival times at integer multiples of  $t_{rev} = k\pi / (\omega + \Delta + |\alpha|^2 \frac{K}{2})$ . Distinguishing  $\Delta$  from  $K$  requires performing this experiment for several  $\alpha$ . The cavity self-Kerr will result in a photon-number dependent revival time.

### Stark shift

An alternative method for extracting the self-Kerr of the cavity is to use off-resonant drives, or “pumps” to induce Stark shifts on the transmon and cavity mode. If we apply an off-resonant tone, or a “pump” on the cavity mode such that the detuning is larger than the intrinsic linewidth  $\Delta > \kappa$ , so that we only populate the cavity mode with “virtual photons” that decay at rate  $1/\Delta$ . We ramp the start and end of the pulse with a smoothly varying function—either a tanh-shape or a gaussian-shape—to minimize the frequency response of any transients that may resonantly excite the resonant mode. By performing spectroscopy as a function of the pump strength, we can determine the mode detuning as a function of the drive strength. For the transmon and cavity mode, the respective detunings are found to be

$$\Delta_q = -\chi|\xi|^2 \quad \Delta_c = -K|\xi|^2 \quad (5.15)$$

Then by comparing the relative magnitude of the Stark shift on the transmon and cavity and knowing the strength of the dispersive shift, we can extract the self-Kerr of the cavity. This is especially useful for extracting the self-Kerr of low-Q modes like readout resonators where the occupation is rapidly damped via coupling to the output port.

### 5.3.3 cross-Kerr between qubit and cavity

The dispersive shift between a transmon and cavity represents the fundamental interaction central to our cavity-transmon quantum logic. The interaction Hamiltonian for a qubit mode  $q$  and cavity mode  $c$  given as:

$$\mathcal{H}_{int} = \chi \hat{q}^\dagger \hat{q} \hat{c}^\dagger \hat{c} \quad (5.16)$$

Additionally, it can be important to include higher-order terms related to the dispersive interaction. Two sixth-order terms are given as

$$\mathcal{H}_{int} = \frac{\chi_{qcc}}{2} \hat{q}^\dagger \hat{q} \hat{c}^\dagger \hat{c}^\dagger \hat{c} \hat{c} + \frac{\chi_{qqc}}{2} \hat{q}^\dagger \hat{q}^\dagger \hat{q} \hat{q} \hat{c}^\dagger \hat{c} \quad (5.17)$$

The first term, also parameterized as  $\chi'$ , can be thought of as a qubit-state dependent cavity self-Kerr term. Equivalently, we can think of this term as adding a cavity-state dependent contribution to the magnitude of the dispersive interaction, where the dispersive shift between the  $n$  and  $n + 1$  level is photon-number dependent:  $\chi(n) = \chi_{qc} - n\chi_{qcc}$ . This term is generally opposite sign from  $\chi_{qc}$  and we generally see the magnitude of the dispersive shift decrease with increasing photon number. Though  $\chi_{qcc}$  arises from a sixth-order interaction, in practice we find that its magnitude is on the same order as the cavity self-Kerr, and its effect should not be discounted especially when using multi-photon cavity states. The second term represents a modification on the dispersive shift when using higher levels of the transmon qubit. It has not been used directly as a part of this thesis, but this term was crucial for the experiment performed in [164], where the higher-level of a transmon was used to generate a two-cavity joint parity measurement without matching  $\chi_{qc}$ .

As with most Hamiltonian terms, there are several possible approaches to measure this term. Here we detail two independent methods for extracting the magnitude of the dispersive interaction. Crucially, we find that these two experiments give consistent results for the measurement of the dispersive interaction. A third method, described in [176] measures the relative phase evolution of neighboring Fock states  $|n\rangle$  and  $|n + 1\rangle$  by using photon-number selective qubit

rotations to implement a phase gate on the cavity state.

### Number-splitting spectroscopy

In the strong-dispersive regime of cQED, it is possible to resolve individual photon-number dependent qubit resonances, a phenomenon called “number-splitting” [151, 168]. Based on Equation 5.16, the frequency of the transmon mode is detuned by  $\chi$  for each new photon in the cavity. To measure this spectrum, we perform a displacement on a cavity state, initializing it to a coherent state  $|\alpha\rangle$ . Immediately after we perform spectroscopy to extract the spectrum of the transmon qubit. We observe a series of peaks that correspond to the photon number distribution of the cavity state (for a coherent state, this is Poisson-distributed). Because a saturation experiment can require a long pulse that approaches the lifetime of the cavity mode, we generally choose to perform  $\pi$ -pulse spectroscopy using a selective transmon pulse, such that  $\sigma_t > 1/\chi$ , or on the order of a few  $\mu s$ .

The number-splitting experiment can also resolve higher-order effects of the dispersive interaction. In particular, we can not only measure  $\chi_{qc}$ , but also  $\chi_{qcc}$  by extracting the location of each number-splitting peak. The determination of the dispersive shift through number-splitting spectroscopy is exceedingly simple, and requires no calibration other than tuning up a spectrally-narrow  $\pi$ -pulse. In particular, unlike the next method, number-splitting does not require an exact calibration of the displacement amplitude. All that is required is that the cavity displacement does inject photons into the cavity. Of course, this experiment can be used to calibrate cavity displacement amplitudes, though the quality of this calibration is dependent on quality of the  $\pi$ -pulse as a function of detuning. For example, the spectroscopy pulse can be a function of the frequency dependence of the transmission through the input drive lines. In the case of large  $\chi$  and large photon number, this detuning can give rise to an appreciable frequency-dependence in  $\pi$ -pulse amplitude as a result of imperfections in the input chain.

The other higher-order term in Equation 5.17,  $\chi_{qqc}$  requires at least two excitations in the transmon qubit mode. We may probe this term by treating the  $|e\rangle \leftrightarrow |f\rangle$  transition of the transmon qubit as an effective qubit and performing a number-splitting experiment within this

manifold. By comparing the dispersive shift in this excited manifold,  $\chi_{ef}$ , with the shift in the  $|g\rangle \leftrightarrow |e\rangle$  manifold, where  $\chi_{ge} = \chi_{qc}$ , we calculate this sixth-order correction to be  $\chi_{qqc} = \chi_{ef} - \chi_{ge}$ . This “e-f number-splitting” experiment is important when the experiment results manipulating the  $|f\rangle$  transition of the transmon, for example, in [164].

This experiment is useful when the system is in the strong dispersive regime, where the dispersive shift is much larger than the intrinsic linewidth of the transmon resonance,  $\chi \gg \Gamma_q$ . Additionally, because an exact calibration of the photon number is not necessary for number-splitting spectroscopy, this technique can be used to measure the dispersive shift for both high-Q cavities as well as low-Q cavities. In the latter case, though the cavity state will experience decay during the course of the spectroscopy experiment, this method can still be used provided that the initial displacement is large enough so that the spectroscopy pulse can partially excite the transmon. We expect a degradation in the signal due to decay during the pulse and the unavoidable measurement-induced dephasing [168] that arises from the exact interaction we seek to measure.

### Qubit state revivals

We can also use a time-domain approach to extract the dispersive interaction through a Ramsey interferometric experiment [158]. After initializing the cavity in a coherent state  $|\alpha\rangle$ , we perform a Ramsey experiment on the transmon qubit. The effect of the natural dispersive interaction is to entangle the cavity state with the transmon state:

$$\begin{aligned}
 \pi/2\text{-pulse} : & \quad \frac{1}{\sqrt{2}} |\alpha\rangle (|g\rangle + |e\rangle) \\
 \text{Ramsey delay, } t : & \quad |g, \alpha\rangle + |e, \alpha e^{-i\chi t}\rangle \\
 \pi/2\text{-pulse} : & \quad \frac{1}{2} [|g\rangle (|\alpha\rangle - |\alpha e^{-i\chi t}\rangle) + |e\rangle (|\alpha\rangle + |\alpha e^{-i\chi t}\rangle)]
 \end{aligned} \tag{5.18}$$

At the end of the experiment, we measure the state of the transmon qubit. The effect of the dispersive interaction is to entangle the qubit with the cavity; by projecting out the cavity state, the transmon is left in an incoherent mixture, and we observe an apparent dephasing of the

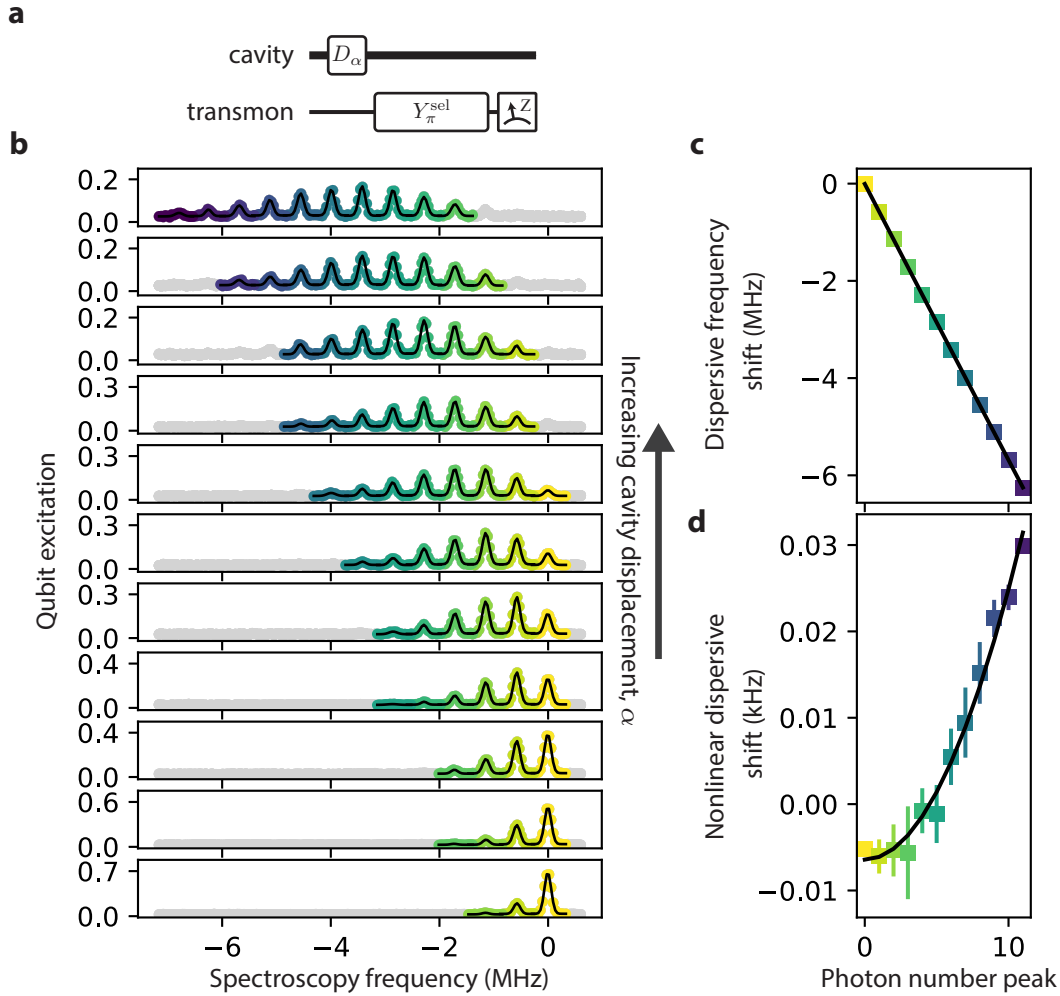


Figure 5.6 | **Qubit number-splitting spectroscopy.** **a**, The pulse sequence detailing the measurement of the dispersive shift of the transmon frequency due to the dispersive interaction. After a displacement that populates the cavity with a coherent state of  $|\alpha\rangle$ , we sweep the frequency of a spectrally narrow (compared to  $\chi$ )  $\pi$ -pulse on the transmon to determine the photon-number dependent transition frequency. A saturation pulse can also be used at the cost of reduced transmon signal. **b**, Shown here is spectroscopy on the transmon for different cavity displacements, from  $\alpha = 0.5$  at the bottom to  $\alpha = 2.5$  at the top. As the displacement increases, we populate successively higher photon numbers. Each solid line is a fit to a distinct peak, color coded from yellow ( $n = 0$ ) to dark purple ( $n = 11$ ), from which we extract the frequency. While a global fit is certainly possible, in this method, we do not require precise calibration of the displacement amplitude. **c**, The frequency of the qubit transition is plotted as a function of the photon number. We take an average of each frequency extracted from the spectroscopy experiment in **b**. The error bars in the frequency is smaller than the size of the markers. The line is a second-order polynomial fit to the data. From this we extract a linear dispersive shift of  $\chi/2\pi = -571 \pm 1\text{kHz}$  and a nonlinear shift of  $\chi'/2\pi = 0.3 \pm 0.1\text{kHz}$ . **d**, We subtract the linear component  $n\chi$  from the data in **c** to better visualize the nonlinear component of the dispersive shift. From here we see the data are well described by a quadratic.

transmon qubit. Notice that at certain times  $t = 2\pi/\chi$ , the qubit and cavity are disentangled and we observe revivals in the qubit coherence. The probability to find the transmon in the excited state is given as [158],

$$\begin{aligned} P_e &= \frac{1}{2} (1 + \text{Re} [\langle \alpha | \alpha e^{-i\chi t} \rangle]) \\ &= \frac{1}{2} \left[ 1 + e^{|\alpha|^2 (\cos(\chi t) - 1)} \cos(|\alpha|^2 \sin(\chi t)) \right] \end{aligned} \quad (5.19)$$

This model excludes several effects, including cavity decay and nonlinearity in the dispersive interaction. Cavity decay,  $\kappa$  can be included by modifying the static photon number population with a time dependent term:  $|\alpha|^2 \rightarrow |\alpha|^2 e^{-\kappa t}$ . The nonlinearity in the dispersive interaction,  $\chi_{qcc}$ , can be observed in this experiment as shift in the qubit revival times as a function of the size of the initial displacement,  $t = 2\pi / (\chi - |\alpha|^2 \chi_{qcc})$  [158]. Larger nonlinearities (or larger photon numbers) will result in imperfect qubit state revivals as the qubit and cavity are no longer exactly disentangled due to the dispersion in the dispersive shift.

This method is particularly useful for measuring small  $\chi$  which may be more difficult to extract from a spectroscopy measurement. Indeed, a version of this experiment was used in [137] to extract both a photon number calibration as well as the  $\chi$  for a transmon coupled to a low-Q mode where the revival time due to  $\chi$  is longer than the coherence time of the transmon,  $T_2^R < 2\pi/\chi$ . However, it is important for the photon number in the cavity to be mostly constant during the Ramsey measurement as photon decay will cause dephasing of the transmon and destructively alter the rate of phase accumulation of the transmon state. As such, we typically apply this approach for extracting the dispersive shift for long-lived cavity modes.

#### 5.3.4 cross-Kerr between two qubits

The coupling between two qubits, often parameterized as  $\zeta$ , results in the familiar cross-Kerr Hamiltonian between qubit modes  $q_1$  and  $q_2$

$$\mathcal{H}_\zeta = -\zeta \hat{q}_1^\dagger \hat{q}_1 \hat{q}_2^\dagger \hat{q}_2 = -\zeta |e_1 e_2\rangle \langle e_1 e_2| \quad (5.20)$$

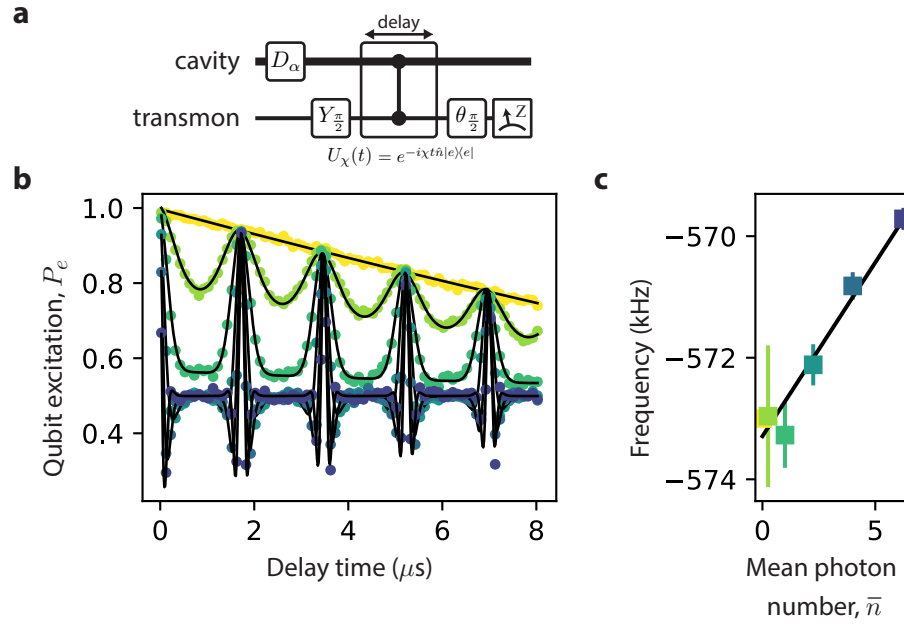


Figure 5.7 | **Transmon-cavity Ramsey interferometry.** **a**, The pulse sequence describing the measurement of the dispersive interaction via Ramsey interferometry. The experiment begins with a displacement of the cavity to a coherent state  $|\alpha\rangle$ . We then perform a Ramsey experiment on the transmon. The dispersive interaction causes the photon-number dependent qubit components to acquire phase at different rates. These phases will realign at periodic intervals at periodic intervals,  $t_{rev} = 2\pi/\chi$ . The dispersive coupling will induce periodic entanglement and disentanglement between the transmon and cavity. Measuring the transmon qubit alone will result in apparent dephasing and revivals in the qubit coherence, which is our meter for the strength of dispersive interaction. **b**, Shown here are transmon-cavity Ramsey experiments while varying the initial displacement, from  $\alpha = 0$  (in yellow) to  $\alpha = 2.5$  (in dark purple). Each experiment is fit to Equation 5.19 modified to include a component for the dephasing time,  $T_2$ . **c**, We extract the revival frequency for each experiment, and plot them as a function of the initial mean photon population. The data are fit to a line, where the y-intercept corresponds to the linear dispersive shift and the slope corresponds to the nonlinear dispersive shift. From this we extract a linear dispersive shift of  $\chi/2\pi = -573 \pm 1\text{kHz}$  and a nonlinear shift of  $\chi'/2\pi = 0.6 \pm 0.1\text{kHz}$ .

We often take the two-level approximation  $\hat{q}^\dagger \hat{q} \rightarrow |e\rangle\langle e|$  which results in the form shown in the second equality. The contributions to the dispersive interaction between two transmons has been discussed in [99, 148], and arise from two sources: direct dipole coupling between the two transmons and a cavity-mediated coupling related to the detunings of the transmons to the cavity and the individual  $\chi$  of each transmon to the cavity.

We can measure  $\zeta$  either through spectroscopy or via a Ramsey-style experiment. Both methods rely on the fact that this coupling terms serves to shift the frequency of one qubit by  $\zeta$  conditioned if the other qubit is in the excited state.

### Spectroscopic method

For the spectroscopic approach, we perform two spectroscopy experiments on the first qubit, one when the second qubit is either initialized in  $|g\rangle$  and one when the second qubit is initialized in  $|e\rangle$ . The difference between the first qubit's resonance frequency for the pair of experiments is  $\zeta$ . We perform  $\pi$ -pulse spectroscopy instead of saturation spectroscopy to minimize the effect of decay of the second qubit during the spectroscopy of the first qubit.

### Time-domain method

For small  $\zeta$ , it can be more effective to use a time-domain approach. We detail an example of this experiment in [Figure 5.8](#). We perform a Ramsey experiment on a target qubit when the control qubit is either initialized in  $|g\rangle$  or  $|e\rangle$ . By extracting and comparing the frequency of Ramsey oscillations, we directly measure the additional detuning when the control qubit is in the excited state as a frequency shift of the target qubit. In practice, we often perform a constant delay variant of the Ramsey experiment, which we call a ‘‘Ramsey phase’’ experiment. We prefer this Ramsey phase method as it avoids complications associated with decay of control transmon during the course of a  $T_{2R}$  experiment. We perform a Ramsey experiment at a fixed time, while varying the phase,  $\theta$ , of the second  $\pi/2$ -pulse (relative to the first pulse). We extract the phase of the resulting sinusoidal oscillation, to determine the detuning:  $\phi = \delta\omega \cdot t$ . Again, by comparing the phase shift between a Ramsey phase experiment where the second qubit is initialized in either

$|g\rangle$  or  $|e\rangle$ , the strength of the qubit-qubit coupling,  $\zeta$ , can be extracted.

### 5.3.5 cross-Kerr between two cavities

The cross-Kerr between two cavities represents the coupling between two bosonic modes, quantified through the interaction Hamiltonian between cavity modes  $t$  and  $c$  as  $\mathcal{H}_{ab} = \chi_{ab} \hat{a}^\dagger \hat{a} \hat{b}^\dagger \hat{b}$ . This interaction can be used to perform direct cavity-cavity operations. For example, this term is used (at least indirectly) to enable parametric interactions, such two-mode squeezing or beam-splitter operations [137, 138, 143? ]. In other cases—such as the teleported gate experiment—we view this coupling term as an unwanted residual interaction. As we continue to assemble more complex multi-cavity devices, it is becoming increasingly important to quantify the cross-Kerr between two cavities, especially if they are long-lived. In the case of the cross-Kerr between a storage and readout cavity, this interaction term can lead to a skew in the readout signal of a transmon qubit. The cavity-cavity cross-Kerr behaves in the same way as the transmon-cavity dispersive interaction. For certain experiments [158], it was important to calibrate out the effect of this cavity-cavity cross-Kerr on the measurement of the transmon qubit.

We can use slightly modified techniques discussed in previous sections for a transmon and cavity to measure the cavity-cavity cross-Kerr. There are two distinct cases that should be considered: first, the cross-Kerr between a storage cavity and a readout cavity; second, the cross-Kerr between two storage cavities. In both cases, we will utilize a transmon qubit coupled to one or both modes as a meter for the state of one of the cavities. Here, we will survey some of these techniques.

#### Measuring cross-Kerr via spectroscopy

As before, spectroscopy may be the most straightforward method to measure the cross-Kerr between cavities. We first inject photons into the control cavity, either using a coherent state  $|\alpha\rangle$  or a Fock state  $|n\rangle$ , and then perform cavity spectroscopy on the target cavity. The measured frequency shift of the target cavity resonance is proportional to the cross-Kerr:  $\delta\omega_c = \bar{n}\chi_{ab}$ .

We then perform cavity spectroscopy on the target cavity with an ancillary transmon qubit.

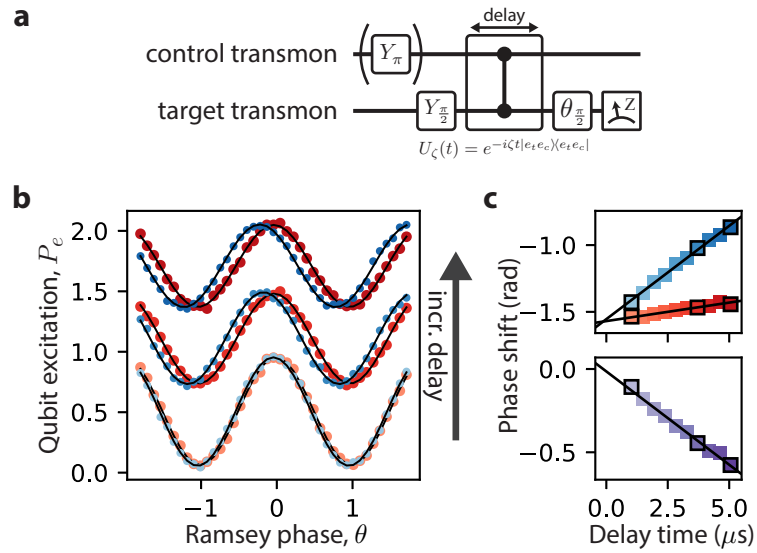


Figure 5.8 | **Transmon-Transmon cross-Kerr measurement via Ramsey interferometry.** **a**, The pulse sequence describing the measurement of the dispersive interaction via dual Ramsey phase experiments. In this experiment, we exploit the fact that one transmon (i.e. control) induces a qubit-state dependent frequency shift of  $\zeta$  on the other transmon (i.e. target). We use a Ramsey-style experiment to extract the frequency difference when the control transmon is in  $|g\rangle$  and  $|e\rangle$ . For each pair of Ramsey phase experiments, we fix the delay time and vary the phase,  $\theta$ , of the second  $\pi/2$ -pulse. **b**, Here we show several representative Ramsey-phase experiments at different delays, from  $t = 1 \mu s$  (bottom) to  $t = 5 \mu s$  (top). For each delay, we perform an experiment when the control qubit is left in  $|g\rangle$  (red) and an experiment when the control qubit is initialized to be in  $|e\rangle$  (blue). We fit the resulting oscillations, fixing the frequency and extracting the phase. **c**, (Top) We plot the fit phases for control qubit in  $|g\rangle$  (blue) and  $|e\rangle$  (red) as a function of delay time. When the control qubit is in  $|g\rangle$ , the phase shift is only dependent on the drive detuning from the transmon transition frequency; here, we see a small detuning in the red points. When the control qubit is in  $|e\rangle$ , the phase shift is equal to the sum of the detuning and the transmon-transmon interaction term  $\zeta$ . We extract the rate of phase shift (a frequency) from the slope (black lines). (Bottom) We show the phase difference  $\Delta\phi = \phi_e - \phi_g$  as a function of the delay time. From a linear fit, the slope corresponds to the transmon-transmon interaction term,  $\zeta/2\pi = 18 \pm 1 \text{ kHz}$ .

There will be an additional complication if the transmon qubit is coupled to both cavity modes as the frequency of the transmon will be shifted by the dispersive interaction with the control cavity. Since the initial displacement on the control cavity is known beforehand, the adjustment on the transmon qubit can be pre-determined. If the control cavity is a low-Q mode, then it is also possible to add a delay after the cavity spectroscopy pulse and before the transmon selective  $\pi$ -pulse to allow for control cavity photons to decay. The resolution of this experiment is ultimately set by the linewidth of the cavity resonance (as well as the bandwidth of the spectroscopy pulse on the target cavity). As such, it is generally preferable to perform spectroscopy on the longer-lived cavity mode to move further into the strong-dispersive regime. To be more precise, to resolve  $\chi_{ab}$  in spectroscopy, one must use a cavity spectroscopy tone with duration  $\tau > 1/\chi_{ab}$ . For example, if  $\chi_{ab}/2\pi = 10$  kHz, then we should choose a spectroscopy tone with  $\tau > 100$  ns. With readout cavity lifetimes on the order of 100 – 1000 ns, the readout cavity will likely be completely depleted of photons by the end of the cavity spectroscopy tone. If we are in the number splitting regime, then the readout population is not necessary as we can directly extract  $\chi_{ab}$  from the number-split peaks. If we are not resolved, then the average detuning as a function of displacement amplitude can provide an upper bound to  $\chi_{ab}$ .

### Measuring cross-Kerr via measuring cavity rotating frame

It is possible to measure the cross-Kerr through using time-domain methods. We will propose an approach that closely follows the measurement of cavity self-Kerr described in [subsection 5.3.2](#). In this measurement, we rely on a linear frequency shift of the target cavity when the control cavity is populated with photons. When the control cavity is initialized into a coherent state  $|\alpha\rangle$ , the frequency of the target cavity will be detuned by  $\Delta = |\alpha|^2\chi_{ab}$ . This detuning can be directly measured using previously the previously-described measurement protocol. In order to isolate the cross-Kerr  $\chi_{ab}$  from the self-Kerr and any other detuning, this experiment should be performed as a function  $\alpha$ .

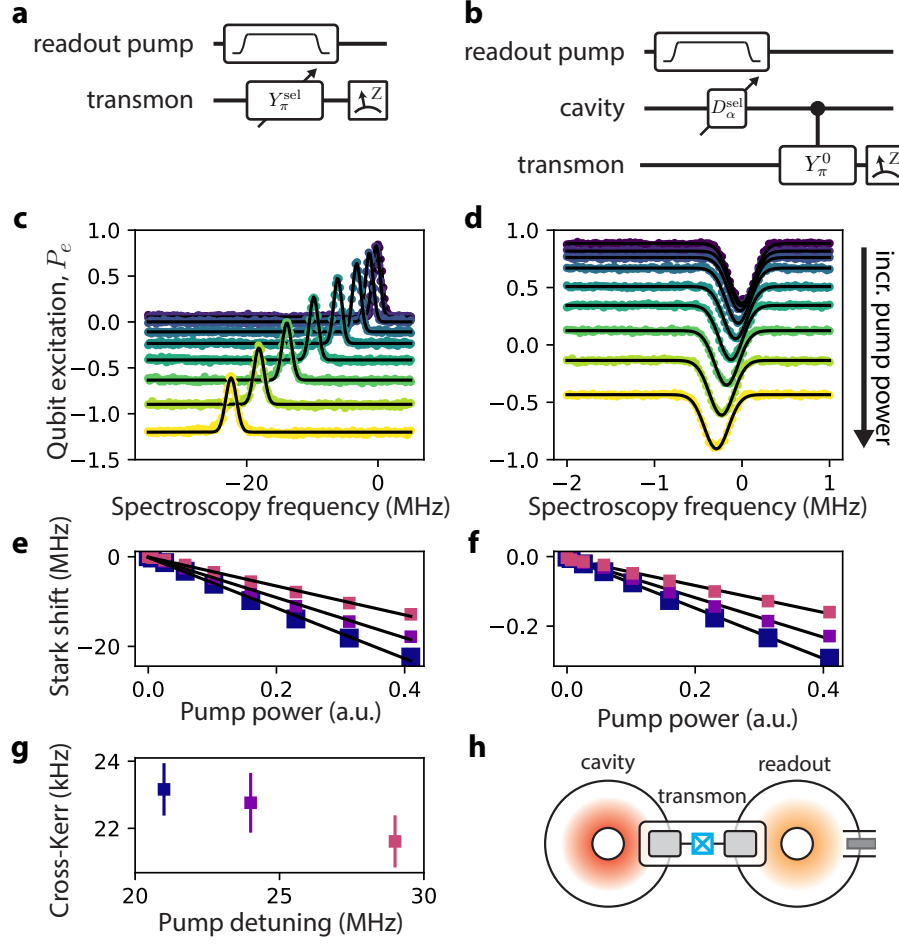


Figure 5.9 | **Cavity-readout cross-Kerr measurement via Stark shifts.** **a** and **b**, Experimental protocol for performing Stark shift spectroscopy on the transmon (left) and cavity (right) in the presence of an off-resonant drive on the readout cavity (or any other cavity). **c** and **d**, For a fixed pump detuning  $\Delta_{\text{pump}} = 21$  MHz, we perform stark-shift spectroscopy on the transmon (left) and cavity (right). Each trace and color is a different pump power setting, with increasing power from top to bottom. The data show that as the pump power increases, the detuning of the mode increases. We fit each trace to extract the resonance frequency of the mode; the fit is indicated in black. **e** and **f**, We plot the resonance frequencies as a function of pump power,  $|\xi_r|^2$ , (here, in DAC<sup>2</sup> units). The Stark shift is linear in the pump power, with a fit indicated in black. The Stark shift of the qubit scales as  $\Delta_q = \chi_{qr}|\xi_r|^2$ , and the cavity, the stark shift scales as  $\Delta_c = \chi_{cr}|\xi_r|^2$ . The extracted slopes from the fit is proportional to  $\chi_{qr}$  or  $\chi_{cr}$  for the qubit and cavity, respectively. We have repeated the experiment for several different detunings: 21 MHz (blue), 24 MHz (purple), and 29 MHz (red). **g**, We extract the cross-Kerr for each series of pump detunings using the ratio of the Stark shifts and an independently measured  $\chi_{rq}/2\pi = 1.8$  MHz. From the data, we infer the cross-Kerr between the cavity and readout to be  $\chi_{cr}/2\pi = 22.5(8)$  kHz. **h**, We show a schematic of the experimental system, consisting of two cavities that are coupled by a transmon. We apply a pump (noted in grey) on the readout.

### Measuring cross-Kerr via Stark shift

There are a few options to measure the cross-Kerr between two cavities by measuring the relative Stark shifts. We will take the case of measuring the cross-Kerr between a high-Q cavity (labeled  $c$ ) and a low-Q cavity (labeled  $r$ ), both of which are coupled to a qubit (labeled  $q$ ). The goal is to extract  $\chi_{cr}$ . An example of this experiment is detailed in [Figure 5.9](#). In this experiment we perform Stark shift spectroscopy on both the transmon and the high-coherence cavity. We apply a detuned pump on the readout resonator and vary the applied power,  $|\xi_r|^2$ , and detuning,  $\Delta_{\text{pump}}$  (we do note that the detuning also affects the pump power). For a given pump detuning, the stark shift on the transmon and cavity will scale with the power linearly:

$$\Delta_q = -\chi_{qr}|\xi_r|^2 \quad \Delta_c = -\chi_{cr}|\xi_r|^2 \quad (5.21)$$

For the same  $|\xi_r|^2$ , we can write a simple relation

$$\chi_{cr} = \frac{\Delta_c}{\Delta_q} \times \chi_{qr}. \quad (5.22)$$

If we can extract  $\chi_{qr}$  through an independent measurement, then we can directly compute the cavity-readout cross-Kerr.

Performing the experiment in this manner is intentional. One can consider a variant where the pump is applied to the high-coherence cavity. We would then be required to measure the stark shift on the low-Q readout cavity. Given that  $\chi_{cr}$  can be on the order of kHz, the detection of a frequency shift that is several orders of magnitude smaller than the linewidth of the readout (which is roughly MHz) is difficult and noisy. A far better choice is to perform stark-Shift spectroscopy on the high-Q mode where one can use selective pulses for high-resolution spectroscopy.

## 5.4 State preparation

The quality of any experiment is directly impacted by the the initial state preparation of the system into a known state. We will focus on implementing a protocol for system-wide ground

state preparation, leaving the preparation of other states to subsequent steps in a given protocol. More specific to our cQED systems, there are two broad reasons why we may consider an active approach for system preparation. First, the most straightforward approach to ground state preparation is to wait for a nominally cold system to thermalize to the ground state. As our coherence times continue to increase, this thermalization time has also increased, limiting our experimental repetition time to around 10 ms, an experimental cadence that has made some of our experiments rather tedious to perform. Rapid system reset is an attractive capability that would allow us to increase the experimental repetition rate. Second, the assumption that our system naturally thermalizes to the ground state is phenomenologically not the case. Given that we thermalize our quantum systems to roughly 20 mK, we would expect a negligible thermal excited-state population,  $P_{\text{excited}} < 10^{-6}$ . This is not the case in many cQED systems in the lab and across other cQED labs. We observe anomalous equilibrium population of our transmon qubits that range from 1 – 10%. Currently the sources for this additional equilibrium population is unknown, but several potential candidates include improper thermalization, additional input/output line noise, or mechanical vibrations. Clearly, further investigation is needed to understand how to effectively thermalize our devices to the mixing chamber of the dilution refrigerator.

Allowing the system to reach thermal equilibrium, therefore, is not a viable approach for effective ground state preparation. Instead active, measurement-based protocols for state preparation are used in our experiments for initializing the system-wide ground state [172, 189, 190]. These measurement-based protocols can be split into two categories, depending whether real-time feedback is available. If feedback is not available, then a postselected protocol can be used to choose only the cases when the ground state is successfully prepared. This protocol was used in [50]. On the other hand, if real-time feedback is available, then ground state preparation can be achieved through measurement-based cooling protocols. These protocols allow us to keep every experimental run as opposed to postselection which excises experimental runs where the system is not in the ground state. Feedback protocols also have the advantage that the system can be cooled using an adaptive protocol at a rate that is faster than the natural decay rate of the each mode in the system. This is especially useful when initializing long-lived cavity states

into the ground state, where we can achieve an experimental repetition time about an order of magnitude faster than postselected routines. We will detail a fairly general protocol for preparing the ground state for a transmon and storage cavity that was used for the teleported gate experiment.

Our feedback cooling protocol is diagrammed in [Figure 5.10](#). It consists of three parts: (1) reset the transmon qubits to  $|g\rangle$ , (2) empty the cavities to the vacuum state, (3) check that the transmon qubits are still in the ground state. In Step 1, the transmon qubit is first measured; if the result indicates that the qubit is in the excited state  $|e\rangle$ , then the controller dynamically applies a  $\pi$  pulse to flip the state down to  $|g\rangle$ . This process is repeated several times to build confidence that the transmon is in  $|g\rangle$ , continuing to the next step only if there have been three consecutive “g” measurement results. In our experiment, we cool both transmon qubits simultaneously, and so the signature for successful measurement is the joint ground state  $|gg\rangle$ . In Step 2, to cool the cavities, we apply simultaneous  $\pi$  pulses on the two transmon qubits that flips the each qubit when and only when their respective data qubit cavities are in the vacuum state  $|0\rangle$ . We use long  $\sigma = 1\mu s > 1/\chi$  to ensure that we are selective on the transmon resonance frequency when the cavity is in  $|0\rangle$ . This protocol also provides a check that the bus cavity is in the vacuum state as well. These selective pulses have a duration that is an appreciable fraction of transmon coherence times, and thus have a lower probability of correctly flipping the qubit ( $\sim 90\%$ ). To account for this diminished contrast, we repeat this process three times, only continuing when we have three consecutive successful measurements. If a failure occurs indicating that the data qubit cavities have some finite population, then we apply a four-wave mixing process (Q-switch) that rapidly evacuates population in the data qubit cavities into the readout resonator with a time constant of  $\tau \sim 100$  ns [\[138\]](#). We then return to Step 1. When we successfully complete Step 2, we then perform a feedback cooling check similar to Step 1 to ensure that the transmon qubits are in the ground state. This last step typically takes less than  $10\mu s$ , which is far shorter compared to the estimated heating rate of the data qubit cavities of  $10 - 100$  ms. This cooling protocol is efficient, enabling an experimental repetition period of around  $1$  ms, though with a faster Q-switch, the cavity evacuation could be made faster. Using

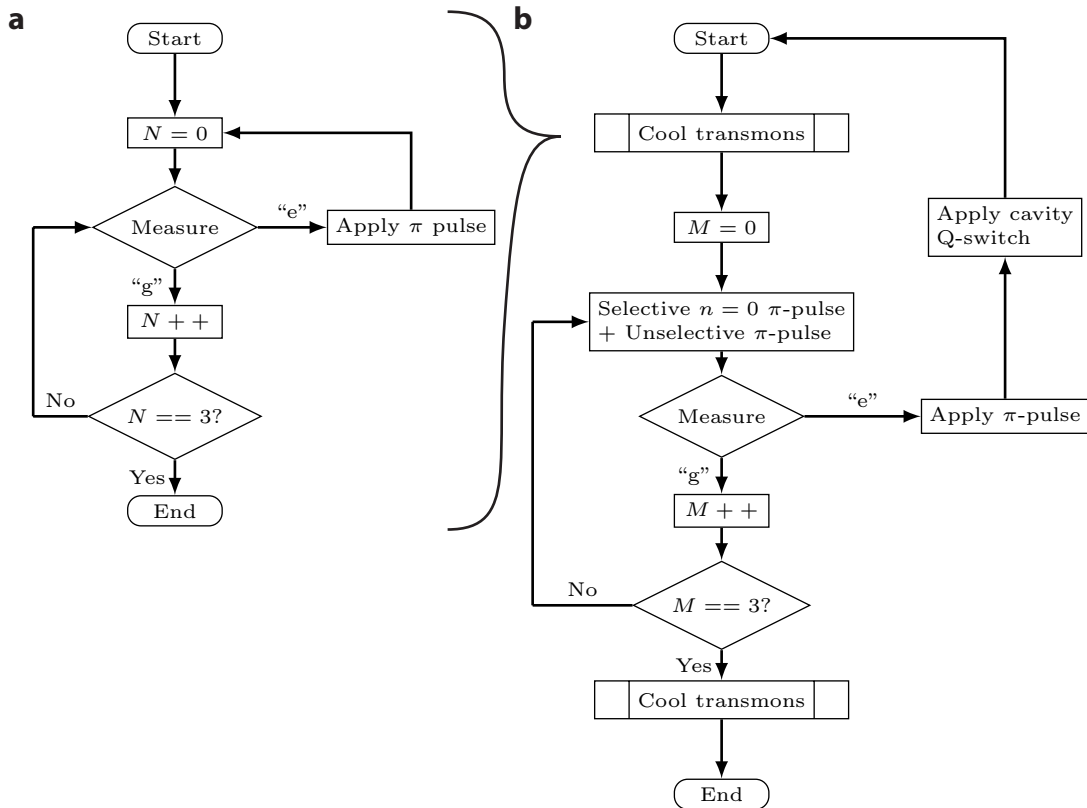


Figure 5.10 | **Feedback cooling sequences.** Measurement-based feedback sequences used for system-wide ground state preparation. **a** Cooling sequence used to reset both of the transmon (communication) qubits. To increase confidence in the ground state preparation, we require three consecutive measurements that both qubits are in the ground state before accepting the reset has succeeded. **b** Cooling sequence used to reset the entire system. The transmon cooling sequence is used as a subroutine for the full system reset. We apply a long selective  $\pi$  pulse on each transmon that flips the transmon qubit only when the data qubit and bus are both in the vacuum state. An additional unselective  $\pi$ -pulse so that the successful measurement outcome indicates that the transmon qubit is in the ground state.

this feedback cooling protocol, we are able to initialize our transmon and cavities in the ground state with  $> 99\%$  state fidelity.

## 5.5 Analysis methods

In this section, we discuss our methods for characterizing the states and processes that we produce in experiment. We first describe the general process for quantum state reconstruction through performing quantum state tomography (QST), casting it as a matrix inversion problem. This protocol is general, and we specialize it for performing tomography on (multi-)qubit systems as well as multi-level (e.g. cavity) systems. The result of this analysis is a procedure for state reconstruction that can readily be converted to an experimental recipe.

### 5.5.1 Quantum state tomography

#### Writing the tomography problem

Given a state that we create experimentally, how do we know what we have created? The experimental reconstruction of an unknown quantum state  $\hat{\rho}$  is achieved by performing *quantum state tomography*. The general idea is to perform a set of measurements on the state to extract properties (or correlations) of that state through repeated preparations and measurements. Only by performing such ensemble measurements can we determine the state that was experimentally produced.

The first step is to determine the set of measurements that are sufficient to determine the quantum state. One way to do this is to generate a set of measurement operators  $\{\hat{M}_k\}$  from which we extract a set of probabilities  $\pi_k = \text{Tr}[\hat{M}_k \cdot \hat{\rho}]$ . The set of measurement operators must form a complete basis in order to gain sufficient information about the state. In practice, we modify this approach. In most experimental platforms (including our cQED architecture), we are limited to a few measurement operators and instead rely on unitary operations to give us access to the necessary properties of the state. For this discussion, we define a POVM with the elements  $\{\hat{E}_m\}$  a tomographically-complete set of operations  $\{\hat{U}_r\}$  to act on the unknown state.

The probability of measuring outcome  $m$  when using operation  $r$  is then given by

$$\pi_{m,r} = \text{Tr} \left[ \hat{E}_m \hat{U}_r \hat{\rho} \hat{U}_r^\dagger \right], \quad (5.23)$$

The next step is to decompose the density matrix into a useful basis  $\{\hat{\rho}_a\}$ , generically written as

$$\hat{\rho} = \sum_a^{N_a} p_a \cdot \hat{\rho}_a \quad (5.24)$$

We want to determine the coefficients  $p_a$ , which we can combine into a single column vector,  $\vec{P}$  for convenience.

Applying this decomposition to [Equation 5.23](#) yields

$$\pi_{m,r} = \sum_a p_a \cdot \text{Tr} \left[ \hat{E}_m \hat{U}_r \hat{\rho}_a \hat{U}_r^\dagger \right] \longrightarrow \vec{M} = \mathbf{T} \cdot \vec{P}, \quad (5.25)$$

where  $\vec{M}$  measurement-outcome column-vector, and  $\vec{P}$  is the vector representation of the density operator, and  $\mathbf{T}$  is the linear tomography matrix that relates the quantum state to measurement outcomes. It is critical to note that the quantity  $\text{Tr} \left[ \hat{E}_m \hat{U}_r \hat{\rho}_a \hat{U}_r^\dagger \right]$  is known and therefore the whole  $\mathbf{T}$  matrix can be immediately generated.

Then, in principle, the quantum state can be simply reconstructed by  $\vec{P} = T^{-1} \vec{M}$ . Note that for  $N_m$  measurement settings and  $N_r$  tomography operations, the tomography matrix has dimension  $[N_m \cdot N_r, N_a]$ , and is in general a non-square matrix. In the following, we describe how we specify the measurements and tomography operations to generate the tomography matrix  $\mathbf{T}$  for various states on which we perform we perform state tomography. Given our formalism, this amounts to (1) determining an appropriate basis for  $\hat{\rho}$ , (2) choosing the tomography operators  $\{\hat{U}_r\}$ , and (3) determining the POVM  $\{\hat{E}_m\}$ . By specifying these three components of QST, we can directly compute the expected  $\mathbf{T}$ . After experimentally extracting the measurement outcomes  $\vec{M}$ , we can determine the density operator. Given this general formalism, we describe how we define these components for the particular cases of qubit state tomography and of cavity Wigner tomography.

### Qubit state tomography

For tomography on qubits, it is convenient to decompose the state in the Pauli basis

$$\hat{\rho} = \sum_a p_a \cdot \hat{\sigma}_a, \quad (5.26)$$

where  $\hat{\sigma}_a \in \{\hat{\sigma}_I, \hat{\sigma}_x, \hat{\sigma}_y, \hat{\sigma}_z\}^{\otimes N_q}$ . are the generalized Pauli operators for an  $N_q$ -qubit quantum state. This vector is often called the *Pauli vector* and encodes the same information as the density operator.

Now for the set of tomography operations. While four operations (rotations) per qubit are sufficient to perform tomography, we use an overcomplete set of rotations, with  $N_r = 6$ . For each qubit, we perform the set of rotations including identity,  $\pi/2$ -pulses, and  $\pi$ -pulses:

$$\{\hat{I}, \hat{R}_x(\pi), \hat{R}_x(\pm\frac{\pi}{2}), \hat{R}_y(\pm\frac{\pi}{2})\}. \quad (5.27)$$

This results in a total of  $N_r^{N_q} = 6^2 = 36$  tomography operations.

Now we need to specify the measurement operators. One common choice to implement is the joint projector,  $\hat{M}_{\text{joint}} = |0^{\otimes N_q}\rangle\langle 0^{\otimes N_q}|$ , which is the projector onto the ground state. This joint measurement is useful for performing tomography on a multi-qubit register with using a binary (two-valued) measurement apparatus (see examples, [50, 99]).

We will focus on another useful POVM, one that is used for performing tomography for the teleported gate experiment described in [chapter 6](#). We consider state tomography on a pair of qubit ( $N_q = 2$ ) where we have the capability to measure the  $\hat{Z}$  projection for each qubit independently, thus extracting two bits of information for each experiment. The POVM for such a measurement contains four elements,  $\{\hat{P}_{00}, \hat{P}_{01}, \hat{P}_{10}, \hat{P}_{11}\}$ , where each element is ideally the two-qubit projector  $\hat{P}_{jk} = |jk\rangle\langle jk|$ .

For this two-qubit example, the Pauli vector  $\vec{P}$  has dimension  $[4^{N_q} \times 1] \rightarrow [16 \times 1]$ . We define  $\vec{M}_{jk}$  as measurement outcomes when the  $jk$  POVM element is applied; this is a column vector with dimension  $[N_r^2 \times 1] \rightarrow [36 \times 1]$ . Finally for each POVM element, we define the

tomography matrix  $\mathbf{T}_{jk}$ , which has dimension  $[N_r^2 \times 4^{N_q}] \rightarrow [36 \times 16]$ . Now we can assemble the parts together to set up the matrix problem:

$$\begin{pmatrix} \vec{M}_{00} \\ \vec{M}_{01} \\ \vec{M}_{10} \\ \vec{M}_{11} \end{pmatrix} = \begin{pmatrix} \mathbf{T}_{00} \\ \mathbf{T}_{01} \\ \mathbf{T}_{10} \\ \mathbf{T}_{11} \end{pmatrix} \begin{pmatrix} p_0 \\ p_1 \\ \vdots \\ p_n \end{pmatrix}. \quad (5.28)$$

In practice, our experimentally realized measurement operators may deviate from the ideal operator; such bias can influence the quality of the state reconstruction. To address this, we can perform a calibration to directly extract the experimental measurement operator. We prepare each computational state  $|jk\rangle$ ,  $j, k \in \{0, 1\}$  and perform our two-bit measurement. The experimental POVM elements  $\{\hat{P}_{jk}\}$  are then given as

$$\hat{P}_{jk} = \begin{pmatrix} Pr(\text{"00"}| |jk\rangle) & & & \\ & Pr(\text{"01"}| |jk\rangle) & & \\ & & Pr(\text{"10"}| |jk\rangle) & \\ & & & Pr(\text{"11"}| |jk\rangle) \end{pmatrix}, \quad (5.29)$$

where  $Pr(\text{"ab"}| |jk\rangle)$  represents the probability that we measure outcome "ab" when preparing the state  $|jk\rangle$ . This analysis assumes that the measurement operator is only sensitive to  $\hat{Z}$  component of the qubit state, and from previous work performing quantum detector tomography [50], we find this a reasonable assumption.

### Cavity Wigner tomography

While our cavity states are naturally expressed in the Fock basis,

$$\hat{\rho} = \sum_{mn} p_{mn} |n\rangle\langle m|, \quad (5.30)$$

we have found a more experimentally natural approach to perform cavity state tomography by measuring the cavity Wigner function [71, 191] (for, more details in a cQED context, see [158, 159]). The Wigner function is a tomographically-complete description of a cavity state, and it is straightforward to measure in our cQED systems.

In this context, the most practical definition for the Wigner function is that it is a measurement of the photon-number parity at a point in the oscillator phase space:

$$W(\alpha) = \frac{2}{\pi} \text{Tr} \left[ \hat{D}_\alpha^\dagger \hat{\rho} \hat{D}_\alpha \hat{\Pi} \right], \quad (5.31)$$

where the parity operator is defined as  $\hat{\Pi} = \exp[-i\pi\hat{a}^\dagger\hat{a}]$ .

The protocol for performing Wigner tomography is that we perform many displacements  $\hat{D}_k \equiv \hat{D}(\beta_k)$ , and for each displacement we measure the value of the Wigner function. What remains is a prescription to relate the Wigner function to the density operator expressed in the Fock basis. We follow the steps detailed in [191] and describe an efficient algorithm to extract the Wigner function for a given  $\hat{\rho}$ . We decompose  $\hat{\rho}$  in the Fock-basis:  $\hat{\rho} = \sum_{m,n}^{N_c} \rho_{m,n} |m\rangle\langle n|$ , truncating at a maximum photon number  $N_c$ , and applying to Equation 5.31:

$$\begin{aligned} W_k &= \frac{2}{\pi} \sum_{m,n} \rho_{m,n} \text{Tr} \left[ |m\rangle\langle n| \hat{D}_k \hat{\Pi} \hat{D}_k^\dagger \right] \\ &= \frac{2}{\pi} \sum_{m,n} \rho_{m,n} \langle n| \hat{D}_k^\dagger \hat{\Pi} \hat{D}_k |m\rangle \\ &= \frac{2}{\pi} \sum_{m,n} \rho_{m,n} W_{m,n}(\beta_k) \end{aligned} \quad (5.32)$$

The matrix elements  $W_{m,n}(\beta)$  can be efficiently calculated using the relation [191]

$$\begin{aligned} W_{m,n}(\beta) &\equiv \langle n| \hat{D}(\beta) \hat{\Pi} \hat{D}(\beta)^\dagger |m\rangle \\ &= (-1)^m e^{-|\beta|^2} (2\beta)^{m-n} \sqrt{\frac{n}{m}} L_n^{(n-m)}(|\beta|), \end{aligned} \quad (5.33)$$

where  $L_n^{(m-n)}$  is a generalized Laguerre polynomial. Thus, the tomography matrix elements has elements  $\mathbf{T}_{[k,mn]} = W_{m,n}(\beta_k)$ .

### 5.5.2 Quantum process tomography

In addition to characterizing quantum states, we will also be interested to analyze the quality of quantum processes, for example, the unitary operations we perform on our qubits. Such analysis is important to validate that an experimentally implemented operation is faithful to the intended process. We aim to extract a process matrix that encodes how any input quantum state will be transformed by the operation. This is described by defining a superoperator  $\mathcal{E}(\cdot)$  that acts on the set of density operators  $\hat{\rho}$ .

$$\hat{\rho}_{\text{out}} = \mathcal{E}(\hat{\rho}_{\text{in}}) \quad (5.34)$$

We can describe the quantum process via a Krauss decomposition

$$\mathcal{E}(\hat{\rho}_{\text{in}}) = \sum_m \hat{K}_m \hat{\rho}_{\text{in}} \hat{K}_m^\dagger \quad (5.35)$$

We can express these Krauss operators  $\hat{K}_m$  in a fixed basis of operators  $\hat{K}_i$ , where  $\hat{K}_m = \sum_i k_i \hat{K}_i$ . For example, one common basis is simply the “elemental basis”:  $\hat{K}_{i=m,n} = |m\rangle\langle n|$ . For process tomography on qubits, the generalized  $N_q$ -qubit Pauli basis,  $\{\hat{\sigma}_m\}$  is also a common choice. Using this basis, we can write describe the quantum process according to the “ $\chi$ -matrix representation”:

$$\mathcal{E}(\hat{\rho}_{\text{in}}) = \sum_{mn} \chi_{mn} \hat{\sigma}_m \hat{\rho}_{\text{in}} \hat{\sigma}_n, \quad (5.36)$$

Another common process matrix representation is the Pauli-transfer representation [62], which describes a quantum process rather elegantly and intuitively. Given an input and output quantum state described in the Pauli basis,  $\hat{\rho}_{\text{in,out}} \rightarrow \vec{P}_{\text{in,out}}$ , we define a superoperator  $\mathcal{R}$  that transforms the input quantum state into the output quantum state

$$\vec{P}_{\text{out}} = \mathcal{R} \vec{P}_{\text{in}}. \quad (5.37)$$

The Pauli transfer matrix  $\mathcal{R}$  describes how the elements of the Pauli vector are changed under the action of this quantum process.

We can extract the Pauli transfer matrix quite easily. We prepare a tomographically complete set of input states (which we assume are perfect), enact the process, and perform quantum state tomography for each. Now we have a set of input states and output states. We assemble each state tomography setting as an additional column in [5.37](#) to generate an input and output matrix,  $\mathbf{P} = (\vec{P}_0 \dots \vec{P}_k)$ . Then extracting  $\mathcal{R} = \mathbf{P}_{\text{out}} \cdot \mathbf{P}_{\text{in}}^{-1}$ .

The key idea here is that quantum process tomography requires measuring quantum state tomography for many different states. Because quantum processes are linear (CPTP) maps, we can use these set of input states to predict what happens when we put them in superposition.

### 5.5.3 Reconstruction techniques

Though it is possible to directly calculate the density operator from inverting  $\mathbf{T}$ , noise and other experimental imperfections can result in unphysical reconstructed  $\hat{\rho}$ , possibly violating one or more of the requirements of non-negative eigenvalues, Hermiticity, or unit trace. We address this issue by utilizing a Maximum Likelihood Estimation (MLE) fit to the data. Given gaussian statistics, the probability to observe the experimental measurement outcomes  $\{f_m\}$  for a given  $\rho$  is given by

$$\mathcal{L}(\{f_m\}|\rho) = \frac{1}{\mathcal{N}} \prod_m \exp \left[ -\frac{[\pi_m(\rho) - f_m]^2}{2\sigma_m^2} \right], \quad (5.38)$$

where  $\pi_m$  is the expected value for a given experimental setting (given generally in [Equation 5.23](#)). We are interested in maximizing this probability by performing a search over all physical  $\rho$ . To simplify this problem, we consider the logarithm of [Equation 5.38](#) and assume the data are sampled from independent and identical distributions,  $\sigma_r^m \rightarrow \sigma$ . Given these we have the following residual sum-of-squares equation

$$\ln \mathcal{L}(\{f_m\}|\rho) = \sum_m [\pi_m(\rho) - f_m]^2, \quad (5.39)$$

where we have dropped the negative sign to emphasize that this function is strictly non-negative and convex. Our reconstruction minimizes the log-likelihood function, [Equation 5.39](#). In order to specify a physical  $\rho$ , we specify this problem as a constrained semi-definite program, using

CVXPY [192, 193] to solve the convex optimization problem

$$\begin{aligned} \rho_{MLE} = \operatorname{argmin}_{\rho} \quad & \ln \mathcal{L}(\{f_m\}|\rho) \\ \text{subject to} \quad & \rho \geq 0, \rho^\dagger = \rho, \operatorname{Tr} \rho = 1 \end{aligned} \tag{5.40}$$

# 6

## Teleportation of a quantum gate

In this chapter we present the experimental implementation of a CNOT gate between two logical qubits using a protocol known as gate teleportation. The original proposal for the teleported gate was described in 1999 [44], and we implement a modified version of the protocol from [55]. In contrast to more conventional approaches for implementing two-qubit gates, the teleported operation relies on shared entanglement and local operations and classical communication (LOCC), and our implementation utilizes real-time adaptive control to implement a gate that is deterministic.

We begin this chapter by describing a promising approach for constructing a quantum computer, the quantum modular architecture, for which the teleported gate is a critical component. We then introduce the teleported gate protocol in [section 6.2](#). The next three sections, [section 6.4](#), [section 6.3](#), and [section 6.5](#), describe the details of our implementation of the teleported gate; in particular, how we perform this gate between logical qubits encoded in the states of high-coherence superconducting cavities. In [section 6.6](#), we demonstrate all of the necessary components for the gate, and in [section 6.7](#), we describe the process for putting these components together for the teleported gate. Next, [section 6.8](#) provides the main experimental results that prove that we have implemented a teleported CNOT gate. We then provide a thorough analysis of the performance of the gate in [section 6.9](#) and [section 6.10](#), showing that for the most part, the teleported gate performs as we expect based on its constituent parts. Finally, in [section 6.11](#) we discuss reasonable modifications to our experiment to further its performance.

## 6.1 Modular quantum systems

The remarkable progress in quantum control and coherence across numerous physical implementations, including superconducting qubits, has led to exploration into the specific requirements and construction of a scalable quantum computer [86, 194]. The challenges of building a functional quantum computer abound. The first challenge in addressing the errors and imperfections in our physical qubits necessitate the implementation of quantum error correction. Several physical qubits will be composed to form a logical qubit, a two-dimensional subspace that takes advantage of symmetry properties and redundancy to allow the detection and correction of the dominant errors on physical qubits. Then we must demonstrate adequate quantum control over the logical qubits to achieve universal quantum computation by implementing both single qubit and multi-qubit operations on the encoded quantum information. In order to demonstrate fault-tolerant quantum computation, we will eventually have to ensure that the logical gates are compatible with the error-correction protocol and do not introduce new (uncorrectable) types of errors.

Alongside this development, one must consider how these qubits will be connected together. There are several distinct challenges that must be addressed in determining an appropriate quantum architecture. Residual interactions and crosstalk across the quantum device can introduce additional errors that will be difficult to mitigate. Achieving target design parameters (e.g. coherences and Hamiltonian terms) to a given specification across a large-scale device require a level of precision and reproducibility that become ever more demanding [86]. There are also additional practical questions of physically connecting the necessary input and outputs to physically control and measure the device [170]. Finally, once the device is constructed, validating and benchmarking this quantum device will require new, scalable techniques. These and other challenges motivate a careful approach that can manage the complexity of building a quantum computer.

One common theme that emerges in the development of almost any large-scale, complex system, both in nature and man-made, is the idea of modularity [195]. Such an approach relies on

splitting a system into more manageable subsystems, specialized to perform a single task. These subsystems are composed of individual controllable elements that can be separately designed and optimized. These subsystems are combined to perform more complex tasks, themselves becoming subsystems for ever more complex operations. Thus a modular approach lends itself as a hierarchical strategy to manage complex systems. Modularity as a design principle is pervasive. In nature, we can find examples of in biology [196, 197]; e.g. organelles that perform distinct functions in a cell or even organs that compose a human body. Starting from the early days of the digital computing era [198], modular design influenced nearly every stage of development<sup>1</sup>; today, nearly every computer system, from the personal computer to a supercomputer, is constructed according to some modular architecture.

### 6.1.1 The quantum modular architecture

We can apply this paradigm to the construction of a quantum computer, an compelling approach that we call the quantum modular architecture. The backbone of this architecture is the development of a quantum network [37] (Figure 6.1a). We envision a distributed network of modules, which are small quantum processors that can be well-controlled, execute quantum error correction, and easily produced. Each module is a small quantum processor that is composed of two separately optimized subsystems (Figure 6.1b): first, data qubits that function as quantum memories and are logically encoded to be error correctable; and second, communication qubits that mediate interactions between different modules through distributed entanglement. These modules are linked together through communication channels that are used to distribute entanglement throughout the network. This architecture uses distributed entanglement as a vital quantum resource for performing multi-qubit operations between qubits in different modules. Crucial to this architecture—and the topic of this experimental work—is the technique for performing these multi-qubit operations. These operations are enabled through teleportation and allow the data qubits to be well-isolated, offering a systematic path for minimizing crosstalk and

---

1. Indeed, von Neumann took great inspiration from biological systems when developing the formalism for fault-tolerant (classical) computing, noting that reliability of whole biological systems despite the unreliability of individual components [198]

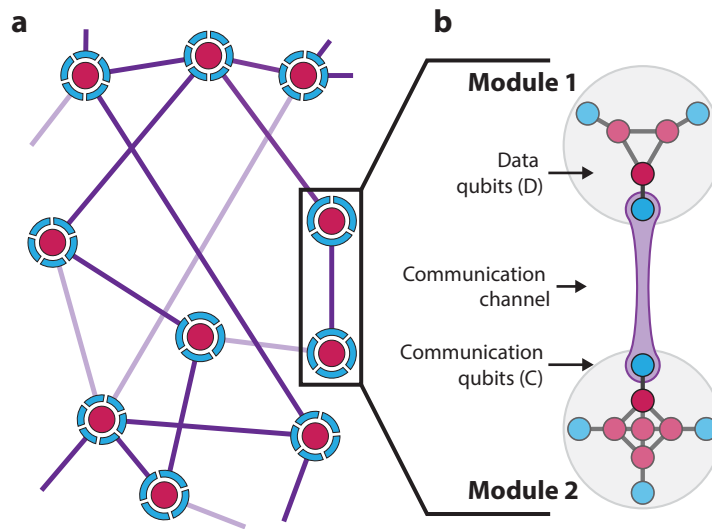


Figure 6.1 | **Constructing a quantum modular architecture.** **a**, In this network overview of the modular quantum architecture, modules are represented as nodes of a quantum network and are composed of: data qubit(s) (magenta) and communication qubit(s) (cyan). Coupling between modules is generated through potentially reconfigurable communication channels that may be enabled (dark purple line) or disabled (light purple line). **b**, Each module houses a small quantum processor capable of high fidelity operations among data qubits and communication qubits.

residual interactions across the entire network even while scaling the system. So far, elementary quantum networks have demonstrated the transmission of quantum information and the generation of entanglement between communication qubits [94, 142, 199, 200, 201]. It will be necessary to implement entangling operations between logical data qubits to perform universal quantum computation using these networks.

In the context of quantum computation, there are a number of distinct advantages when considering a quantum modular architecture.

1. It presents a *hierarchical approach* to assemble individual components of the quantum computer together.
2. Each module within the network will *individually testable*, which allows for very precise system-wide optimization and lowers the requirements for simultaneous optimization.
3. In principle, the modular architecture allows for *all-to-all connectivity*, which can have

significant benefits in reducing overhead for designing fault-tolerant quantum protocols.

4. The modular architecture results in a *general purpose* quantum device that can be reconfigured as necessary.
5. The modular architecture *improves isolation* among components within different modules and *reduces crosstalk* throughout the network even while scaling the size of the system.

The architecture as is currently envisioned takes advantage of many of the specific advantages of the 3D cQED platform. In our work, we demonstrate a teleported CNOT gate that is both deterministic and operates on logically-encoded data qubits. We implement two modules that each consist of a superconducting microwave cavity as the data qubit and a transmon as the communication qubit. Here, we generate entanglement between communication qubits via a local quantum bus that individually couples to each communication qubit. Our implementation can be adapted in the future to incorporate schemes for generating remote entanglement [142, 201, 202, 203], necessary for a scalable quantum modular architecture. Here, we use a hardware-efficient approach [21, 204] to logically encode each data qubit within the states of a long-lived cavity mode. Importantly, despite the added complexity of our logical encoding, we implement high-fidelity control over both data and communication qubit within each module. We use real-time adaptive control enabled by the use of our FPGA-based controller to implement a deterministic CNOT operation between to logical qubits.

## 6.2 Basics of gate teleportation

In this section, we walk through the basics of the teleported gate protocol. In contrast to conventional approaches that use direct interactions, the modular quantum architecture will require quantum teleportation to enact entangling operations [35, 44]. Teleportation has been used in a variety of platforms to transfer a quantum state between two remote systems [38, 39, 41, 205, 206, 207, 208, 209]. The teleportation of a two-qubit quantum gate expands on quantum state teleportation and describes the protocol for a unitary operation between two unknown

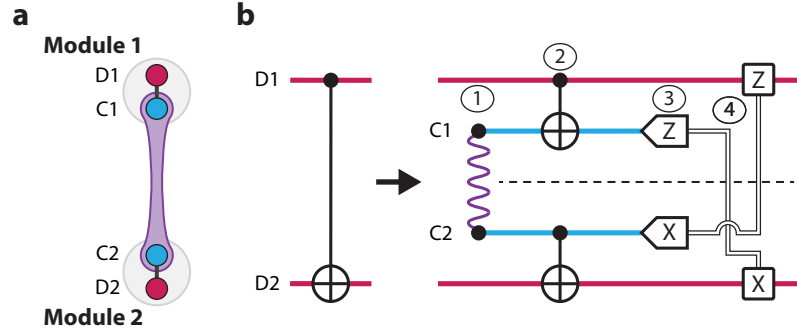


Figure 6.2 | **Quantum modules and the teleported CNOT circuit.** **a**, A module, at minimum, consists of a data qubit (D) and communication qubit (C). Gates between data qubits in different modules are accomplished through the implementation of a teleported gate. **b**, The teleported CNOT circuit requires (1) entanglement between C1 and C2 (purple meander), (2) local operations, (3) measurement of C1 and C2, and (4) classical communication (double lines) and feedforward operations.

states with a protocol that circumvents the necessity for direct interaction between the two data qubits [44, 55] (Figure 6.2). Instead, these teleportation-based protocols utilize a previously prepared entangled state of the communication qubits, local operations within each module, and classical communication between modules [44, 55, 210]. Previously, similar protocols have been demonstrated between two physical data qubits without real-time classical communication [211, 212, 213], where the desired operation is extracted probabilistically through postselection.

### 6.2.1 Walkthrough of the teleported gate

Here we walk-through the teleported CNOT gate in Figure 6.2b. To better distinguish the data from communication qubit, we will use numerical kets  $\{|0\rangle, |1\rangle\}$  for the data qubit and energy-level kets  $\{|g\rangle, |e\rangle\}$  for the communication qubit.

1. We initialize the system in a general two-qubit state for the data qubit  $|\psi_{12}\rangle$  and the anti-symmetric Bell state  $|\Psi^+\rangle = (|ge\rangle + |eg\rangle)/\sqrt{2}$  for the two communication qubits.

$$|\psi_{12}\rangle |\Psi^+\rangle = (a|00\rangle + b|01\rangle + c|10\rangle + d|11\rangle) \otimes \frac{1}{\sqrt{2}} (|ge\rangle + |eg\rangle), \quad (6.1)$$

where the data qubit state described by four complex probability amplitudes that obey the

normalization constraint,  $|a|^2 + |b|^2 + |c|^2 + |d|^2 = 1$ . For the remainder of the discussion we will incorporate the appropriate normalization into these coefficients.

2. First, we perform the control-module local CNOT, a data-qubit controlled, communication-qubit target gate:

$$\begin{aligned} |\psi\rangle_{\text{CNOT}_{\text{control}}} &= a |00ge\rangle + a |00eg\rangle + b |01ge\rangle + b |01eg\rangle \\ &\quad + c |10ee\rangle + c |10gg\rangle + d |11ee\rangle + d |11gg\rangle \end{aligned} \quad (6.2)$$

3. Second, we perform the target-module local CNOT, a communication-qubit controlled, data-qubit target gate:

$$\begin{aligned} |\psi\rangle_{\text{CNOT}_{\text{target}}} &= a |01ge\rangle + a |00eg\rangle + b |00ge\rangle + b |01eg\rangle \\ &\quad + c |11ee\rangle + c |10gg\rangle + d |10ee\rangle + d |11gg\rangle \end{aligned} \quad (6.3)$$

4. Next, in order to measure the  $\hat{X}$ -basis on the target-module communication-qubit, we perform a  $\pi/2$ -rotation on the target-module communication-qubit that takes  $|g\rangle \rightarrow |g\rangle + |e\rangle$  and  $|e\rangle \rightarrow |g\rangle - |e\rangle$ .

$$\begin{aligned} |\psi\rangle_{\text{CNOT}} &= a (+ |01gg\rangle - |01ge\rangle + |00eg\rangle + |00ee\rangle) \\ &\quad + b (+ |00gg\rangle - |00ge\rangle + |01eg\rangle + |01ee\rangle) \\ &\quad + c (+ |10gg\rangle + |10ge\rangle + |11eg\rangle - |11ee\rangle) \\ &\quad + d (+ |11gg\rangle + |11ge\rangle + |10eg\rangle - |10ee\rangle) \end{aligned} \quad (6.4)$$

Now we measure the communication qubits, and we write the outcomes  $|g\rangle \rightarrow "0"$  and

$|e\rangle \rightarrow \text{“1”}$ .

$$\begin{aligned}
 \text{“00”} : |\psi_{00}\rangle &= a |01\rangle + b |00\rangle + c |10\rangle + d |11\rangle \\
 \text{“01”} : |\psi_{01}\rangle &= -a |01\rangle + b |00\rangle + c |10\rangle + d |11\rangle \\
 \text{“10”} : |\psi_{10}\rangle &= a |00\rangle + b |01\rangle + c |11\rangle + d |10\rangle \\
 \text{“11”} : |\psi_{11}\rangle &= a |00\rangle + b |01\rangle - c |11\rangle - d |10\rangle
 \end{aligned} \tag{6.5}$$

And the feedforward single-qubit operations bring the states to

$$\begin{aligned}
 \text{“00”} : \hat{I}\hat{X} |\psi_{00}\rangle &= a |00\rangle + b |01\rangle + c |11\rangle + d |10\rangle = \hat{U}_{\text{CNOT}} |\psi\rangle \\
 \text{“01”} : \hat{Z}\hat{X} |\psi_{01}\rangle &= \hat{U}_{\text{CNOT}} |\psi\rangle \\
 \text{“10”} : \hat{I}\hat{I} |\psi_{10}\rangle &= \hat{U}_{\text{CNOT}} |\psi\rangle \\
 \text{“11”} : \hat{Z}\hat{I} |\psi_{11}\rangle &= \hat{U}_{\text{CNOT}} |\psi\rangle
 \end{aligned} \tag{6.6}$$

And each of these implements a CNOT operation.

## 6.3 Logical qubits

Executing quantum operations on error-protected logical qubits is a critical milestone in the development of fault-tolerant quantum computation [86]. Logical qubits have been used to experimentally demonstrate quantum error detection and correction [21, 88, 214, 215, 216, 217, 218, 219] as well as single logical-qubit operations [185, 220, 221]; however, the extension to multi-qubit operations remains a much-needed capability for universal quantum computation. The central challenge in implementing these operations—and also for scaling up quantum systems—is introducing the couplings necessary for the desired operation while minimizing the unwanted interactions to preserve individual coherence and control.

Implementing operations on logical qubits is more demanding and complex than the equivalent operation using physical qubits and places additional requirements on all aspects of these systems. This added complexity stems from the redundant encoding that is a prerequisite for quantum error correction, and first adds an overhead in logical qubit error rate. Logical qubits

are typically composed of multiple physical qubits (or multiple levels of an oscillator, in our case), and there will be additional challenges to suppress classical and quantum crosstalk sufficiently to perform accurate manipulations within an encoded subspace. Furthermore, logical qubit operations are typically constructed from several distinct elements; while each may individually be faithful to its intended operation, it will be necessary to experimentally verify that the compiled operation does not introduce unexpected errors. These considerations motivate efforts—such as our teleported gate—to construct and validate logical quantum systems both to advance computational capabilities and to reveal experimental nonidealities.

### 6.3.1 Binomial logical encoding

The high-dimensional cavity modes that define our data qubits allow for a wide range of encodings. For our demonstration of the teleported CNOT, we have chosen to logically-encode each of the data qubits as one of the recently-developed bosonic binomial quantum codes [204],

$$|0_L\rangle = |2\rangle, \quad |1_L\rangle = \frac{1}{\sqrt{2}}(|0\rangle + |4\rangle), \quad (6.7)$$

specified in the photon-number basis of the cavity. The two basis states have even photon-number parity. When this logical qubit functions as a quantum memory, the dominant error channel for this system is single-photon loss, an error channel that transforms the basis states into states of odd photon-number parity. Importantly, in this encoding the quantum information is still preserved in this error subspace, such that photon-number parity measurements—which can be implemented with high fidelity in our system [21]—can be used in an error-correction protocol to detect and correct single-photon loss events in the cavity. To illustrate the logical Bloch sphere, we prepared the six cardinal states and characterized each state by measuring the Wigner function of the data qubit (Figure 6.3). The Wigner function provides not only a strikingly visual representation of the logical qubit state, but also completely specifies the underlying cavity state, a capability analogous to full state tomography of the constituent physical qubits that compose a logical qubit.

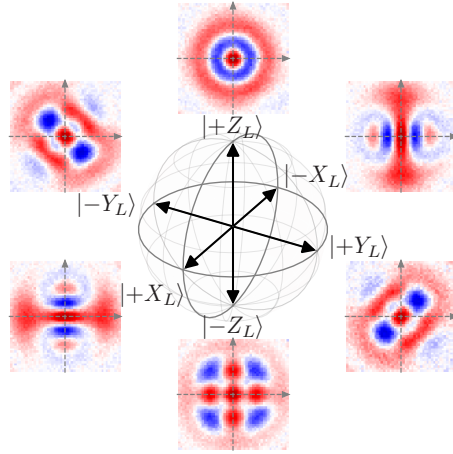


Figure 6.3 | **Logical Bloch sphere for the binomial code encoding.** The data qubit is logically encoded in the binomial code basis and the Wigner function for each of the six cardinal states  $\{\pm\hat{Z}_L, \pm\hat{X}_L, \pm\hat{Y}_L\}$  is shown.

### 6.3.2 Fock encoding

We also demonstrate the teleported gate using a simple Fock encoding, with basis states  $|0\rangle$  and  $|1\rangle$ , utilizing the lowest two energy levels of the cavity to specify the data qubit. We note that this basis is not a logical-encoding according to our definition as it does not allow for quantum error correction; however, by specifying the data qubits in this simple basis, we can extract an upper-bound to the performance of the teleported gate using our current device.

## 6.4 Physical implementation

### 6.4.1 Device implementation

Here we describe the design of the device used for the teleported gate experiment. Our system consists of three 3D cavities, two Y-shaped transmon superconducting qubits, and two Purcell-filtered readout resonator. Our device (Figure 6.4) is constructed from a single machined block of high-purity (4N) Aluminum that physically forms the three 3D cavities as well as the package that houses sapphire chips on which the transmon qubits and quasi-planar readout resonators are

defined. Each cavity is constructed as a 3D  $\lambda/4$ -transmission line resonator, with a cylindrical outer conductor of diameter 9.5 mm and stub with inner conductor of diameter 3.2 mm. The bottom of the stub transitions into the Al block, thus electrically connecting to the outer conductor and establishing a ground termination. The other end is terminated as an open connection and transforms into a vacuum cylindrical waveguide. These two boundary conditions establish the  $\lambda/4$  resonant structure for the cavity mode. The stub lengths dictate the resonance frequency, and the two data qubit cavities have center pin lengths of 12.7 mm and 13.2 mm, while the bus cavity has a stub length of 11.7 mm. The far-end of all three cylindrical waveguides are closed off with a separate Al cap. This waveguide, physically necessary for machining the cavity stub, also serves to isolate the cavity electromagnetic mode from a potentially lossy seam formed by the opening at the top of the waveguide. Based on the cutoff frequency of 20 GHz, the seam energy participation in the cavity mode is  $< 10^{-8}$ . For the transmon qubits to gain access to the cavities, tunnels are opened up in the Al block perpendicular to the axial axis of the cavities. We position two such tunnels so that each individually intersects with one data qubit cavity and the bus cavity. The tunnels are located at a height near the top of the stubs to maximize the electric field coupling between the cavity and transmon qubit. Into these tunnels, we insert a sapphire chip onto which we have lithographically printed the transmon qubit and readout resonator. The entire machined Al package is chemically etched around  $100\ \mu\text{m}$  to improve the surface quality by removing machining damage [161].

On the sapphire chip, the transmon qubit is designed with Y-shaped antenna pads [164] to couple to three distinct modes: the cavity that encodes the data qubit, the bus, and the readout resonator. When the chip is inserted in the tunnel, the two arms of the antenna protrude into the space of data qubit and bus cavity. This enables capacitive coupling between each cavity and the transmon qubit (and to a lesser degree, mode mixing between the two 3D cavities). On the opposite side of these antenna pads, we print two strips of Al that form the centerpin of quasi-planar  $\lambda/2$  stripline resonators. One functions as the readout resonator mode and the other functions as a Purcell filter [150] to protect the transmon qubit and 3D cavities from spontaneous emission into the readout resonator. The striplines are constructed with meanders to decrease the

module	mode	Energy relaxation time, $\tau_{1ph}$ or $T_1$ ( $\mu\text{s}$ )	Ramsey dephasing time, $T_2^R$ ( $\mu\text{s}$ )	Echo dephasing time, $T_2^E$ ( $\mu\text{s}$ )
1	data	1150	390	–
	communication	65 – 69	11 – 14	18 – 20
	readout	0.1	–	–
2	data	1100	390	–
	communication	67 – 77	18 – 22	22 – 24
	readout	0.1	–	–
	bus	230	–	–

Table 6.1 | **System coherences.**

physical footprint of each resonator while maintaining a particular mode frequency. The readout resonator (and filter mode) is strongly coupled to a  $50\Omega$  transmission line for fast readout of the transmon qubit state. We use a standard electron-beam lithography process to simultaneously define the transmon qubits and stripline resonators. Our transmon qubit Josephson junctions are defined with the Bridge-free shadow mask process [111]. Each chip is diced from a wafer of  $430\mu\text{m}$  c-plane sapphire to dimensions of  $5.5\text{ mm} \times 27.5\text{ mm}$ .

### 6.4.2 System characterization

The system of nine modes can be split up into two categories: nearly-linear harmonic oscillator modes (describing the cavities, resonators, and filters) and anharmonic bosonic modes (describing the transmon qubits). In this work we utilize the lowest two levels of the transmon qubits. A detailed table of coherences in our experiment is provided in [Table 6.1](#).

To understand our system Hamiltonian we first define a few primitives. We have removed the factor of  $\hbar$  in the Hamiltonian for clarity.

- Kerr oscillator Hamiltonian, which describes an anharmonic oscillator

$$\mathcal{H}_O(\hat{a}) = \omega_a \hat{a}^\dagger \hat{a} - \frac{K_a}{2} \hat{a}^\dagger \hat{a}^\dagger \hat{a} \hat{a}, \quad (6.8)$$

where  $\omega_a$  represents the resonance frequency and  $K_a$  is the self-Kerr, or anharmonicity, for mode  $\hat{a}$ .

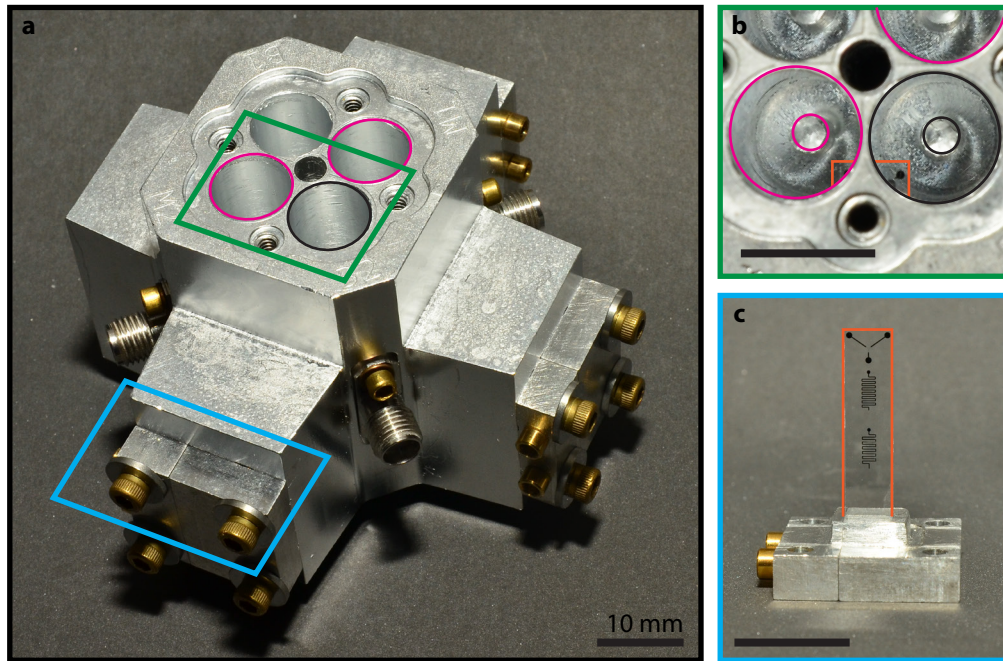


Figure 6.4 | **Overview of teleported gate device.** **a** Photograph of full device assembly. The machined Al package contains four coaxial  $\lambda/4$  3D cavities, three of which are used in this work. The cavities that serve as data qubits and bus are outlined in pink and black, respectively. A detailed photograph of the cavities is shown in **b**. Two clamps anchor each sapphire chip, one is highlighted in blue and is detailed in **c**. The visible connectors are input ports for each cavity; the input/output ports for the transmon and readout resonators are on the underside of the device and thus not visible. **b** Top-down photograph of cavities. We illustrate the three cavities using the same color scheme in **a**; the inner circle represents the inner conductor that defines the cavity mode. The orange outline shows the sapphire chip inserted into the device package. Also visible are the antenna pads of the transmon that enable coupling to each cavity. **c** Photograph of sapphire chip on which the transmon and readout resonators are fabricated. The sapphire chip is outlined in orange and contains several elements: from the top of the figure moving down, the Y-shaped transmon qubit, the readout resonator, and the Purcell filter.

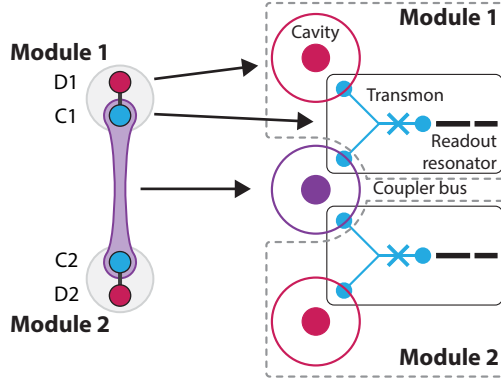


Figure 6.5 | **Experimental realization of the teleported gate.** Each module consists of a data qubit defined as a coaxial  $\lambda/4$  3D cavity (magenta), a communication qubit defined as a Y-shaped transmon qubit (cyan), and a Purcell-filtered, quasi-planar,  $\lambda/2$  stripline readout resonator (black). In this experiment, the two modules are linked by an additional mode realized as a coaxial  $\lambda/4$  3D cavity (purple) that serves as a bus mode.

- Dispersive coupling Hamiltonian, which describes the dispersive interaction between two modes  $\hat{a}$  and  $\hat{b}$ :

$$\mathcal{H}_{\text{disp}}(\hat{a}, \hat{b}) = \underbrace{-\chi_{ab}\hat{a}^\dagger\hat{a}\hat{b}^\dagger\hat{b}}_{\mathcal{H}_{\text{disp}}^{(0)}(\hat{a}, \hat{b})} + \underbrace{\chi'_{ab}(\hat{a}^\dagger)^2(\hat{a})^2\hat{b}^\dagger\hat{b}}_{\mathcal{H}_{\text{disp}}^{(1)}(\hat{a}, \hat{b})}, \quad (6.9)$$

where  $\chi_{ab}$  is the dispersive interaction between modes  $a$  and  $b$  and  $\chi'_{ab}$  is the nonlinear dispersive interaction (i.e. an interaction dependent on the number of photons in each mode). Typically we take  $\hat{b}$  as the transmon mode, and since we will operate in the two-level subspace, we can safely ignore the other nonlinear term,  $\hat{a}^\dagger\hat{a}(\hat{b}^\dagger)^2(\hat{b})^2$ , can be ignored. Otherwise, we will be explicit if we only consider one of the dispersive terms.

We can then write the Hamiltonian for each module, which includes one 3D cavity with operator,  $\hat{c}$ ; one transmon qubit,  $\hat{q}$ ; and one readout resonator,  $\hat{r}$  (the filter resonator is not included as it is never directly populated and thus, does not participate in the Hamiltonian dynamics of the system).

$$\mathcal{H}_{\text{module}}(\hat{c}, \hat{q}, \hat{r}) = \mathcal{H}_O(\hat{c}) + \mathcal{H}_O(\hat{q}) + \mathcal{H}_O(\hat{r}) + \mathcal{H}_{\text{disp}}(\hat{c}, \hat{q}) + \mathcal{H}_{\text{disp}}(\hat{r}, \hat{q}) + \mathcal{H}_{\text{disp}}^{(0)}(\hat{c}, \hat{r}). \quad (6.10)$$

The relevant parameters includes the mode frequencies ( $\omega_c, \omega_q, \omega_r$ ); the self-Kerrs ( $K_c, K_q, K_r$ ); the dispersive interaction between the readout resonator and transmon ( $\chi_{rq}$  and  $\chi'_{rq}$ ); and finally, the cross-Kerr between the cavity and readout resonator ( $\chi_{cr}$ ). In practice, we neglect a few terms: first, the self-Kerr of readout resonator,  $K_r$ , which typically causes a small perturbation on the readout resonator response during transmon measurement; and second, the nonlinear interaction term between cavity and readout resonator,  $\chi'_{cr}$ , is small as both modes are nearly-linear harmonic oscillators and can be ignored. Hamiltonian parameters for each module are tabulated in [Table 6.2](#).

Next, we group the main terms that participate in the dynamics for entangling the two transmon (communication) qubits: the two transmon qubits ( $\hat{q}_1$  and  $\hat{q}_2$ ) and bus cavity ( $\hat{b}$ ). This Hamiltonian is described as follows:

$$\mathcal{H}_{\text{coupling}}(\hat{q}_1, \hat{q}_2, \hat{b}) = \mathcal{H}_O(\hat{q}_1) + \mathcal{H}_O(\hat{q}_2) + \mathcal{H}_O(\hat{b}) + \mathcal{H}_{\text{disp}}(\hat{b}, \hat{q}_1) + \mathcal{H}_{\text{disp}}(\hat{b}, \hat{q}_2) + \mathcal{H}_{\text{disp}}(\hat{q}_1, \hat{q}_2), \quad (6.11)$$

The relevant parameters includes the mode frequencies ( $\omega_{q_1}, \omega_{q_2}, \omega_b$ ) and the self-Kerrs ( $K_{q_1}, K_{q_2}, K_r$ ) as well as the interaction terms between the bus and each qubit,  $\chi_{bq_{1,2}}$  and  $\chi'_{bq_{1,2}}$ . Importantly, we also include the direct interaction between the two transmon qubits,  $\chi_{q_1q_2}$ . This term, as we will see, is the dominant residual coupling between the two modules. As we operate in the two-level subspace of both transmon qubits, the nonlinear interaction terms,  $\chi'_{q_{1,2}q_{2,1}}$ , do not play a role in the dynamics of our experiment. Hamiltonian parameters for this subsystem are tabulated in [Table 6.2](#).

### 6.4.3 Assessing independence of the modules

A defining characteristic of modular architectures—which makes it advantageous for scaling quantum systems—is that data qubits are housed in separate modules to ensure that residual interactions can be made vanishingly small. Here, the modules in our experiment are coupled via local means, and we assess the validity of treating them separately by discussing the magnitude of residual interactions in our system. Our implementation requires purely local (capacitive) coupling

Subsystem and mode	Mode frequency	Mode coupling, $\chi_{ij}/(2\pi)$ (MHz)		
		Data	Comm.	Readout
1 - data	5123.6	$1.1 \times 10^{-3}$	$0.573 + 0.00061\hat{n}$	$\leq 10^{-3}$
2 - comm.	4387.7	—	131.2	2.7
1 - readout	7720.0	—	—	—
2 - data	5275.0	$1.8 \times 10^{-3}$	$0.843 + 0.0014\hat{n}$	$\leq 10^{-3}$
2 - comm.	4559.2	—	123.2	2.8
2 - readout	7735.4	—	—	—
Subsystem and mode	Mode frequency	Bus	1 - comm.	2 - comm.
Coupler - bus cavity	5692.8	$3 \times 10^{-4}$	$0.319 + 0.001\hat{n}$	$0.455 + 0.001\hat{n}$
1 - comm.	4387.7	—	—	0.019
2 - comm.	4559.2	—	—	—

Table 6.2 | Measured Hamiltonian parameters.

to build the Hamiltonians discussed above and, if uncontrolled, some of these interactions can extend to disparate parts of the system.

The dominant residual interaction in our system is  $\chi_{q_1q_2}$ , the direct coupling between the two transmon qubits. This term arises from a combination of two contributions [148]: a direct dipole-like coupling and a cavity-mediated interaction. In our system, this term arises primarily from the mutual interaction with the cavity mode. This term remains a perturbation on our experiment for three reasons: first, the magnitude of this interaction is over an order of magnitude smaller than other relevant terms in the Hamiltonian; second, we choose the anti-symmetric, single-excitation Bell pair for the communication (transmon) qubits where this term does not statically participate; third, we design our local operations to be insensitive to a small frequency transmon qubit frequency shift.

Next, we consider the cross-Kerr interactions between the data qubit and the bus:  $\chi_{c;b}$ . Experimentally, we have bounded this term to be less than a few kHz via Stark shift measurements, consistent with a fourth order approximation, where we estimate the interaction to be,  $\chi_{cb} \approx \chi_{qb}\chi_{qc}/(2K_q) \approx 1\text{kHz}$ , where mode  $q$  represents the transmon qubit that couples to both data qubit and bus. This interaction term is never directly involved during the teleported gate protocol. First, the bus cavity only is manipulated during the communication qubit Bell state generation step and otherwise it is left in the vacuum state where this term does not contribute

to any system dynamics. Even during the Bell state generation, the bus is driven off-resonantly and the bus is never directly populated.

The final residual interaction is the direct coupling between the two data qubits  $\chi_{c_1 c_2}$ . This term describes the rate at which the two cavities naturally entangle and is a metric with which we compare the interaction time for our teleported gate. We have not extracted statistically significant measurements of this residual interaction term. Indeed, from the simulated Hamiltonian from black box quantization, we roughly expect couplings on the order of 1 – 10 Hz, an immeasurably small quantity in our system compared to all other interaction strengths. Indeed, this bound on the coupling rate is at least an order of magnitude smaller than the data qubit decay rate,  $\kappa/2\pi \approx 160$  Hz. Given this analysis, we conclude that for the purpose of our work, the two data qubits are non-interacting despite the local nature of our device package.

Though these simplifications are reasonable, we note that in a future implementation with remote logical qubit modules, these residual interactions will be completely obviated.

## 6.5 Implementation of the teleported CNOT protocol

Here, we provide a more detailed description of our implementation of the teleported CNOT gate. In [Figure 6.6](#), we show a detailed circuit representation of the teleported CNOT protocol, and in [Figure 6.7](#), we illustrate the timing for the entire protocol.

Our experiment begins with a system-wide ground state preparation using a measurement-based feedback protocol previously discussed in [section 5.4](#). After all components of the system are initialized in the ground state, a chosen initial state is encoded onto the data qubits ([section 6.3](#)). This is accomplished by generating the initial state in the communication qubits and then applying an encoding optimal control pulse that transfers this state onto the logical basis of the data qubits ([subsection 6.6.2](#)). After this encoding step, the communication qubits end in the ground state ready for further use. Next, we generate an entangled pair between the communication qubits, and during this operation, the data qubits store the encoded quantum information ([subsection 6.6.1](#)). Next, we perform the requisite local operations between the

data and communication qubits by applying optimal control pulses within each module (subsection 6.7.2). Next, both communication qubits are measured in the appropriate basis ( $\hat{Z}$  and  $\hat{X}$ ) and subsequently reset to the ground state for reuse (subsection 6.6.3). The measurement outcomes are distributed and the appropriate feedforward operations are applied to implement a deterministic operation, one that is independent of the measurement outcome. Finally, we analyze the output state by performing Wigner tomography or logical quantum state tomography (QST) on the data qubits (section 5.5). Our implementation of Wigner tomography matches the sequences used in [158], requiring a Ramsey sequence that maps the photon number parity of the cavity state onto the state of the communication qubit. Our implementation of logical QST requires a decoding step, where we use an optimal control pulse to map the encoded data qubit state onto the communication qubits. We then proceed with standard QST by performing the required rotations and measurements directly on the communication qubit.

## 6.6 Assembling the teleported gate

### 6.6.1 Generating communication qubit Bell pair

The teleported CNOT starts with the generation of entanglement in the communication qubits to create a communication channel between the two modules (Step 1 in Figure 6.2b). In our implementation, we use the Bell state  $|\Psi^+\rangle = (|ge\rangle + |eg\rangle) / \sqrt{2}$ , though any chosen maximally-entangled state is acceptable, requiring only small modifications to later steps of the protocol. The state is generated by performing a resonator-induced phase (RIP) gate [222] on the bus and single-qubit rotations on the communication qubits. The Bell state generation occurs while the data qubits store quantum information; the static dispersive interaction, if not accounted for, will naturally entangle the data and communication qubits. Because it is necessary for the two qubits within each module to be disentangled at the end of this step, we modify our Bell pair generation protocol and implement a refocused RIP sequence [222] to echo away this unwanted interaction independent of the data qubit encoding scheme. An important consequence of the Bell state generation protocol is that the dispersive interaction induces a known, deterministic

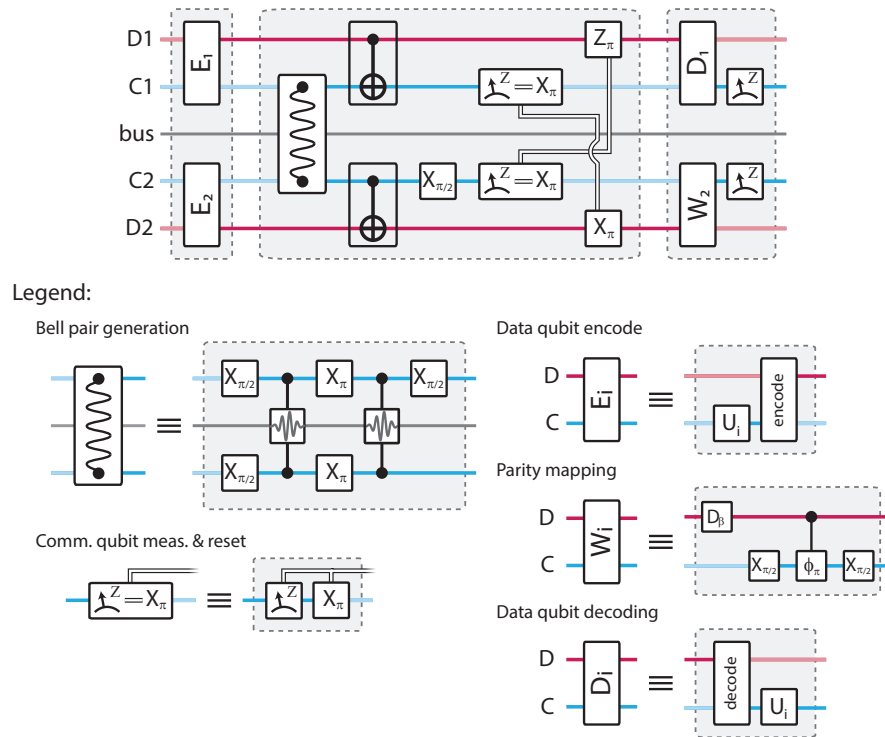


Figure 6.6 | **Detailed circuit diagram for the teleported CNOT gate protocol.** Top: Pulse sequence for an example experiment. Bottom: Legend for specific circuit blocks. In the first panel, we show our sequence for encoding quantum information onto the data qubit. In the second panel, we illustrate our implementation of the teleported CNOT gate. We show the pulse sequence used to implement the communication qubit Bell state generation. For the communication qubit measurements, we apply a  $\pi/2$  rotation on C2 in order to measure  $\hat{X}$ . After the measurement we also perform a measurement-based reset of both C1 and C2 before performing feedforward operations on the data qubits. In the third panel, we detail two possible sequences for extracting the data qubit state. For module 1, we perform logical tomography on the data qubits by decoding the data qubit onto the communication qubit and performing the appropriate tomography rotations on the communication qubit. For module 2, we perform Wigner tomography by performing a parity mapping sequence on the communication qubit.

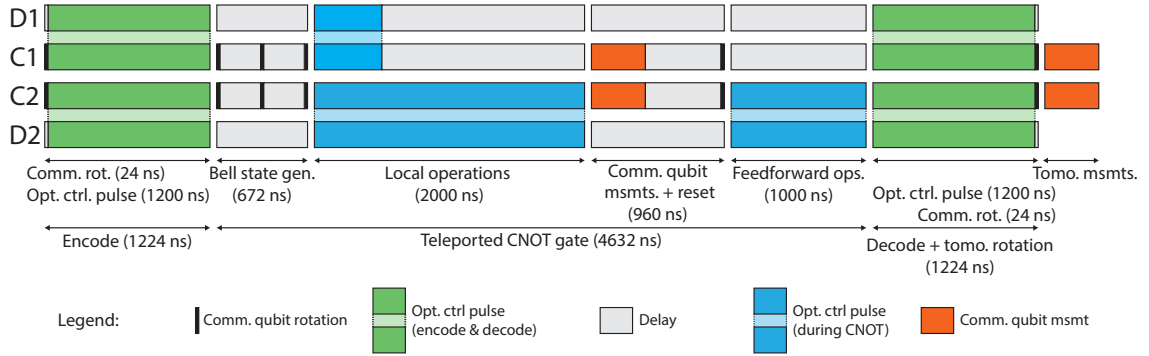


Figure 6.7 | **Teleported CNOT gate timing diagram.** The teleported CNOT is illustrated taking the relative timing of each element into account. The diagram is color-coded with the following designations: single communication qubit rotations in black; encode and decode (optimal control) operations in green; the teleported CNOT local operations (also optimal control) in blue; and the measurements in orange. This presentation provides a visual representation of the relative durations for each part of the protocol. The teleported CNOT takes in total around 4.6  $\mu$ s.

reference frame shift on each of the data qubits; these are accounted for in subsequent steps of the teleported gate protocol. Using this modified sequence, we have generated a Bell pair between the communication qubits in  $\sim 680$  ns with state fidelity of  $(97 \pm 1)\%$  as determined from quantum state tomography ([subsection 6.6.1](#)).

### Additional details

The teleported CNOT protocol begins with the entanglement of the two communication qubits; in this section, we provide additional details on our implementation of this sequence. As discussed in the Main Text, we use a resonator induced phase (RIP) gate to generate a Bell pair between the two communication qubits [222, 223]. We apply an off-resonant, shaped drive  $\epsilon(t)$  with a carrier frequency detuned from the bus resonance frequency by  $\Delta_0 \approx 20$  MHz which induces a qubit-state dependent Stark shift on the bus. This drive induces a displacement of the bus oscillator:  $\xi_\Delta = -\frac{i\epsilon_d}{2(i\Delta + \kappa/2)}$ . The size of this displacement is dependent on the detuning between the drive frequency and the qubit-state dependent cavity frequency; within the two-transmon manifold  $|ij\rangle$ , where  $i, j \in \{g, e\}$ , the corresponding detunings given as  $\Delta_{ij} = \Delta_0 + \chi_{ij}$ , where  $\chi_{ij}$  corresponds to the total dispersive shift for state  $|ij\rangle$ . In our experiment, we operate in the low-loss regime

where  $\kappa \ll \Delta$  so that  $\xi_\Delta \approx -\frac{\epsilon_d}{2\Delta}$ . This bus displacement gives rise to a Stark shift of the transmon frequency by an amount that is dependent nonlinearly with the total dispersive shift,  $\delta_{ij} = \chi_{ij}|\xi_{ij}|^2$ . This Stark shift generates a transmon-state dependent phase:  $\phi_{ij} = \int \delta_{ij}(t)dt$ . The quantity that describes the magnitude of entanglement is  $\phi_{ent} = \phi_{ee} - \phi_{eg} - \phi_{ge} - \phi_{gg}$ , which extracts the non-separable two-qubit phase contribution from the single qubit phase contributions. For approximately equal  $\chi$ , we can simplify this expression  $\phi_{ent} = \frac{\chi^2}{2\Delta^3} \int |\epsilon_d(t)|^2 dt$ . We detail our tuneup protocol in [Figure 6.8](#).

In our experiment, we utilize a RIP pulse of length  $T = 300$  ns of the form:  $\epsilon(t) = A[\cos(\pi \cos(\pi t/T)) + 1]$  in order to minimize residual photon population left in the bus cavity at the end of the pulse [\[222\]](#). We implement a refocused-RIP sequence that includes two RIP pulses that sandwich a  $\pi$ -pulse; this sequence is utilized to “echo” away the always-on dispersive interaction between the communication-qubit (transmon) and its data-qubit (cavity). We are able to achieve an entangling phase of  $\phi_{ent} = \pi$  in 672 ns, and combined with single communication qubit rotations, create the Bell state  $|\Phi^+\rangle = (|ge\rangle + |eg\rangle)/\sqrt{2}$  with state fidelity of  $(97 \pm 1)\%$ . Our error bar is a average of several experiments and roughly accounts for systematic errors in our experiment; statistical errors are smaller in this experiment,  $<1\%$ , as extracted from a bootstrap analysis. In [Figure 6.9a](#) and [Figure 6.9b](#), we show the experimentally measured two qubit Bell state.

### 6.6.2 Implementing local operations

Next, local operations performed within each module entangle the data and communication qubits (Step 2 in [Figure 6.2b](#)). Our local operations are implemented using optimal control techniques which enable universal quantum control between the data and communication qubits [\[185\]](#) ([subsection 5.2.3](#)). We generate all of our local operations with pulse lengths between 1  $\mu$ s and 2  $\mu$ s. Characterization of these logical operations yields single data qubit and two-qubit (between the data and communication qubits) gate fidelities of  $\sim 97\%$  and  $\sim 94\%$ , respectively.

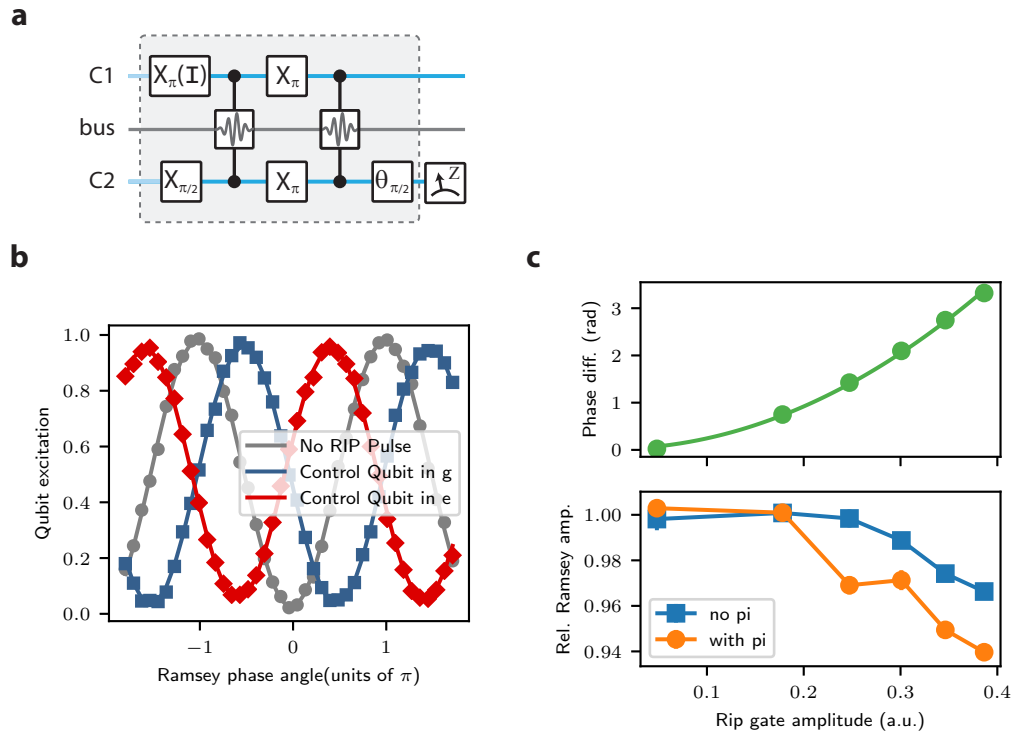


Figure 6.8 | **RIP gate tune-up protocol.** **a** A refocused RIP sequence is used to entangle the two communication qubits, explicitly including the bus. This experiment to calibrate the RIP pulse amplitude, detuning, and length are similar to a Ramsey phase-style experiment. To measure the entangling phase, the target qubit (C1) is initialized either in  $|e\rangle$  or  $|g\rangle$  by performing a  $\pi$ -pulse or identity, the RIP sequence is performed with varying angle ( $\theta_{\pi/2}$ ) on C2 for the second  $\pi/2$ -pulse, and finally, C2 is measured. **b** Characteristic sinusoidal oscillations of the target qubit state are observed while varying the angle  $\theta_{\pi/2}$ . The phase of the oscillations depend on the communication qubit initialization (blue square for  $|g\rangle$  and red diamonds for  $|e\rangle$ ), and the phase difference between the two experiments is a hallmark of an entangling phase. Here, the RIP gate amplitude is set to achieve a  $\pi$  phase difference between the two RIP experiments. A reference experiment where the RIP pulse amplitude is set to zero is shown (grey circles); we observe only a small reduction in amplitude when the RIP pulses are included as compared to this reference experiment. **c** The experiment in **b** is performed for several RIP gate amplitudes and the extracted entangling phase is extracted (top) as well as the relative oscillation amplitude as compared to the reference (bottom). The entangling phase is ideally proportional to the RIP gate power ( $\phi \propto \epsilon^2$ ), and a quadratic fit is shown indicating that the data is consistent with the expected trend.

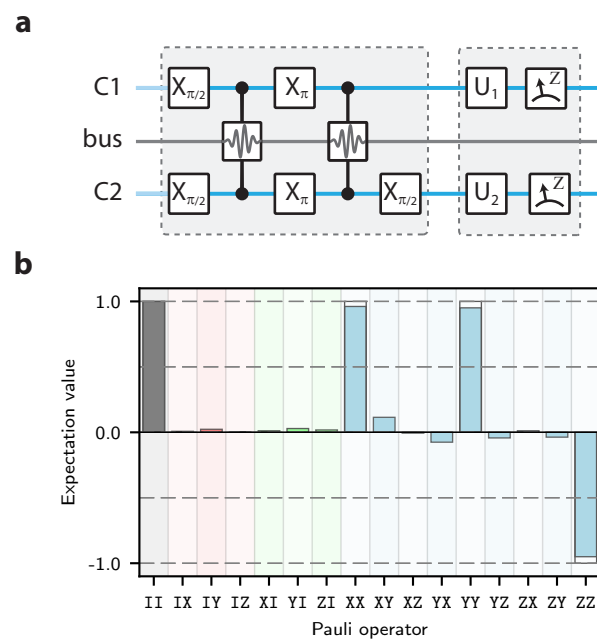


Figure 6.9 | **Generation of communication qubit Bell pair.** **a** After generating the Bell state (first block), QST is performed on both of the qubits to assess the quality of the entangled state. **b** Experimentally measured Pauli vector components of the two communication qubits. The generated state is  $(|ge\rangle + |eg\rangle) / \sqrt{2}$  with the ideal denoted as hollow bars. For this reconstruction, we take 10,000 averages per tomography setting.

### Defining local operations

We can group the pulses required for this work into three categories: single-qubit operations on the encoded data (cavity) qubit, entangling data-communication (cavity-transmon) operations, and cavity-transmon encoding/decoding pulses. For clarity we use the subscripts  $c$  and  $q$  to denote the cavity and transmon state, respectively.

1. The single-qubit operations,  $\hat{U}^s$ , are specified with the following state transfers:  $|0_L\rangle_c |g\rangle_q \rightarrow \hat{U}^s |0_L\rangle_c |g\rangle_q$  and  $|1_L\rangle_c |g\rangle_q \rightarrow \hat{U}^s |1_L\rangle_c |g\rangle_q$ . Here, we only specify that the transmon qubit begins and ends in the ground state, an assumption we make in our experiment to allow easier generation of pulses.
2. The teleported CNOT operation requires two different entangling operations. First, the entangling local operation for the module containing the control data qubit (D1) requires a cavity-controlled, transmon-target local CNOT, requiring the state transfers

$$\begin{aligned} |0_L\rangle_c (\alpha |g\rangle_q + \beta |e\rangle_q) &\rightarrow |0_L\rangle_c (\alpha |g\rangle_q + \beta |e\rangle_q) \\ |1_L\rangle_c (\alpha |g\rangle_q + \beta |e\rangle_q) &\rightarrow |1_L\rangle_c (\beta |g\rangle_q + \alpha |e\rangle_q). \end{aligned}$$

In practice, this operation closely matches a photon-number parity operation, requiring only transmon pulses in a Ramsey-like operation that flips the quantum amplitudes  $\alpha$  and  $\beta$  for the transmon qubit if the cavity is in  $|1_L\rangle$ . Our numerically-defined does reflect this intuition, though generally the extracted pulses will be quite complex.

Second, the entangling local operation for the module containing the target data qubit (D2) requires a transmon-controlled, cavity-target local CNOT, requiring the state transfers

$$\begin{aligned} (\alpha |0_L\rangle_c + \beta |1_L\rangle_c) |g\rangle_q &\rightarrow (\alpha |0_L\rangle_c + \beta |1_L\rangle_c) |g\rangle_q \\ (\alpha |0_L\rangle_c + \beta |1_L\rangle_c) |e\rangle_q &\rightarrow (\beta |0_L\rangle_c + \alpha |1_L\rangle_c) |e\rangle_q. \end{aligned}$$

Here, the logical cavity state is flipped ( $|0_L\rangle_c \leftrightarrow |1_L\rangle_c$ ) when the transmon qubit is in the excited state  $|e\rangle_q$ , a more challenging operation due to the nontrivial transitions among

different Fock states.

To aid the GRAPE algorithm in finding an acceptable solution, we expand the search to include those that perform the desired unitary up to single-qubit  $\hat{Z}$ -phase freedoms on both the qubit and the cavity. This generalization can offer, in some cases, dramatic speed-ups in computation time, while only requiring simple modifications in the pulse sequence.

3. The start of every experiment requires preparation of the cavities into a given initial state. We implement an encoding pulse that takes an arbitrary transmon state and maps it onto the encoded cavity state:

$$\left( \alpha |g\rangle_q + \beta |e\rangle_q \right) |0\rangle_c \rightarrow |g\rangle_q \left( \alpha |0_L\rangle_c + \beta |1_L\rangle_c \right).$$

Thus, to prepare a general logical cavity state, we initialize the ground state in both the transmon and cavity, perform a simple single-qubit transmon rotation for the desired initial state, and apply the encoding pulse to load the state onto the cavity, also returning the transmon to the ground state.

In order to perform logical tomography on the cavity states, we apply decoding pulses that map the logical cavity state onto the transmon qubit, essentially reversing the encoding pulse resulting in the following state transfer

$$\left( \alpha |0_L\rangle_c + \beta |1_L\rangle_c \right) |g\rangle_q \rightarrow |0\rangle_c \left( \alpha |g\rangle_q + \beta |e\rangle_q \right).$$

The simulated fidelities for all of our optimal control operations are in excess of  $\mathcal{F} > 99\%$ . Note that this optimization does not include the presence of loss and decoherence as we numerically integrate the Schrodinger equation. After developing these pulses, we apply them in a full Lindblad master equation simulation that accounts for these nonidealities to extract an expected operation fidelity; typically these fidelities are measured to be 1 – 3% lower, depending on the pulse length. We provide an exhaustive list in [Table 6.3](#).

Encoding	Module	Operation ( $\hat{U}$ )	Pulse length ( $\mu\text{s}$ )	Infidelity (%)	
				Predicted ( $1 - \mathcal{F}_{\text{sim}}$ )	Expt. $\Delta\mathcal{F} = (\mathcal{F}_{\text{E+D}} - \mathcal{F}_{\text{expt}})$
Binomial	1	$\hat{U}_{\text{E+D}}$	1.2 each	6.9	$(1 - \mathcal{F}_{\text{E+D}}) = 7.1$
		$\hat{X}_\pi$	1.4	3.7	2.4
		$\hat{X}_{\pm\pi/2}, \hat{Y}_{\pm\pi/2}$	1.4-1.5	3.5	3.2
		$\hat{U}_{\text{CNOT},1}$	0.6	–	–
Binomial	2	$\hat{U}_{\text{E+D}}$	1.2 each	4.4	$(1 - \mathcal{F}_{\text{E+D}}) = 5.3$
		$\hat{X}_\pi$	1.0	2.4	2.1
		$\hat{X}_{\pm\pi/2}, \hat{Y}_{\pm\pi/2}$	1.0 - 1.5	2.3	2.6
		$\hat{U}_{\text{CNOT},2}$	2.0	5.4	–
Fock	1	$\hat{U}_{\text{E+D}}$	0.6 each	4.1	$(1 - \mathcal{F}_{\text{E+D}}) = 3.1$
		$\hat{X}_\pi$	0.7	1.6	1.4
		$\hat{X}_{\pm\pi/2}, \hat{Y}_{\pm\pi/2}$	0.7	1.8	1.3
		$\hat{U}_{\text{CNOT},1}$	0.9	–	–
Fock	2	$\hat{U}_{\text{E+D}}$	0.6 each	2.3	$(1 - \mathcal{F}_{\text{E+D}}) = 2.5$
		$\hat{X}_\pi$	0.9	1.3	0.7
		$\hat{X}_{\pm\pi/2}, \hat{Y}_{\pm\pi/2}$	0.7	1.2	0.6
		$\hat{U}_{\text{CNOT},2}$	1.0	2.9	–

Table 6.3 | **Local operation infidelities.** Predicted and experimental results for optimal control pulses encoded in the Binomial and Fock bases. The predicted infidelity ( $1 - \mathcal{F}_{\text{sim}}$ ) is taken from a time-domain simulation that includes finite coherences of the transmon and cavity. The experimental infidelity is calculated from the difference of two separate QPT experiments. We first perform process tomography on only the encode-decode process,  $\hat{U}_{\text{E+D}} = \hat{U}_{\text{dec}}\hat{U}_{\text{enc}}$ , to extract  $\mathcal{F}_{\text{E+D}}$  for each module and encoding. Each experiment that involves the cavity requires an encoding and decoding pulse. We then perform QPT on the process that includes the operation under test,  $\hat{U}$ , and extract a process fidelity  $\mathcal{F}_{\text{expt}}$  on the combined process  $\hat{U}_{\text{dec}}\hat{U}\hat{U}_{\text{enc}}$ . Note that this fidelity includes the contribution of the encode and decode operations. We report the difference of the two experiments to estimate the fidelity of the target operation alone:  $\Delta\mathcal{F} = (\mathcal{F}_{\text{E+D}} - \mathcal{F}_{\text{expt}})$ .

### Effect of leakage

As introduced in [subsection 6.6.2](#), errors during the teleported CNOT operation generally manifest themselves as codespace leakage errors (e.g. data qubit states outside of the subspace  $\{|2\rangle, (|0\rangle + |4\rangle)/\sqrt{2}\}$ ). Therefore, these are important errors to include. In our experiments, when the data qubit states are decoded back onto the communication qubit, these leakage states are also mapped onto the communication two-dimensional subspace. Importantly, we do not attempt to postselect to remove these leakage cases. However, the behavior of our optimal control operations are specified only within the encoded subspace; the behavior of the operation outside the codespace is unconstrained when they are numerically optimized. Thus, it is not immediately clear how data qubit leakage errors are manifest within the communication qubit subspace. We use time-domain simulations to gain insight into the effect of leakage errors on tomography and fidelity calculations. We act the decode operation on a set of data qubit input states that are outside of the logical codespace (e.g.  $|1\rangle$  or  $(|0\rangle - |4\rangle)/\sqrt{2}$ ) and analyze the resulting communication qubit state. We typically find the final communication qubit state to be mixed with relative populations between  $|g\rangle\langle g|$  and  $|e\rangle\langle e|$  dependent on the particular input state. If these populations were equal, then leakage errors on the data qubit would be mapped to depolarizing-type errors on the transmon. For a given state outside the codespace, one should not expect this behavior; however, the ensemble behavior of errors in a particular protocol can approximate a depolarizing channel. To gain insight into the amount of bias that data qubit state leakage will introduce into our experimental tomography, we have performed time-domain simulations of the experimental tomography protocol, comparing extracted fidelities to the expected quantity. In general, we find that the fidelities extracted from a decode-style tomography experiment are only slightly different than the expected process fidelity, typically higher by around 0.5%. This bias in the tomography is a relatively small effect when we also include the decoherence induced by the decode process itself, which introduces around 3% infidelity. As such, leakage errors have minimal effect on our tomography, and we do not attempt to account for this bias in our fidelity calculations.

### 6.6.3 Measurement and feedback

After the entangling local operations, we perform measurements on the communication qubits (Step 3 in [Figure 6.2b](#)), thereby effecting a unitary operation between only the two data qubits. It is critical that the measurements do not reveal information about the state of the data qubits. In our protocol, this is accomplished by individual measurements of the communication qubits in the  $\hat{Z}$  and  $\hat{X}$  bases, which lead to four uniformly distributed outcomes. Each outcome heralds a unitary operation between the two data qubits that is a CNOT gate up to single-qubit operations. As a result, high-fidelity measurements are necessary to correctly determine the particular operation enacted on the data qubits. In our system, we achieve single-shot state assignment fidelities of the communication qubits around 99%.

Finally, ensuring that the protocol implements the desired CNOT operation independent of measurement outcome requires classical communication and feedforward operations (Step 4 in [Figure 6.2b](#)). Two classical bits of information are needed to communicate measurement results between modules. This information is used to apply feedforward operations, transforming the protocol into a deterministic operation and thus completing the teleportation. In our experiment, it is required that the measurements be non-destructive to the communication qubits as they are used for subsequent steps of our protocol. For our protocol, these measurements also induce a conditional reference phase shift on the data qubits dependent on measurement outcome ([section 6.7](#)). Tracking these phases accurately is critical for all subsequent operations on the data qubits. To enable both the measurements and the feedforward, we employ a real-time controller [\[21\]](#) to orchestrate quantum programs for our experiment, combining control, measurement, state estimation, and feedforward in a single integrated system. For every experimental run, this controller handles the distribution of classical information between the two modules, dynamically updating the reference phases and applying the appropriate feedforward operations, all within a fraction of the lifetime ( $\sim 1\%$ ) of the communication qubits. We have independently analyzed the measurement and feedforward process to have a combined fidelity of  $\sim 97\%$ , excluding the data qubit operations.

### Transmon measurement

In this experiment, each module is connected to a separate JPC for fast, high-fidelity measurement of the transmon qubit. We achieve single-shot assignment fidelities around 99.4%, largely limited by transmon decay during the measurement pulse of 600 ns. We define assignment fidelity as the average of probabilities of correctly assigning the state when we prepare the transmon in  $|g\rangle$  and  $|e\rangle$ :  $F_{assign} = [\text{Pr}("g" | |g\rangle) + \text{Pr}("e" | |e\rangle)] / 2$ . This high quality measurement, coupled with the real-time capabilities of our quantum controller, enable classically conditional operations based on an extracted measurement result. The length of time from the start of a measurement pulse to the application of a conditioned operation is around 1000 ns, which includes measurement pulse length (600 ns), cable delays (200 ns), integration and state estimation latencies (200 ns).

It is critical that the two communication qubit measurements be independent for the demonstration of the teleported gate. In order to assess the measurement crosstalk, we perform a Rabi experiment and perform simultaneous measurements on both communication qubits (Figure 6.10a). Our results Figure 6.10b and Figure 6.10c indicate that the measurements are highly selective to the qubit addressed. From our data, we estimate the measurement crosstalk—defined to be the ratio of the measurement contrast of measuring the directly coupled qubit to that of measuring the isolated qubit—to be  $< 10^{-4}$ . In future implementations of this experiment where the two modules are physically separate, the measurement crosstalk will be completely negligible.

#### 6.6.4 Analyzing transmon reset

The success of the teleported CNOT requires reliable measurements of each communication qubit. As discussed previously our JPC-enabled single-qubit readout has assignment fidelities in excess of 99%. In our implementation of the teleported gate, the communication qubits serve dual roles: both to store inter-module entanglement and also to enable complex data qubit operations via optimal control pulses. Therefore, after the measurement of the communication qubits in our protocol, we perform a feedback reset of both communication qubits to the ground state to recycle them for the following single-qubit operations and tomography steps. These measurements are

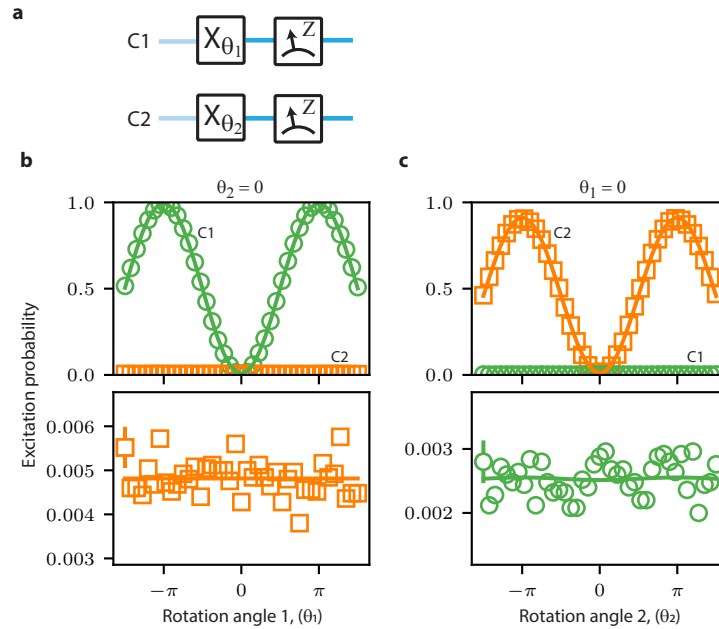


**Figure 6.10 | Assessing independence of single qubit measurements.** **a** Rabi experiment pulse sequence to extract measurement crosstalk. After initializing both communication qubits in the ground state, both qubits are rotated by  $\hat{X}$ -rotations with independent angles  $\theta_1$  and  $\theta_2$  for C1 and C2, respectively. Subsequently, measurements are performed on modules 1 and 2 and the result is recorded. **b** and **c** Measurement crosstalk experimental results. For **b** (**c**), C2 (C1) is kept in the ground state, and a Rabi experiment is performed on C1 (C2). The measurement results are shown for C1 (green circles) and C2 (orange squares). For clarity, we describe the results focusing on **b**; the discussion is the same for **c**, save swapping C1 and C2. Top panel: the C1 measurement results illustrate high contrast oscillations, while the C2 measurement results remains close to zero, as expected when the communication qubit measurements are independent. Bottom panel: Zoom in for measurement results on C2. The lack of structure in the data indicate that the measurement of C2 does not infer any information about the state of C1. To estimate the measurement crosstalk, we perform sinusoidal fits the data by fixing the frequency and phase of the oscillation and extracting an amplitude and offset. Each point in this experiment consists of 25,000 experiments. For data in the top panels, error bars are much smaller than the marker; for data in the bottom panels, we represent a typical error bar to be within the spread of the points. The slightly reduced contrast in **c** is specific to this calibration experiment, potentially due to drifts of transmon relaxation rate during the many hours of acquisition.

required to be highly-quantum non-demolition to both the communication qubit as well as the data qubits.

We perform the following experiment to test both the measurement as well as the reset. First, we initialize the two communication qubits in an equal superposition of computational states:  $|\psi_{init}\rangle = (|gg\rangle + |ge\rangle + |eg\rangle + |ee\rangle)/4$ . Next, we perform measurements on each qubit allowing the control computer to perform real-time state estimation. Conditioned on the measurement results, we apply a  $\pi$ -pulse if the qubit was measured to be in the excited state. Finally, we analyze the state via conditioned state tomography to assess the quality of the reset. The resulting tomograms are shown in [Figure 6.11](#). We extract state infidelities to the joint ground state  $|gg\rangle$  of  $<1\%$  for the case when we measured both qubits in the ground state, outcome “00”. We observe single-qubit infidelities of 2% and 4% when each qubit is measured to be in the excited state. The result from outcome “11” indicates that these infidelities are additive and any crosstalk in the measurement or control is negligible. From these results, we find an average reset infidelity of  $\sim 3\%$ , primarily limited by decay during the measurement and subsequent controller latency. From this experiment we establish that our system enjoys highly accurate and QND single-qubit measurements.

## 6.7 Tuning up the teleported CNOT

### 6.7.1 Logical vs. Reference phases

When manipulating logical qubits, it is necessary to distinguish two types of phase shifts: logical phase shifts and reference-frame phase shifts. A logical phase shift is a phase shift between the two logical basis states, and is generated by the logical  $\hat{Z}$  operator,  $\hat{Z}_L(\phi) = \text{diag}[1, e^{i\phi}]$ :

$$\alpha |0_L\rangle + \beta |1_L\rangle \longrightarrow \alpha |0_L\rangle + \beta e^{i\phi} |1_L\rangle = \alpha |2\rangle + \frac{\beta}{\sqrt{2}} e^{i\phi} (|0\rangle + |4\rangle), \quad (6.12)$$

On the other hand, a reference-frame phase shift is generated by the phase-shift operator,

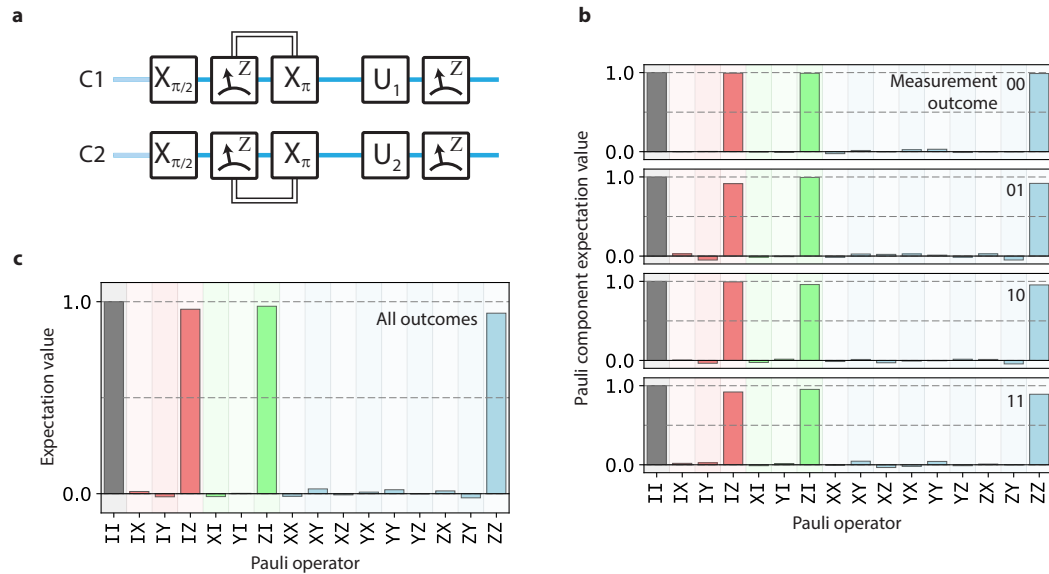


**Figure 6.11 | Communication qubit measurement and reset.** **a** Pulse sequence for testing communication qubit measurement and reset. The two communication qubits (transmons) are initialized in the joint state  $(|gg\rangle + |ge\rangle + |eg\rangle + |ee\rangle)/2$ . The two qubits are then measured and if the measurement indicates that the state is projected to  $|e\rangle$  a  $\pi$ -pulse is applied to flip the state to the ground state. Conditional QST is performed to analyze the quality of measurement and reset. This measurement and reset protocol is used in the teleported gate. **b** Experimentally measured Pauli vector components conditioned on the measurement outcome. We assign a “0” (“1”) to indicate that the measurement projected the qubit to be in  $|g\rangle$  ( $|e\rangle$ ). For all outcomes, we find high fidelity to the two-qubit ground state,  $|gg\rangle$  as expected with ground state fidelities  $\{00 : 99.3\%, 01 : 95.7\%, 10 : 97.7\%, 11 : 94.2\%\}$ . From these results, we establish that the measurement and feedback processes for each qubit are independent; from the single-qubit reset infidelities, we expect a measurement fidelity of  $1 - (0.993 - 0.957) - (0.993 - 0.957) = 0.948$ , which is consistent with the result for measurement outcome 11. **c** Experimentally measured state after measurement-based reset. Measurement results from **b** are combined, and the compiled results illustrate that the reset protocol is high-fidelity and independent of measurement outcome. The fidelity of this reconstructed two-qubit state to  $|gg\rangle$  is 96.9%.

$\hat{U}_{\text{ref.}}(\theta) = \exp[-i\theta\hat{a}^\dagger\hat{a}]$ , which acts on the physical levels of the state,

$$\alpha|0_L\rangle + \beta|1_L\rangle \longrightarrow \hat{U}_{\text{ref.}}(\theta)[\alpha|0_L\rangle + \beta|1_L\rangle] = e^{i2\theta} \left[ \alpha|2\rangle + \frac{\beta}{\sqrt{2}} \left( e^{-i2\theta}|0\rangle + e^{i2\theta}|4\rangle \right) \right] \quad (6.13)$$

While  $\hat{Z}$ -phases and reference phases are equivalent for a single physical qubit (and this equivalence has been previously utilized to implement  $\hat{Z}$ -gates through software reference phase updates [224]), these phases have distinct effects on a logical qubit state. In particular, for our cQED system, the dispersive interaction,  $H_I = \chi\hat{a}^\dagger\hat{a}|e\rangle\langle e|$ , naturally generates a reference-frame phase shift when the communication-qubit is in the  $|e\rangle$  state; for a time  $t$ , the total phase accumulation is given as  $\theta = \chi t$ . Correct determination of these reference phase shifts are critical to the successful application of our optimal control pulses; these pulses must be applied with the correct phase relative to the logical Bloch sphere for the data-qubit. In the following sections, we detail our tune-up protocol, establishing how we keep track of the reference phases necessary for the implementation of the teleported CNOT gate. Crucially these phases are determined either from direct measurements or from the Hamiltonian and pulse sequence timing, and are known in advance.

### 6.7.2 Reference phases due to Bell state generation

We consider the reference-phase shift induced by the Bell state generation to determine the phase-adjustment necessary for the local CNOT operations. This is necessary as the data-qubit states encode quantum information prior to generation of the communication-qubit Bell pair as would be typical in any algorithm that uses the teleported CNOT. During the Bell generation step, each communication-qubit induces a reference frame shift on its respective data-qubit according to their dispersive interaction. Our Bell generation is similar to a spin-echo sequence, and so the length of time that the communication qubit is in the excited state half time for half of the duration of the operation, or  $T_{\text{Bell}}/2 = 336$  ns. This results in estimated phase shifts of the control and target data-qubit of 1.21 rad and 1.78 rad, respectively.

For a more realistic measurement of this phase shift, we perform the following experiment

that takes into consideration finite pulse timings and other experimental details (Figure 6.12). Here, we utilize a pulse sequence similar to the Bell generation protocol; in this case, we remove the bus drives to keep the communication qubits in a separable state. We first displaced the data qubit (cavity) to the coherent state  $|\alpha\rangle = 2$ . Then, we perform a sequence similar to the Bell state generation, except we use a bus drive amplitude of zero to keep the two communication qubits separable. Next, we either initialize the communication qubit in  $|g\rangle$  or  $|e\rangle$  as two separate experimental variations. Then, we continue with the sequence, and at the end of the protocol, perform a  $\pi$  pulse if the communication qubit was initialized in  $|e\rangle$ . In this way, for both results, the communication qubit will be left in the excited state (the ground state could also be used). These two experiments allow us to check that the refocusing  $\pi$ -pulse does indeed disentangle the data qubits by the end of the sequence. At the end of the protocol, the data qubit state will have evolved from  $|\alpha\rangle \rightarrow |\alpha e^{i\phi}\rangle$  where  $\phi = \chi T_{\text{Bell}}/2$ , and we measure  $\phi$  by performing a series of data qubit displacements  $D_\alpha = 2$  with varying phases. We extract phase shifts of  $\phi = 1.81$  for both communication qubit initial states, indicating that the data and communication qubit will be left separable at the end of the Bell state generation protocol. We find that our experimentally phase is in close agreement ( $\sim 1\%$ ) with the simple estimation.

### 6.7.3 Reference phases due to measurements

Next, we consider the reference phases accumulated during the communication-qubit measurements. These phases, in contrast to the previous section, are now conditioned on the measurement outcome. When the communication-qubit is measured in  $|g\rangle$ , the data-qubit acquires no additional reference phase; however, when the communication-qubit is measured in  $|e\rangle$ , then the data-qubit acquires a total reference phase  $\theta_M = \chi T_M$ , where  $T_M$  and is the duration of the total measurement process, including measurement pulse, integration, and state estimation.

To experimentally extract the measurement-outcome dependent phases, we prepared the input state  $|\psi_{in}\rangle = \left| +\hat{X}_L \right\rangle \left| +\hat{X}_L \right\rangle$ , and applied the teleported CNOT. Here, the CNOT is invariant to the input state; thus, the output state should remain as the separable state  $|\psi_{in}\rangle$ . We extract the resulting state and perform Wigner tomography on each data-qubit. The effect of these ref-

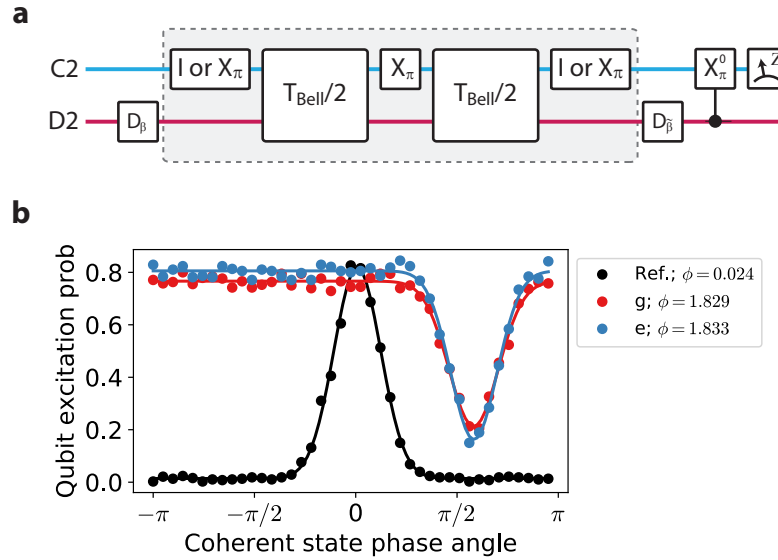


Figure 6.12 | **Measurement reference phase due to Bell state generation.** **a** Pulse sequence for measuring Bell state generation reference phase shift. Pulses  $D_\beta$  indicate data qubit displacements of  $\beta$ ;  $X_\pi$  indicate communication qubit  $\hat{X}$ -rotations of angle  $\theta$ ;  $X_\pi^0$  indicates a communication qubit rotation of angle  $\pi$  that is selective on the data qubit having zero photons. The block labeled  $T_{\text{Bell}}$  indicates a time delay during which the data qubit undergoes a communication qubit state-dependent phase shift. In this sequence we either initialize the communication qubit in  $|g\rangle$  or  $|e\rangle$  by performing identity (I) or a  $\pi$ -pulse ( $\hat{X}_\pi$ ). The shaded section indicates the sequence that is similar to the Bell state generation protocol. For this experiment, the second displacement is related to the initial displacement by  $\tilde{\beta} = -\beta e^{i\phi}$ . **b** Experimental results indicating the final phase of the data qubit coherent state as a function of phase angle. Data are presented as dots; gaussian fits to the data are shown as lines. The center of the gaussian peak (or dip) represents the phase of the coherent state. We perform a reference experiment (Ref, in black) that removes the shaded section of the pulse sequence, and we measure a peak at phase angle  $0$ , as expected. Results where we initialize the communication qubit state in  $|g\rangle$  (g, in red) or  $|e\rangle$  (e, in blue) illustrate an average reference phase shift of  $\phi = 1.831$  rad. Importantly, extracted phases for both experiments closely match, indicating that the final state of the data qubit does not depend on initial state of the communication qubit.

reference phase shifts will induce a rotation in the IQ-plane of the state and can be parameterized by  $\theta$ :  $|\hat{X}_L(\theta)\rangle = (|0\rangle + e^{i2\theta}\sqrt{2}|2\rangle + e^{i4\theta}|4\rangle)/\sqrt{2}$ . The resulting Wigner functions (Figure 6.13) are then used to extract a set of eight phases (one phase for each measurement outcome, for each data-qubit) to account for the reference frame shift induced by the measurement.

Due to the probabilistic nature of the communication measurements, our controller performs a critical task to store these phases in memory, selecting the correct phase depending on the measurement outcome for each experimental shot. In Figure 6.13, we account for this reference frame shift and note the extracted Wigner functions are all correctly aligned. The extracted phases should be considered as a persistent reference frame update that is applied to all subsequent operations on the data qubits; here, we apply these phases to both the feedforward operations as well as the decoding operations. In our encoding, a logical  $\hat{Z}_L$  phase-flip where  $\phi = \pi$  is equivalent to a reference phase shift of  $\theta = \pi/2$ . Therefore, we apply the feedforward  $\hat{Z}$  operation in software by conditionally updating the phase of the cavity drive for the control module.

#### 6.7.4 Communication qubit measurement basis

In contrast to the reference phase shifts induced by the dispersive interaction as discussed in the previous two sections, the choice of basis of the communication qubit measurements can induce a logical phase and therefore plays an important role in determining the exact operation of the teleported gate. In particular, we study the effect of changing the measurement basis on C2, which notionally should be a  $\hat{X}$  measurement. In the following experiment (Figure 6.14), we run the teleported gate while sweeping the phase of the  $\pi/2$ -pulse on C2 prior to the communication qubit measurements (outlined in red in Figure 6.14a). The C2 measurement operator is given generally as  $\hat{M}(\theta) = \cos(\theta)\hat{X} + \sin(\theta)\hat{Y}$ , where  $\theta$  is the chosen angle of the  $\pi/2$  pulse; that is, we are rotating the measurement basis around the equator of the Bloch sphere of C2. Ideally,  $\theta = 0$  to achieve the desired  $\hat{X}$  measurement; however, we expect an offset in this measurement angle due to single qubit phases acquired during the previous local operation (where the optimal control pulse induces reference phase shifts on both the data and communication qubit).

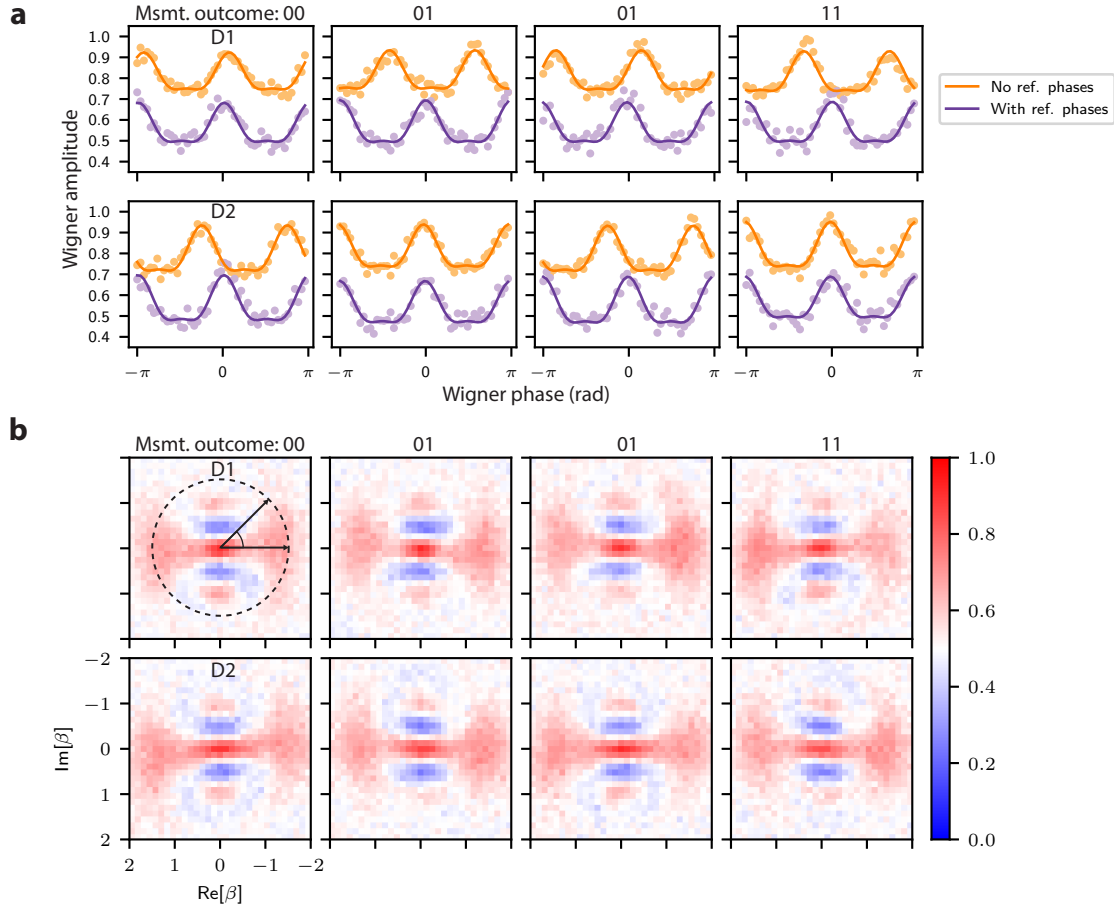


Figure 6.13 | **Measurement-induced reference phase shift.** For all data, we perform the teleported CNOT on the maximal superposition state  $(|0_L\rangle + |1_L\rangle)_{D1} \otimes (|0_L\rangle + |1_L\rangle)_{D2} / 2$ . The CNOT is invariant on this particular input state and so the output state is ideally separable, which allows analysis of the output state via single qubit Wigner tomography. The ideal state for each data qubit should be  $|+X_L\rangle = (|0_L\rangle + |1_L\rangle) / \sqrt{2}$ , a horizontally-oriented kitten state. For both **a** and **b**, the top row represents the result from data qubit 1 (the control qubit) and the bottom row represents the result from data qubit 2 (the target qubit). Each column represents a different measurement outcome of the communication qubits. **a** One-dimensional phase-cut of the Wigner function for the output state. In each panel, the top data (orange) represents case when the reference phases are not accounted for, and we observe different reference phase shifts for each measurement outcome. The solid line represents a fit to the data for target  $|+X_L\rangle$  rotated in the IQ space. Taking these reference phases into consideration, applying them in real-time, we find the bottom data (purple), where we observe that all measurement outcomes have the same reference phase. The data without accounting for reference phases (orange) is vertically offset for clarity. **b** Wigner function of the output state when accounting for reference phases. For all outcomes, the target data qubit state,  $|+X_L\rangle$ , is generated with the appropriate reference phase.

In our experiment, we perform the teleported gate on the input state,  $|\psi_{\text{in}}\rangle = (|0_L\rangle + |1_L\rangle)|0_L\rangle$  while varying the measurement angle  $\theta$ . For simplicity, we perform the experiment without feedforward operations and extract conditioned QST for each measurement angle. For the measurement angle that corresponds to an  $\hat{X}$ -measurement, we expect to generate the following conditioned states:  $\{|\Psi_L^+\rangle, |\Psi_L^-\rangle, |\Phi_L^+\rangle, |\Phi_L^-\rangle\}$  (if we had added feedforward operations, then we would ideally generate the even Bell state  $|\Phi_L^+\rangle$ ). Our results are illustrated in [Figure 6.14b](#), where we plot selected Pauli operators. For each measurement outcome, we find that the two-qubit parity  $\langle ZZ \rangle$  is conserved over all measurement angles indicating that we generate a maximally entangled state independent of angle; however, we observe oscillations in the transversal two qubit operators,  $\langle XX \rangle, \langle XY \rangle, \langle YX \rangle, \langle YY \rangle$ . These oscillations are expected and indicate that the choice of measurement angle induces a logical phase on the output state. We also observe that the contrast of the output state is constant over all measurement angles. From this experiment, we extract the optimal measurement angle to implement the teleported CNOT operation. The observations from this experiment suggests that the choice of measurement basis may also allow for tuning of the particular teleported operation.

## 6.8 Demonstrating the teleported CNOT gate

Therefore, by consuming a shared entangled pair and communicating two classical bits of information, this procedure effects a CNOT operation between the data qubits without requiring a unitary operation between the two modules after the generation of the shared entangled pair. Having demonstrated all of the elements necessary for realizing the teleported CNOT gate, we characterized the full two-qubit gate through a series of four separate analyses.

### 6.8.1 Generating the CNOT truth table

In the first analysis, we verified the classical behavior of the gate by generating a truth table for the set of computational states. We prepared the data qubits each of the four states  $\{|0_L0_L\rangle, |0_L1_L\rangle, |1_L0_L\rangle, |1_L1_L\rangle\}$  and enacted the teleported CNOT on each, ideally leading to the

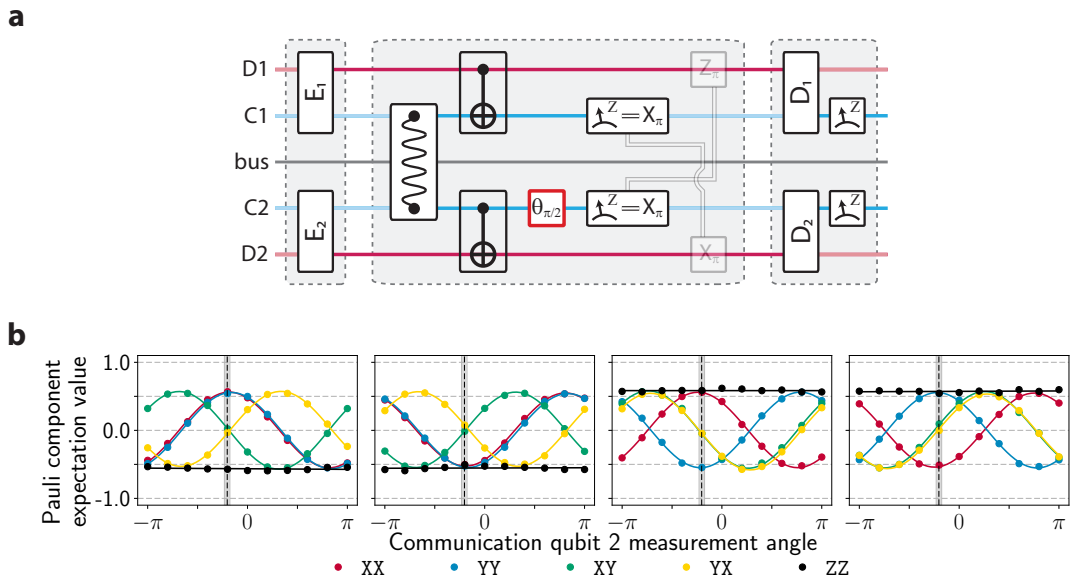


Figure 6.14 | **Communication qubit 2 measurement angle.** **a** Pulse sequence for tuning up C2 measurement angle. The experiment is similar to Figure 6.6, with two main modifications. First, in this experiment, the  $\pi/2$ -pulse on C2 (outlined in red) is varied; second, the feedforward operations are left out. For each measurement angle, we perform conditioned QST on the output state. **b** Measured Pauli components as a function of C2 measurement angle, conditioned on measurement outcome. The experiment described in **b** is performed on the input state  $(|0_L\rangle + |1_L\rangle)|0_L\rangle$  and the teleported operation is performed while varying angle  $\theta$ . Results from density matrix reconstruction is shown as dots, and a fit to the data is shown as lines. The optimal measurement angle to implement the teleported CNOT operation is highlighted with the dashed vertical line with uncertainty in its value as the shaded grey region.

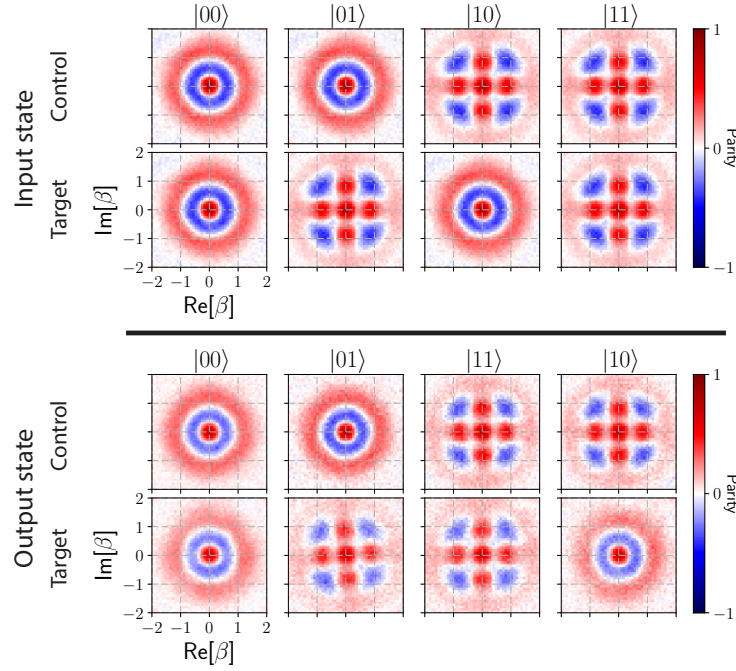


Figure 6.15 | **Teleported CNOT truth table.** Individual cavity Wigner functions illustrating the action of the teleported CNOT on the logical computational states. The left two columns show experimental Wigner functions illustrating all four logical computational states as input states, and the right two columns show the extracted Wigner functions after performing the teleported CNOT operation, illustrating the correct classical behavior of the gate.

output states:  $\{|0_L 0_L\rangle, |0_L 1_L\rangle, |1_L 1_L\rangle, |0_L 1_L\rangle\}$ . We extracted both the input and output states by measuring Wigner functions for each data qubit. Our results (Figure 6.15) provide qualitative validation of the teleported CNOT on the computational basis states.

### 6.8.2 Generating a logical Bell state

In the second analysis, we have demonstrated that it is a distinctly quantum operation by using the teleported CNOT to generate entanglement between two logical qubits. We prepared the data qubits in the separable initial state  $|\psi_{\text{in}}\rangle = (|0_L\rangle + |1_L\rangle)|0_L\rangle/\sqrt{2}$  and performed the gate. The ideal output state is the Bell state  $|\Phi_L^+\rangle = (|0_L 0_L\rangle + |1_L 1_L\rangle)/\sqrt{2}$ . We verified that our teleported CNOT generates this logical qubit Bell pair using two separate methods, which together highlight our ability to characterize the data qubits both on a logical level (i.e. the encoded two-dimensional subspace) as well as on a physical level (i.e. the multi-dimensional cavity state).

### Quantum correlations

In the first method, we performed a pair of experiments to show that the state exhibits quantum correlations. Given the target state  $|\Phi_L^+\rangle$ , when we measure the control qubit in the logical  $\hat{Z}_L$  basis and find it in  $|0_L\rangle$  ( $|1_L\rangle$ ), we expect the target qubit to be  $|0_L\rangle$  ( $|1_L\rangle$ ). We enacted the logical  $\hat{Z}_L$  measurement and, conditioned on the result, performed physical-qubit tomography on the target data qubit by measuring its Wigner function. Experimentally, the logical measurement of the control data qubit is accomplished by first, decoding the state of the data qubit onto the communication qubit and then, measuring the desired observable on the communication qubit (Figure 6.16a). As expected, we observed strong  $\hat{Z}$ -correlations between the control and target data qubits (Figure 6.16b, top). Next, we rotated the measurement basis and performed  $\hat{X}_L$  measurements of the control data qubit. Conditioned on the control data qubit in  $|\pm X_L\rangle = (|0_L\rangle \pm |1_L\rangle)/\sqrt{2}$ , we experimentally found the target data qubit to be in the expected state  $|\pm X_L\rangle$  (Figure 6.16b, bottom), thus establishing  $\hat{X}$ -correlations between the two data qubits. These two complementary experiments confirm the non-classical nature of the experimental logical Bell state and indicate that our gate produced a non-separable two-qubit state.

#### 6.8.3 Upper bound to logical Bell state fidelity

From the quantum correlation experiment we want to estimate the logical Bell state fidelity. We closely follow the approach described in Refs [138, 199]. The ideal logical Bell state is  $|\Phi^+\rangle = (|00\rangle + |11\rangle)_{D_1 D_2}/\sqrt{2}$ . For the rest of this section we drop the subscripts. A general two-qubit density operator  $\rho$  can be represented as the following,  $\rho = \sum_{i,j=0}^3 \rho_{ij} |i\rangle\langle j|$ . The fidelity of  $\rho$  to the target Bell state  $|\Phi^+\rangle$  is given as

$$\mathcal{F}_{\text{Bell}} = \frac{1}{2} (\rho_{00} + \rho_{33} + \text{Re}(\rho_{30}) + \text{Re}(\rho_{03})) = \frac{1}{2} (\rho_{00} + \rho_{33} + 2 \text{Re}(\rho_{30})) \quad (6.14)$$

The first two terms can be computed from the fraction of counts where the measurement outcomes are correlated. We discuss how we extract the measurement quantities below.

We can determine a strict lower bound for  $\text{Re}(\rho_{30})$  through the following analysis. First, we

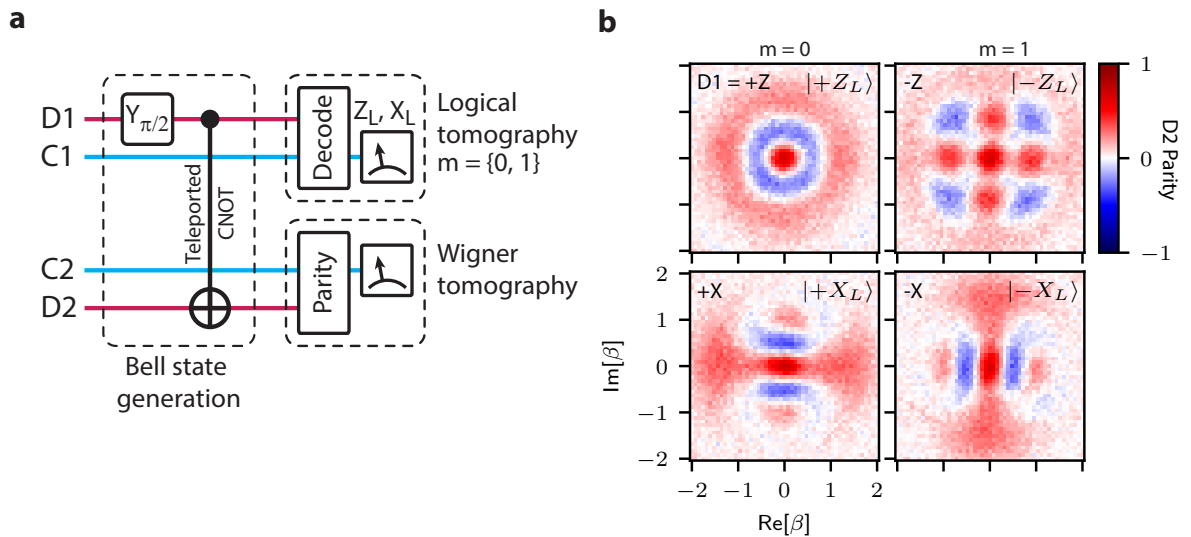


Figure 6.16 | **Quantum correlations of a logical Bell state** **a**, Bell state generation and tomography circuit. The logical Bell state  $|\Phi_L^+\rangle$  is first created using the teleported CNOT gate between D1 and D2. The subsequent state is analyzed by performing either physical tomography by measuring the Wigner function or logical tomography by measuring the logical operators. **b**, Quantum correlations of a logical Bell state. The logical Bell state  $|\Phi_L^+\rangle$  is first created using the teleported CNOT gate. The control qubit (D1) is measured in either the logical  $Z_L$  and  $X_L$  bases by a decoding sequence. Conditioned on this result ( $m = 0, 1$ ), physical-qubit tomography is performed on the target qubit (D2) by measuring its Wigner function. The control qubit is measured in either the logical  $\hat{Z}_L$  basis (top) and  $\hat{X}_L$  basis (bottom), and Wigner tomography is performed on the the target qubit conditioned on the measurement result,  $m = 0$  (left) and  $m = 1$  (right). Correlations between the measurement result and measured state signal the generation of an entangled state between D1 and D2.

transform  $\rho$  into the X-basis by rotating both qubits by  $\pi/2$  around the y-axis.

$$\tilde{\rho} = \left( \hat{Y}_{\pi/2} \otimes \hat{Y}_{\pi/2} \right) \rho \left( \hat{Y}_{\pi/2} \otimes \hat{Y}_{\pi/2} \right)^\dagger \quad (6.15)$$

In this transformed frame, we find the following equality between  $\rho$  and  $\tilde{\rho}$ ,

$$\tilde{\rho}_{00} + \tilde{\rho}_{33} - \tilde{\rho}_{11} - \tilde{\rho}_{22} = 2(\operatorname{Re}(\rho_{30}) + \operatorname{Re}(\rho_{21})). \quad (6.16)$$

The off-diagonal elements is bounded by the diagonal components with the relation

$$|\operatorname{Re}(\rho_{21})| \leq \sqrt{\rho_{11}\rho_{22}}. \quad (6.17)$$

Then the off-diagonal element in [Equation 6.14](#) is satisfied with the inequality

$$2\operatorname{Re}(\rho_{30}) \geq \tilde{\rho}_{00} + \tilde{\rho}_{33} - \tilde{\rho}_{11} - \tilde{\rho}_{22} - 2\sqrt{\rho_{11}\rho_{22}} \quad (6.18)$$

Then in terms of quantities that we can extract from our correlation experiments, the fidelity has a strict lower-bound

$$\mathcal{F}_{\text{Bell}} \geq \frac{1}{2} (\rho_{00} + \rho_{33} + \tilde{\rho}_{00} - 2\sqrt{\rho_{11}\rho_{22}} + \tilde{\rho}_{33} - \tilde{\rho}_{11} - \tilde{\rho}_{22}) \quad (6.19)$$

We can translate this equation into quantities accessible from our experiment. We write  $P_1(i)$  to be the probability of measuring the control data qubit (D1) to be in state  $|i\rangle$ ;  $P_2(j|i_1)$  represents the conditional probability of finding the target data qubit (D2) to be in state  $|j\rangle$  given that the control qubit was found to be in state  $|i\rangle$ . Then, [Equation 6.19](#) can be written in terms of these quantities as

$$\begin{aligned} \mathcal{F}_{\text{Bell}} \geq \frac{1}{2} & \left( P_1(0)P_2(0|0) + P_1(1)P_2(1|1) - 2\sqrt{P_1(1)P_2(0|1)P_1(0)P_2(1|0)} \right. \\ & \left. + P_1(+ )P_2(+|+) + P_1(-)P_2(-|-) - P_1(-)P_2(+|-) - P_1(+ )P_2(-|+) \right) \end{aligned} \quad (6.20)$$

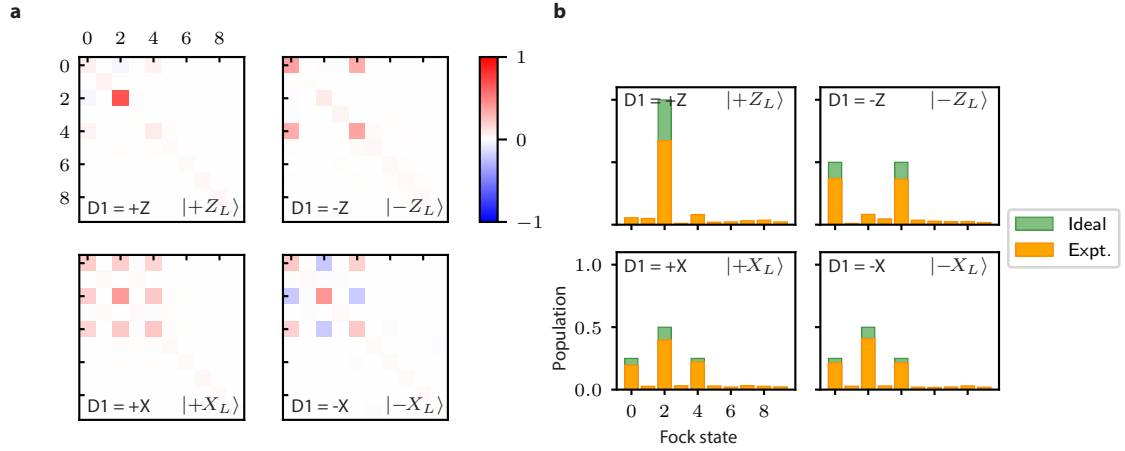


Figure 6.17 | **State reconstruction for the logical Bell state.** **a** Density matrix (real part) for conditioned Wigner tomography. We reconstruct the density matrix associated with each experimentally measured Wigner function in the Main Text, Figure 3b. Our experimental results are similar to the ideal save for reduced contrast. The imaginary component of the density matrix is ideally zero; our reconstructed state also has small imaginary components. **b** Photon number populations. The diagonal components of the density matrix—corresponding to the populations of each photon number state—are shown for each conditioned state. The ideal populations are shown in green, and the experimental results are shown in orange.

We calculate the probabilities  $P_1(\cdot)$  directly from the statistics of the logical measurement of the control qubit. To determine the conditional probability, we reconstruct the cavity state following the procedure described in [section 5.5](#). We show the results of this reconstruction in [Figure 6.17](#). We then compute the conditional probability by computing the fidelity of the reconstructed state  $\rho_{D2}$  to the target state  $|i\rangle$ :  $P_2(i|j) = \langle i|\rho_{D2}|i\rangle$ . Based on these calculations, we calculate a lower bound in the entangled state fidelity to be  $\mathcal{F}_{\text{Bell}} \geq (55 \pm 2)\%$ , without correcting for preparation or measurement errors. This lower bound is consistent with the state fidelity extracted from logical QST.

### Logical quantum state tomography

In the second method, we analyzed the joint state within the logical subspace of the two data qubits by performing quantum state tomography. Quantum state tomography is performed using the same decoding technique as the logical qubit measurement discussed above. We

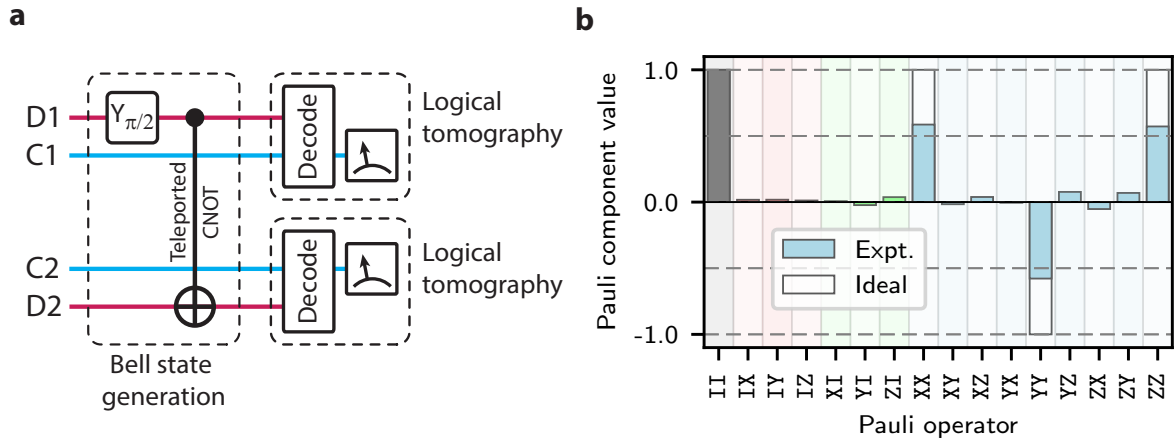


Figure 6.18 | **Quantum state tomography of logical Bell state.** **a**, Bell state generation and tomography circuit. The logical Bell state  $|\Phi_L^+\rangle$  is first created using the teleported CNOT gate between D1 and D2. After generating  $|\Phi_L^+\rangle$ , we perform logical tomography on both data qubits decoding the state onto the communication qubit. **b**, After generating  $|\Phi_L^+\rangle$ , logical qubit tomography is performed on both the control and target qubit. The reconstructed state, represented in the Pauli basis, confirms the teleported CNOT has generated the target Bell state. We show the reconstructed state in the Pauli basis:  $\rho = \sum_i p_i \hat{\sigma}_i$  where  $\hat{\sigma}_i$  are the generalized Pauli operators.

reconstructed the two-qubit state in the Pauli basis (Figure 6.18), extracting a state fidelity  $\mathcal{F}_{\text{Bell}} = (68 \pm 1)\%$  and concurrence  $\mathcal{C} = (0.37 \pm 0.01)$ , exceeding the threshold for a classically correlated state. These quantities include imperfections associated with logical state preparation and decoding operations, which together contribute about 6% infidelity for each data qubit. Importantly, using the teleported CNOT, we have generated a Bell state between logical qubits encoded as multi-photon states that, from inspection of the reconstructed density operator, has dominant two-qubit Pauli components (e.g. two-qubit parity,  $\langle ZZ \rangle = 0.57$ ) and near-zero single-qubit Pauli components (e.g. single-qubit parities,  $\langle IZ \rangle = 0.01$  and  $\langle ZI \rangle = 0.04$ ).

#### 6.8.4 Analyzing the role of feedforward

Our implementation of the teleported gate as a deterministic operation requires reliable classical communication and feedforward operations. In this third analysis, we investigated the importance of these elements by performing the previously-described data qubit entanglement sequence with-

out applying the feedforward operations (Step 4 in [Figure 6.2b](#)). Instead, we recorded the measurement outcomes and extracted four conditioned output states. Without these feedforward operations, each measurement outcome  $\{00, 01, 10, 11\}$  ideally occurs with probability  $1/4$  and heralds one of four Bell states:  $\{|\Psi_L^+\rangle, |\Psi_L^-\rangle, |\Phi_L^+\rangle, |\Phi_L^-\rangle\}$ , where  $|\Psi^\pm\rangle = (|01\rangle \pm |10\rangle)/\sqrt{2}$  and  $|\Phi^\pm\rangle = (|00\rangle \pm |11\rangle)/\sqrt{2}$ . Our results ([Figure 6.19](#); top, first four panels) are consistent with the ideal, save for reduced contrast, and we extracted conditioned fidelities of  $\{69\%, 66\%, 69\%, 66\%\}$  and outcome frequencies of  $\{0.25, 0.26, 0.24, 0.25\}$ . Crucially, the fact that we generated different Bell pairs indicates that each conditional operation is a CNOT gate up to single qubit operations. Without real-time knowledge of these measurement outcomes, these states will all add incoherently, resulting in a completely mixed state where all information has been lost, ([Figure 6.19](#); top, All). If we instead postselected on the measurement outcomes, the operation is left as a probabilistic two-qubit gate, achieving the target operation only  $1/4$  of the time ([Figure 6.19](#); top, measurement outcome 10). Therefore, it is only when we combine real-time classical communication and feedforward that we can implement a deterministic teleported operation that performs the correct process independent of measurement outcome ([Figure 6.19](#), bottom).

### 6.8.5 Quantum Process tomography

Finally, for the fourth analysis we fully characterized the logical process for the teleported CNOT gate. We performed quantum process tomography on the two logical qubits and our reconstructed process matrices show qualitative agreement with the expected process ([Figure 6.20](#)). From the experimental reconstruction, we calculate a process fidelity of  $\mathcal{F}_{\text{pro}} = (68 \pm 2)\%$  without accounting for logical encoding or decoding steps that subtract from the extracted gate fidelity. With these corrections included, we infer a process fidelity of  $\mathcal{F}_{\text{gate}} = (79 \pm 2)\%$  for our teleported CNOT gate. To evaluate the experimental performance of the teleported gate, we assembled an error budget that combines the infidelity of each element of the gate, accounting for the known imperfections of our system. From this analysis ([section 6.10](#)), we expect a gate fidelity of  $\mathcal{F}_{\text{thy}} \approx (84 \pm 3)\%$ , which is consistent with experimental results. This indicates that

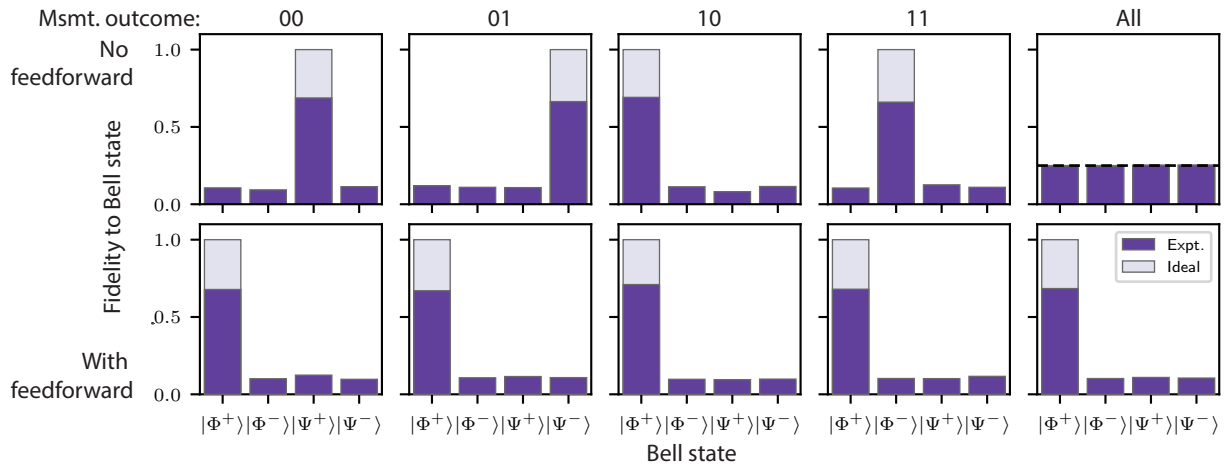


Figure 6.19 | **Effect of feedforward operations.** The teleported CNOT is applied to  $|\psi_{in}\rangle = (|0_L\rangle + |1_L\rangle)|0_L\rangle/\sqrt{2}$  and the fidelity of the resulting state to each of the four Bell states is extracted. Feedforward operations are not applied (top), and each measurement outcome  $\{00, 01, 10, 11\}$  results in a different Bell state. If all measurement results are compiled together, the resulting state is completely mixed (All). On the other hand, if the feedforward operations are applied (bottom), then the correct state  $|\Phi^+\rangle$  is found for every measurement outcome.

other nonidealities, such as residual interactions or imperfect system characterization, are smaller effects in our system. Indeed, as logical qubit operations—such as our teleported gate—are typically constructed from several distinct elements, it is necessary to experimentally verify that the compiled operation does not introduce unexpected errors. These considerations motivate efforts to construct and validate logical quantum systems both to reveal experimental nonidealities and to advance computational capabilities.

## 6.9 Extended Teleported CNOT results

### 6.9.1 Teleported CNOT performance

Figure 6.21 and Figure 6.22 show comprehensive process results for the teleported CNOT gate for both binomial and Fock encodings, respectively. In addition to the compiled results, we also provide the measurement outcome-conditioned processes to further highlight the role of classical communication and feedforward for the teleported gate.

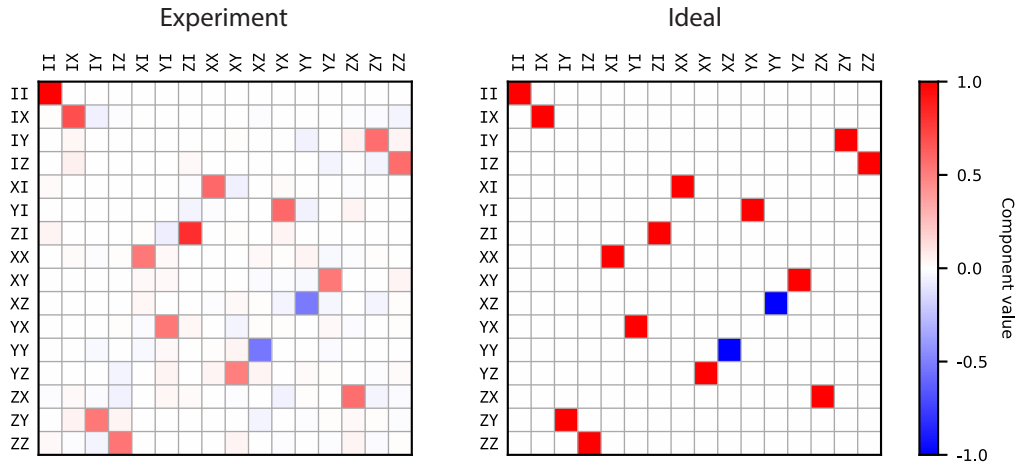


Figure 6.20 | **Quantum process tomography of the teleported CNOT gate.** We represent the quantum process  $\mathcal{R}_{\text{CNOT}}$  in the Pauli transfer representation, in which the process map is expressed in the Pauli basis:  $\vec{P}_{out} = \mathcal{R}_{\text{CNOT}} \vec{P}_{in}$ , given input and output state Pauli vectors  $\vec{P}_{in,out}$ . Agreement between the experimentally reconstructed (left) and ideal (right) process indicates the successful implementation of a deterministic teleported CNOT gate.

From these results, we quantify the performance of the teleported gate by calculating the process fidelity of the entire operation. We describe two quantities:

1.  $\mathcal{F}_{\text{pro}}$ : The process fidelity is extracted from the combined operation  $\mathcal{E}_{\text{all}} = \hat{U}_{\text{dec}} \hat{U}_{\text{CNOT}} \hat{U}_{\text{enc}}$ , and includes the effect of the encoding and decoding pulses in the fidelity.
2.  $\mathcal{F}_{\text{gate}}$ : The inferred gate fidelity is calculated from  $\mathcal{F}_{\text{pro}}$  relative to the fidelity of only the encode and decode pulses,  $\mathcal{F}_{\text{E+D}}$ . Explicitly,  $\mathcal{F}_{\text{gate}} = \mathcal{F}_{\text{pro}} + (1 - \mathcal{F}_{\text{E+D}})$ .

Additional details on the tomography method is provided in [section 5.5](#).

As described in [subsection 6.6.2](#), the encoding and decoding processes are accomplished through the use of optimal control pulses. The fidelities of the encode and decode operations are taken from [Table 6.3](#),

$$\text{Encode/decode (Binomial): } 1 - \mathcal{F}_{\text{E+D}} = (6.9 + 4.4)\% = 11.3\%$$

$$\text{Encode/decode (Fock): } 1 - \mathcal{F}_{\text{E+D}} = (4.1 + 2.3)\% = 6.4\%$$

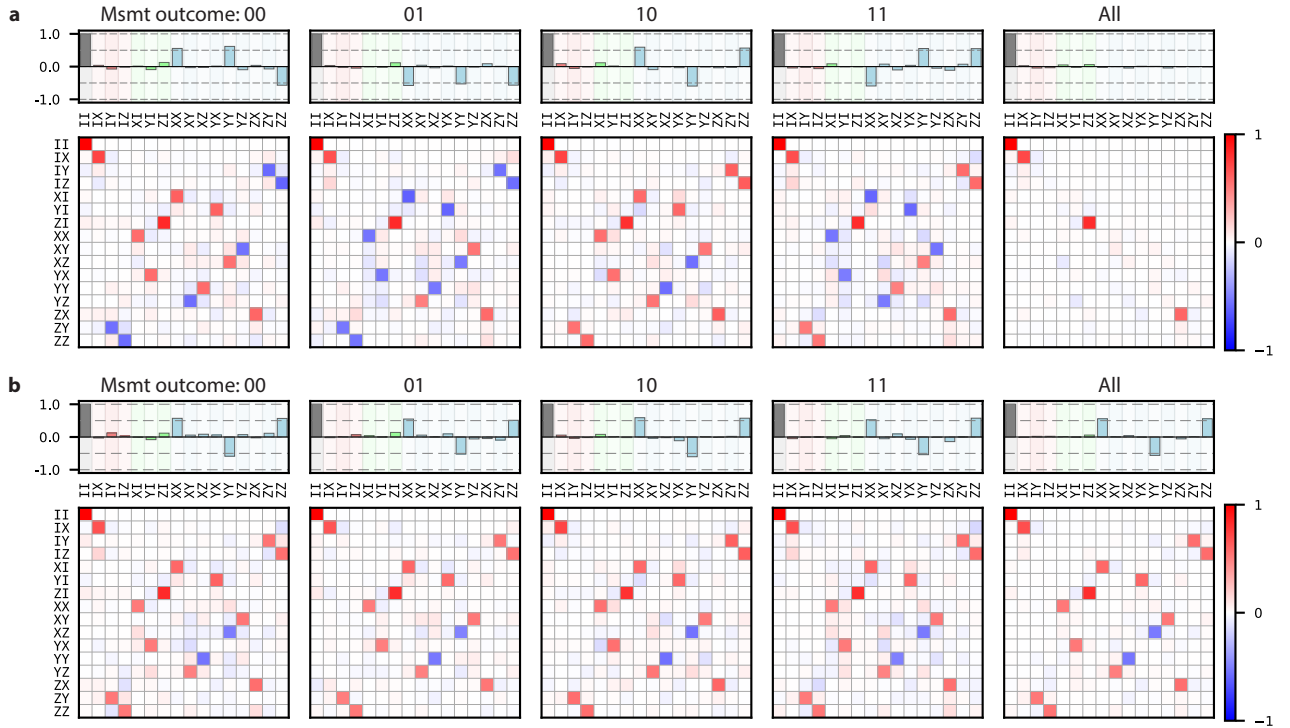


Figure 6.21 | **Extended Binomial QPT data.** For each panel, we plot both the process matrix in the Pauli transfer representation (below) as well as a reconstructed state represented in the Pauli basis (above). For the reconstructed state, we choose the input state  $(|0\rangle + |1\rangle)|0\rangle/\sqrt{2}$ , which should result in the following Bell state when the CNOT is applied:  $|\Phi^+\rangle = (|00\rangle + |11\rangle)/\sqrt{2}$ . The ideal process for each panel is represented by the dominant components taken to  $\pm 1$  and small components taken to 0. **a** Conditioned QPT results when the feedforward operations are not applied. The first four panels (labeled: 00, 01, 10, 11) represent the process conditioned on measurement outcome. Each qualitatively has the same features (e.g. the same non-zero elements of the process matrix); however, the differing signs between the four outcome indicates that each process is modified by single-qubit operations. When all measurement results are combined (labeled: All), most of the features are washed away and only certain Pauli operators are left invariant by the process:  $\{II, IX, ZI, ZX\}$ . Notably, these operators are exactly the feedforward operations that would normally be applied. This behavior can also be observed in the state tomography results (above), where each measurement outcome heralds a different Bell state ( $\{|\Psi^+\rangle, |\Psi^-\rangle, |\Phi^+\rangle, |\Phi^-\rangle\}$ ); when taken all together, the states add incoherently, resulting in a completely mixed state. **b** Conditioned QPT results when the feedforward operations are applied. Here, all measurement outcomes (00, 01, 10, 11) indicate the same process, that of the CNOT process. Therefore, when the measurement outcomes are all taken together (All), the compiled process is that of a CNOT gate. Each tomography setting in this dataset consists of 2500 averages; we perform a total of six pre- and post-rotations for QPT, leading to a total of  $6^4 = 1296$  experiments for QPT.

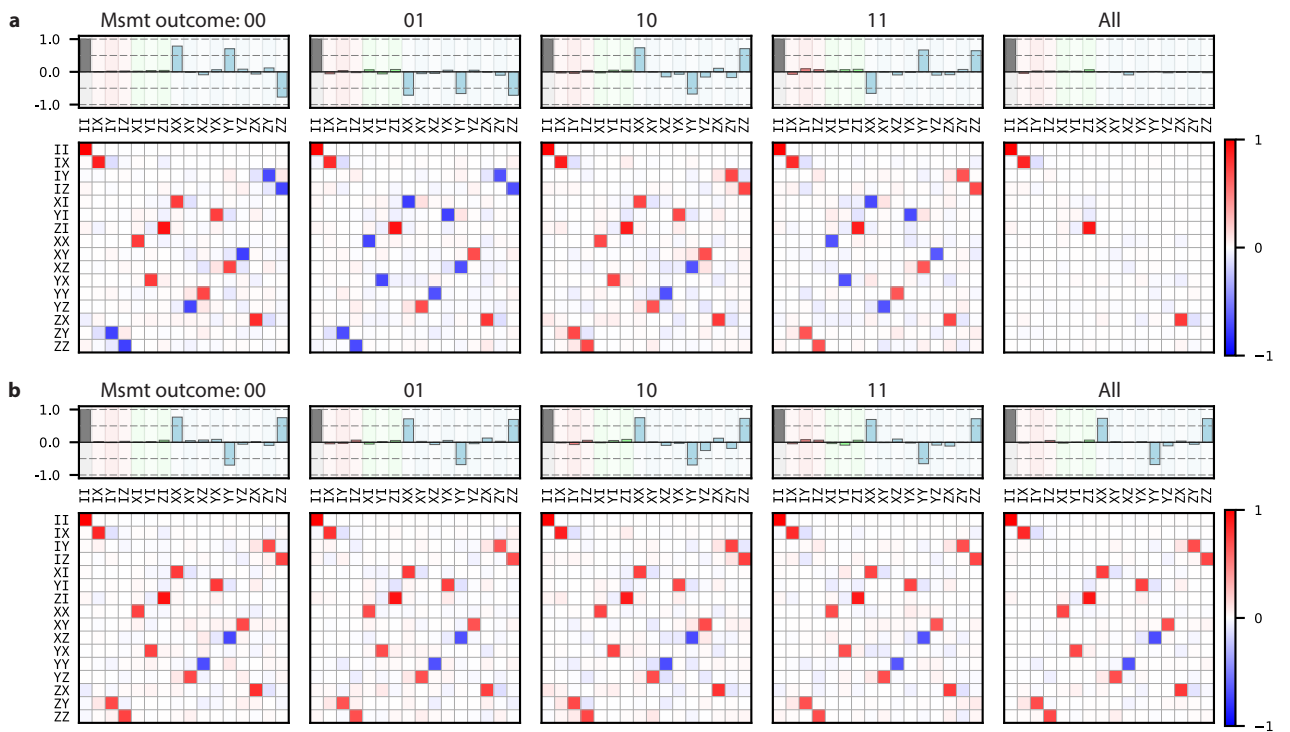


Figure 6.22 | **Extended Fock QPT data.** Data is presented in the same format as in [Figure 6.21](#).

Encoding	Feedforward (FF)	Measurement outcome, $\mathcal{F}_{\text{pro}} (\mathcal{F}_{\text{gate}})$ , (%)				
		00	01	10	11	All
Binomial	w/ FF	68 (79)	67 (78)	70 (81)	68 (79)	68 (79)
	no FF	71 (82)	68 (80)	70 (82)	68 (79)	N/A
Fock	w/ FF	82 (88)	79 (86)	81 (88)	79 (86)	80 (87)
	no FF	83 (89)	80 (87)	80 (87)	78 (84)	N/A

Table 6.4 | **Experimental process fidelities.** The raw process fidelity  $\mathcal{F}_{\text{pro}}$  and process fidelity corrected for finite tomography gate fidelity  $\mathcal{F}_{\text{gate}}$  are shown for each conditioned outcome (00 to 11) as well as the unconditioned results.

Here, we use the simulated process fidelities to conservatively estimate the gate fidelity; the experimentally extracted fidelities would result in a slightly high teleported CNOT gate fidelity. The compiled experimental results for the teleported CNOT are provided in [Table 6.4](#).

## 6.10 Error budget

In this section we provide further details on the estimates of gate error as presented in the Main Text. Our approach reflects and expands upon an error model described in Ref. [55]: the total gate error  $p_{\text{CNOT}}$  is given as the additive error contribution from each element of the teleported gate. For identical modules with the same error rates, we can write a simple expression for the total error rate:

$$p_{\text{CNOT}} = p_{\text{Bell}} + 2p_{\text{LO}} + 2p_{\text{Msmt}} + 2p_{\text{FF}}, \quad (6.21)$$

where  $p_{\text{Bell}}$ ,  $p_{\text{LO}}$ ,  $p_{\text{Msmt}}$ ,  $p_{\text{FF}}$  are the error probabilities for the entangled pair generation, the local operations, the communication qubit measurements, and the feedforward operations, respectively. We consider each element independently, estimating the total loss from a combination of experimentally measured and simulated quantities. Therefore, our estimate of the gate fidelity accounts for all known non-idealities of the system, providing an upper bound in the actual experimental performance. This estimate provides a useful benchmark to assess the potential for other unknown sources of loss. In the following subsections we will tabulate the combined errors for each module for each step, and we will use the symbol  $\tilde{p}_s$  to denote the error probability for step  $s$  for both modules 1 and 2. In relation to above,  $\tilde{p}_s \approx 2p_s$ . The error bars reported for

each element are estimated from systematic run-to-run variation.

### Communication qubit Bell pair

The communication qubit Bell pair is generated with the same pulse sequence independent of data qubit encoding. Our characterization of the Bell pair in [subsection 6.6.1](#) is performed when both data qubits are not encoded and left in the vacuum state, and serves as an upper bound to the Bell pair fidelity when used in the teleported CNOT. We set the error probability of the communication qubit Bell pair from this bare state fidelity,  $p_{\text{Bell}}$ :

$$\text{Comm. qubit Bell pair: } p_{\text{Bell}} = 1 - \mathcal{F}_{\text{Bell}} = (3 \pm 1) \%$$

When the Bell state generation sequence is applied during the teleported gate, the encoded data qubit state will induce a dispersion in the communication qubit frequency, potentially affecting the quality of communication qubit pulses. To account for this, we use short pulses ( $\sigma = 6$  ns) which have a bandwidth approaching two orders of magnitude larger than this dispersion. In principle, it is possible to characterize the communication qubit Bell pair when the data qubits are initialized in an encoded state; in practice, the presence of data qubit photons makes it difficult to perform reliable state tomography. As such, we use the above quantity for the purpose of this calculation.

### Local operations

We perform a local operation within each module, which are implemented via optimal control pulses. For the control module (module 1), we perform a local CNOT that is controlled by the data qubit, targeting the communication qubit. This operation is a photon-number parity mapping for the Fock encoding [\[158\]](#) and a “super-parity” (e.g.  $0 \pmod{4}$  vs.  $2 \pmod{4}$ ) mapping for the Binomial encoding; as such, the operation time for the binomial encoding (500 ns) is about half the length as compared to the Fock encoding (900 ns). The operation fidelities for the binomial and Fock encodings are 2% and 3%, respectively ([Table 6.3](#)). For the target module (module 2), the CNOT is now controlled by the communication qubit, targeting the data qubit. This is a highly

nontrivial operation: when the communication qubit is in  $|e\rangle$ , the operation flips the logical basis states,  $(|0\rangle + |4\rangle)/\sqrt{2} \leftrightarrow |2\rangle$ . As a result, in order to achieve a high fidelity operation, we use a 2000 ns optimal control pulse. The total local operation infidelity for the binomial and Fock encodings are  $(5 \pm 3)\%$  and  $(3 \pm 2)\%$ , respectively (Table 6.3). The errors are estimated from the range of measured coherence times.

In addition to the infidelity associated with each optimal control pulse, it is also important to consider the timing of the two pulses (Figure 6.7). In our experiment, both pulses start at the same time, but can have different pulse lengths. This alignment results in a delay between the local operation and the communication qubit measurement for module 1, during which the communication qubit may suffer a  $T_1$  error. Importantly,  $T_2$  errors are projected out during the subsequent  $\hat{Z}$  measurement and do not contribute to the infidelity of this component. This decay will cause an error in the measurement outcome assignment in the subsequent measurement, introducing additional infidelity to the 00 and 01 paths while reducing the probability of measuring outcomes 10 and 11. For the binomial and Fock encodings, we estimate this additional infidelity to be  $p_{T_1} \approx 0.025$  and  $0.002$ , respectively. Therefore, we can describe the path-dependent error probabilities,  $p_{LO,i}$  for  $i \in \{00, 01, 10, 11\}$ :

$$\text{Local operations (Binomial): } \tilde{p}_{LO,i} = (\{10, 10, 7, 7\} \pm 3)\%$$

$$\text{Local operations (Fock): } \tilde{p}_{LO,i} = (\{6, 6, 6, 6\} \pm 2)\%$$

### Communication qubit measurements

Measurement of the communication qubits can suffer from two general types of errors: assignment errors and measurement-decay errors. An assignment error is characterized by inferring the incorrect communication qubit state (e.g. assigning the state  $|eg\rangle$  as 00 instead of 10). Measurement-decay errors represent the case when the communication qubit undergoes a relaxation event during the measurement process. In the latter case, the resulting qubit state as well as the measurement outcome may not reflect the state prior to measurement. For the teleported CNOT, either error will lead to the application of incorrect communication qubit reset pulse as well as the incorrect feedforward operation in the teleported CNOT. Furthermore, if the communication

qubit is not properly reset to the ground state, then all subsequent optimal control pulses, including feedforward and decoding pulses, will fail. To holistically account for these errors, we use our results from [subsection 6.6.3](#), where we measurement the fidelity of resetting the communication qubits to the ground state. From this experiment we find the following measurement-outcome dependent errors,  $p_{M_{smt},i}$  for  $i \in 00, 01, 10, 11$ :

$$\text{Comm. qubit measurements: } \tilde{p}_{M_{smt},i} = (\{1, 4, 2, 6\}) \%$$

### Feedforward operations

Depending on measurement outcome, the teleported CNOT requires single-qubit feedforward operations, a  $\hat{Z}$  and  $\hat{X}$  operation on module 1 and 2, respectively. We implement the logical Z operation in software by updating the phase reference of the data qubit, which adds no time and has unit fidelity. Therefore, we only need to consider the infidelity when the  $\hat{X}$  feedforward operation is applied to module 2. This operation has an infidelity of 3% and 2% for the binomial and Fock encoding, respectively, and is applied only for outcomes 00 and 01. The additional error probabilities,  $\tilde{p}_{FF,i}$  associated with the feedforward operations are given as:

$$\text{Feedforward operations (Binomial): } \tilde{p}_{FF,i} = (\{3, 3, 0, 0\} \pm 1) \%$$

$$\text{Feedforward operations (Fock): } \tilde{p}_{FF,i} = (\{2, 2, 0, 0\} \pm 1) \%$$

### Total infidelity

From the previous sections, we extract the total gate error,  $p_{\text{CNOT}}$ , as

$$p_{\text{CNOT}} = p_{\text{Bell}} + \tilde{p}_{\text{LO}} + \tilde{p}_{M_{smt}} + \tilde{p}_{FF} \quad (6.22)$$

The results from this section are summarized in [Table 6.5](#). We extract conditioned errors for the teleported gate of  $p_{\text{CNOT},i} = (\{16, 20, 13, 16\} \pm 3) \%$  for the Binomial encoding and  $p_{\text{CNOT},i} = (\{12, 15, 12, 15\} \pm 2)$  for the Fock encoding. From these conditioned results, we expect total gate errors of  $p_{\text{CNOT}} = (16 \pm 3) \%$  and  $p_{\text{CNOT}} = (13 \pm 2) \%$  for the binomial and Fock encoding,

Encoding	Gate component	Measurement outcomes				
		00	01	10	11	All
Binomial	Bell generation, $p_{\text{Bell}}(\%)$	3	3	3	3	3
	Local operations, $p_{\text{LO},i}(\%)$	10	10	7	7	8
	Communication qubit measurements, $p_{\text{Msm},i}(\%)$	1	4	2	6	3
	Feedforward operations, $p_{\text{FF},i}(\%)$	3	3	0.0	0.0	2
	Total infidelity, $p_{\text{CNOT},i}(\%)$	17	20	12	16	16
Fock	Bell generation, $p_{\text{Bell}}(\%)$	3	3	3	3	3
	Local operations, $p_{\text{LO},i}(\%)$	6	6	6	6	6
	Communication qubit measurements, $p_{\text{Msm},i}(\%)$	1	4	2	6	3
	Feedforward operations, $p_{\text{FF},i}(\%)$	2	2	0	0	1
	Total infidelity, $p_{\text{CNOT},i}(\%)$	12	15	11	15	13

Table 6.5 | **Error budget, theory.**

respectively. From Table 6.4, our inferred gate infidelities are  $1 - \mathcal{F}_{\text{CNOT}}^{\text{inf}} = (21 \pm 2)\%$  and  $(13 \pm 2)\%$ , both of which are consistent with our error model.

### 6.10.1 Contributions to infidelity

By using numerical simulations, we have estimated the relative contributions of loss that limit the performance of the teleported CNOT. Finite  $T_2$  and  $T_1$  of the transmon qubits are the two dominant sources of infidelity in our experiment, accounting for roughly 70% and 25% of the total infidelity, respectively. In our implementation, the finite cavity lifetime accounts for 4% of the total infidelity, limiting the gate fidelity at 98%. However, single photon errors are, in principle, detectable through implementing a quantum error correction scheme, which has not been done in this implementation. At the level of our measurement precision, we are not able to observe significant limitations due to unexpected interactions or control errors.

## 6.11 Discussion

Building on our results, there exist well-defined prescriptions to further improve each element of the teleported gate. In the present implementation, the dominant source of infidelity is the finite coherence of both communication qubits ( $T_2 \approx 15 \mu\text{s}$ ), which accounts for about 70% of the

total gate error. Though increasing transmon coherence is a straightforward approach to improve gate performance, a more robust solution may be to pursue alternate implementations of the communication qubit itself. For example, replacing the transmon qubit with a high-Q cavity will directly address this dominant source of infidelity in the present experiment. Furthermore, recent work demonstrating local operations between two cavities [225] illustrates that a module containing error-correctable data and communication qubits can be realized without sacrificing quantum control. In addition to local operations, the performance of the teleported gate also depends on the quality of the shared entangled pair and communication qubit measurements. Since the shared entangled pair can be prepared prior to the teleported operation, the gate is agnostic to how the entanglement is generated. Therefore, the protocol can take advantage of a variety of approaches, including deterministic [226] and probabilistic [227] schemes, and should benefit from entanglement purification protocols [55, 228]. Measurements directly impact the performance of teleportation-based protocols, and strategies that boost measurement fidelity such as robust, repeated measurements [55] may be readily integrated into the teleported CNOT gate. Finally, since our implementation is compatible with various logical data qubit encodings, it may be possible to tailor the encoding to account for the dominant error channels associated with the gate (in the current implementation, codespace leakage errors), potentially addressing issues of fault-tolerance. Importantly, these improvements to our implementation may be pursued while preserving the framework of the teleported gate protocol.

This result is not only the first demonstration of a gate between logical qubits, but also the first demonstration of a deterministic teleported two-qubit gate. A compelling advantage of our work is that the teleported gate is itself modular and uses relatively modest elements, all of which are part of the standard toolbox necessary for quantum computation in general. Therefore, ongoing progress to improve any of the elements will directly increase gate performance. Furthermore, the teleported CNOT protocol used in this work is but one example of an extensive family of two-qubit operations that may be implemented using these same resources [44, 55, 210]. Such teleportation-based gates are important primitives for the implementation of a modular architecture and may be part of a broader approach to fault-tolerant quantum computation [44, 92, 229]. The next step

---

will be to demonstrate nonlocal teleported gates between spatially separate modules, requiring remote entanglement. Building on our results and recent demonstrations of remote entanglement in cQED systems [201, 202], it should be possible to integrate these technologies in the future.

# 7

## Conclusions and perspectives

Superconducting qubits have made steady and impressive progress in the past several years towards advancing our understanding and our control of these increasingly complex systems. We have reported our efforts to capitalize on these achievements, which has led to the demonstration of a teleported gate. Moving forward, it will be increasingly important to consider how we might build off of our proof-of-principle demonstrations to achieve more lofty goals. These new milestones will require the careful combination of physics and engineering as we increase both system complexity as well as computational capabilities of our quantum systems. As the field of quantum information processing moves from an “age of adolescence” into an “age of maturity”<sup>1</sup>, our future goals will become qualitatively different and ever more demanding. This development indicates that there will be more exciting developments in the years to come. In the final sections of this thesis, we will consider some extensions of the work described in this thesis, focusing on the future directions toward the quantum modular architecture.

---

1. This assessment of the state of quantum information processing was heard first at the IBM ThinkQ 2015 conference during a presentation by Isaac Chuang.

## 7.1 Future work toward the quantum modular architecture

### 7.1.1 Remote modules

As mentioned in [chapter 6](#), perhaps one of the most important future directions for the teleported gate will be to demonstrate the gate between two remote modules. This extension is crucial for the development of a distributed quantum network of modules, and further, will completely eliminate any residual interactions between modules. There will be additional challenges incurred in connecting physically separate modules, particularly in the quality of the remote entangled pair, which directly impacts the performance of any teleported operation. It is critical to generate high-fidelity entangled pairs for the quantum modular architecture. Current implementations for remote entanglement, while promising demonstrations, generate entangled pairs with too low fidelity to be used for the teleported gate.

There have been several demonstrations of remote entanglement generation in cQED, broadly separated into two categories: entanglement-by-measurement and direct state transfer. One recent demonstration of the former [\[201\]](#) realized the heralded entanglement of two transmon qubits using a concurrent protocol with flying single-photon states and a novel microwave single-photon detector. The detector acts as a which-path eraser by performing a joint measurement of the two qubits. Such a scheme has the advantage that it is robust to photon loss, the loss of a flying photon results in a detectable failed attempt.

Another promising approach first proposed in [\[226\]](#) and experimentally demonstrated in cQED in [\[142, 203, 230\]](#) generated entanglement between two remote qubits through direct state transfer from a sender module to a receiver module. The state from the sender is partially converted into a flying state, traveling through a coaxial transmission line before being absorbed by the receiver module. This method for remote entanglement is nominally a deterministic process, but crucially relies on a low-loss communication channel. This loss can, in principle, be tolerated by encoding the transmitted quantum information using error-correctable states [\[142\]](#). Efficient error correction on the receiver can be used to restore the state if an error had occurred during the transfer.

As the teleported gate performance is directly impacted by the fidelity of the entangled pair, improvements to the quality of this entanglement may still be required. One approach to generate these high-fidelity entangled pairs is to utilize entanglement purification (or distillation) [55, 228, 231]. An entanglement purification protocol describes a process by which one can probabilistically generate a higher fidelity entangled state from a collection of low fidelity entangled states. One can also think of such a scheme as a quantum error detection. We leave the description of the purification protocol to be described elsewhere (e.g. in [55]), noting that these protocols use the same elements as the teleported gate. Instead we will on some considerations for the design of a purification protocol within the modular architecture.

Implementing a purification protocol will incur additional complexity for the communication qubits within each module. Such a module will require, at minimum, two communication qubits as the simplest purification protocol requires two entangled pairs. We can envision two approaches to generate multiple entangled pairs and to connect two such modules together. First, if we use a single communication channel to connect the two modules, then we will have to generate the two entangled pairs sequentially. This requires operations to swap the entangled state from one communication qubit pair to the other. While the second entangled pair is generated, the first pair will have to be stored in a memory mode. Second, each entangled pair could be generated using a dedicated communication channel, thus enabling parallelism in the initial entanglement generation. A sequential approach has the benefit of fewer communication channels at the cost of increasing the requirements for the design of the module. The parallel approach can have benefits in terms of requiring fewer operations and speed at the cost of potentially introducing additional error mechanisms.

Entanglement purification protocols typically address bit-flip ( $\hat{X}$ ) and/or phase-flip ( $\hat{Z}$ ) errors. However, in a physical implementation the exact error model will depend crucially on the exact implementation of the qubits used (e.g. transmon or cavity), the initial entanglement generation protocol, and the local operations and measurements required for the purification purification. Tailoring the purification protocol to the actual errors in the entangled pairs will be necessary if there is any expectation to improve the fidelity of an entangled pair shared between two modules.

There are likely specialized entanglement and purification protocols that directly take advantage of our specific cavity-based cQED hardware. In particular, the multi-level structure of the cavity can encode multiple qubits of information; perhaps, this can allow for a hardware-efficient entanglement generation protocol where a single pair of cavities can be used to perform the entanglement purification protocol.

### 7.1.2 Towards error-correctable logical gates

So far, logical qubits have been used to demonstrate quantum error correction [21] and logical operations [166, 185] in similar, yet separate, experimental systems. A necessary capability moving forward is implementing a logical qubit that can perform quantum error correction *and* perform single- and two-qubit logical gates. Such a goal is an important step toward fault-tolerant quantum computation. Crucial to the success of developing and implementing error-correctable logical gates is understanding what types of errors to correct. For example, the logical encoding for the teleported gate is amenable to a QEC protocol that corrects against single photon loss, an error mechanism that is dominant when the logical qubit is used as a quantum memory. On the other hand, the dominant errors that the teleported gate induces are codespace leakage errors. Addressing these errors will require sophisticated erasure-correction codes to detect (and perhaps correct) when we suffer an error during the gate. Therefore, while it may suffice (and indeed be necessary) to protect these logical qubits from single photon loss when the logical qubit is idling, such a QEC protocol may not be sufficient when performing computations on the logical qubits. Therefore, an outstanding task toward is to develop logical gates and QEC protocols that complement each other to address the actual errors that arise during a computation.

We can also point to several intermediate goals that will improve the performance of our logical operations as we continue to develop techniques toward these error-correctable logical gates. The transmon qubit functions as both the communication qubit and an ancilla for implementing logical operations on the data qubits. As it is the system's least coherent element, we have found that our teleported gate performance is ultimately limited by the transmon coherence. Improvements in the transmon coherence will naturally lead to a higher-fidelity teleported operation.

An alternative direction for improving the teleported gate is to investigate whether it is possible to implement optimal control pulses that are less sensitive to the coherence properties of the transmon, perhaps by using higher levels of the transmon qubit or by using off-resonant drives that do not directly excite the transmon qubit.

Another possibility that warrants exploration is to implement the required local operations through driving parametrically-activated multi-photon transitions (see related work in [137, 138, 142, 201, 203, 232]). Indeed, the proposal in [233] for universal quantum computation with error-correctable Schrödinger cat states describes how to perform universal quantum computation using a combination of engineered two-photon dissipative processes combined with displacements. Here, the transmon is not directly excited and serves as an off-resonant, nonlinear resource for the cavity. Furthermore, ongoing work in realizing these multi-photon processes may even lead to logical operations that are tolerant to transmon loss.

### 7.1.3 Building the quantum module

The requirements for implementing teleported operations between modules provides a simple, yet comprehensive checklist for determining the functionality required for a module. A module requires: (1) data qubit(s) for quantum information storage and processing; (2) communication qubits for interfacing the data qubit with the outside world; (3) the ability to perform high-fidelity local operations between them; (4) high-fidelity measurements of the communication qubits; and (5) robust entanglement generation between the communication qubits. Our demonstrated gate represents an existence proof that it is indeed possible to assemble such disparate components (3D cavities and transmons) that perform distinct functions (long-lived quantum memory vs. short-lived readout resonator) into modules. Furthermore, we showed that it is possible to assemble several (separately implemented) computational capabilities together to perform a complex algorithm in a way that performs as expected from the individual parts. This separation of functions is one of the main motivations for pursuing the quantum modular architecture. Given our discussions from the previous sections, it is likely that each of these elements will undergo significant modifications from the current realization used for the teleported gate experiment. However

the approach for building the modules will remain the same: designing, testing, and validating building blocks individually, the combining them to explore the capabilities and shortcomings of the integrated module.

As a few concrete steps moving forward, we can also consider hardware modifications to the communication qubit. One possibility is to replace the transmon for a high-coherence 3D cavity, which would increase the coherence time of the communication qubit by over an order of magnitude and allow for more sophisticated communication qubit encodings. A cavity-based communication qubit will also result in a module that is compatible with an error-correctable remote entanglement scheme as described before [142]. This modification introduces additional complexities in the design and requirements for the module. First, we will have to build an appropriate interface between the cavity-based communication qubit to the communication channel in such a way that enables a remote entanglement protocol that does not adversely affect other parts of the module. Second, to implement local operations, we will require local operations that are now between two cavity modes. These local cavity operations require a mixing element (e.g. transmon) to couple the two cavities together. Recent [225] and ongoing work (Gao et al. 2018 in prep) indicate that this is a capability that can be readily achieved.

Additionally, as many of these multi-cavity operations rely on the four-wave mixing property of the Josephson junction, there has been recent work in realizing three-wave mixing elements such as the superconducting non-linear asymmetric inductive (SNAIL) elements [234] that may be used to enable the requisite interactions. Such a three-wave mixing interaction can have certain advantages over the customary four-wave version, for example, eliminating undesired frequency shifts that are present in a four-wave mixing element. Integration of such a new quantum circuit will require addressing several new complications, most pressing of which is the to introduce magnetic flux to bias the SNAIL element without spoiling any high coherence elements within the same package. Far from a impediment, the ability to construct and assemble novel quantum circuits using Josephson junctions, inductors, and capacitors (and when necessary, resistors) is a distinct and powerful trait of superconducting qubits.

### 7.1.4 Connecting the modules

One of the least-developed components of the modular architecture is the way we will distribute entanglement across throughout the network. There are significant architectural questions that need to be addressed, most important of which is determining the connectivity of the quantum network. Whether the connections between modules are fixed or programmable will have dramatic consequences on the design and implementation of quantum algorithms. It is currently an open question regarding the required connectivity of such a router, though it is believed that a quantum processor with higher-connectivity requires fewer gates (and presumably higher performance as a result) to implement a given algorithm [219]. Therefore, defining the properties and constructing such a quantum router is an important future step toward the development of the modular architecture. There are other practical questions in building a quantum signal routing system with low-enough dissipation, sufficient bandwidth and directionality will also influence the scheme for implementing a particular scheme for remote entanglement as well as dictating the design of the communication qubit-channel interface.

### 7.1.5 Tools to applications

Finally, moving another step beyond the practical and design aspects of building a modular quantum computer, we must consider *how* we want to use it to eventually solve practical problems. From choosing a computationally-interesting problem for a quantum computer to solve, we will have to tailor the algorithm to the modular architecture in a way that takes advantage of the connectivity and high-quality components that comprise the quantum network. Carefully defining the short-term, mid-term, and long-term applications will play an important role in dictating the implementation of the modular architecture.

## 7.2 Closing remarks

While there are many open questions that must be addressed, the prospects for realizing a general-purpose quantum computing are quite encouraging. One reason for this optimistic outlook stems

from the rapid and remarkable progress that the field has achieved in terms understanding and controlling these increasingly complex quantum devices. Indeed, at the beginning of this thesis work, it would be difficult to imagine the level of sophistication and the achievements that is standard today. One can only imagine the discoveries and accomplishments in the years to come. It is, therefore, exciting, and humbling, to have contributed a small part toward this endeavor. In closing, we return to an early assessment for prospects of quantum information processing, and we expect this statement to continue to hold true in the years to come:

“Now the case is considerably stronger that, in principle, there is no fundamental obstacle to building a functioning quantum computer that is capable of performing computationally interesting tasks.” - J. Preskill [8]

# Bibliography

- [1] G. Dyson, *Turing's Cathedral: The Origins of the Digital Universe* (Vintage Books, 2012).
- [2] D. Silver, A. Huang, C. J. Maddison, A. Guez, L. Sifre, G. van den Driessche, J. Schrittwieser, I. Antonoglou, V. Panneershelvam, M. Lanctot, S. Dieleman, D. Grewe, J. Nham, N. Kalchbrenner, I. Sutskever, T. Lillicrap, M. Leach, K. Kavukcuoglu, T. Graepel, and D. Hassabis, *Nature* **529**, 484 (2016).
- [3] R. P. Feynman, *International Journal of Theoretical Physics* **21**, 467 (1982).
- [4] D. Deutsch, *Proceedings of the Royal Society A: Mathematical, Physical and Engineering Sciences* **400**, 97 (1985).
- [5] P. W. Shor, *SIAM Journal on Computing* **26**, 1484 (1997).
- [6] L. K. Grover, in *Proceedings of the twenty-eighth annual ACM symposium on Theory of computing - STOC '96* (ACM Press, New York, New York, USA, 1996) pp. 212–219.
- [7] C. H. Bennett, E. Bernstein, G. Brassard, and U. Vazirani, *SIAM Journal on Computing* **26**, 1510 (1997).
- [8] J. Preskill, *Proceedings of the Royal Society A: Mathematical, Physical and Engineering Sciences* **454**, 469 (1998).
- [9] S. Aaronson, (2005), [arXiv:0502072 \[quant-ph\]](https://arxiv.org/abs/0502072) .
- [10] S. Aaronson, *Scientific American* **298**, 62 (2008).
- [11] P. W. Shor, *Physical Review A* **52**, R2493 (1995).
- [12] D. P. DiVincenzo and P. W. Shor, *Physical Review Letters* **77**, 3260 (1996).
- [13] A. R. Calderbank and P. W. Shor, *Physical Review A* **54**, 1098 (1996).
- [14] D. Gottesman, *Stabilizer Codes and Quantum Error Correction*, Ph.D. thesis, California Institute of Technology (1997), [arXiv:9705052 \[quant-ph\]](https://arxiv.org/abs/9705052) .
- [15] J. Blumoff, *Multiqubit experiments in 3D circuit quantum electrodynamics*, Ph.D. thesis, Yale University (2017).
- [16] M. A. Nielsen and I. L. Chuang, *Quantum Computation and Quantum Information: 10th Anniversary Edition*, 10th ed. (Cambridge University Press, New York, NY, USA, 2011).

- [17] M. M. Wilde, *Quantum Information Theory* (Cambridge University Press, Cambridge, 2013) [arXiv:1106.1445](#) .
- [18] J. Preskill, in *Lecture Notes for Ph219/CS219*, July (2015).
- [19] R. Glauber, *Physical Review Letters* **10**, 84 (1963).
- [20] S. Haroche and J. M. Raimond, *Exploring the Quantum: Atoms, Cavities, and Photons* (Oxford Univ. Press, Oxford, 2006).
- [21] N. Ofek, A. Petrenko, R. Heeres, P. Reinhold, Z. Leghtas, B. Vlastakis, Y. Liu, L. Frunzio, S. M. Girvin, L. Jiang, M. Mirrahimi, M. H. Devoret, and R. J. Schoelkopf, *Nature* **536**, 441 (2016).
- [22] S. Bravyi and A. Kitaev, *Physical Review A* **71**, 022316 (2005).
- [23] J. Cohen, W. C. Smith, M. H. Devoret, and M. Mirrahimi, *Physical Review Letters* **119**, 060503 (2017).
- [24] V. B. Braginsky and F. Y. Khalili, *Reviews of Modern Physics* **68**, 1 (1996).
- [25] V. B. Braginsky and F. Y. Khalili, *Quantum Measurement*, edited by K. S. Thorne (Cambridge University Press, Cambridge, 1992).
- [26] J. Preskill, in *Lecture Notes for Physics 219: Quantum Information and Computation*, Vol. 1 (2004) Chap. 1, pp. 3–22.
- [27] W. Gerlach and O. Stern, *Zeitschrift fur Physik* **9**, 349 (1922).
- [28] R. P. Feynman, *The Feynman lectures on physics* (Reading, Mass. : Addison-Wesley Pub. Co., c1963-1965., 1963).
- [29] A. Einstein, B. Podolsky, and N. Rosen, *Physical Review* **47**, 777 (1935).
- [30] S. J. Freedman and J. F. Clauser, *Physical Review Letters* **28**, 938 (1972).
- [31] A. Aspect, P. Grangier, and G. Roger, *Physical Review Letters* **49**, 91 (1982).
- [32] A. Aspect, J. Dalibard, and G. Roger, *Physical Review Letters* **49**, 1804 (1982).
- [33] J. S. Bell, *Physics* **1**, 195 (1964).
- [34] J. F. Clauser, M. A. Horne, A. Shimony, and R. A. Holt, *Physical Review Letters* **23**, 880 (1969).
- [35] C. H. Bennett, G. Brassard, C. Crépeau, R. Jozsa, A. Peres, and W. K. Wootters, *Physical Review Letters* **70**, 1895 (1993).
- [36] H.-J. Briegel, W. Dür, J. I. Cirac, and P. Zoller, *Physical Review Letters* **81**, 5932 (1998), [arXiv:1511.00407](#) .
- [37] H. J. Kimble, *Nature* **453**, 1023 (2008).

- [38] D. Bouwmeester, J.-W. Pan, K. Mattle, M. Eibl, H. Weinfurter, and A. Zeilinger, [Nature](#) **390**, 575 (1997).
- [39] A. Furusawa, J. L. Sørensen, S. L. Braunstein, C. A. Fuchs, H. J. Kimble, and E. S. Polzik, [Science](#) **282**, 706 (1998).
- [40] M. Riebe, H. Häffner, C. F. Roos, W. Hänsel, J. Benhelm, G. P. T. Lancaster, T. W. Körber, C. Becher, F. Schmidt-Kaler, D. F. V. James, and R. Blatt, [Nature](#) **429**, 734 (2004).
- [41] X.-s. Ma, S. Zotter, J. Kofler, R. Ursin, T. Jennewein, Č. Brukner, and A. Zeilinger, [Nature Physics](#) **8**, 480 (2012).
- [42] J.-G. Ren, P. Xu, H.-L. Yong, L. Zhang, S.-K. Liao, J. Yin, W.-Y. Liu, W.-Q. Cai, M. Yang, L. Li, K.-X. Yang, X. Han, Y.-Q. Yao, J. Li, H.-Y. Wu, S. Wan, L. Liu, D.-Q. Liu, Y.-W. Kuang, Z.-P. He, P. Shang, C. Guo, R.-H. Zheng, K. Tian, Z.-C. Zhu, N.-L. Liu, C.-Y. Lu, R. Shu, Y.-A. Chen, C.-Z. Peng, J.-Y. Wang, and J.-W. Pan, [Nature](#) **549**, 70 (2017).
- [43] S. Pirandola, J. Eisert, C. Weedbrook, A. Furusawa, and S. L. Braunstein, [Nature Photonics](#) **9**, 641 (2015).
- [44] D. Gottesman and I. L. Chuang, [Nature](#) **402**, 390 (1999).
- [45] W. K. Wootters, [Physical Review Letters](#) **80**, 2245 (1998).
- [46] R. Jozsa, [Journal of Modern Optics](#) **41**, 2315 (1994).
- [47] A. Gilchrist, N. K. Langford, and M. A. Nielsen, [Physical Review A](#) **71**, 062310 (2005).
- [48] P. Aliferis, D. Gottesman, and J. Preskill, (2005), [arXiv:0504218 \[quant-ph\]](#) .
- [49] A. Uhlmann, [Reports on Mathematical Physics](#) **9**, 273 (1976).
- [50] J. Z. Blumoff, K. Chou, C. Shen, M. Reagor, C. Axline, R. T. Brierley, M. P. Silveri, C. Wang, B. Vlastakis, S. E. Nigg, L. Frunzio, M. H. Devoret, L. Jiang, S. M. Girvin, and R. J. Schoelkopf, [Physical Review X](#) **6**, 031041 (2016).
- [51] A. Jamiołkowski, [Reports on Mathematical Physics](#) **3**, 275 (1972).
- [52] M.-D. Choi, [Linear Algebra and its Applications](#) **10**, 285 (1975).
- [53] D. P. DiVincenzo, [Fortschritte der Physik](#) **48**, 771 (2000), [arXiv:0002077v3 \[arXiv:quant-ph\]](#) .
- [54] C. M. Dawson and M. A. Nielsen, [Quantum Info. Comput.](#) **6**, 81 (2006).
- [55] L. Jiang, J. M. Taylor, A. S. Sørensen, and M. D. Lukin, [Physical Review A](#) **76**, 062323 (2007).
- [56] E. Knill and R. Laflamme, [Physical Review A](#) **55**, 900 (1997).
- [57] D. Aharonov and M. Ben-Or, [Arxiv preprint](#) (1996), [arXiv:9611025 \[quant-ph\]](#) .

- [58] D. Gottesman, (2009), [arXiv:arXiv:0904.2557v1](https://arxiv.org/abs/0904.2557v1) .
- [59] D. Bacon, CSE 599d - Quantum Computing Lecture Notes, University of Washington (2006).
- [60] A. G. Fowler, A. M. Stephens, and P. Groszkowski, *Physical Review A - Atomic, Molecular, and Optical Physics* **80**, 1 (2009), [arXiv:arXiv:0803.0272v4](https://arxiv.org/abs/0803.0272v4) .
- [61] D. S. Wang, A. G. Fowler, A. M. Stephens, and L. C. L. Hollenberg, *Quantum Info. Comput.* **10**, 456 (2010).
- [62] J. M. Chow, J. M. Gambetta, A. D. Córcoles, S. T. Merkel, J. A. Smolin, C. Rigetti, S. Poletto, G. A. Keefe, M. B. Rothwell, J. R. Rozen, M. B. Ketchen, and M. Steffen, *Physical Review Letters* **109**, 060501 (2012).
- [63] R. Barends, J. Kelly, A. Megrant, A. Veitia, D. Sank, E. Jeffrey, T. C. White, J. Mustus, A. G. Fowler, B. Campbell, Y. Chen, Z. Chen, B. Chiaro, A. Dunsworth, C. Neill, P. O'Malley, P. Roushan, A. Vainsencher, J. Wenner, A. N. Korotkov, A. N. Cleland, and J. M. Martinis, *Nature* **508**, 500 (2014).
- [64] C. J. Ballance, T. P. Harty, N. M. Linke, M. A. Sepiol, and D. M. Lucas, *Physical Review Letters* **117**, 060504 (2016).
- [65] L. M. K. Vandersypen and I. L. Chuang, *Reviews of Modern Physics* **76**, 1037 (2005).
- [66] J. I. Cirac and P. Zoller, *Physical Review Letters* **74**, 4091 (1995).
- [67] C. Monroe, D. M. Meekhof, B. E. King, W. M. Itano, and D. J. Wineland, *Physical Review Letters* **75**, 4714 (1995).
- [68] D. Leibfried, R. Blatt, C. Monroe, and D. Wineland, *Reviews of Modern Physics* **75**, 281 (2003).
- [69] J. Benhelm, G. Kirchmair, C. F. Roos, and R. Blatt, *Nature Physics* **4**, 463 (2008).
- [70] M. Saffman, T. G. Walker, and K. Mølmer, *Reviews of Modern Physics* **82**, 2313 (2010), [arXiv:arXiv:0909.4777v2](https://arxiv.org/abs/0909.4777v2) .
- [71] J. M. Raimond, C. Sayrin, S. Gleyzes, I. Dotsenko, M. Brune, S. Haroche, P. Facchi, and S. Pascazio, *Physical Review Letters* **105**, 213601 (2010).
- [72] D. J. Wineland, *Annalen der Physik* **525**, 739 (2013).
- [73] C. Monroe and J. Kim, *Science* **339**, 1164 (2013).
- [74] E. Knill, R. Laflamme, and G. J. Milburn, *Nature* **409**, 46 (2001).
- [75] P. Kok, W. J. Munro, K. Nemoto, T. C. Ralph, J. P. Dowling, and G. J. Milburn, *Reviews of Modern Physics* **79**, 135 (2007), [arXiv:0512071 \[quant-ph\]](https://arxiv.org/abs/0512071) .
- [76] D. Loss and D. P. DiVincenzo, *Physical Review A* **57**, 120 (1998).

- [77] B. E. Kane, *Nature* **393**, 133 (1998).
- [78] R. Hanson, L. P. Kouwenhoven, J. R. Petta, S. Tarucha, and L. M. K. Vandersypen, *Reviews of Modern Physics* **79**, 1217 (2007), [arXiv:0610433 \[cond-mat\]](#) .
- [79] F. A. Zwanenburg, A. S. Dzurak, A. Morello, M. Y. Simmons, L. C. Hollenberg, G. Klimeck, S. Rogge, S. N. Coppersmith, and M. A. Eriksson, *Reviews of Modern Physics* **85**, 961 (2013), [arXiv:arXiv:1206.5202v1](#) .
- [80] S. Haroche, *Reviews of Modern Physics* **85**, 1083 (2013).
- [81] D. D. Awschalom, L. C. Bassett, A. S. Dzurak, E. L. Hu, and J. R. Petta, *Science (New York, N.Y.)* **339**, 1174 (2013).
- [82] M. V. G. Dutt, L. Childress, L. Jiang, E. Togan, J. Maze, F. Jelezko, A. S. Zibrov, P. R. Hemmer, and M. D. Lukin, *Science* **316**, 1312 (2007).
- [83] P. C. Maurer, G. Kucsko, C. Latta, L. Jiang, N. Y. Yao, S. D. Bennett, F. Pastawski, D. Hunger, N. Chisholm, M. Markham, D. J. Twitchen, J. I. Cirac, and M. D. Lukin, *Science (New York, N.Y.)* **336**, 1283 (2012).
- [84] L. Gordon, J. R. Weber, J. B. Varley, A. Janotti, D. D. Awschalom, and C. G. Van de Walle, *MRS Bulletin* **38**, 802 (2013), [arXiv:1003.1754](#) .
- [85] N. Kalb, A. A. Reiserer, P. C. Humphreys, J. J. W. Bakermans, S. J. Kamerling, N. H. Nickerson, S. C. Benjamin, D. J. Twitchen, M. Markham, and R. Hanson, *Science* **356**, 928 (2017).
- [86] M. H. Devoret and R. J. Schoelkopf, *Science* **339**, 1169 (2013).
- [87] I. L. Chuang, L. M. K. Vandersypen, X. Zhou, D. W. Leung, and S. Lloyd, *Nature* **393**, 143 (1998).
- [88] D. G. Cory, M. D. Price, W. Maas, E. Knill, R. Laflamme, W. H. Zurek, T. F. Havel, and S. S. Somaroo, *Physical Review Letters* **81**, 2152 (1998).
- [89] M. A. Nielsen, E. Knill, and R. Laflamme, *Nature* **396**, 52 (1998).
- [90] T. P. Harty, M. A. Sepiol, D. T. C. Allcock, C. J. Ballance, J. E. Tarlton, and D. M. Lucas, *Physical Review Letters* **117**, 140501 (2016).
- [91] D. Kielpinski, C. Monroe, and D. J. Wineland, *Nature* **417**, 709 (2002).
- [92] C. Monroe, R. Raussendorf, A. Ruthven, K. R. Brown, P. Maunz, L.-M. Duan, and J. Kim, *Physical Review A* **89**, 022317 (2014).
- [93] C.-W. Chou, J. Laurat, H. Deng, K. S. Choi, H. de Riedmatten, D. Felinto, and H. J. Kimble, *Science* **316**, 1316 (2007).
- [94] S. Ritter, C. Nölleke, C. Hahn, A. Reiserer, A. Neuzner, M. Uphoff, M. Mücke, E. Figueroa, J. Bochmann, and G. Rempe, *Nature* **484**, 195 (2012).

- [95] W. Pfaff, B. J. Hensen, H. Bernien, S. B. van Dam, M. S. Blok, T. H. Taminiau, M. J. Tiggelman, R. N. Schouten, M. Markham, D. J. Twitchen, and R. Hanson, *Science* **345**, 532 (2014).
- [96] A. Wallraff, D. I. Schuster, A. Blais, L. Frunzio, R. S. Huang, J. Majer, S. Kumar, S. M. Girvin, and R. J. Schoelkopf, *Nature* **431**, 162 (2004).
- [97] J. Majer, J. M. Chow, J. M. Gambetta, J. Koch, B. R. Johnson, J. A. Schreier, L. Frunzio, D. I. Schuster, A. A. Houck, A. Wallraff, A. Blais, M. H. Devoret, S. M. Girvin, and R. J. Schoelkopf, *Nature* **449**, 443 (2007).
- [98] D. I. Schuster, *Vasa*, Ph.D. thesis (2007).
- [99] M. D. Reed, *Entanglement and Quantum Error Correction with Superconducting Qubits*, Ph.D. thesis, Yale University (2013).
- [100] S. M. Girvin, (2013), [arXiv:1302.5842](https://arxiv.org/abs/1302.5842) .
- [101] U. Vool and M. Devoret, *International Journal of Circuit Theory and Applications* **45**, 897 (2017), [arXiv:1610.03438](https://arxiv.org/abs/1610.03438) .
- [102] A. Caldeira and A. Leggett, *Annals of Physics* **149**, 374 (1983).
- [103] B. Josephson, *Physics Letters* **1**, 251 (1962).
- [104] B. D. Josephson, *Reviews of Modern Physics* **46**, 251 (1974).
- [105] M. Devoret, in *Fluctuations Quantiques/Quantum Fluctuations*, edited by S. Reynaud, E. Giacobino, and J. Zinn-Justin (Elsevier, New York, 1997) pp. 351 – 386.
- [106] S. M. Girvin, in *Quantum Machines: Measurement and Control of Engineered Quantum Systems* (Oxford University Press, 2014) pp. 113–256.
- [107] S. M. Girvin, M. H. Devoret, and R. J. Schoelkopf, *Physica Scripta* **T137**, 014012 (2009).
- [108] T. Van Duzer, *Principles of Superconductive Devices and Circuits*, 2nd ed., edited by P. Hall (New York, 1998).
- [109] M. Tinkham, *Introduction to Superconductivity: Second Edition (Dover Books on Physics) (Vol i)*, second ed. (Dover Publications, 2004).
- [110] G. J. Dolan, *Applied Physics Letters* **31**, 337 (1977).
- [111] F. Lecocq, I. M. Pop, Z. Peng, I. Matei, T. Crozes, T. Fournier, C. Naud, W. Guichard, and O. Buisson, *Nanotechnology* **22**, 315302 (2011).
- [112] J. M. Martinis, *Quantum Information Processing* **8**, 81 (2009).
- [113] J. M. Martinis, M. H. Devoret, and J. Clarke, *Physical Review Letters* **55**, 1543 (1985).
- [114] J. Clarke, A. N. Cleland, M. H. Devoret, D. Esteve, and J. M. Martinis, *Science* **239**, 992 (1988).

- [115] J. E. Mooij, T. P. Orlando, L. Levitov, L. Tian, C. H. van der Wal, and S. Lloyd, *Science* **285**, 1036 (1999).
- [116] I. Chiorescu, Y. Nakamura, C. J. P. M. Harmans, and J. E. Mooij, *Science* **299**, 1869 (2003).
- [117] C. H. van der Wal, A. C. J. ter Haar, F. K. Wilhelm, R. N. Schouten, C. J. P. M. Harmans, T. P. Orlando, S. Lloyd, and J. E. Mooij, *Science* **290**, 773 (2000).
- [118] V. Bouchiat, D. Vion, P. Joyez, D. Esteve, and M. H. Devoret, *Phys. Scr. Physica Scripta* **76**, 165 (1998).
- [119] Y. Nakamura, Y. A. Pashkin, and J. S. Tsai, *Nature* **398**, 786 (1999).
- [120] J. Koch, T. M. Yu, J. Gambetta, A. A. Houck, D. I. Schuster, J. Majer, A. Blais, M. H. Devoret, S. M. Girvin, and R. J. Schoelkopf, *Physical Review A* **76**, 42319 (2007), [arXiv:0703002v2 \[cond-mat\]](https://arxiv.org/abs/0703002v2) .
- [121] V. E. Manucharyan, J. Koch, L. I. Glazman, and M. H. Devoret, *Science* **326**, 113 (2009).
- [122] J. A. Schreier, A. A. Houck, J. Koch, D. I. Schuster, B. R. Johnson, J. M. Chow, J. M. Gambetta, J. Majer, L. Frunzio, M. H. Devoret, S. M. Girvin, and R. J. Schoelkopf, *Physical Review B* **77**, 180502 (2008).
- [123] D. Wineland, C. Monroe, W. Itano, B. King, D. Leibfried, D. Meekhof, C. Myatt, and C. Wood, *Fortschritte der Physik* **46**, 363 (1998).
- [124] E. M. Purcell, *Physical Review* **69** (1946).
- [125] D. Kleppner, *Physical Review Letters* **47**, 233 (1981).
- [126] E. T. Jaynes and F. W. Cummings, *Proceedings of the IEEE* **51**, 89 (1963).
- [127] J. H. Eberly, N. B. Narozhny, and J. J. Sanchez-Mondragon, *Physical Review Letters* **44**, 1323 (1980).
- [128] M. Brune, F. Schmidt-Kaler, A. Maali, J. Dreyer, E. Hagley, J. M. Raimond, and S. Haroche, *Physical Review Letters* **76**, 1800 (1996).
- [129] M. Devoret, (1996).
- [130] G. Burkard, R. H. Koch, and D. P. DiVincenzo, *Physical Review B* **69**, 064503 (2004).
- [131] S. E. Nigg, H. Paik, B. Vlastakis, G. Kirchmair, S. Shankar, L. Frunzio, M. H. Devoret, R. J. Schoelkopf, and S. M. Girvin, *Physical Review Letters* **108**, 240502 (2012).
- [132] F. Solgun, D. W. Abraham, and D. P. DiVincenzo, *Physical Review B* **90**, 134504 (2014).
- [133] R. M. Foster, *Bell System Technical Journal* **3**, 259 (1924).
- [134] O. Brune, *Synthesis of a finite two-terminal network whose driving-point impedance is a prescribed function of frequency*, *Ph.D. thesis*, Massachusetts Institute of Technology (1931).

- [135] A. A. Houck, J. A. Schreier, B. R. Johnson, J. M. Chow, J. Koch, J. M. Gambetta, D. I. Schuster, L. Frunzio, M. H. Devoret, S. M. Girvin, and R. J. Schoelkopf, [Physical Review Letters](#) **101**, 4 (2008).
- [136] M. Malekakhlagh, A. Petrescu, and H. E. Türeci, [Physical Review Letters](#) **119**, 073601 (2017).
- [137] Z. Leghtas, S. Touzard, I. M. Pop, A. Kou, B. Vlastakis, A. Petrenko, K. M. Sliwa, A. Narla, S. Shankar, M. J. Hatridge, M. Reagor, L. Frunzio, R. J. Schoelkopf, M. Mirrahimi, and M. H. Devoret, [Science](#) **347**, 853 (2015).
- [138] W. Pfaff, C. J. Axline, L. D. Burkhardt, U. Vool, P. Reinhold, L. Frunzio, L. Jiang, M. H. Devoret, and R. J. Schoelkopf, [Nature Physics](#) **13**, 882 (2017), [arXiv:1612.05238](#) .
- [139] J. M. Chow, *Quantum Information Processing with Superconducting Qubits*, Ph.D. thesis, Yale University (2010).
- [140] A. Clerk, M. H. Devoret, S. M. Girvin, F. Marquardt, and R. J. Schoelkopf, [Reviews of Modern Physics](#) **82**, 1155 (2010), [arXiv:0810.4729](#) .
- [141] F. Motzoi, J. Gambetta, P. Rebentrost, and F. Wilhelm, [Physical Review Letters](#) **103**, 110501 (2009).
- [142] C. Axline, L. Burkhardt, W. Pfaff, M. Zhang, K. Chou, P. Campagne-Ibarcq, P. Reinhold, L. Frunzio, S. M. Girvin, L. Jiang, M. H. Devoret, and R. J. Schoelkopf, (2017), [arXiv:1712.05832](#) .
- [143] S. Rosenblum, Y. Gao, P. Reinhold, C. Wang, C. Axline, L. Frunzio, S. Girvin, L. Jiang, M. Mirrahimi, M. Devoret, and R. Schoelkopf, [e-print](#) (2017), [arXiv:1709.05425](#) .
- [144] M. Hatridge, S. Shankar, M. Mirrahimi, F. Schackert, K. Geerlings, T. Brecht, K. M. Sliwa, B. Abdo, L. Frunzio, S. M. Girvin, R. J. Schoelkopf, and M. H. Devoret, [Science](#) **339**, 178 (2013).
- [145] N. Bergeal, F. Schackert, M. Metcalfe, R. Vijay, V. E. Manucharyan, L. Frunzio, D. E. Prober, R. J. Schoelkopf, S. M. Girvin, and M. H. Devoret, [Nature](#) **465**, 64 (2010).
- [146] A. Narla, *Flying Qubit Operations in Superconducting Circuits*, Ph.D. thesis, Yale University (2017).
- [147] S. Shankar, M. Hatridge, Z. Leghtas, K. M. Sliwa, A. Narla, U. Vool, S. M. Girvin, L. Frunzio, M. Mirrahimi, and M. H. Devoret, [Nature](#) **504**, 419 (2013).
- [148] M. Dalmonte, S. I. Mirzaei, P. R. Muppalla, D. Marcos, P. Zoller, and G. Kirchmair, [Physical Review B](#) **92**, 174507 (2015).
- [149] M. Reagor, W. Pfaff, C. Axline, R. W. Heeres, N. Ofek, K. Sliwa, E. Holland, C. Wang, J. Blumoff, K. Chou, M. J. Hatridge, L. Frunzio, M. H. Devoret, L. Jiang, and R. J. Schoelkopf, [Physical Review B](#) **94**, 014506 (2016).

- [150] C. Axline, M. Reagor, R. Heeres, P. Reinhold, C. Wang, K. Shain, W. Pfaff, Y. Chu, L. Frunzio, and R. J. Schoelkopf, [Applied Physics Letters](#) **109**, 042601 (2016).
- [151] D. I. Schuster, A. A. Houck, J. A. Schreier, A. Wallraff, J. M. Gambetta, A. Blais, L. Frunzio, J. Majer, B. Johnson, M. H. Devoret, S. M. Girvin, and R. J. Schoelkopf, [Nature](#) **445**, 515 (2007).
- [152] a. a. Houck, D. I. Schuster, J. M. Gambetta, J. a. Schreier, B. R. Johnson, J. M. Chow, L. Frunzio, J. Majer, M. H. Devoret, S. M. Girvin, and R. J. Schoelkopf, [Nature](#) **449**, 328 (2007).
- [153] B. R. Johnson, M. D. Reed, A. A. Houck, D. I. Schuster, L. S. Bishop, E. Ginossar, J. M. Gambetta, L. DiCarlo, L. Frunzio, S. M. Girvin, and R. J. Schoelkopf, [Nature Physics](#) **6**, 663 (2010).
- [154] H. Paik, D. I. Schuster, L. S. Bishop, G. Kirchmair, G. Catelani, a. P. Sears, B. R. Johnson, M. J. Reagor, L. Frunzio, L. I. Glazman, S. M. Girvin, M. H. Devoret, and R. J. Schoelkopf, [Physical Review Letters](#) **107**, 240501 (2011).
- [155] M. Reagor, *Superconducting Cavities for Circuit Quantum Electrodynamics*, Ph.D. thesis, Yale University (2015).
- [156] C. Wang, C. Axline, Y. Y. Gao, T. Brecht, Y. Chu, L. Frunzio, M. H. Devoret, and R. J. Schoelkopf, [Applied Physics Letters](#) **107**, 162601 (2015).
- [157] G. Kirchmair, B. Vlastakis, Z. Leghtas, S. E. Nigg, H. Paik, E. Ginossar, M. Mirrahimi, L. Frunzio, S. M. Girvin, and R. J. Schoelkopf, [Nature](#) **495**, 205 (2013).
- [158] B. Vlastakis, G. Kirchmair, Z. Leghtas, S. E. Nigg, L. Frunzio, S. M. Girvin, M. Mirrahimi, M. H. Devoret, and R. J. Schoelkopf, [Science \(New York, N.Y.\)](#) **342**, 607 (2013).
- [159] L. Sun, A. Petrenko, Z. Leghtas, B. Vlastakis, G. Kirchmair, K. M. Sliwa, A. Narla, M. Hatridge, S. Shankar, J. Blumoff, L. Frunzio, M. Mirrahimi, M. H. Devoret, and R. J. Schoelkopf, [Nature](#) **511**, 444 (2014).
- [160] T. Brecht, *Micromachined Quantum Circuits*, Ph.D. thesis, Yale University (2017).
- [161] M. Reagor, H. Paik, G. Catelani, L. Sun, C. Axline, E. Holland, I. M. Pop, N. A. Masluk, T. Brecht, L. Frunzio, M. H. Devoret, L. Glazman, and R. J. Schoelkopf, [Applied Physics Letters](#) **102**, 192604 (2013).
- [162] C. Wang, Y. Y. Gao, I. M. Pop, U. Vool, C. Axline, T. Brecht, R. W. Heeres, L. Frunzio, M. H. Devoret, G. Catelani, L. I. Glazman, and R. J. Schoelkopf, [Nature Communications](#) **5**, 5836 (2014).
- [163] C. Rigetti, J. M. Gambetta, S. Poletto, B. L. T. Plourde, J. M. Chow, A. D. Córcoles, J. A. Smolin, S. T. Merkel, J. R. Rozen, G. A. Keefe, M. B. Rothwell, M. B. Ketchen, and M. Steffen, [Physical Review B](#) **86**, 100506 (2012).

- [164] C. Wang, Y. Y. Gao, P. Reinhold, R. W. Heeres, N. Ofek, K. Chou, C. Axline, M. Reagor, J. Blumoff, K. M. Sliwa, L. Frunzio, S. M. Girvin, L. Jiang, M. Mirrahimi, M. H. Devoret, and R. J. Schoelkopf, *Science* **352**, 1087 (2016), [arXiv:1601.05505](#) .
- [165] A. P. Sears, *Extending Coherence in Superconducting Qubits : from microseconds to milliseconds*, Ph.D. thesis (2013).
- [166] K. S. Chou, J. Z. Blumoff, C. S. Wang, P. C. Reinhold, C. J. Axline, Y. Y. Gao, L. Frunzio, M. H. Devoret, L. Jiang, and R. J. Schoelkopf, (2018), [arXiv:1801.05283](#) .
- [167] J. M. Gambetta, A. D. Córcoles, S. T. Merkel, B. R. Johnson, J. A. Smolin, J. M. Chow, C. A. Ryan, C. Rigetti, S. Poletto, T. A. Ohki, M. B. Ketchen, and M. Steffen, *Physical Review Letters* **109**, 240504 (2012).
- [168] J. Gambetta, A. Blais, D. I. Schuster, A. Wallraff, L. Frunzio, J. Majer, M. H. Devoret, S. M. Girvin, and R. J. Schoelkopf, *Physical Review A* **74**, 042318 (2006).
- [169] A. P. Sears, A. Petrenko, G. Catelani, L. Sun, H. Paik, G. Kirchmair, L. Frunzio, L. I. Glazman, S. M. Girvin, and R. J. Schoelkopf, *Physical Review B* **86**, 180504 (2012).
- [170] T. Brecht, W. Pfaff, C. Wang, Y. Chu, L. Frunzio, M. H. Devoret, and R. J. Schoelkopf, *npj Quantum Information* **2**, 16002 (2016).
- [171] P. Wang, L. Qin, X.-Q. Li, and F. Nori, , **9** (2014), [arXiv:1404.3870](#) .
- [172] Y. Liu, *Quantum Feedback Control of Multiple Superconducting Qubits*, Ph.D. thesis, Yale University (2016).
- [173] A. P. Petrenko, *Enhancing the Lifetime of Quantum Information with Cat States in Superconducting Cavities*, Ph.D. thesis, Yale University (2017).
- [174] J. Gambetta, W. A. Braff, A. Wallraff, S. M. Girvin, and R. J. Schoelkopf, *Physical Review A* **76**, 012325 (2007).
- [175] C. A. Ryan, B. R. Johnson, J. M. Gambetta, J. M. Chow, M. P. da Silva, O. E. Dial, and T. A. Ohki, *Physical Review A* **91**, 022118 (2015).
- [176] R. W. Heeres, B. Vlastakis, E. Holland, S. Krastanov, V. V. Albert, L. Frunzio, L. Jiang, and R. J. Schoelkopf, *Physical Review Letters* **115**, 137002 (2015).
- [177] J. M. Chow, L. DiCarlo, J. M. Gambetta, F. Motzoi, L. Frunzio, S. M. Girvin, and R. J. Schoelkopf, *Physical Review A* **82**, 040305 (2010).
- [178] E. Magesan, J. M. Gambetta, and J. Emerson, *Physical Review A* **85**, 042311 (2012).
- [179] J. M. Epstein, A. W. Cross, E. Magesan, and J. M. Gambetta, *Physical Review A* **89**, 062321 (2014), [arXiv:1308.2928](#) .
- [180] H. Ball, T. M. Stace, S. T. Flammia, and M. J. Biercuk, *Physical Review A* **93**, 022303 (2016).

- [181] T. Proctor, K. Rudinger, K. Young, M. Sarovar, and R. Blume-Kohout, [Physical Review Letters](#) **119**, 130502 (2017).
- [182] J. Kelly, R. Barends, B. Campbell, Y. Chen, Z. Chen, B. Chiaro, A. Dunsworth, A. G. Fowler, I.-C. Hoi, E. Jeffrey, A. Megrant, J. Mutus, C. Neill, P. J. J. O'Malley, C. Quintana, P. Roushan, D. Sank, A. Vainsencher, J. Wenner, T. C. White, A. N. Cleland, and J. M. Martinis, [Physical Review Letters](#) **112**, 240504 (2014).
- [183] P. J. O'Malley, J. Kelly, R. Barends, B. Campbell, Y. Chen, Z. Chen, B. Chiaro, A. Dunsworth, A. G. Fowler, I. C. Hoi, E. Jeffrey, A. Megrant, J. Mutus, C. Neill, C. Quintana, P. Roushan, D. Sank, A. Vainsencher, J. Wenner, T. C. White, A. N. Korotkov, A. N. Cleland, and J. M. Martinis, [Physical Review Applied](#) **3**, 1 (2015), [arXiv:1411.2613](#).
- [184] Z. Chen, J. Kelly, C. Quintana, R. Barends, B. Campbell, Y. Chen, B. Chiaro, A. Dunsworth, A. G. Fowler, E. Lucero, E. Jeffrey, A. Megrant, J. Mutus, M. Neeley, C. Neill, P. J. J. O'Malley, P. Roushan, D. Sank, A. Vainsencher, J. Wenner, T. C. White, A. N. Korotkov, and J. M. Martinis, [Physical Review Letters](#) **116**, 020501 (2016).
- [185] R. W. Heeres, P. Reinhold, N. Ofek, L. Frunzio, L. Jiang, M. H. Devoret, and R. J. Schoelkopf, [Nature Communications](#) **8**, 94 (2017).
- [186] C. K. Law and J. H. Eberly, [Physical Review Letters](#) **76**, 1055 (1996).
- [187] S. Krastanov, V. V. Albert, C. Shen, C.-L. Zou, R. W. Heeres, B. Vlastakis, R. J. Schoelkopf, and L. Jiang, [Physical Review A](#) **92**, 040303 (2015), [arXiv:1502.08015](#).
- [188] N. Khaneja, T. Reiss, C. Kehlet, T. Schulte-Herbrüggen, and S. J. Glaser, [Journal of Magnetic Resonance](#) **172**, 296 (2005).
- [189] D. Ristè, C. C. Bultink, K. W. Lehnert, and L. DiCarlo, [Physical Review Letters](#) **109**, 240502 (2012), [arXiv:1207.2944](#).
- [190] D. Ristè and L. DiCarlo, in [Superconducting Devices in Quantum Optics](#) (Springer, Cham, 2016) pp. 187–216.
- [191] U. Leonhardt, [Measuring the Quantum State of Light](#) (Cambridge University Press, New York, 1997).
- [192] M. Grant and S. Boyd, in [Recent Advances in Learning and Control](#), Lecture Notes in Control and Information Sciences, edited by V. Blondel, S. Boyd, and H. Kimura (Springer-Verlag Limited, 2008) pp. 95–110.
- [193] M. Grant and S. Boyd, “[CVX: Matlab Software for Disciplined Convex Programming, version 2.1](#),” (2014).
- [194] J. M. Gambetta, C. E. Murray, Y.-K.-K. Fung, D. T. McClure, O. Dial, W. Shanks, J. W. Sleight, and M. Steffen, [IEEE Transactions on Applied Superconductivity](#) **27**, 1 (2017), [arXiv:1605.08009](#).

- [195] H. A. Simon, [Proceedings of the American Philosophical Society](#) **106**, 467 (1962).
- [196] L. H. Hartwell, J. J. Hopfield, S. Leibler, and A. W. Murray, [Nature](#) **402**, C47 (1999).
- [197] G. P. Wagner, M. Pavlicev, and J. M. Cheverud, [Nature Reviews Genetics](#) **8**, 921 (2007).
- [198] J. Von Neumann, *Automata studies* **34**, 43 (1956).
- [199] H. Bernien, B. Hensen, W. Pfaff, G. Koolstra, M. S. Blok, L. Robledo, T. H. Taminiau, M. Markham, D. J. Twitchen, L. Childress, and R. Hanson, [Nature](#) **497**, 86 (2013).
- [200] D. Hucul, I. V. Inlek, G. Vittorini, C. Crocker, S. Debnath, S. M. Clark, and C. Monroe, [Nature Physics](#) **11**, 37 (2014).
- [201] A. Narla, S. Shankar, M. Hatridge, Z. Leghtas, K. M. Sliwa, E. Zalys-Geller, S. O. Mundhada, W. Pfaff, L. Frunzio, R. J. Schoelkopf, and M. H. Devoret, [Physical Review X](#) **6**, 031036 (2016).
- [202] N. Roch, M. E. Schwartz, F. Motzoi, C. Macklin, R. Vijay, A. W. Eddins, A. N. Korotkov, K. B. Whaley, M. Sarovar, and I. Siddiqi, [Physical Review Letters](#) **112**, 170501 (2014).
- [203] P. Campagne-Ibarcq, E. Zalys-Geller, A. Narla, S. Shankar, P. Reinhold, L. D. Burkhardt, C. J. Axline, W. Pfaff, L. Frunzio, R. J. Schoelkopf, and M. H. Devoret, (2017), [arXiv:1712.05854](#) .
- [204] M. H. Michael, M. Silveri, R. T. Brierley, V. V. Albert, J. Salmilehto, L. Jiang, and S. M. Girvin, [Physical Review X](#) **6**, 031006 (2016), [arXiv:1602.00008](#) .
- [205] M. Riebe, H. Häffner, C. F. Roos, W. Hänsel, J. Benhelm, G. P. T. Lancaster, T. W. Körber, C. Becher, F. Schmidt-Kaler, D. F. V. James, and R. Blatt, [Nature](#) **429**, 734 (2004).
- [206] M. D. Barrett, J. Chiaverini, T. Schaetz, J. Britton, W. M. Itano, J. D. Jost, E. Knill, C. Langer, D. Leibfried, R. Ozeri, and D. J. Wineland, [Nature](#) **429**, 737 (2004).
- [207] J. F. Sherson, H. Krauter, R. K. Olsson, B. Julsgaard, K. Hammerer, I. Cirac, and E. S. Polzik, [Nature](#) **443**, 557 (2006).
- [208] S. Olmschenk, D. N. Matsukevich, P. Maunz, D. Hayes, L.-M. Duan, and C. Monroe, [Science](#) **323**, 486 (2009).
- [209] L. Steffen, Y. Salathe, M. Oppliger, P. Kurpiers, M. Baur, C. Lang, C. Eichler, G. Puebla-Hellmann, A. Fedorov, and A. Wallraff, [Nature](#) **500**, 319 (2013).
- [210] J. Eisert, K. Jacobs, P. Papadopoulos, and M. B. Plenio, [Physical Review A](#) **62**, 052317 (2000).
- [211] Y.-F. Huang, X.-F. Ren, Y.-S. Zhang, L.-M. Duan, and G.-C. Guo, [Physical Review Letters](#) **93**, 240501 (2004).

- [212] W.-B. Gao, A. M. Goebel, C.-Y. Lu, H.-N. Dai, C. Wagenknecht, Q. Zhang, B. Zhao, C.-Z. Peng, Z.-B. Chen, Y.-A. Chen, and J.-W. Pan, [Proceedings of the National Academy of Sciences](#) **107**, 20869 (2010).
- [213] V. P. K., D. Joy, B. K. Behera, and P. K. Panigrahi, (2017), [arXiv:1709.05697](#) .
- [214] J. Chiaverini, D. Leibfried, T. Schaetz, M. D. Barrett, R. B. Blakestad, J. Britton, W. M. Itano, J. D. Jost, E. Knill, C. Langer, R. Ozeri, and D. J. Wineland, [Nature](#) **432**, 602 (2004).
- [215] A. Córcoles, E. Magesan, S. J. Srinivasan, A. W. Cross, M. Steffen, J. M. Gambetta, and J. M. Chow, [Nature Communications](#) **6**, 6979 (2015).
- [216] J. Kelly, R. Barends, A. G. Fowler, A. Megrant, E. Jeffrey, T. C. White, D. Sank, J. Y. Mutus, B. Campbell, Y. Chen, Z. Chen, B. Chiaro, A. Dunsworth, I.-C. Hoi, C. Neill, P. J. J. O'Malley, C. Quintana, P. Roushan, A. Vainsencher, J. Wenner, A. N. Cleland, and J. M. Martinis, [Nature](#) **519**, 66 (2015).
- [217] D. Ristè, S. Poletto, M.-Z. Huang, A. Bruno, V. Vesterinen, O.-P. Saira, and L. DiCarlo, [Nature Communications](#) **6**, 6983 (2015).
- [218] J. Cramer, N. Kalb, M. A. Rol, B. Hensen, M. S. Blok, M. Markham, D. J. Twitchen, R. Hanson, and T. H. Taminiau, [Nature Communications](#) **7**, 11526 (2016).
- [219] N. M. Linke, M. Gutierrez, K. A. Landsman, C. Figgatt, S. Debnath, K. R. Brown, and C. Monroe, (2017), [arXiv:arXiv:1611.06946v2](#) .
- [220] J. Zhang, R. Laflamme, and D. Suter, [Physical Review Letters](#) **109**, 100503 (2012).
- [221] D. Nigg, M. Mueller, E. A. Martinez, P. Schindler, M. Hennrich, T. Monz, M. A. Martin-Delgado, and R. Blatt, , **7** (2014), [arXiv:1403.5426](#) .
- [222] H. Paik, A. Mezzacapo, M. Sandberg, D. T. McClure, B. Abdo, A. D. Córcoles, O. Dial, D. F. Bogorin, B. L. T. Plourde, M. Steffen, A. W. Cross, J. M. Gambetta, and J. M. Chow, [Physical Review Letters](#) **117**, 250502 (2016).
- [223] A. W. Cross and J. M. Gambetta, [Physical Review A](#) **91**, 032325 (2015).
- [224] D. C. McKay, C. J. Wood, S. Sheldon, J. M. Chow, and J. M. Gambetta, [Physical Review A](#) **96**, 022330 (2017).
- [225] S. Rosenblum, P. Reinhold, M. Mirrahimi, L. Jiang, L. Frunzio, and R. J. Schoelkopf, , **1** (2018), [arXiv:1803.00102](#) .
- [226] J. I. Cirac, P. Zoller, H. J. Kimble, and H. Mabuchi, [Physical Review Letters](#) **78**, 3221 (1997).
- [227] S. D. Barrett and P. Kok, [Physical Review A](#) **71**, 060310 (2005).
- [228] C. H. Bennett, G. Brassard, S. Popescu, B. Schumacher, J. A. Smolin, and W. K. Wootters, [Physical Review Letters](#) **76**, 722 (1996), [arXiv:9511027 \[quant-ph\]](#) .

- [229] N. H. Nickerson, Y. Li, S. C. Benjamin, E. Dennis, A. Kitaev, A. Landahl, J. Preskill, H. Bombin, R. Raussendorf, J. Harrington, D. S. Wang, A. G. Fowler, L. C. L. Hollenberg, A. G. Fowler, M. Mariani, J. M. Martinis, A. N. Cleland, W. Dür, H.-J. Briegel, L. Jiang, Y. Li, S. C. Benjamin, D. L. Moehring, E. Campbell, K. Fujii, K. Yamamoto, J. Edmonds, V. Kolmogorov, P. C. Maurer, M. Steger, C. Horsman, G. Duclos-Cianci, D. Poulin, J. R. Wootton, D. Loss, J. Ghosh, A. G. Fowler, M. R. Geller, S. C. Benjamin, B. W. Lovett, J. M. Smith, J. Benhelm, G. Kirchmair, C. F. Roos, R. Blatt, N. Y. Yao, and Y. Ping, [Nature Communications](#) **4**, 1756 (2013).
- [230] P. Kurpiers, P. Magnard, T. Walter, B. Royer, M. Pechal, J. Heinsoo, Y. Salathé, A. Akin, S. Storz, J.-C. Besse, S. Gasparinetti, A. Blais, and A. Wallraff, [, 1](#) (2017), [arXiv:1712.08593](#).
- [231] W. Dür and H. J. Briegel, [Reports on Progress in Physics](#) **70**, 1381 (2007).
- [232] S. Touzard, A. Grimm, Z. Leghtas, S. O. Mundhada, P. Reinhold, R. Heeres, C. Axline, M. Reagor, K. Chou, J. Blumoff, K. M. Sliwa, S. Shankar, L. Frunzio, R. J. Schoelkopf, M. Mirrahimi, and M. H. Devoret, [, 1](#) (2017), [arXiv:1705.02401](#).
- [233] M. Mirrahimi, Z. Leghtas, V. V. Albert, S. Touzard, R. J. Schoelkopf, L. Jiang, and M. H. Devoret, [New Journal of Physics](#) **16**, 045014 (2014).
- [234] N. E. Frattini, U. Vool, S. Shankar, A. Narla, K. M. Sliwa, and M. H. Devoret, [Applied Physics Letters](#) **110**, 222603 (2017), [arXiv:1702.00869](#).